INFORMATION TO USERS

This manuscript has been reproduced from the microfilm master. UMI films the text directly from the original or copy submitted. Thus, some thesis and dissertation copies are in typewriter face, while others may be from any type of computer printer.

The quality of this reproduction is dependent upon the quality of the copy submitted. Broken or indistinct print, colored or poor quality illustrations and photographs, print bleedthrough, substandard margins, and improper alignment can adversely affect reproduction.

In the unlikely event that the author did not send UMI a complete manuscript and there are missing pages, these will be noted. Also, if unauthorized copyright material had to be removed, a note will indicate the deletion.

Oversize materials (e.g., maps, drawings, charts) are reproduced by sectioning the original, beginning at the upper left-hand corner and continuing from left to right in equal sections with small overlaps.

ProQuest Information and Learning
300 North Zeeb Road, Ann Arbor, MI 48106-1346 USA
800-521-0600

Optical Tomography by Time-Resolved Diffuse Reflectance Measurements

William F. Long

Department of Chemistry
McGill University,
Montréal, Québec
Canada

October 2000

A thesis submitted to the Faculty of Graduate Studies and Research in partial fulfillment of the requirements of the degree of Doctor of Philosophy

Abstract

The understanding of the interaction of light with a scattering/absorbing medium provides a foundation needed for developing many applications in diagnostic medicine and industry. The objective of this research was to obtain quantitative depth-resolved information about absorbing constituents in a scattering medium.

Initially, the project focussed on quantification in samples where scattering and absorber concentration were variable. Using time resolved reflectance measurements, a series of statistical descriptors of the photon time distributions were calculated. Stepwise multilinear regression was used to formulate linear models from optimal linear combinations of the descriptors. It was found that the scattering coefficient, absorption coefficient and apparent particle diameter could be estimated to within 9, 10 and 7 % of their reference values respectively.

An array of radial reflectance measurements on layered scattering/absorbing samples was made to obtain information sensitive to sub-surface changes in absorption. As an initial approach to depth-resolved quantification, classical tomographic reconstruction techniques were used. However, due to the ambiguity of the reconstruction, extremely poor estimates of the sub-surface absorption resulted. Chemometric methods were then employed for enhanced quantification. By using stepwise multilinear regression with time-resolved data, the absorption coefficient in the top region of a sample could be estimated to within 2%. However, errors in the absorption coefficient estimations deep within a sample remained high.

Further improvements in sample quantification were made by linearizing the reconstruction problem. By using *a priori* information about sample composition in

upper regions, subsequent calibrations for lower regions were directed. Estimations of the absorption coefficient deep within a sample with hierarchical locally weighted calibration were obtainable at greater than 50% accuracy. This represented a 20% improvement at all sample depths over stepwise multilinear regression.

Confocal illumination and detection optics was also used for discriminating highly scattered photons from light, which follows a geometric path through a sample. When confocal optics were used together with information from the rising edge of time distribution, little enhancement in quantification was observed in comparison to an integrated signal. This important finding demonstrates that the confocal optical detection should be considered when imaging in scattering/absorbing media.

Résumé

La compréhension des interactions entre la lumière et un milieu diffractant fournit les bases requises au developpement de nombreuses applications en médecine diagnostique et en industrie. Le but de ce project était d'obtenir de l'information quantitative sur la distribution en profondeur des composantes absorbantes d'un milieu diffractant.

Initialement, le project se penchait sur la quantification d'échantillons dans lesquels les concentrations des éléments absorbants et diffractant variaient. En effectuant des mesures par reflectance dans le domaine temporel, une série de descripteurs statistiques des distributions temporelles photoniques a été calculée. La méthode de *stepwise multilinear regression* a été utilisée pour formuler des modèles linéaires à partir de combinaisons linéaires optimisée des descripteurs. Il a été démontré que les coefficients de diffraction, d'absorption, de même que le diamètre apparent des particles, pouvaient être estimés a 9, 10 et 7 % près de leur valeur de reference respective.

Un ensemble des mesures par reflectance radiale sur des échantillons diffractant/absorbants superposés a été effectué pour obtenir de l'information sur les variations de l'absorption en profondeur. Des techniques de reconstruction tomographiques classiques furent utilisés comme approche initiale de quantification selon une distribution en profondeur. Des très faibles estimés de l'absorption en profondeur ont été obtenus en raison de l'ambiguité de la reconstruction. La quantification a alors été amélioré en utilisant des méthods de chimométrie. Apres avoir appliqué *stepwise multilinear regression* aux données distribuées dans le temps, les coefficients d'absorption dans la partie supérieure d'un échantillon ont pu être estimés a 2% près.

Toutefois, les erreurs pour les coefficients d'absorption mesurés profondément dans l'échantillon sont demeurées élevées.

Des améliorations subséquentes ont été apportées à la quantification des échantillons en linéarisant le problème de reconstruction. En utilisant les informations disponibles sur le composition de la partie supérieure des échantillons, des calibrations subséquentes des parties inférieures ont été. Des estimés de coefficients d'absorption dans les parties profondes d'un échantillon ont été obtenus avec une exactitude de plus de 50%, grâce à une calibration hiérarchique pondérée localement. Ceci se traduisit par une amélioration de 20% sur les estimés a toutes profondeurs par rapport à la méthode de *stepwise multilinear regression*.

La géométrie optique confocale a été également utilisée pour différencier les photons très diffractées de la lumière qui suit un itinéraire géométrique au travers d'un échantillon. Lorsque la géométrie optique confocale a été combinée à l'information contenue dans la section ascendante de la distribution temporelle, des petites améliorations furent observées par rapport à un signal intégré. Cette découverte importante démontre que la détection utilisant la géométrie confocale devrait être considérée pour l'imagerie en milieux diffractants et/ou absorbants.

Table of Contents

List of Tables

List of Figures

List of Abbreviations and Symbols

CAT	computer aided tomography
HCKNN	hierarchical classification with K nearest neighbour analysis
HLRB	hierarchical locally weighted regression and binning
LWR	local weighted regression
MFP	mean free path (mm)
MLR	multiple linear regression
NA	numerical aperture
NIR	near infrared
OCT	optical coherence tomography
OD	optical density
PLS	partial least squares regression
PRESS	predicted residual error sum of squares
SMLR	stepwise multilinear regression
a	logarithm of the area under time distribution
a_f	logarithm of the area under the trailing portion of the time distribution
a_r	logarithm of the area under the rising portion of the time distribution
A	absorption
$A(\mathbf{r},\tau)$	autocorrelation function of the time distribution at a given radius
c	speed of light in vacuum (0.299 mm ps^{-1})
g	mean cosine of the scattering angle
I	intensity
k	kurtosis

l	pathlength (mm)
m_f	mean slope of the trailing portion of the time distribution
m_r	mean slope of the rising portion of the time distribution
p	peak maximum of the time distribution
r	source detection separation (mm)
s	skewness of the time distribution
t	time (ps)
t_f	mean trailing time of the time distribution
t_r	mean rise time of the time distribution
u_n	n^{th} moment of the time distribution
x	direction parallel to sample surface
y	direction parallel to sample surface and orthogonal to x
z	depth into sample (axial direction)
ϕ	solid volume fraction
Φ	relative longitudinal scattering angle
Θ	relative azimuthal scattering angle
τ	time lag or lead (ps)
ε	molar absorptivity (concentration × length)$^{-1}$
λ	wavelength (nm)
υ_p	effective diameter (optical units)
μ_a	absorption coefficient (mm^{-1})
μ_s	scattering coefficient (mm^{-1})

Contribution of Authors

Listed below are the articles included as part of this dissertation and an outline of the responsibility of each author. Overall, Dr. Burns was both thesis supervisor and critical reviewer to Mr. Long.

Chapter 2

Long, W. F.; Burns, D. H. Particle Sizing and Optical Constant Measurement in Granular Samples using Statistical Descriptors of Photon Time-of-Flight Distributions, *Anal. Chim. Acta*, submitted June 2000.

Mr. Long designed the experimental procedure, assembled the time-of-flight instrument, and collected and analyzed all experimental data. Dr. Burns suggested using statistical descriptors for data analysis. The stepwise multi-linear regression routine and the statistical descriptor algorithms originally written by Larry Leonardi were rewritten and expanded upon by Mr. Long. The manuscript prepared for publication was written by Mr. Long and edited by Dr. Burns.

Chapter 3

Long, W. F.; Burns, D. H. Optical Tomographic Reconstruction from Diffuse Remittance in Scattering Media Using Partial Least Squares Estimation, *Anal. Chim. Acta* **1997**, *348*, 553-563.

Mr. Long designed the experimental procedure, assembled the instrument, and collected and analyzed the experimental data. Dr. Burns suggested methods for analyzing the data and aided in the experimental setup. The manuscript prepared for publication was written by Mr. Long and edited by Dr. Burns.

Chapter 4

Long, W. F.; Burns, D. H. Optical Tomography in Scattering Media from Photon Time-of-Flight Diffuse Reflectance Measurements: A Chemometric Approach, *J. Chemom.* **1999**, *13*, 251-264.

Mr. Long designed the experimental procedure, assembled the time-of-flight instrument, and collected the experimental data. Larry Leonardi initially assisted Mr. Long with the instrumentation. Dr. Burns suggested using different chemometric approaches for analyzing the data. The manuscript prepared for publication was written by Mr. Long and edited by Dr. Burns.

Chapter 5

Long, W. F.; Burns, D. H. A Hierarchical Local Weighted Calibration and Classification Approach to Depth Resolved Quantification in Scattering Media using Photon Time-of-Flight Measurements, *Chemom. Intell. Lab. Syst.*, accepted June 2000.

Mr. Long designed the experimental procedure, and collected and analyzed all experimental data. Mr. Long conceived and suggested using hierarchical local weighted

calibration for analyzing the data. Dr. Burns further suggested using a classification approach data analysis. The manuscript prepared for publication was written by Mr. Long and edited by Dr. Burns.

Chapter 6

Long, W. F.; Gributs, C. E.; Burns, D. H. Quantification in Highly Scattering Absorbing Layered Samples using Photon Time-of-Flight Measurements and Confocal Optical Geometry, *Vib. Spectrosc.*, submitted August 2000.

Mr. Long designed the experimental procedure, and set up the experimental equipment. Experimental data was collected by Ms. Gributs. The imaging methodology was developed by Mr. Long. Subsequent data analysis was done by both Mr. Long and Ms. Gributs. Dr. Burns suggested approaches for interpreting the data. The manuscript prepared for publication was written by Mr. Long and edited by Dr. Burns.

Contributions to Original Knowledge

1. A method for estimating the absorption and scattering properties of coated granular samples using statistical descriptors of the diffuse reflectance photon time-of-flight distribution was developed. In particular, changes in sample scattering and absorption were found to be most correlated with statistical descriptors associated with the rising and trailing portions of the time-of-flight distribution, respectively.
2. Several chemometric methods for quantitative depth-resolved imaging in scattering/absorbing media were evaluated. In general, estimates of absorption in the surface regions were better than those determined in lower regions. By incorporating *a priori* knowledge into the overall reconstruction methodology, a 20% improvement was obtained compared with estimates made independently in each region.
3. The autocorrelated photon time-of-flight distribution was evaluated as a means for robust quantification of absorption in scattering media. The autocorrelation function for the solution of the time-resolved diffusion equation was derived. Autocorrelated data was determined to be sensitive to changes in sample composition both in theory and experiment. In addition, by utilizing an optical correlator for detection or an electronic signal mixer, the complexity of instrumentation may be reduced.
4. A system for time-resolved diffuse reflectance measurements using confocal optics was developed for quantification in scattering/absorbing samples. Reasonable estimates of the absorption coefficient were obtained in 3 mm thick samples. In addition, confocal illumination and detection optics were shown to provide a simplified means for obtaining multi-perspective information from layered samples without the need for time-resolved measurements.

Acknowledgments

This major project involved a lot of hard work and I have many people to thank for their support, patience and assistance.

I would like to thank my supervisor Professor David H. Burns, for his encouragement, support and advice throughout my years at McGill. Dave has taught me that "if its not fun its not worth doing" and to "make it so."

I thank the National Sciences and Engineering Research Council (NSERC) and Fonds pour la Formation de Chercheurs et l'Aide à la Recherche (Fonds FCAR) whose financial support have made this research possible.

I also thank Larry Leonardi, Claudia Gributs, He Xiao, Ania Fafara, Mike Rybak and Dan Williams who made my graduate school life interesting. They have been my loyal partners in procrastination.

Finally, I would especially like to thank Stéphane Kordahi, Shahul Nilar and my parents for their support and encouragement.

Chapter 1 Introduction

1.1 Overview

The goal of this research was to investigate and develop methods for non-invasive quantification of absorbing constituents in layered scattering media. Examples of such layered scattering systems include human skin, composite coatings, many fruits and grains and translucent product/container systems. Quantification of the absorbing species in these examples may give measures of tissue health, subsurface corrosion, product freshness and composition. In general, there are two approaches in which layered samples may be quantified: invasively and non-invasively. With an invasive approach, the sample requires modification prior to analysis. Although invasive methods allow for direct analysis, the nature of the technique may be time-consuming, cost-ineffective or produce biased results. With non-invasive techniques of analysis, such as that provided by near infrared spectroscopy, there exists the possibility for rapid analysis with little or no sample preparation. In this study, chemometric analysis of time resolved near-infrared spectroscopic measurements were employed for quantification of scattering media.

The research was divided into three major phases. In the first phase, the scattering and absorption properties of granular samples were quantified using time-resolved diffuse reflectance signals. Sample calibrations were constructed using a series of descriptors sensitive to changes in the photon time-of-flight distribution. This procedure allowed for quantitative estimates of scattering and absorption in samples of unknown composition.

In the second phase of the research, quantification in layered scattering/absorbing samples was done. Both steady-state and time-resolved reflectance measurements were

made to obtain information sensitive to sub-surface sample composition. Chemometric approaches to sample calibration allowed depth-resolved estimates of absorption to be made in samples of unknown composition. In addition, the chemometrical approach to analysis provided a means to investigate the nature of photon propagation in layered media.

In the final phase, time-resolved and steady-state confocal imaging was employed for analysis. With this approach, quantification of absorbing constituents was done without calibration. This method offers the advantage of simple, rapid analysis of layered scattering/absorbing samples.

This dissertation is presented in seven chapters that develop the three phases of the research. The introductory chapter provides an overview of near-infrared analysis of scattering media. The physics of light transport, imaging and quantification methodologies are also presented.

1.2 Introduction to Near Infrared Sample Characterization

In 1800, William Herschel experimented with a prism and a thermometer to determine which color in the visible spectrum was responsible for heat in sunlight. He observed that when the thermometer was positioned past the red end of spectrum, a marked temperature change occurred.[1] He named this invisible light infrared, meaning 'below red'. Over the next eighty years, the infrared portion of the electromagnetic spectrum (typically defined from 750 nm to 2500 nm) remained primarily a curiosity, as it was difficult to make spectroscopic measurements in the region. With the development

of radiation dispersion and detection methods in the 1880s, the work of Abbey and Festing[2] and later by Coblentz[3] led to the recording of infrared spectra of well over one hundred organic compounds. However, it was not until World War II that the use of infrared spectroscopy became more wide spread with the development of commercial instruments for routine analysis.[4]

In the 1950s, further advances in infrared instrumentation provided a means for spectroscopic analysis on a wider range of materials. Spectroscopists primarily concentrated on the mid-IR range from ~1500 to 6000 nm because it was found that many compounds exhibited a unique spectrum or 'fingerprint' in this region.[5] Near infrared assessment of complex samples debuted in the late 1950s when the United States Drug Administration required new methods for rapid analysis of agricultural commodities. Work by Karl Norris demonstrated that diffuse reflectance spectra of complex biological samples could be obtained using NIR light.[6] This important finding led to a vast increase in the range of possible analyses. Currently, NIR spectroscopy is used as an analysis tool in many fields from agriculture to medicine.

In industry, near infrared (NIR) spectroscopy is used in the analysis of latex suspensions for paints,[7] particle sizing[8,9] and for quality control.[10-14] It is also used for pharmaceutical tablet analysis,[15] and determining moisture content in foods.[16-18] The success of the NIR techniques of analysis stem from its speed, ease of sample preparation, multiplicity of analyses from a single spectrum and its non-consumption of the sample.[19]

One of the most exciting applications of NIR spectroscopy is in the analysis of living samples. In clinical medicine, tracking changes in the physiological or metabolic

state of tissue is key in diagnosis. Using NIR light, hemoglobin,[20-24] myoglobin[25-27] and cytochrome aa_3[28-32] levels may be determined *in vivo*. The development of pulse oximetry systems has now revolutionized patient blood oxygenation monitoring.[26,27] Using a pair of NIR wavelengths, the relative amount of oxygenated hemoglobin in blood may be monitored. The success of this non-invasive technique has made pulse oximetry a valuable tool in neonatal and intensive care units.[33-35] Currently, NIR methods are being developed for non-invasive glucose monitoring.[36-39] Although controversy persists about whether this goal has been attained, such a measurement will offer the possibility for rapid analysis of blood sugar levels for diabetic patients. Another approach to critical care monitoring is the determination of lactate levels in whole blood. This is has done using a minimally invasive approach *in vitro*.[40,41]

In addition to patient monitoring, NIR tissue spectroscopy is being used to diagnose disease. Through statistical analysis of NIR tissue spectra collected from a population, spectroscopic markers of disease may be found.[42] Examples include *in situ* measurements of pulmonary edema,[43,44] myocardial disease[45] and pre-cancerous tumours.[46,47]

The region between 600 and 1900 nm provides a 'therapeutic window' in which absorption from water and tissue components are relatively weak. Overtone absorptions arising from infrared transitions from non-adjacent energy levels are prevalent in the region. In addition, combination bands due to the interaction of multiple vibrational modes are common and are typically quite specific to certain tissue components. For instance, the sum and differences of the fundamental vibrational frequencies composing a combination band around 1020 nm arise from N-H bonds in protein. Overall, the

presence of weak O-H, C-H and N-H overtone and combination bands arising from water, fats and proteins allow for quantification in tissue. Table 1.1 lists a few components of tissue along with their corresponding NIR absorbance regions.

Table 1.1 Absorption regions of common tissue components.

Component	NIR absorption region (nm)	Vibration
water	760, 960	O-H str. overtone
fat	900, 913, 1037	C-H str. combination
glucose	2123, 2272, 2325	C-H str. combination
protein	970 – 1020	N-H str. overtone
lactate	2166, 2254, 2292	C-H and N-H str, combination
ammonia	2132, 2232	N-H str. combination
starch	990	O-H str. overtone
hemoglobin	760	electronic transition
myoglobin	755	electronic transition

In tissues where scattering levels are low, NIR light may penetrate up to several centimeters. However when scattering levels are high, a ray of NIR light will become diffuse and follows less well defined paths through the medium. As the incident and scattered light travels through the tissue, the dielectric constant of the medium will influence the properties of the radiation. As such, light scattering in tissue arises from abrupt changes in the refractive indices at cell membranes, mitochondria, collagen and other extra-cellular components.[45] Although light scattering presents challenges for monitoring chemical species with classical spectroscopic techniques, measures of scattering can encode rich structural information about a sample. It is this challenge which drives active research in the area.

Presently, intense research is also being done to image in turbid samples. Tomographic or cross-sectional imaging becomes complicated because visible and NIR light does not take a precise path through the sample. This ambiguity causes problems

for many reconstruction algorithms as they are typically based on the assumption that a straight optical path exists between the radiation source and the detector. In spite of these problems, classical imaging techniques like those found in X-ray Computer Aided Tomography (CAT), have been adapted for NIR imaging in scattering media. Qualitative images of hard and soft tissue in the mouth,[48] oxygen profiles in the neonatal brain[36] and crude cross-section images of the human arm[49] have been produced. Although much progress has been made, it remains difficult to obtain quantitative images when scattering levels are high. It is the subject of this project to tackle the problem of quantification in layered tissue-like analogues.

1.3 The Interaction of Light in Turbid Media

Typically, two major processes occur when NIR radiation interacts with a turbid medium: scattering and absorption. In this section, the physics of these processes is discussed.

1.3.1 Scattering theory

When electromagnetic radiation traversing a medium of a given refractive index crosses a boundary into another material of different refractive index several processes may occur. The radiation may be reflected, refracted or scattered. In addition, a change in polarization of the light may occur. These optical phenomena result in changes in both the direction and properties of the incident light ray. Typically, however, these 'elastic' processes do not involve a change in the frequency of the incident ray.

Elastic scattering may be classified into two main types: Rayleigh scattering and Mie scattering. Table 1.2 gives some approximate refractive index and size criteria for these types of scattering. In Rayleigh scattering, the scatterer may be considered to be a point source of secondary emission.[50] Rayleigh scattering is characteristic of scattering from particles with dimensions much smaller than the incident wavelength. Scattering from particles such as smoke and fog fall into this category.[50]

Table 1.2. Scattering types.

Scattering type	Refractive index requirement*	Size requirement**
Rayleigh	$\lvert(\eta_s/\eta_m - 1)\rvert << 1$	$d_s < 0.05\ \lambda$
Mie	$\lvert(\eta_s/\eta_m - 1)\rvert >> 0$	$d_s > \lambda$

*η_s and η_m are the refractive indices of the scatterer and surrounding medium
**d_s is the major dimension of the scatterer

Lord Rayleigh was the first to investigate the dependence of scattered light intensity on wavelength. He discovered that an incident unpolarized electromagnetic wave interacting with a single particle produced a scattered beam irradiance in the form,

$$E_\theta = \frac{8\pi(\alpha')^2(1+\cos^2\theta)E_0}{\lambda^4 d^2} \tag{1.1}$$

where α' is the polarizability of the particle, λ is the wavelength, θ is the angle between the incident and scattered ray, E_0 is the incident beam irradiance, and d is the distance from the scatterer to the detector. Equation 1.1 predicts that intensity of the scattering radiation intensity is inversely proportional to the fourth power of the wavelength. This wavelength dependence is commonly used to explain the blue color of the sky. During

the day, the short wavelengths of light are efficiently scattered by dust particles and water vapor in the atmosphere at large angles relative to the light path.[50]

Unlike Rayleigh scattering, Mie scattering occurs from large particles of relatively high refractive index. The particles involved are sufficiently large and cannot be considered point sources of secondary emission. Examples of Mie scatterers include, milk fat suspensions, blood cells and collagen fibers. When these particles scatter light, different regions act as distinct scattering centers from which constructive and destructive interference occurs between scattered rays.

Light rays which are scattered backward toward the incident source are very susceptible to destructive interference. This results in a complex scattered intensity distribution envelope which is anisotropic and predominately forward directed. Using Mie theory, the exact form of the angular distribution of scatter intensity or phase function may be computed numerically for many simple geometric shapes.[51,52] However, these computations are tedious and often a simple measure of the broad characteristics of the angular intensity distribution around a scattering center is sufficient. To facilitate such computations, Henyey and Greenstein developed a simple polynomial function which characterizes the broad features of the phase function for a forward scattering particle.[53] The shape of this function is controlled by a variable, g the average cosine of the scattering angle. This variable is defined as,

$$g = \langle \cos\theta \rangle = \int_{4\pi} f(\mathbf{\Omega}, \mathbf{\Omega}') \cos\theta \, d\mathbf{\Omega}' \qquad (1.2)$$

where $f(\Omega,\Omega')$ is the phase function. (Ω represents a space unit vector in the direction the incident ray takes toward a scattering center and Ω' is the vector in the direction a scattered ray takes away from the center.) In general, g describes the anisotropy of the

scattering. For a particle that scatters isotropically, g is 0. If the particle scatters more light toward the forward direction, g is positive ($\theta \rightarrow 0^{o}$). Likewise, if more light is scattered back toward the source, g is negative ($\theta \rightarrow 180^{o}$). Typical values of g for human tissue and for milk fat range from 0.8 to 0.97 in the NIR region. [54]

When considering the optical properties of a collection of particles, as in a suspension, it is convenient to consider each scatterer as an attenuator of light intensity. In general, a light ray traversing through a suspension will experience more scattering events when the density of scatterers is high than when it is low. A comparison between the light attenuation in a bulk scattering medium with one in suspension may be made by expressing the scattering cross section per unit volume. The result is a volume attenuation coefficient or "scattering coefficient", μ_s and has units of reciprocal length. The scattering coefficient may be seen approximately as the number of scattering events that occur per unit pathlength. Conversely, the reciprocal of the scattering coefficient has been termed the mean free path between scattering events (in the absence of light absorption). In the literature, μ_s is stated in units of cm^{-1} or mm^{-1}. In this work μ_s is expressed in mm^{-1}. As an example, μ_s is typically around 15 mm^{-1} for skim milk (1% milk fat) and 52 mm^{-1} for whole milk (3.5% milk fat).[55]

In general, the scattering coefficient is proportional to the number of suspended scatterers per unit volume. However, when the density is sufficiently high, the effect of other nearby scatterers reduces the measured scattering coefficient. This effect suggests that a more complex relationship exists between collections of scattering particles over a broad range of concentrations.[56]

1.3.2 Absorption theory

When light passes through a sample containing an absorbing species, a reduction of intensity occurs. This attenuation is related to the incident light intensity I_0, the concentration of the absorbing species, c, and the pathlength through the sample, l. If the absorber concentration is uniform throughout the sample, then the Beer-Lambert relation may be used to calculate the exiting light intensity, I. This relation may be written as,

$$I = I_0 e^{-\alpha c l} \tag{1.3}$$

where α is the proportionality coefficient. It can be seen that the intensity decreases exponentially with optical pathlength and with absorber concentration. The Beer-Lambert relation is also commonly expressed in terms of an absorbance, A as,

$$A = -\log_{10}\frac{I}{I_0} = \varepsilon c l \tag{1.4}$$

where ε is the molar absorption coefficient, $\varepsilon=\alpha$ /ln 10 and I/I_0 is called the transmittance. The coefficient ε depends on both the absorber and the frequency of the light. The molar absorption coefficient has units of (concentration × length)$^{-1}$ and is normally expressed in M cm^{-1}.

When investigating an absorbing system where ε and the molar concentration of the absorber are not known, it is common to express the constant of proportionality between the absorbance and the pathlength as the absorption coefficient, $\mu_a = 2.303\ \varepsilon\ c$. The Beer-Lambert relation may be then rewritten as $I = I_0 e^{-\mu_a l}$ or $A = \mu_a l$ / 2.303. The quantity μ_a is analogous to μ_s, and may be seen as a measure of the number of "absorption events" per unit pathlength. As with the scattering coefficient, values of μ_a are listed in units of cm^{-1} or mm^{-1}. In this work, units of mm^{-1} are employed throughout.

Typical values of the absorption coefficient range from 0.01 mm^{-1} to 1 mm^{-1} in human tissue in the near infrared. In milk[55] at 632 nm, the absorption coefficient is 0.0005 mm^{-1}.

One of the fundamental assumptions of the Beer-Lambert relation is that absorption is a continuous process. However, in scattering media this assumption may not hold. Examples of non-continuous absorbing systems include smoke and coated powders. In these cases, scattering and absorption are not independent processes. It is only when both the optical pathlength through the scatterers is small relative to the total pathlength and the scatterers themselves are non-absorbing that the Beer-Lambert relation may be used.

1.4 The Propagation of Light in Turbid Media

An understanding of the transport properties of light in scattering media is important for both quantitative and qualitative sample analysis. This knowledge gives the analyst a means in which to interpret the results of an absorbing constituent assay. In a turbid sample, ray path information is ambiguous due to the dispersion of light. This problem complicates analysis as the Beer-Lambert relation may not be applicable for estimating concentrations of absorbing constituents. However, such variations in pathlength through a sample may provide valuable qualitative information for the diagnosis or disease[43-47] or food freshness.[16] The optical pathlength through a sample changes with scattering and absorption levels, wavelength and detection geometry. As shown in Figure 1.1, a photon may take several paths through a sample. Photons may traverse ballistically through a specimen with little or no scattering or take highly random

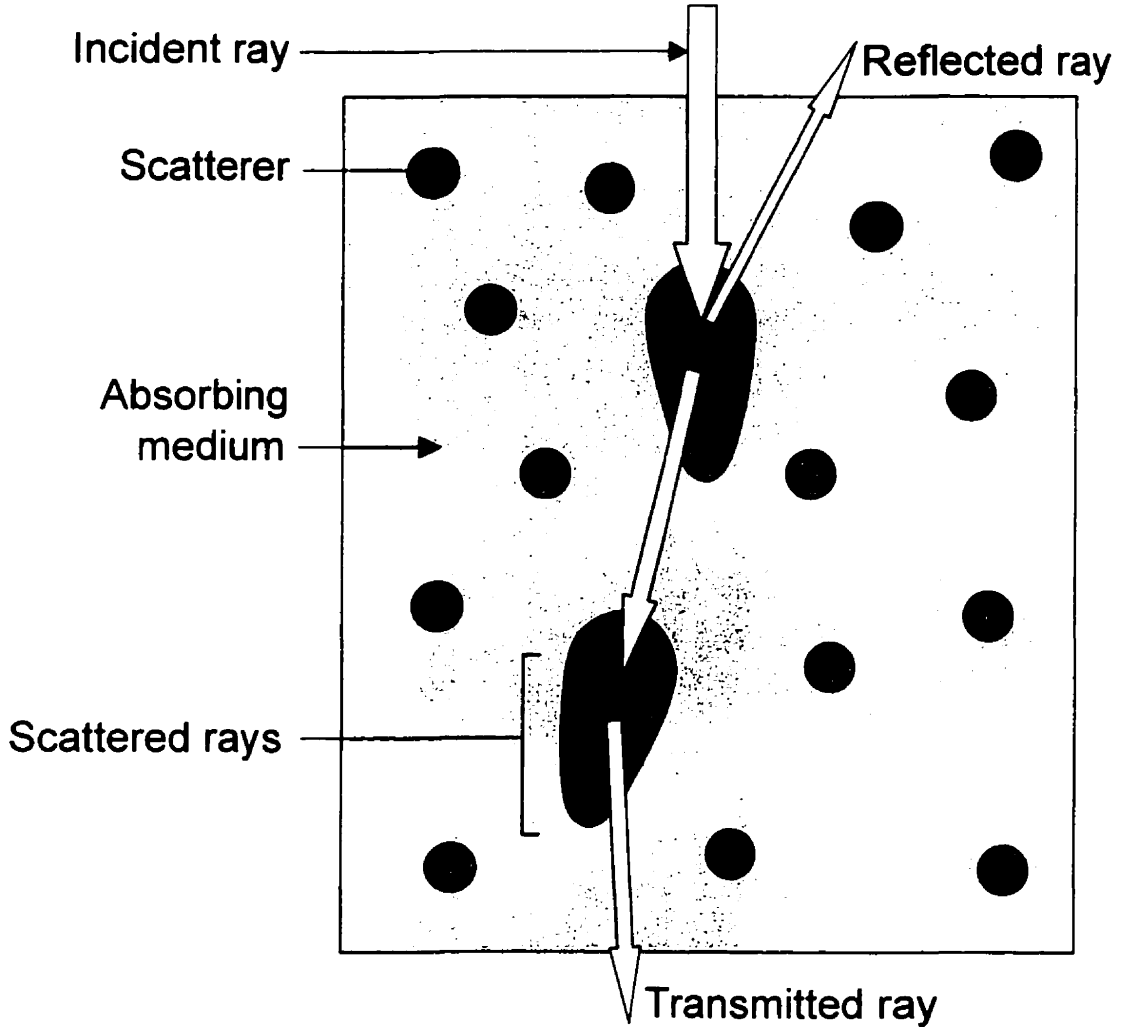

Figure 1.1. The interactions of light in a scattering and absorbing sample.

paths before exiting. Measures of the distribution in optical pathlengths through a specimen may be resolved using photon time-of-flight or frequency domain techniques. The results from these techniques have led researchers to a greater understanding of the interactions of light in scattering media. In this section, theoretical models that describe these time or distance variations are introduced.

1.4.1 Radiative transport theory

Over the last 60 years, many theoretical models have been developed to explain the physics of diffusional transport processes. Models of neutron diffusion were necessary in the development and control of nuclear reactors.[57] One of the fundamental models for neutron diffusion is the Radiative Transport Equation given in Equation 1.5.

$$\underset{\text{I}}{\frac{1}{c}\frac{\partial}{\partial t}} I(\boldsymbol{\Omega},\bar{\rho}) + \underset{\text{II}}{\boldsymbol{\Omega}\cdot\nabla I(\boldsymbol{\Omega},\bar{\rho})} = \underset{\text{III}}{-(\mu_s+\mu_a)I(\boldsymbol{\Omega},\bar{\rho})} + \underset{\text{IV}}{\mu_s\int f(\boldsymbol{\Omega},\boldsymbol{\Omega}')I(\boldsymbol{\Omega},\bar{\rho})d\boldsymbol{\Omega}'} + \underset{\text{V}}{S(\boldsymbol{\Omega},\bar{\rho})} \quad (1.5)$$

This equation attempts to characterize the time dependent nature of particles which traverse a scattering medium. The quantity of interest $I(\Omega,\bar{\rho})$ represents the intensity, speed and direction of neutrons (or photons) at a given point in space. The quantity $\bar{\rho}$ is a collective representation of the space (x,y,z) and time (t) coordinates expressed together as (x,y,z,ct), c is the speed of the particle and Ω is a directional unit vector. Other quantities have been defined previously. For clarity, Equation 1.5 has been split into five terms, (I – V) and a photon will represent the equivalent of the particle. Essentially the equation states that the rate of change of light flux into and out of a given point (I and II) is related to the rate at which light is being attenuated due to absorption and scattering

processes (III), and to the rate at which it is transferred into a given point by neighbouring scattering processes (IV) or by a source (V).

Although this differential equation has been solved analytically in special cases,[57,58] it does not provide a practical model for investigating the nature of light transport in scattering media. Work by Glasstone[57] and Ishimaru[58,59] have reduced Equation 1.5 to a diffusion type equation when the system contains quasi-isotropic scatterers. The result, given in Equation 1.6 is the first order (P1) approximation.[57] The time-dependent diffusion equation may be written as,

$$\frac{1}{c}\frac{\partial}{\partial t}\Phi(\mathbf{r},t) + D\nabla^2\Phi(\mathbf{r},t) = -\mu_a\Phi(\mathbf{r},t) + S(\mathbf{r},t) \qquad (1.6)$$

where D is the diffusion coefficient defined as $[3\mu_a + 3\mu_s(1\text{-}g)]^{-1}$, and $\Phi(\mathbf{r},t)$ is the photon flux at a position $\mathbf{r}$, at time t, and $S(\mathbf{r},t)$ is a source term. The scattering anisotropy in the diffusion coefficient arises in the form of a scalar factor, $(1\text{-}g)$, with the scattering coefficient. This reduced scattering coefficient, $\mu_s' = \mu_s(1\text{-}g)$, may be regarded as an effective isotropic scattering coefficient that represents the cumulative effect of several forward scattering events.

1.4.2 Time dependent solution to the diffusion equation

The diffusion equation given in Equation 1.6 may be solved using Green's functions when the source term is a single, short pulse of light.[60] If the light source is directed into a semi-infinite slab of scatterers, the time-dependent solution for the photon intensity out of the sample some lateral distance **r**, from the source is,

$$I(\mathbf{r},t) = \frac{z_0}{(4\pi cD)^{3/2} t^{5/2}} \exp(-\mu_a ct) \exp\left(\frac{-\mathbf{r}^2}{4ct/D}\right) \tag{1.7}$$

where $z_0 = [(1-g)\mu_s]^{-1}$, c is the speed of light in the medium and D is the diffusion coefficient. Equation 1.7 may be seen as the time-resolved remitted (reflected) light intensity at a detector placed at a source/detector separation distance of **r**. Note that Equation 1.7 is valid when $\mu_s >> \mu_a$ and **r** is sufficiently large that many scattering processes have occurred before light reaches the detector. The remitted light intensity is controlled by three terms. The first term is a scaling factor dependent on the reduced scattering and absorption coefficients, and the speed of light through the medium. The second is a Beer-Lambert absorption term that relates the attenuation of light as a function of distance traveled through an absorbing medium. The third term is analogous to the exponential in Fick's second law of diffusion. This term relates the diffusion of light as a function of time and detector placement.

If the time-resolved remitted light intensity given in Equation 1.7 is plotted as a function of sample composition, the nature of light propagation through a turbid medium may be better understood. Figure 1.2 demonstrates the effect of absorption and scattering changes on the theoretical diffuse reflectance photon time-of-flight distribution as seen by a point detector placed 15 mm away from the source. The sample has a refractive index of 1.33 and contains isotropic scatterers, i.e. g = 0. The initial absorption and scattering coefficients are 0.05 mm^{-1} and 40 mm^{-1} respectively. Changes in absorption and scattering levels were made in +2% increments from the nominal values. It may be seen that from Figure 1.2 that when either absorption or scattering is increased, the overall detected light intensity decreases. When the scattering level is increased and the

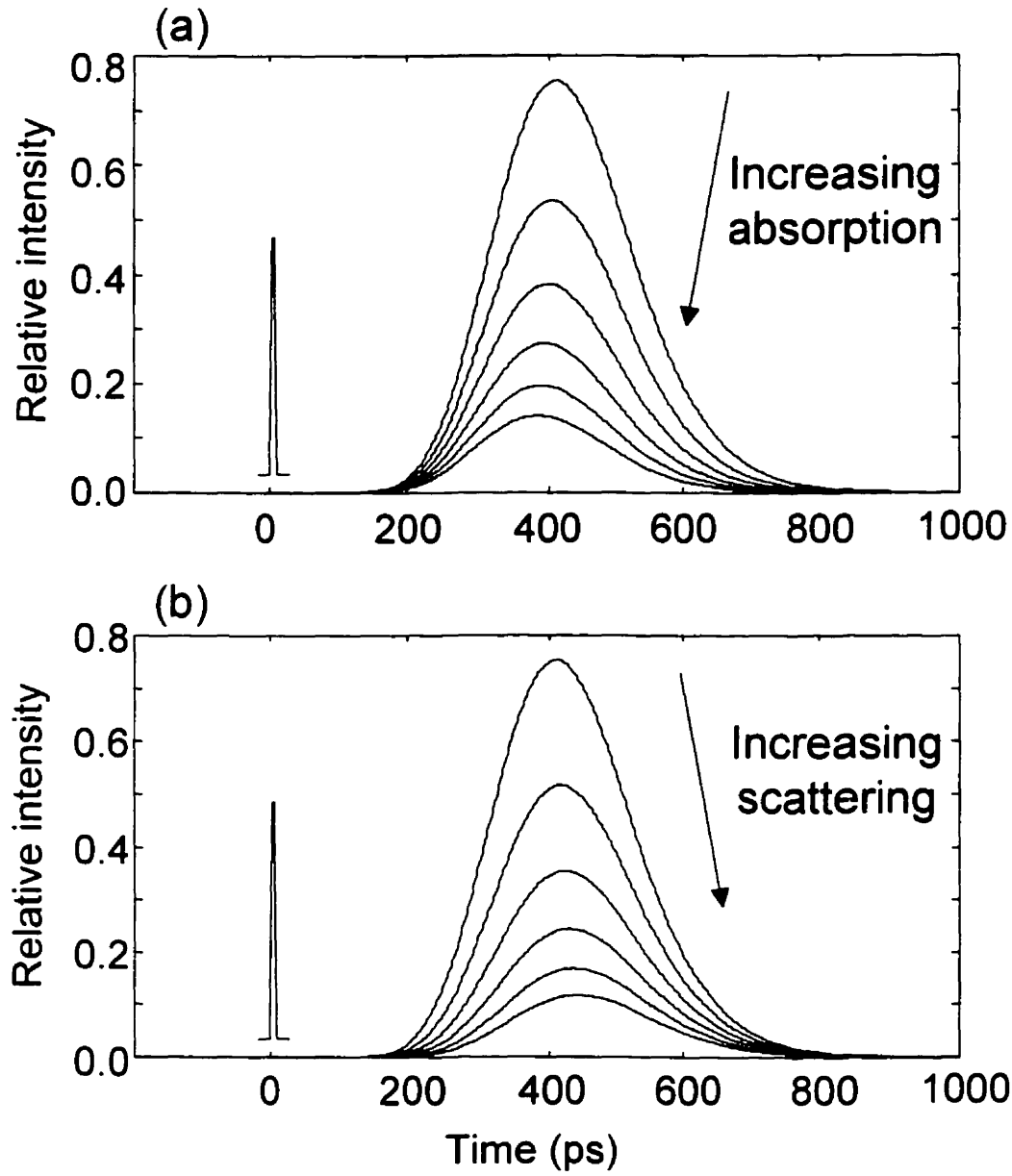

Figure 1.2. Effect of absorption (a) and scattering (b) changes on the theoretical photon time-of-flight distribution. $\mu_a = 0.05$ mm^{-1}, $\mu_s = 40$ mm^{-1}, $g = 0$, r = 15 mm. Changes in absorption and scattering are made in +2 % increments from their nominal values. Arrows point in the direction of the shifting peak maximum as the sample absorption or scattering is varied.

absorption level is held constant, the peak in the time distribution shifts toward longer times and the distribution broadens. This is expected as the light must travel a longer path from source to detector as it undergoes relatively more scattering events. Likewise, the intensity decreases because it is less probable that any given photon will make it to the detector. When absorption level is increased while the scattering is held constant, the peak maximum shifts toward shorter times. This is due to the photons which have been scattered many times having a greater probably of been absorbed before reaching the detector. Thus, it can be seen that changes in scattering and absorption levels have a marked influence of the average pathlength travels through a turbid sample.

The scattering and absorption properties of a turbid sample may be estimated by comparing the measured diffuse reflectance or transmittance signals with those obtained from the diffusion model.[60-62] It has been shown that using the time-resolved diffusion model, estimates of absorption and scattering levels in a homogeneous sample may be made to within 10% of their reference values.[63] The technique, however, is limited to samples which contain high concentrations of scatterers. Estimates of the sample absorption may be made by analyzing the slope of the edge of the photon time distribution.[63]

1.4.3 Monte-Carlo photon modelling

A versatile means by which the interaction of light with a scattering medium may be modeled is by Monte-Carlo simulation. Monte-Carlo simulations of this type involve tracing individual photon histories through the medium.[64,65] During a simulation, photons are released into the system and statistics about the quantity of interest are

determined. The advantage of the technique is that complex inhomogeneous samples of arbitrary absorption, scattering and refractive index and shape may be handled. In addition, the incident light source may be modelled either as a collimated beam[64] or one that is focussed into the sample.[66] For the simulation of light scattering, the Henyey-Greenstein phase function is commonly used.[53] This function is usually mapped such that a pair of random numbers between 0 and 1 correspond to a given scattering angle in space. The free path between scattering events is typically modeled according to a distribution function.[49,57] One of the major disadvantages of the technique is that a large number of photon histories must be followed in order to obtain statistically meaningful results. A computer program that models the time course of a bolus of photons through a layered scattering/absorbing medium is listed in the Appendix.

Another type of Monte-Carlo model is the Random-Walk model.[67] In this method, photon propagation is done over a set of discrete grid points. One of the key advantages of the method is that only a few rules are needed to move the photons forward, to change direction or to simulate an absorption event. However, because this approach constrains the movements of the photons, simulations of anisotropic scattering are not well handled.

1.4.4 Finite-element modelling

Finite Element Methods (FEM) have been increasingly employed for solving photon propagation problems in complex samples.[68,69] The basic concept of the finite element approach is to sub-divide the sample into small elements or nodes and to solve a set of simultaneous equations which describe the physics of each node. A numerical solution of a differential equation is made which describes the photon flux into and out of

each node during a small time interval. The nodes may be spaced regularly throughout the sample or may be more concentrated in regions that are difficult to model. These may be boundaries and regions where the photon flux is anticipated to be large.[70] In addition to handling complex sample geometries, finite element solutions are not statistical in nature. However, the overall quality of the solution is dependent on the time step and the node spacings chosen. Therefore, small time steps may be required to accurately model the diffusion process. Because of this, finite element methods tend to be slow and have not gained wide popularity.

1.4.5 Kubelka-Munk model

In 1931, Kubelka and Munk proposed a theory of light transport in which two light fluxes travel forward and backward in the medium.[71] A number of researchers have since refined the theory and have made extensive comparisons with experimental data.[58] It was found that the K-M theory could describe the variations in remitted light intensity if the source of illumination is diffuse and the medium diffusely scatters light.[58] The technique involves taking both a reflectance and transmission measurement, and by using simple algebra, relative measures of absorption and scattering levels may be made. Although this method is often used in the analysis of powders,[8,9] its empirical nature and the range of validity have not been well established.[58] In addition, when both the scattering and absorption levels vary, the K-M model is difficult to interpret.

1.5 Imaging in Scattering Media

1.5.1 Classical tomography

Tomography, a branch of radiology concerned with the display of cross-section information, has become an important tool in medicine. Today's computed tomography (CT) systems allow for rapid 2D and 3D imaging of the human body from X-ray shadowgrams. These instruments have been made possible in part due to the rapid advancement of computer technology over the last 30 years. However, before the existence of powerful computers and Fourier Transform (FT) based imaging processing methods,[72] ingenious opto- and electro-mechanical instruments were devised to collect and process cross-sectional information.[73,74] Although many design approaches have been investigated, common to all X-ray tomographic systems are means for obtaining multi-perspective information about the specimen.

Multi-perspective information may be obtained in two ways. Either the specimen is precisely rotated between a fixed radiation source and detector, or, a mechanical gantry is rotated around a fixed body. In either case, it is assumed that the radiation beam travels in a known path through the specimen from source to detector. If deviations occur in the radiation path, sample reconstruction becomes ambiguous and a degraded image results.[75]

CT image reconstruction is typically viewed as an inversion problem. This may be thought of as a mathematical approach to resolving the absorption properties of each voxel from a set of multi-perspective intensity measurements. In 1917, Radon discovered that an object may be reconstructed unambiguously using an infinite number of noiseless projections.[76] Although Radon worked out the equations governing image

reconstruction, it was not until 1956 that the first real image reconstructions were made in the field of radio astronomy.[77]

Using the specimen shown in Figure 1.3 as a example, a projection through the sample is shown. This projection or shadowgram represented by $g(x')$ is a line integral along the y' axis at a fixed distance along x'. The quantity $g(x')$, proportional to the total attenuation of the ray through the sample, may be written as,

$$g(x') = \int_{y'} f(x', y')dy' \tag{1.8}$$

where the function $f(x',y')$ represents a 2D sample. The integral may also be stated relative to a fixed xy coordinate system at an angle θ as:

$$g(\theta, x') = \int_{y'} f(x'\cos\theta - y'\sin\theta, x'\sin\theta + y'\cos\theta)\, dy' \tag{1.9}$$

Given a series of projections, several approaches may be used to reconstruct a cross-sectional image of the sample. One of the easiest approaches is by backprojection. In this method, sample reconstruction is done by backprojecting each projection across the image plane. After this is done for each projection, an approximation to the original object is produced. The technique is attractive because it can be easily implemented without the need for complicated mathematics. However, resulting images are only a crude approximation to the original object.[75]

Another common approach to sample reconstruction is the Algebraic Reconstruction Technique or ART. In the ART method developed by Gordon *et al.*, sample reconstruction is done by iterative refinement of an arbitrary initial image.[78] The object is typically represented as a matrix of values. Projections of the object are computed by summing along rows, columns and diagonals of the matrix.

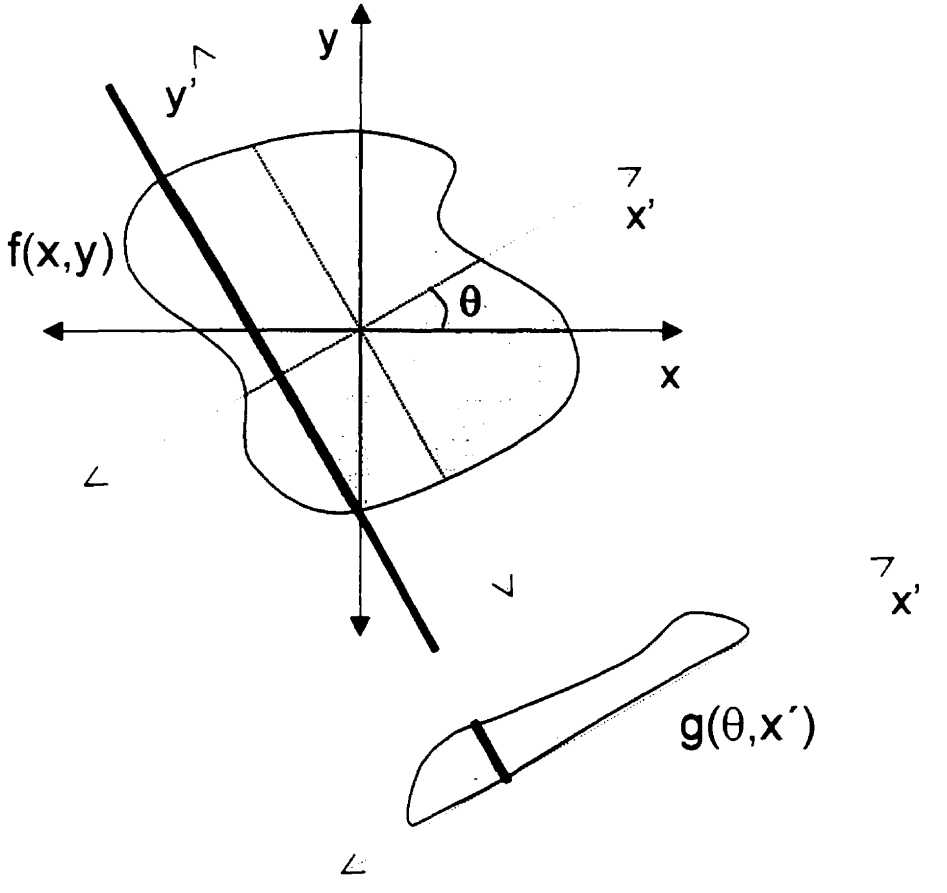

Figure 1.3. One dimensional projection $g(\theta, x')$ of a two dimensional function $f(x,y)$ obtained by integrating along the y' direction.

The algorithm applies successive corrections to the reconstructed object to minimize the difference between the measured and calculated projections. The reconstructed object is slowly refined until either convergence is achieved or satisfactory image quality is obtained. ART methods are attractive because *a priori* information about the sample is easily incorporated into the reconstruction process. The inclusion of *a priori* sample information is important to help constrain the image to meet certain criteria such as non-negativity. Although ART methods are widely used, the number of algebraic computations required may be very large in order to achieve convergence. To avoid such lengthy computations, analytic approaches to image reconstruction are used.

Fourier image reconstruction techniques were first introduced by Bracewell in 1956. However, it was not until after the development of the Fast Fourier Transform and large digital storage systems in the 1960s that this analytic approach to image reconstruction became practical. The key to Fourier based image reconstruction is the Central Section Theorem.[72] This theorem states that a 1D Fourier transform of a projection of a 2D object taken at an angle θ is a radial slice through a 2D Fourier transform of the object at the same angle. A visual description of this concept is given in Figure 1.4. Therefore to reconstruct an image from a series of projections, a computer would 'fill' the 2D Fourier domain with 1D transforms of each projection, and take the inverse 2D Fourier transform of the result.

One of the major problems with Fourier based reconstructions is that many projections are needed to adequately fill the Fourier domain.[75] If projections are not taken at all angles, the Fourier domain will contain a missing cone of information.

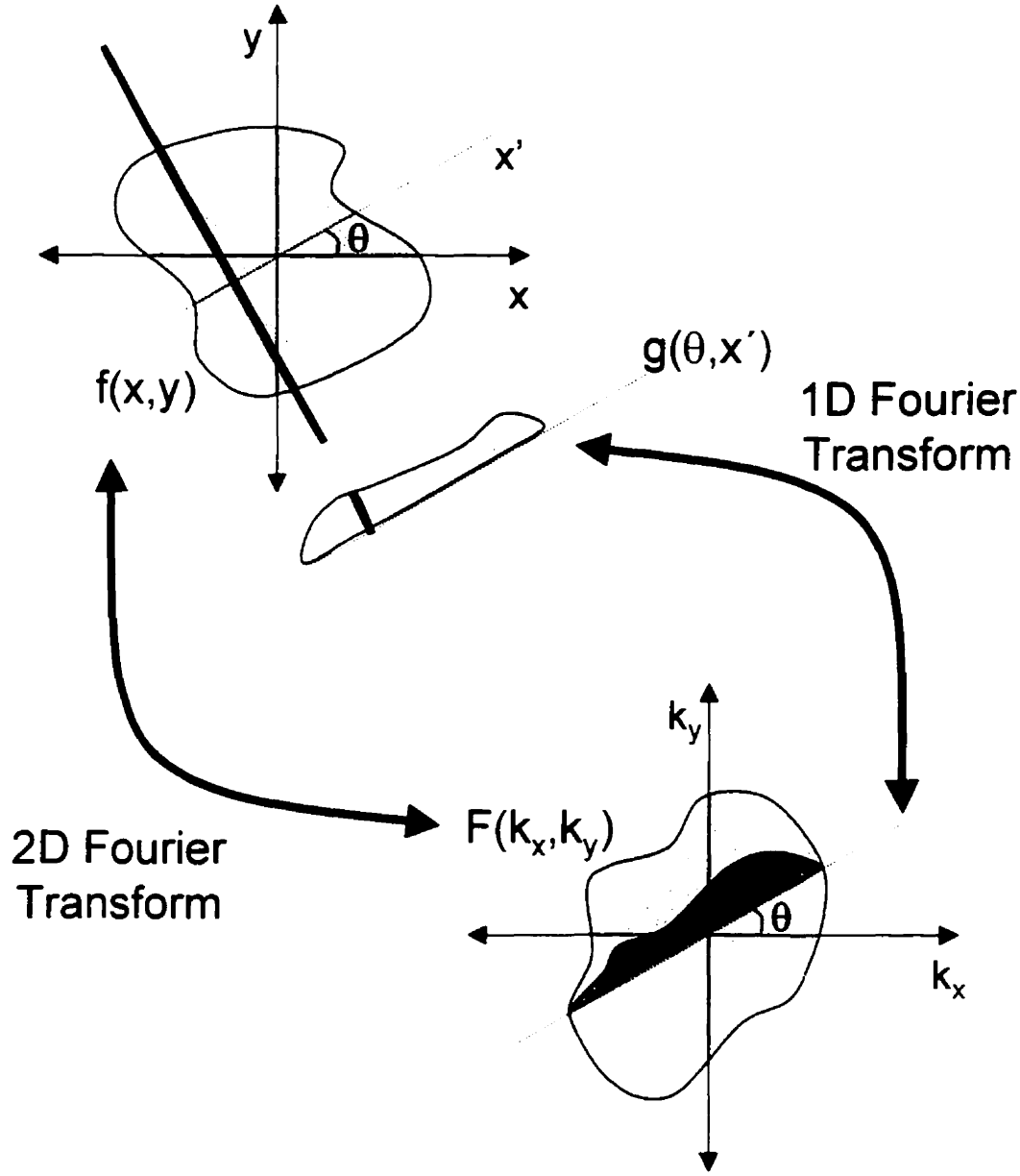

Figure 1.4. Illustration of the Central Section Theorem: The 1D Fourier transform of $g(\theta, x')$ equals the radial slice of $F(k_x,k_y)$ at the same angle θ.

In the image domain, this is manifested as a lack of details in directions where projections were not available. This effect is common to other reconstruction methods as well.[79] To reduce these deleterious effects, progress has been made to recover the missing information by extrapolating from known information into the missing cone.[75,79]

1.5.2 Imaging in scattering media using ballistic light

In general, the fundamental concepts of X-ray CT imaging may be applied for the analysis of a wide variety of samples using NIR light.[80] However, the effects of scattering complicate image reconstruction. The key problem to imaging in absorbing and scattering media is to extract information regarding a given object embedded in the medium. The object of interest, or phantom, often is distinguished by a small variation in the scattering and absorption properties as compared to the surrounding medium.[81] To tackle this problem, great efforts have been made to isolate the component of light that traverses through a sample in the most direct path from source to detector.

If a short pulse of light is transmitted through a scattering medium and is detected, the component of light that arrives earliest will have undergone the fewest scattering events. The ballistic component which has not undergone any scattering retains the coherence properties of the original pulse.[82] Following this component is light which has been scattered only a few times. For tomographic imaging applications, the use of straight-path ballistic light is important. However, if the thickness of the sample exceeds more than 5-10 scattering mean free paths (MFPs), the ballistic light intensity has been estimated to fall below the photon shot noise limit.[81] Therefore for imaging in highly

scattering media, the problem to be solved is how to separate the ballistic or near ballistic light component from the highly scattered light.

Over the last 20 years, various techniques have been employed to suppress scattered light from imaging based on ballistic light. These include time gating, frequency domain, polarization and spatial filtering techniques. In time-gating techniques, the distribution of path lengths through a scattering sample is resolved through the photon time-of-flight distribution. If a transmission measurement is made, the ballistic light component has the shortest time of flight. Time gating the ballistic light component may be achieved with the use of a Kerr gate,[82] a streak camera[83], by photon counting[84] or by optical coherence detection.[48,85-87] Each method has its own advantages and disadvantages, however, the most sensitive include photon counting and coherence detection.

In optical coherence techniques, a Michelson type interferometer is employed. Instruments for optical coherence tomography (OCT) are generally reflectance based. In the system shown in Figure 1.5, a pulse of light travels down a bifurcated fiber optic into a sample, on the illumination arm, and toward a reference mirror on the reference arm. The back reflected light from the sample and reference mirror propagates back down the fiber into a light coupler. A portion of this light is detected. To probe the sample axially, the reference arm pathlength is varied by moving the mirror. As the mirror is moved, interferences occur between light back reflected from the illumination and reference arms and the detected intensity is modulated. The resulting amplitude of the heterodyned signal may be plotted as a function of axial position producing an axial or A-scan.[48] By translating the sample arm traversely, a series of A-scans may be combined to create a

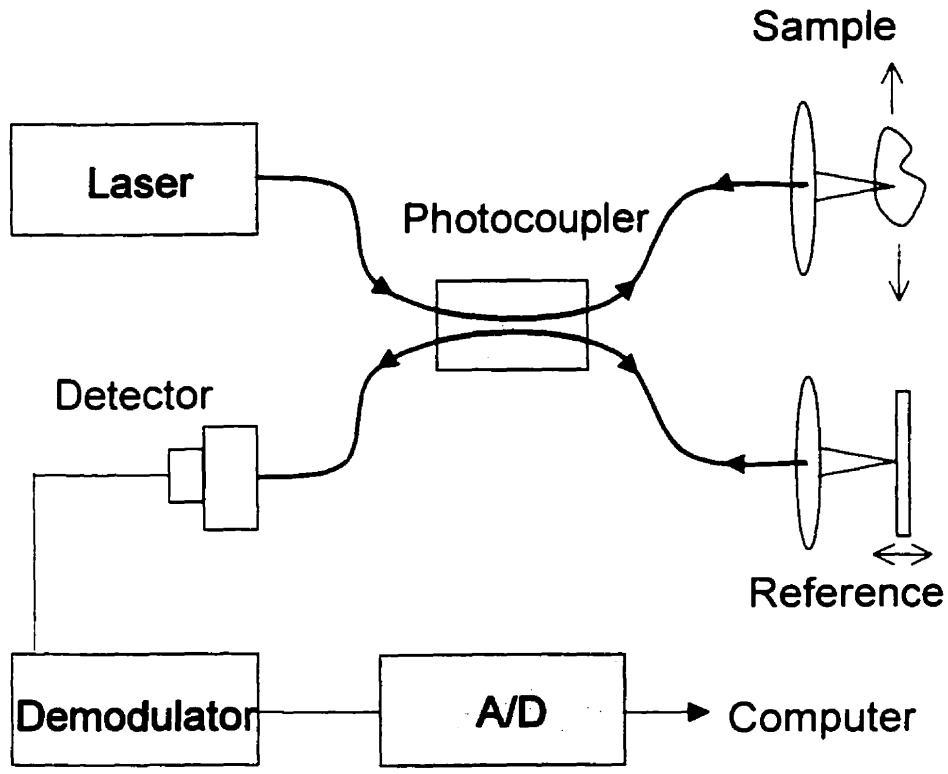

Figure 1.5. Schematic of an Optical Coherence Tomography system.

two dimensional intensity plot or B-scan. In a microscope OCT system, resolutions of <20 μm in the axial and lateral directions can be obtained with a 10 μm incident beam spot size.[48]

In the early 1990s, OCT was first demonstrated as a potentially powerful tool for clinical medicine.[85] Since then it has been used for the diagnosis of disease in the eye and other transparent tissues such as in the intestines.[86] However, imaging in scattering media is difficult since the portion of backscattered photons that pass the interferometric gate of the OCT decays exponentially with probe depth.[87] It has been demonstrated that at even low levels of scatter ($\mu_s = 6\ mm^{-1}$), the maximum probing depth is on the order of 1 to 1.5 mm.[87] Likewise, it remains difficult to obtain quantitative information from OCT as the available models do not account for the complex interference effects of backscattered light in tissue.[87]

For imaging in highly scattering macroscopic systems other techniques such as polarization gating and spatial filtering are better suited for suppressing the detection of the scattered light component. In polarization gating methods, scattered lighted is suppressed because of its random polarization state. Ballistic light, however, retains the polarization of the original beam entering the specimen. The ballistic light component may be selected by aligning the polarizer in the same direction as the incident light. However, in this simple approach, the intensity of the scattered light component is reduced by only one half. Using a polarization modulation technique, the rejection efficiency may be vastly increased.[81] The method resolves the polarization state of the light exiting the sample and uses this information to subtract the diffuse background.[88]

This technique has been shown to be of considerable use when imaging in highly anisotropic scattering media up to depths of 50 MFPs.[89]

In spatial filtering methods, the idea is to allow the ballistic light component to pass through a pinhole while blocking a majority of the scattered light. This type of filter is most efficiently applied to imaging a point object.[90,91] When imaging is done in this manner, a scanning system is used to reconstruct two and three dimensional images. The confocal microscope developed in the 1960s is such an instrument. It may be operated in either reflectance or transmission geometry. A diagram of a simple reflectance mode confocal microscope is given in Figure 1.6. The ability of the confocal optic geometry for depth discrimination in a sample is inherently related to the way scattered light is rejected. When imaging in homogeneously scattering media, it has been demonstrated that imaging in samples on the order of 20 MFPs in thickness may be made in transmission mode and 10 MFPs reflectance mode.[81] Typically, diffraction limited imaging is the goal of using confocal optics. However it is not known to what depth a sample may be imaged when this strict criteria is relaxed. This is one of the goals of this thesis.

1.5.3 Diffuse light imaging

There are several approaches to sample reconstruction based on diffuse light detection from the sample. Typically, tomographic reconstruction from diffuse light measurements requires a theoretical knowledge of photon propagation in the medium. In the 'forward problem' based approach, the optical properties from a sample are estimated by modelling the experimental responses. Data may be derived from transmission

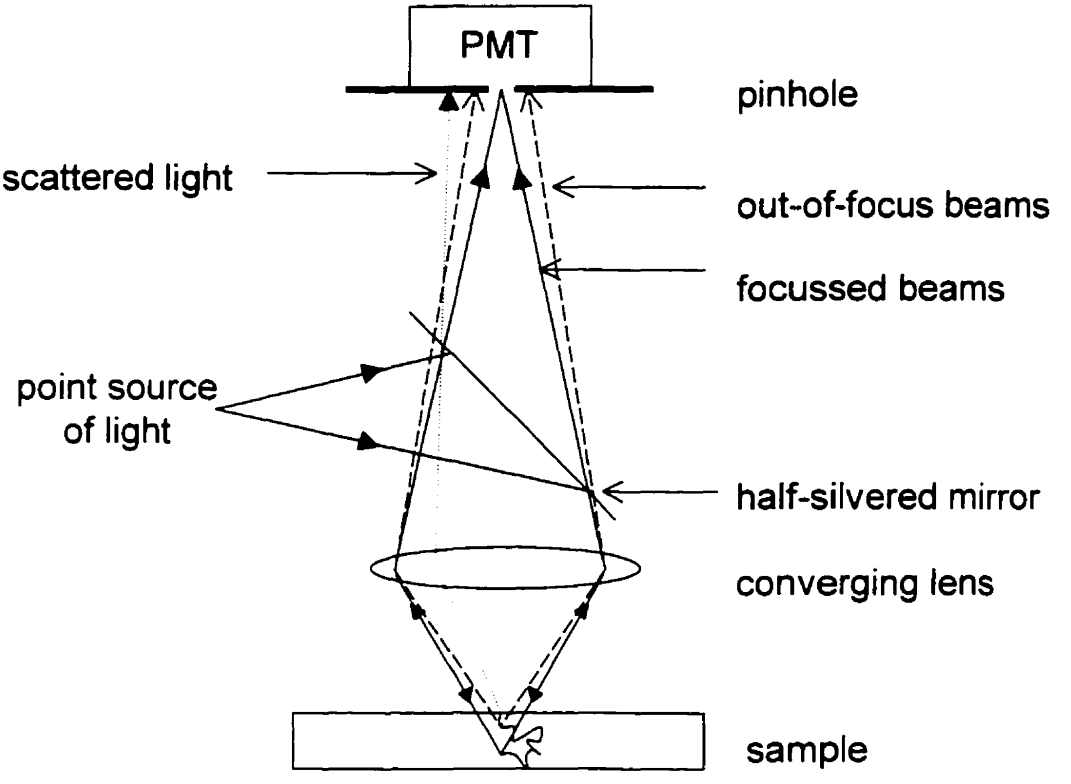

Figure 1.6. Confocal optical geometry in reflectance mode.

measurements either in frequency[92] or time domain,[93,94] or with continuous wave measurements from many spatially distributed detectors.[95] The theoretical model that is typically employed is either the classic diffusion model or one which simulates a defect in an otherwise homogeneous sample.[96] Although the diffusion model has been demonstrated to be of considerable use for sample resolution, it fails when simulating complex media of variable absorption, scattering and refractive index. Current research is directed toward efficient and stable solutions to the forward problem that ideally work without *a priori* knowledge of the sample.[81]

Frequency domain techniques, however, have shown considerable promise for imaging thick scattering samples. With frequency domain measurements, the incident light source is modulated. This modulated light wave gives rise to the concept of photon density waves.[97,98] Photon density waves have wave-like properties and exhibit refraction and interference effects.[98] The practical advantage of the technique is that an inexpensive modulated continuous wave laser may be used in place of a pulsed source. A measure of the detected modulation amplitude and phase properties allow for the determination of the mean path length through the sample. This is typically done by modeling the system using the diffusion approximation of the radiative transport equation with a modulated light source. Based on amplitude and phase measurements of photon density waves, images may be obtained by wave diffraction at inhomogeneities. With this approach, the approximate position, absorption and scattering properties of the defect may be determined.[99]

Recently, methods that combine the use of light and acoustic waves have been employed for tomographic reconstruction in thick samples. The basic concept is to use

light to probe the contrast between the surrounding medium and the object of interest while employing ultrasonic waves to transmit this information through the sample.[81] There are two approaches in which this may be done. In photoacoustic imaging, shown in Figure 1.7a, the incident light beam penetrates the sample and is absorbed by the embedded object. The process of light absorption creates a sound wave that propagates through the sample where it is detected on the surface by an ultrasound transducer. In this approach, first developed by Kruger, either pulsed or modulated light may be used.[100]

In the second approach shown in Figure 1.7b, light is modulated by an ultrasound beam focussed into the sample. The interaction of light with the compressed and rarefied regions of the sample creates a modulation at the same frequency of the ultrasound pulse. The light detected on the sample surface has a modulation amplitude dependent on the efficiency of overlap between regions of high acoustic intensity and light intensity. This acousto-optic technique, developed by Wang, has been used to image objects on the order of ~2 mm using 1 MHz ultrasound waves.[101]

Typically, the embedded objects imaged are in sharp contrast from the surrounding medium, in terms of absorption and density. Because of this, qualitative images are usually reported. Although these acoustic methods may be employed for imaging 5 cm thick liquid scattering samples with millimeter resolution, the transmission properties of ultrasound through many samples is poor.[102] In addition, the transducer must make intimate contact with the object being imaged. This severely limits the possibilities for reproducible, quantitative, on-line analysis.

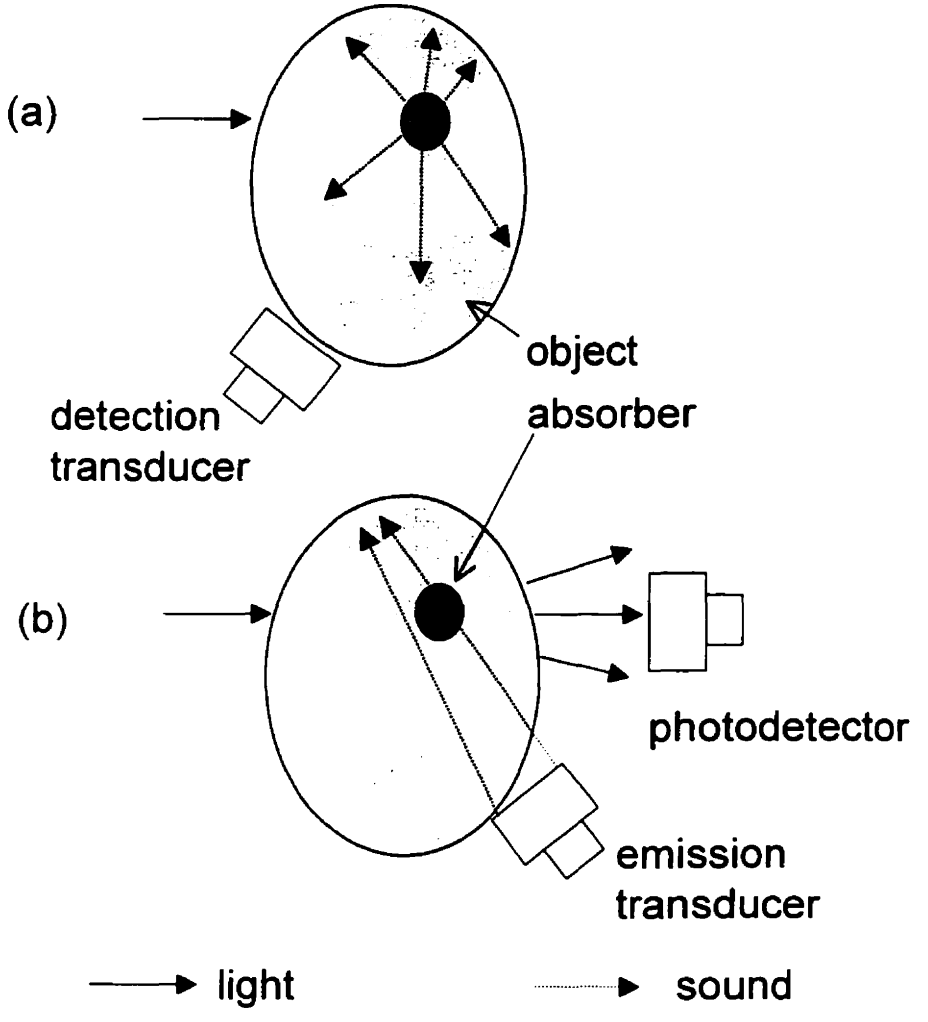

Figure 1.7. Schematic of (a) photoacoustic and (b) acousto-optic tomography systems.

1.5.4 Depth-resolved imaging

Many common materials consist of layers which have different optical properties. Examples include, skin, coatings, thin films, and whole fruit. The layers in biological specimens may be only a few micrometers or as thick as one centimeter in the case of the skull tissue surrounding the brain. One of the early achievements for non-invasive infrared monitoring was in the determination of blood oxygenation status in the brain.[103] Although measurements are possible, the influence of the surrounding skin, skull and meninges is still not well understood.[104] Near-infrared measurements made around the arachnoid (a filamented substructure of the meninges) have since demonstrated similar measures of blood oxygenation state even though the structure is almost free from light absorption and scattering.[104] From this example, it is clear that an understanding of the optical properties of the surrounding tissue is needed to test the accuracy of a bio-diagnostic tool.

In the late 1970s, the photon propagation properties in two layered biological systems were studied using diffuse reflectance signals.[105] Since then, several groups have studied the optical properties of layered samples *in vivo*.[104,106] Theoretical treatments the light diffusion in two-layered media having different refractive indices[107] or with differing absorption coefficients[108,109] have also been developed. An approximate random walk model has provided valuable insight into the diffuse reflectance properties of a two-layered scattering/absorbing sample.[110,111] The results from the random walk model yielded a simple analytical approximation for the surface intensity profile when the absorption coefficient of the upper layer was greater than that of the lower layer.[110]

The approach however provides only semi-quantitative information of layer absorption in a medium containing isotropic scatterers.

In another study, the influence of a two-layered scattering/absorbing system on the quality of the estimated optical properties was determined.[112] Using a least-squares fitting algorithm, the optical properties of the layers were estimated from a simulation of the diffuse reflectance. Both Monte-Carlo and diffusion models were investigated. In general, the classic semi-infinite diffusion model provided a poor measure of absorption and scattering. It was further demonstrated that the quality of the estimated scattering and absorption coefficients was strongly dependent on the source/detector separation distance. In this case, the diffuse reflectance signal at small lateral separations was more dependent on the absorption properties of the upper layer than on the bottom layer. The converse was found at large source/detector separations.

Recently, several groups have investigated time-resolved diffuse reflectance measurements from layered simulated tissue samples. Experiments have been made in gels with different concentrations of titanium dioxide and ink,[104] and in transparent silicone containing polystyrene spheres and charcoal.[113] Work by Hielsher *et al.* have found that measurements of absorption in the lower layer were possible when the upper layer contained a strong absorber.[104] Absorption estimates were made by fitting the decaying portion of the measured time-of-flight profile to the time-dependent solution of the semi-infinite slab diffusion model (Equation 1.7). The estimation was possible since the highly-absorbing upper layer changed only the amplitude of the time-of-flight distribution and not the shape of the decaying portion.[104] However, when the technique

was applied to a multi-layered system, the estimation of absorption coefficients deep within a sample was complex.

Kienle *et al.* have also demonstrated that the scattering and absorption properties of two-layered samples may be estimated over a narrow range from time-resolved and frequency domain measurements.[113] Diffuse reflectance data was collected from three different source/detector separation distances. A solution of the diffusion equation for a two-layered system allowed for optical property estimation in both layers by a fit to the experimental data. The results demonstrated that the reduced scattering and absorption coefficients in both layers may be estimated to within 10% in samples containing low levels of scatterers. In addition, estimates of absorption in the lower layer could be made more precisely in a sample containing a thick upper layer using frequency domain data. In a related investigation, it was found that if the thickness of the top layer was known *a priori*, then estimates of scattering and absorption in both layers were possible from a single time-resolved measurement.

The choice of imaging geometry is also critical to the success of the measurement. When analyzing layered samples, light collection is typically done in reflectance geometry since the integrated signals from a transmission measurement are largely redundant. However, the reflectance geometry presents other challenges when quantifying layered samples. Detected light that penetrates into the deeper layers must pass through the upper layers twice. This ill-conditions most classical approaches to tomographic reconstruction. In this dissertation, methods to reduce the ambiguity in sample quantification are investigated.

Depth-resolved measurements of scattering and absorption are typically made possible by using a theoretical model and a non-linear fitting procedure. Although the radiative transport properties through layered scattering/absorbing samples may be approximated either analytically or by Monte-Carlo simulation, these models are quite limited. The refractive index, scattering coefficient and anisotropy of a real sample can not be perfectly modelled. Without a sophisticated physical model, accurate quantification in samples even of moderate complexity have not been possible. It is the focus of this project to find new approaches for quantification in layered scattering/absorbing media.

1.6 Research Objectives

The goal of this research is to make quantitative depth resolved measurements in scattering/absorbing media. Towards this end, this work has been divided into a series of chapters each which provide insight into the effect of scattering and absorbing constituents on sample quantification.

In Chapter 2, quantification is done in granular samples. Estimates of scattering, absorption and particle size are made using statistical descriptors of the photon time-of-flight distribution from diffuse reflectance measurements. An analysis of the optimal linear combinations of descriptors chosen by a stepwise multilinear regression routine correlated to a particular sample property will allow insight into the nature of photon propagation in granular media. The extent to which quantification may be made is compared with similar work done in liquid samples.

In Chapters 3 and 4, tomographic reconstruction of layered scattering/absorbing specimens is investigated. Both steady state and time-resolved reflectance measurements were done to obtain information sensitive of changing layer composition. Partial least squares and stepwise multilinear regression techniques are then employed for constructing linear models of absorption in a given sample region. Using this approach, the extent to which estimates of absorption may be made in each layer independently is determined.

Tomographic reconstruction of layered samples is further considered in Chapters 5 and 6. Using knowledge gained from work done in Chapters 3 and 4, more directed approaches to sample quantification are done. In Chapter 5, tomographic reconstruction is made by employing *a priori* information to improve estimates of absorption deep within a sample. In Chapter 6, confocal optics is used to suppress detection highly scattered light. In addition to providing enhanced quantification, the work presented in Chapters 5 and 6 demonstrate the limits to which subtle changes in absorption may be determined deep in a highly scattering specimen.

1.7 References

1. Herschel, W. Experiments of the Solar and Terrestrial Rays that Occasion Heat; *Philos. Trans R. Soc. Lond.* **1800**, *90*, 293-326.
2. Abney, W. W.; Festing, E. R. On the Influence of the Atomic Grouping in the Molecules of Organic Bodies on their Absorption in the Infrared Region of the Spectrum; *Philos. Trans R. Soc. Lond.* **1881**, *172*, 887-918.
3. Coblentz, W. W. *Investigation of Infrared Spectra*; Carneige Institution of Washington Publications: Washington D.C., 1905, p 5.
4. Barnes, R. B. Infrared Spectroscopy: Industrial Applications; *Ind. Eng. Chem. Anal. Ed.* **1943**, *15*, 659-709.
5. Ingle, J. D.; Crouch, S. R. *Spectrochemical Analysis*; Prentice Hall: New Jersey, 1998, p. 408.
6. Massie, D. R.; Norris, K. H. Spectral Reflectance and Transmittance Properties of Grains in the Visible and Near Infrared; *Trans. Am. Soc. Agr. Eng.* **1965**, *8*, 598-600.
7. Richter, S. M.; Shinde, R. R.; Balgi, G. V.; Sevick-Muaraca, E. M. Particle Sizing using Frequency Domain Photon Migration; *Part. Part. Charact.* **1998**, *15*, 9-15.
8. Ilari, J. L.; Martens, H.; Isaksson, T. Determination of Particle Size in Powders by Scatter Correction in Diffuse Near-Infrared Reflectance; *Appl. Spectrosc.* **1988**, *42*, 722-728.
9. Burger, T.; Kuhn, J.; Caps, R.; Ficke, J. Quantitative Determination of the Scattering and Absorption Coefficients from Diffuse Reflectance and Transmittance

Measurements: Application to Pharmaceutical Powders; *Appl. Spectrosc.* **1997**, *51*, 309-3317.

10. Ciurczak, E. W. Analytical Applications of Near Infrared Spectroscopy; *Chemtech* **1992**, *22*, 374-380.
11. Root, D. E.; Hall, J. W. NIR Process Analysis; *Med. Electr.* **1997**, *28*, 64-66.
12. Valdes, E. V.; Summers, J. D. Determination of Crude Protein and Fat in Carcass and Breast Muscle Samples of Poultry by Near Infrared Reflectance Spectroscopy; *Poultry Science* **1986**, *65*, 485-490.
13. Davies, A. M. C.; Brocklehurst, T. F. Near Infrared Reflectance Analysis of Oil Concentration in an Emulsion: A Study of Oil and Water Migrations in Mayonnaise-Based Salad Dressings; *J. Sci. Food Agri.* **1986**, *37*, 310-316.
14. Lin, J.; Brown, C. W. Near-IR Fiber-Optic Temperature Sensor; *Appl. Spectrosc.* **1993**, *47*, 62-68.
15. Aldrige, P. K.; Mushinsky, R. F.; Andino, M.M.; Evans, C. L. Identification of Tablet Formulations Inside Blister Packages by Near-Infrared Spectroscopy; *Appl. Spectrosc.* **1994**, *48*, 1272-1276.
16. Kaffka, K. J.; Norris, K. H.; Rosza-Kiss, M. Determining Fat, Protein and Water Content of Pastry Products by the NIR Technique; *Acta. Aliment.* **1982**, *11*, 199-217.
17. Wehling, R. L. Determination of Moisture in Cheddar Cheese by Near Infrared Reflectance Spectroscopy; *J. Associ. Offi. Anal. Chemists* **1988**, *71*, 571-574.
18. Eisenbrand, J.; Baumann, K. Lichtabsorptionsmessungen aus Flussigen Durchsichtigen Lebensmitteln im Nahen Infrarot; *Deutsche Lebensmittel-Rundschau* **1969**, *65*, 169-172.

19. Norris, K. H. *Agricultural Handbook;* 2nd ed.; Martens, G. C.; Shenk, J.S.; Barton, F. E., Eds.; U.S. Government Printing Office: Washington, D.C., 1989, p6.

20. Wariar, R.; Gaffke, J. N.; Haller, R. G.; Bertocci, L. A. A Modular NIRS System for Clinical Measurement of Impaired Skeletal Muscle Oxygenation; *J. Appl. Physiol.* **2000**, *88*, 315-325.

21. Belardinelli, R.; Barstow, T. J.; Porszasz, J.; Wasserman, K. Changes in Skeletal Muscle Oxygenation During Incremental Exercise Measured with Near Infrared Spectroscopy; *Eur. J. Appl. Physiol.* **1995**, *70*, 487-492.

22. McCully, K. K.; Iotti, S.; Kendrick, K.; Wang, Z.; Posner, J. D.; Leigh, J.; Chance, B. Simultaneous In Vivo Measurements of HbO_2 Saturation and PCr Kinetics After Exercise in Normal Humans; *J. Appl. Physiol.* **1994**, *77*, 5-10.

23. Mancini, D. M.; Bolinger, L.; Li, H.; Chance, B.; Wilson, J. R. Validation of Near-Infrared Spectroscopy in Humans; *J. Appl. Physiol.* **1994**, *77*, 2740-2747.

24. Haida, M.; Chance, B. A Method to Estimate the Ratio of Absorption Coefficients of Two Wavelengths using Phase Modulated Near Infrared Light Spectroscopy; *Adv. Exp. Med. Biol.* **1994**, *345*, 829-835.

25. Luebbers, D. W. Chemical In Vivo Monitoring by Optical Sensors in Medicine; *Sensors and Actuators B* **1993**, *1*, 252-262.

26. Arakaki, L. S. L.; Kushmerick, M. J.; Burns, D. H. Myoglobin Oxygen Saturation Measured Independently of Hemoglobin in Scattering Media by Optical Reflectance Spectroscopy; *Appl. Spectrosc.* **1996**, *50*, 697-707.

27. Arakaki, L. S. L.; Burns, D. H. Multispectral Analysis for Quantitative Measurements of Myoglobin Oxygen Fractional Saturation in the Presence of Hemoglobin Interference; *Appl. Spectrosc.* **1992**, *46*, 1919-1928.

28. Cope, M.; van der Zee, P.; Essenpries, M.; Arridge, S. R.; Delpy, D. T. Data Analysis Methods for Near Infrared Spectroscopy of Tissue: Problems in Determining the Relative Cytochrome aa_3 Concentration; *Proc. SPIE* **1991**, *1431*, 251-262.

29. Copper, C. E.; Springett, R. Measurement of Cytochrome Oxidase and Mitochondrial Energetics by Near-Infrared Spectroscopy; *Phil. Trans. R. Soc. Lond. B* **1997**, *352*, 669-676.

30. Gagnon, R. E.; Gagnon, F. A.; Macnab, A. J. Comparison of 13 Published Cytochrome C Oxidase Near-Infrared Spectroscopy Algorithms; *Eur. J. Appl. Physiol.* **1996**, *74*, 487-495.

31. Copper, C. E.; Delpy, D. T.; Nemoto, E. M. The Relationship of Oxygen Delivery to Absolute Hemoglobin Oxygenation and Mitochondrial Cytochrome Oxidase Redox State in the Adult Brain: A Near Infrared Spectroscopy Study; *J. Biochem.* **1998**, *332*, 627-632.

32. Hoshi, Y.; Hazeki, O.; Kakihana, Y.; Tamura, M. Redox Behavior of Cytochrome Oxidase in the Rat Brain Measured by Near-Infrared Spectroscopy *J. Appl. Physiol.* **1997**, *85*, 1842-1848.

33. Vreman, H. J.; Ronquillo, R. B.; Ariagno, R. L.; Schwartz, H. C.; Stevenson, D. K. Interference of Fetal Hemoglobin with the Spectrophotometric Measurement of Carboxyhemoglobin *Clin. Chem.* **1988**, *34*, 975-977.

34. Wickramasinghe, Y. A. B. D.; Faris, F.; Rolfe, P.; Thorniley, M.; Houston, R.; Zhang, K.; Spencer, S. A.; Doyle, M.; O'Brien, S. Perinatal Monitoring of Cerebral Oxidative Metabolism by NIRS; In *Making Light Work: Advances in Near Infrared Spectroscopy*; Murray, I.; Cowe, I. A., Eds.; VCH, 1992, pp. 616-621.

35. Chou, C.; Han, C. Y.; Kuo, W. C.; Huang, Y. C.; Feng, C. M.; Shyu, J. C. Noninvasive Glucose Monitoring In Vivo with an Optical Heterodyne Polarimeter; *Appl. Opt.* **1998**, *37*, 3553-3557.

36. Burnmeister, J. J.; Arnold, M. A. Evaluation of Measurement Sites for Non-Invasive Blood Glucose Sensing with Near-Infrared Transmission Spectroscopy; *Clin. Chem.* **1999**, *45*, 1621-1627.

37. Arnold, M. A. Non-Invasive Glucose Monitoring *Curr. Opin. Biotech.* **1996**, *7*, 46-49.

38. Heise, H. M.; Marbach, R.; Koschinsky, T. H.; Gries, F. A. Non-Invasive Blood Glucose Sensors Based on Near Infrared Spectroscopy; *Artif. Org.* **1994**, *18*, 439-447.

39. Robinson, M. R.; Eaton, R. P.; Haaland, D. M.; Koepp, C. W.; Thomas, E. V. Non-Invasive Glucose Monitoring in Diabetic Patients: A Preliminary Evaluation; *Clin. Chem.* **1992**, *38*, 1618-1621.

40. Lafrance, D.; Lands, L. C.; Hornby, L.; Burns, D. H. Near-Infrared Spectroscopic Measurement of Lactate in Human Plasma; *Appl. Spectrosc.* **2000**, *54*, 300-303.

41. Kuhr, W. G.; Korf, J. Extracellular Lactic Acid as an Indicator of Brain Metabolism: Continuous On-Line Measurement in Conscious, Freely Moving Rats with Intrastriatal Dialysis; *J. Cerebral Blood Flow Metabol.* **1988**, *8*, 130-138.

42. Carney, J. M.; Landrum, W.; Mayes, L.; Zou, Y.; Lodder, R. A. Near-Infrared Spectrophotometric Monitoring of Stroke-Related Changes in the Protein and Lipid Composition of Whole Gerbil Brains; *Anal. Chem.* **1993**, *65*, 1305-1313.

43. Shibata, S.; Ohdan, H.; Noriyuki, T.; Yoshioka, S.; Asahara, T.; Dohi, K. Novel Assessment of Acute Lung Injury by In Vivo Near-Infrared Spectroscopy; *Am. J. Respir. Crit. Care Med.* **1999**, *160*, 317-323.

44. Leonardi, L.; Burns, D. H.; Oppenheimer, L.; Michel, R. P. Near Infrared Diffuse Reflectance Spectroscopy for the Determination of Pulmonary Edema; in preparation.

45. Lui, K. Z.; Dixon, I. M. C.; Mantsch, H. H. Distribution of Collagen Deposition in Cardiomyopathic Hamster Hearts Determined in Infrared Microscopy; *Cardiovascular Pathology* **1999**, *8*, 41-47.

46. Fantini, S., Walker, S. A.; Franceschini, M. A.; Kaschke, M.; Schlag, P. M.; Moesta, K. T. Assessment of the Size, Position, and Optical Properties of Breast Tumors In Vivo by Noninvasive Optical Methods; *Appl. Opt.* **1998**, *37*, 1982-1989.

47. Weissleder, R.; Tung, C. H.; Mahmood, U.; Bagdanov, A. In Vivo Imaging of Tumors with Protease-Activated Near-Infrared Fluorescent Probes; *Nature Biotech.* **1999**, *17*, 375-378.

48. Colston, B. W.; Everett, M. J.; Da Silva, L. B.; Otis, L. L.; Stroeve, P.; Nathal, H. Imaging of Hard- and Soft-Tissue Structure in the Oral Cavity by Optical Coherence Tomography; *Appl. Opt.* **1998**, *37*, 3582-3585.

49. Zhang, K.; Rolfe P.; Wickramasinghe, Y. A. B. D. Study of NIR Imaging Reconstruction Algorithm; *Proc. SPIE.* **1993**, *2082*, 21-29.

50. van de Hulst, H. C. *Multiple Light Scattering, Tables, Formulas and Applications*; Academic Press: New York, 1980.

51. Kerker, M. *The Scattering of Light and Other Electromagnetic Radiation*; Academic Press: New York, 1969, pp. 31-39.

52. Bohren, C. F.; Huffman, D. R. *Absorption and Scattering of Light by Small Particles*; John Wiley and Sons: New York, 1983.

53. Henyey, L. G.; Greenstein, J. L. Diffuse Radiation in the Galaxy; *Ap. J.* **1937**, *85*, 70-83.

54. van Staveren, H. J.; Moes, C. J. M.; van Marle, J.; Prahl, S. A.; van Gemert, M. J. C. Light Scattering in Intralipid-10% in the Wavelength Range of 400-100 nm; *Appl. Opt.* **1991**, *30*, 4507-4514.

55. Waterworth, M. D.; Tarte, B. J.; Joblin, A. J.; van Doorn, T.; Niesler, H. E. Optical Transmission Properties of Homogenized Milk Used as a Phantom Material in Visible Wavelength Imaging; *Austral. Phys. Eng. Sci. Med.* **1995**, *18*, 39-44.

56. Hunter, R. J. *Foundations of Colloid Science*; Oxford University Press: Oxford, 1989, Vol 2.

57. Glasstone, S. *Principles of Nuclear Reactor Engineering*; Van Nostrand: Princeton, 1955.

58. Ishimaru, A. *Wave Propagation and Scattering in Random Media*; Academic Press: New York, 1978.

59. Ishimaru, A. Diffusion of a Pulse in Densely Distributed Scatterers; *J. Opt. Soc. Am.* **1978**, *68*, 1045-1050.

60. Arridge, S. R.; Cope, M.; Delpy, D. T. The Theoretical Basis for the Determination of Optical Pathlengths in Tissue: Temporal and Frequency Analysis; *Phys. Med. Biol.* **1992**, *37*, 1531-1560.

61. Kohl, M.; Watson, R.; Cope, M. Optical Properties of Highly Scattering Media Determined from Changes in Attenuation, Phase, and Modulation Depth; *Appl. Opt.* **1997**, *36*, 105-115.

62. Kuga, Y.; Ishimaru, A. Experiments on Picosecond Pulse Propagation in a Diffuse Medium; *J. Opt. Soc. Am.* **1983**, *73*, 1812-1815.

63. Patterson, M. S.; Chance, B.; Wilson, B. C. Time Resolved Reflectance and Transmittance for the Non-Invasive Measurement of Tissue Optical Properties; *Appl. Opt.* **1989**, *28*, 2331-2336.

64. Flock, S. T.; Patterson, M. S.; Wilson, B. C.; Wyman, D. R. Monte Carlo Modeling of Light Propagation in Highly Scattering Tissues - I: Model Predictions and Comparison with Diffusion Theory; *IEEE Trans. Biomed Eng.* **1989**, *36*, 1162-1168.

65. Okada, E.; Schweiger, M.; Arridge, S. A.; Firbank, M.; Delpy, D. T. Experimental Validation of Monte Carlo Finite-Element Methods for the Estimation of the Optical Path Length in Inhomogeneous Tissue; *Appl. Opt.* **1996**, *35*, 3362-3371.

66. Wang, L. V.; Liang, G. Absorption Distribution of an Optical Beam Focused into a Turbid Medium; *Appl. Opt.* **1999**, *38*, 4951-4958.

67. Weiss, G. H. Statistical Properties of the Penetration of Photons into a Semi-Infinite Turbid Medium: A Random-Walk Analysis; *Appl. Opt.* **1998**, *37*, 3558-3593.

68. Arridge, S. R.; Schweiger, M. Direct Calculation of the Moments of the Distribution of Photon Time-of-Flight in Tissue with a Finite-Element Method; *Appl. Opt.* **1995**, *34*, 2683-2687.

69. Arridge, S. R.; Schweiger, M. Photon-Measurement Density Functions. Part 2: Finite-Element-Method Calculations; *Appl. Opt.* **1995**, *34*, 8026-8037.

70. Trim, D. W.; *Applied Partial Differential Equations*; Kent: Boston, 1990.

71. Kubelka, P.; Munk, F. Ein Beitrag zur Optik der Farbanstriche; *Z. Tech. Phys.* **1931**, *12*, 593-604.

72. Bracewell, R. N. *The Fourier Transform and its Applications*; McGraw: New York, 1965.

73. Gmitro, A. F.; Gindi, G. R. Computed Tomography Videography: An Electooptical System for Video-Rate Image Reconstruction; *Appl. Opt.* **1985**, *24*, 4040-4045.

74. Bates, R. T.; Peters, T. M. Towards Improvements In Tomography; *New Zealand J. Sci.* **1971**, *14*, 883-896.

75. Brooks, R. A.; Di Chiro, G. Theory of Image Reconstruction in Computed Tomography; *Image Reconstruction in Computed Tomography* **1975**, *117*, 561-570.

76. Radon, J. On the Determination of Functions from their Integrals Along Certain Manifolds; *Berichte uber die Verhandlungen der koniglich Saechsischen Gesellschaft der Wissenshaften zu Leipzig Mathematisch-Physische Klasse* **1917**, *69*, 262-278.

77. Bracewell, R. N. Strip Integration in Radio Astronomy; *Aust. J. Phys.* **1956**, *9*, 198-217.

78. Gordon, R. A Tutorial on ART; *IEEE Trans. Nucl. Sci.* **1974**, *NS-21*, 78-93.

79. Hayner, D. A.; Jenkins, W. K. *Advances in Computer and Image Processing*; JAI Press: New York, 1984, Vol. 1, pp. 83-144.

80. Colak, S. B.; Papaioannou, D. G.; 't Hooft, G. W.; van der Mark, M. B.; Schomberg, H.; Paasschens, J. C. J.; Melissen, J. B. M.; van Asten, N. A. A. J. Tomographic Image Reconstruction from Optical Projections in Light-Diffusing Media; *Appl. Opt.* **1997**, *36*, 180-213.

81. Rudolph, R.; Kempe, M. Topic Review Trends in Optical Biomedical Imaging; *J. Mod. Opt.* **1997**, *44*, 1617-1642.

82. Liang, X.; Wang, L.; Ho, P. P.; Alfano, R. R. Time-Resolved Polarization Shadowgrams in Turbid Media; *Appl. Opt.* **1997**, *36*, 2984-2989.

83. Das, B. B., Liu, F.; Alfano, R. R. Time-Resolved Fluorescence and Photon Migration Studies in Biomedical and Model Random Media; *Reports on Progress in Physics* **1997**, *60*, 227-292.

84. Small, E. W. Laser Sources and Microchannel Plate Detectors for Pulse Fluorometry; In *Topics in Fluorescence Spectroscopy;* Lakowicz, J. R. Ed.; Plenum Press: New York, 1991, Vol. 1.

85. Huang, D.; Swanson, E. S.; Lin, C. P.; Shuman, J. S.; Stinson, W. G.; Chang, W.; Hee, H. R.; Flotte, T.; Gregory, K.; Puliafito, C. A.; Fujimoto, J. G. Optical Coherence Tomography; *Science* **1991**, 254, 1178-1181.

86. Izatt, J. A.; Kulkarni, M. D.; Wang, H. W.; Kobayashi, K.; Sivak, M. V. Optical Coherence Tomography and Microscopy in Gastrointestinal Tissues; *IEEE Journal of Selected Topics in Quantum Electronics.* **1996**, 2, 1017-1028.

87. Schmitt, J. M.; Knuettel A. Model of Optical Coherence Tomography of Heterogeneous Tissue; *J. Opt. Soc. Am. A* **1997**, *19*, 1231-1242.

88. Horinaka, H.; Hashimoto, K.; Wada, K.; Umeda, T.; Cho, Y.; Optical CT Imaging in Highly Scattering Media by Extraction of Photons Preserving Initial Polarization; *Proc. SPIE* **1996**, *2873*, 54-57.

89. Demos, S. G.; Alfano, R. R. Temporal Gating in Highly Scattering Media by the Degree of Optical Polarization; *Opt. Lett.* **1996**, *21*, 161-163.

90. Minsky, M. *U.S. Patent 3013467*, 19 Dec., 1961, Filed 7 Nov., 1957.

91. Kempe, M.; Genack, A. Z.; Rudolph, W.; Dorn, P. Ballistic and Diffuse Light Detection in Confocal and Heterodyne Imaging Systems; *J. Opt. Soc. Am. A* **1997**, *14*, 216-223.

92. Fishkin, J.; Gratton, E.; van de Ven, M. J.; Mantulin, W. W. Diffusion of Intensity Modulated Near-Infrared Light in Turbid Media; *Proc. SPIE* **1991**, *1431*, 122-129.

93. Gonatas, C. P. Optical Diffusion Imaging Using a Direct Inversion Method; *Phys. Rev. E* **1995**, *52*, 4361-4365.

94. Grosenick, D.; Wabnitz, H.; Rinneberg, H. Time-Resolved Imaging of Solid Phantoms for Optical Mammography; *Appl. Opt.* **1997**, 36, 221-231.

95. Arridge, S. R.; van der Zee, P.; Cope, M.; Delpy, D. T. Reconstruction Methods for Infrared Absorption Imaging; *Proc. SPIE* **1991**, *1431*, 204-215.

96. Feng, S.; Zeng, F.; Chance, B. Photon Migration in the Presence of a Single Defect: A Perturbation Analysis; *Appl. Opt.* **1995**, 34, 3826-3837.

97. Tromberg, B. J.; Svaasand, L. O.; Tsey, T. T.; Haskell, R. C. Properties of Photon Density Waves in Multiple-Scattering Media; *Appl. Opt.* **1993**, *32*, 607-616.

98. Kohl, M.; Watson, R.; Cope, M. Optical Properties of Highly Scattering Media Determined from Changes in Attenuation, Phase, and Modulation Depth; *Appl. Opt.* **1997**, *36*, 105-115.

99. Patterson, M. S.; Moulton, J. D.; Wilson, B. C.; Berndt, K. W.; Lakowicz, J. R. Frequency-Domain Reflectance for the Determination of the Scattering and Absorption Properties of Tissue; *Appl. Opt.* **1991**, *30*, 4474-4482.

100. Kruger, R. A; Liu, P.; Fang, Y.; Appledorn, C. R. Photoacoustic Ultrasound (PAUS) – Reconstruction Tomography; *Med. Phys.* **1995**, 22, 1605-1609.

101. Yao, G.; Wang, L. V. Theoretical and Experimental Studies of Ultrasound-Modulated Optical Tomography in Biological Tissue; *Appl. Opt.* **2000**, 39, 659-664.

102. Wang, L.; Zhao, X. Ultrasound-Modulated Optical Tomography of Absorbing Objects Buried in Dense Tissue-Simulating Turbid Media; *Appl. Opt.* **1997**, 36, 7277-7282.

103. Joebsis, F. F. Noninvasive Infrared Monitoring of Cerebral and Myocardial Oxygen Sufficiency and Circulatory Parameters; *Science* **1977**, *19*, 1264-1267.

104. Hielscher, A. H.; Liu, H.; Chance, B.; Tittel, F. K.; Jacques, S. L. Time-Resolved Photon Emission from Layered Turbid Media; *Appl. Opt.* **1996**, *35*, 719-728.

105. Takatani, S.; Graham, M. D. Theoretical Analysis of Diffuse Reflectance from a Two-Layer Tissue Model; *IEEE Trans. Biomed. Eng.* **1979**, *26*, 656-664.

106. Cui, W.; Ostrander, L. E. The Relationship of the Surface Reflectance Measurements to Optical Properties of Layered Biological Media; *IEEE Trans. Biomed. Eng.* **1992** *39*, 194-201.

107. Keijzer, M.; Star, W. M.; Storchi, P. R. M. Optical Diffusion in Layered Media; *Appl. Opt.* **1988**, *27*, 1820-1824.

108. Alexandrakis, G.; Farrell, T. J.; Patterson, M. S. Monte Carlo Diffusion Hybrid Model for Photon Migration in a Two-Layer Turbid Medium in the Frequency Domain; *Appl. Opt.* **2000**, *39*, 2235-2244.

109. Kienle, A.; Patterson, M. S.; Doegnitz, N.; Bays, R.; Wagnieres, G.; van den Burgh, H. Noninvasive Determination of the Optical Properties of Two-Layered Turbid Media; *Appl. Opt.* **1998**, *37*, 779-790.

110. Taitelbaum, H.; Havlin, S.; Weiss, G. H. Approximate Theory of Photon Migration in a Two-Layer Medium; *Appl. Opt.* **1989**, *28*, 2245-2249.

111. Nossal, R.; Kiefer, J.; Weiss, G. H.; Bonner, R.; Taitelbaum, H.; Havlin, S. Photon Migration in Layered Media; *Appl. Opt.* **1988**, *27*, 3382-3391.

112. Farrell, T. J.; Patterson, M. S.; Essenpreis, M. Influence of Layered Tissue Architecture on Estimates of Tissue Optical Properties Obtained from Spatially Resolved Diffuse Reflectometry; *Appl. Opt.* **1998**, *37*, 1958-1972.

113. Kienle, A.; Glanzmann, T.; Wagnieres, G.; van den Bergh, H. Investigation of Two-Layered Turbid Media with Time-Resolved Reflectance; *Appl. Opt.* **1998**, *37*, 6852-6862.

Chapter 2 Particle Sizing and Optical Constant Measurement in Granular Samples using Statistical Descriptors of Photon Time-of-Flight Distributions

Quantitative analysis of granular samples is important to the pharmaceutical and food industries. Solid granular samples are typically composed of loosely packed scatterers of a high index of refraction. For finely divided solid materials, a significant portion of the volume is air. If the particle absorbs light, the absorber may be present inside of the granule itself or coating it. Due to the properties of granular samples, absorption of light is not a continuous process as it traverses the sample. Referring to the diffusion approximation solution given in Equation 1.7, the light intensity decays exponentially as a function of distance traveled. In a medium where absorption is not continuous, but instead associated with scattering events, the Beer-Lambert type relationship assumed in Equation 1.7 may not be valid.

Estimates of the scattering and absorption coefficient in homogeneous milk samples using time-of-flight diffuse reflectance measurement have been made previously in this laboratory. Statistical descriptors of the broad features of the time distributions were used for quantification. Stepwise multi-linear regression of the descriptors was used to determine the optimal combination of descriptors correlated with changes in absorption and scattering. Results demonstrated that descriptors associated with the trailing edge of the time profile were most correlated with absorption changes in a sample. Likewise, descriptors of the rising edge of the time distribution were correlated

with changes in the scattering level. It is unclear whether similar descriptors are appropriate for quantifying composition changes in granular media.

In this study, measurements are made in homogeneous granular samples. This provides a fundamental basis for which many scattering samples need to be analyzed such as those later used for tomographic analysis.

2.1 Abstract

A method is described for optical constant estimation and particle sizing in granular samples using diffuse reflectance measurements. Statistical descriptors of the time-resolved photon distributions were used to obtain information inherent to absorption and scattering processes in a sample. Changes in a sample's absorption and scattering properties and apparent particle diameter were simultaneously estimated using stepwise multi-linear regression (SMLR) and partial least squares regression (PLS). Models were constructed using time distributions taken at both single and multiple radial displacements between source and detector. SMLR estimates of absorption and particle diameter required descriptors related to the trailing and rising edges of the time profiles respectively. The inclusion of multiperspective information allowed for improved estimates for all quantities. Using statistical descriptors, a robust means for simplifying complex photon time distributions into measurable parameters was found. It was found that the SMLR model gave slightly better results compared with the PLS model. The absorption coefficient, scattering coefficient and apparent particle diameter were estimated to within 10, 9 and 7% of their respective reference values with SMLR. In the

future, this approach may be used as a means in which to develop practical instrumentation for on-line, real-time characterization of absorbing granular media.

2.2 Introduction

Particle sizing of powders and granular samples are of great importance to many areas such as in pharmaceutical formulation and abrasive manufacturing. Among the range of particle sizing techniques commonly used, optical methods are particularly attractive for remote or on-line analysis. Optical techniques provides a means for rapid and precise measurement in a wide range of samples such as aerosols, dry powders, and suspensions.[1-5] For particle sizing in the range of 0.1 μm to 1000 μm, single scattering techniques such as dynamic-light- or forward-angle-scattering may be used for particle size determinations of dilute concentrations of scatterers.[2] With dense suspensions or powders however, light is multiply scattered and the mathematical solution becomes ambiguous.

Measurements of the diffusely backscattered light from a powder or suspensions reflectance measurements have been used for particle size estimations.[6,7] In addition to physical property assessment of a sample, diffuse reflectance methods offer an advantage over other techniques by allowing the potential for concurrent chemical quantification. For relative measures of absorption and scattering, Kubelka-Munk (K-M) theory was developed to provide a simple model of two or more light fluxes in scattering media.[8,9] In this approach, the scattering and absorption processes are assumed to be independent of each other. Although K-M theory oversimplifies the interactions of light with a sample, this model has been successful for physical quantification of pharmaceutical

powders of constant chemical composition.[7] However when both scattering and absorption properties change simultaneously, the K-M approach has large error.

An alternative approach, diffusion approximation of the radiative transport equation describes the time evolution of a short pulse of light as it propagates through a sample to the detector.[10-14] The characteristics of the detected photon profile at a given source to detector separation distance is a function of the optical constants, μ_s and μ_a which quantify the number of scattering and absorption events per unit length. When used for a limited range of variation in scattering or absorption, the diffusion model provides estimates to within 10% of the measured time distributions.[12] Recently, Richter *et al.* have used a diffusion theory for particle sizing of non-absorbing titanium dioxide suspensions using frequency domain measurements.[15] Estimates of the scattering coefficient alone were made by modelling the response with diffusion theory. Mean particle size was then derived from the scattering estimate using Mie theory. Their results suggested that particle sizing of suspensions in the sub-micrometer range is possible with this technique.

Currently, the application of diffusion theory has been limited to small particle size ranges and changes in absorption. When used on large particle sizes or when particle absorption also changes, the diffusion model produces large errors.[10] In addition, it is not clear whether the particle sizing technique based on the scattering coefficient and Mie theory may be extended to a broader particle size range.

Using the diffusion approximation, it has been demonstrated that estimates of scattering are possible when the sample has a homogeneous refractive index and absorption occurs independent of scattering.[8,16] In granular samples however, there is

no optical uniformity and absorption events are linked with scattering and reflection processes. For non-suspended media, this approximation may not hold and may present difficulties for accurate quantification.

Recently, we have demonstrated that the absorption and scattering coefficients may be accurately estimated using statistical descriptors of photon time-of-flight distributions in liquid samples.[10] Although the scattering and absorption coefficients could be estimated in liquid samples containing sub-micrometer sized scatterers, it is not clear whether estimates are possible in granular samples. The information gained from the use of descriptors would be helpful for developing analytical models.

The goal of this work is to examine the use of statistical descriptors of diffuse reflectance time-resolved photon migration as a means for optical constant estimation and particle sizing of granular samples from 25 μm to 500 μm. Changes in sample absorption and scattering properties, and apparent particle diameter are simultaneously estimated using two regression techniques of the statistical descriptors: stepwise multi-linear regression (SMLR) and partial least squares regression (PLS). The effect of light collection geometry on obtaining optimal estimates is discussed. The accuracy of absorption coefficient estimates and scattering estimates based on Mie theory is compared with previous work on liquid samples. Results show similarities both in the estimation accuracy and in the types of statistical descriptors chosen when compared to liquid samples.

2.3 Experimental Work

The experimental apparatus developed for time-resolved diffuse reflectance measurements is shown in Figure 2.1. The heart of the system is a time-correlated single photon counting instrument which is similar to devices found in fluorescence life-time studies.[17] A mode-locked Ti:Sapphire laser (Mira 900B, Coherent, Santa Clara, CA) pumped by an Argon laser (Innova 310, Coherent) was used to produce laser pulses with a repetition rate of 76 MHz. The pulse shape of the laser was measured using an optical autocorrelator and was found to have a width of 170 fs. The laser was tuned to 780nm for the experiment and the power was measured as 0.51 W corresponding to peak pulse powers of 51 kW.

The output beam was split by a beamsplitter after which 4% of the light was focused onto a fast photodiode (ET2000, Electro-Optics Technology Inc., Traverse City, MI). The remaining portion of the pulse was attenuated by a neutral density filter and directed onto the sample using a computer controlled mirror galvanometer (CX660, General Scanning Inc., Watertown, MA). With the aid of a lens and a mirror, the light was introduced into the sample perpendicular to its face. A pair of lenses focused the light exiting the sample cell at a particular point onto a cooled microchannel plate photomultiplier tube (MCP) (R3808U, Hamamatsu Corp., Bridgewater, NJ). This optical arrangement allowed light originating from other points on the surface of the cell to be rejected. Output from the photodiode and MCP were each connected to separate constant fraction discriminators (CFD) (Model 2126, Canberra Industries Inc., Meriden, CT). Logic pulses from the CFDs were sent into a time-to-amplitude converter (TAC) (Model 2145, Canberra). The MCP response was used to start the TAC timing and the

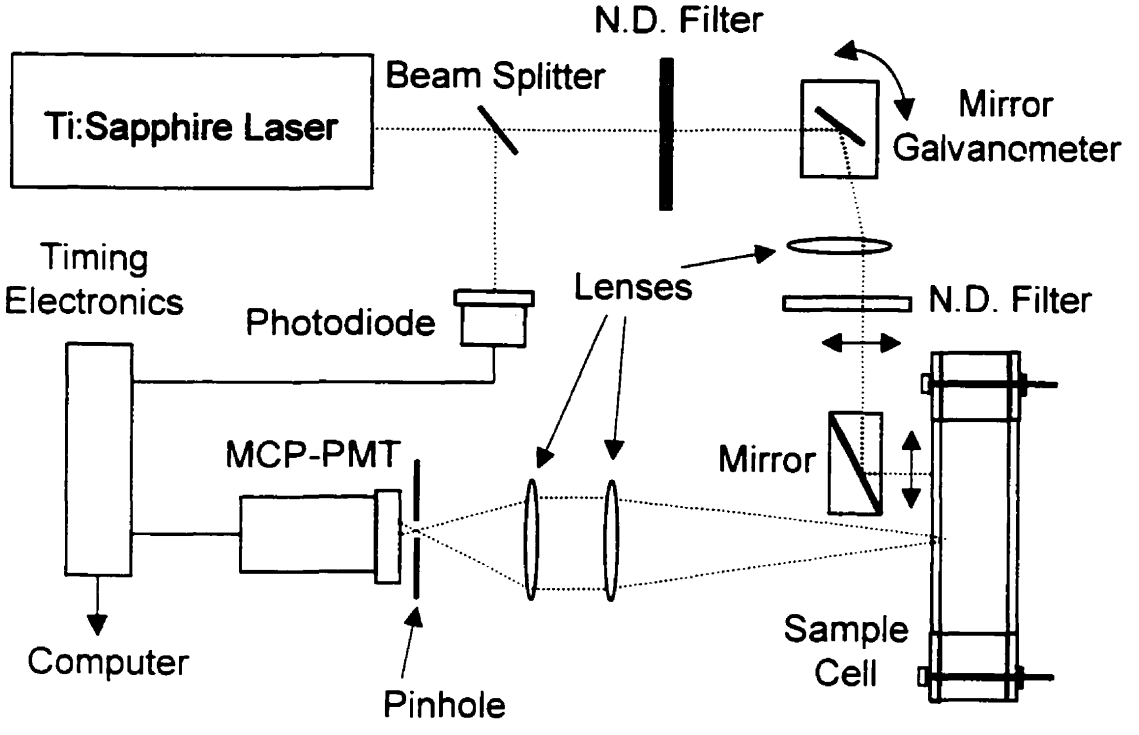

Figure 2.1. Diffuse reflectance photon time-of-flight instrumentation.

photodiode response stopped the timing. The DC voltage output of the TAC was proportional to the elapsed time between the start and stop pulses. The TAC output was digitized using a 400 kHz 12-bit A/D converter (AT2000, National Instruments, Austin, TX) resulting in time increments of 4.9 ps. The instrument response with no sample present was measured to be 280 ps FWHM. Software running on a PC written in C was used for data acquisition, beam positioning and time binning.

The 20mm deep sample container consisted of a black reservoir fitted with a 40 × 50 mm glass window, 0.15 mm in thickness. The window was designed with a groove separating the source from the detector so that internal reflections in the glass did not interfere with light collection.

Granular silica samples of four different sieve sizes (18-32, 32-63, 100-200, 200-500 μm) were used (ICN Biometerials, NJ). Each silica sample was poured into methanol with the addition of dye (Dr. Ph. Martin's Transparent Water Color #33 Black, Hollywood, FL). The solvent was removed *in vacuo* with agitation to reduce non-uniformities in the coating process. Samples were stirred and dried at 110°C for two hours prior to analysis.

Time distributions were recorded at three source/detector separations (5, 10 and 15 mm) and with varying sample composition. Each acquisition required 6 minutes with total counts ranging from 1.8×10^5 to 9.6×10^5 in each distribution. High frequency periodic noise due to the time-to-amplitude converter was reduced by smoothing the measured time profiles.[17] A Gaussian smoothing window (σ = 25 ps) was used to reduce the magnitude of the periodic noise by 94%. A series of 23 distinct samples were analyzed with replicate measurements. The set was comprised of four different granular

silica samples each with several different dye concentrations. Examples of the photon time distributions after preprocessing are shown in Figures 2.2 and 2.3. Further data preprocessing and sectioning into calibration and prediction sets is discussed in the analysis section.

2.4 Sample Characterization

2.4.1 Particle size distribution

For particle sizing of ground or crushed materials, the normal distribution may be used as a reasonable approximation of the particle size distribution after seiving.[18,19] This distribution of particle diameters x is written as,

$$p(x) = \frac{\phi}{\sqrt{2\pi\sigma^2}} e^{-(x-\bar{x})^2/2\sigma^2} \tag{2.1}$$

where ϕ is the solid volume fraction, $\bar{x}$ is the mean particle size, and σ the standard deviation. This distribution was assumed to hold for the samples under investigation. Using specific sieving efficiency data furnished by ICN Pharmaceuticals, Inc. (Costa Mesa, CA.) the mean particle size and standard deviation were determined using Equation 2.1. The solid volume fraction ϕ, was calculated as the density ratio between the powder and crystalline silica. For particle sizing, the "apparent particle size" given by $\bar{x}/\phi$ was used. This quantity may be seen as an approximation to the average length between scattering events (μ_s^{-1}).

2.4.2 *Scattering coefficient determination*

Given the sample's particle size distribution, Mie theory was used to estimate the weighted average scattering coefficient. To facilitate calculation of the scattering coefficient, samples were assumed to be composed of spherical homogeneous particles, as a reasonable first order approximation.[1,2] This method was used to approximate the scattering coefficients of the samples, however it is recognized that the particles are not spherical and may not be well modeled. The mean scattering coefficient is written as,

$$\mu_s = \int_0^{\infty} \frac{3Q_{scat}(x,n,\lambda)}{2x}\, p(x)\, dx \qquad (2.2)$$

where $Q_{scat}(x,n,\lambda)$ is the scattering efficiency for a given sphere diameter, x, relative refractive index, n (n_{silica}/n_{air}) and wavelength, λ (evaluated at 780 nm). Scattering efficiencies were computed numerically using an algorithm by Bohren and Huffman.[16]

2.4.3 *Absorption properties*

The silica samples were coated with a dye which absorbs strongly at the probe wavelength (780 nm). The dye was assumed to homogeneously coat the silica. The average absorption coefficient for each sample was calculated as $\mu_a = 2.303\ \varepsilon\ c$ where ε is the extinction coefficient of the dye (1.28×10^{-3} $ppm^{-1}mm^{-1}$) and c is the average dye concentration in ppm per unit mass of powder. The range of absorption coefficients determined for the particles spanned between 0.00 mm^{-1} to 0.50 mm^{-1}.

2.5 Analysis

2.5.1 Statistical descriptors

To understand the relationship of the different portions of the time profiles, statistical descriptors were used. Such an approach in the future, will allow for real-time sample characterization by directly analyzing the time resolved signals with simple electrical circuits. The statistical descriptor set included in this study is given in Table 2.1 with their mathematical representations. As in previous work with liquid samples[10], photon time-of-flight distributions were decomposed into moments, rising and trailing times, slopes, and peak maxima after logarithmic processing. Area descriptors (a_x) were also computed, however, the logarithm was taken after integrating. The area descriptors are proportional to the steady state signal and are analogous to a classical reflectance measurement. Contributions to the total signal from the initial (rising) and latter (trailing) portions of the time distribution were measured. The area of the rising and trailing portions (a_r and a_f respectively) describe the portion of early and late photons that reach the detector. Likewise, the mean rising and trailing times (t_r and t_f) describe average times early and late photons respectively take to traverse the sample. Rising and trailing slopes (m_r and m_f) and peak maxima (p) were included as they are markedly affected by changes in sample absorption and scattering.[11] Moments (u_1-u_4) were also included as they have been shown to be a good descriptor of the overall shape of time distribution.[20] First and second moments (u_1 and u_2) of the time distribution describe the mean time and the variance of the distribution respectively. The mean time is known to relate the rate of change of measured intensity to the change in absorption.[20] The third moment (u_3) was included in the descriptor set as it related to the skewness (s) which measures the degree

of the time-distribution symmetry. The fourth moment (u_4) and kurtosis (k) strongly weight the tailing edge of the time-distribution.

Table 2.1. Statistical descriptors computed from the diffuse reflectance time-of-flight profiles.

Statistical Descriptor	Expression
Log area, a	$\log \int_0^{t_{max}} f(t)dt$
Log area of the rising portion, a_r	$\log \int_0^{t_{peak}} f(t)dt$
Log area of the trailing portion, a_f	$\log \int_{t_{peak}}^{t_{max}} f(t)dt$
Mean time of the rising portion, t_r	$\int_0^{t_{peak}} t \log(f(t))dt$
Mean time of the trailing portion, t_f	$\int_{t_{peak}}^{t_{max}} t \log(f(t))dt$
Mean slope of rising portion, m_r	$\frac{1}{t_{peak} - t_{thresh}} \int_{t_{thresh}}^{t_{peak}} \frac{d}{dt} \log(f(t))dt$
Mean slope of trailing portion, m_f	$\frac{1}{t_{thresh} - t_{peak}} \int_{t_{peak}}^{t_{thresh}} \frac{d}{dt} \log(f(t))dt$
1^{st}, 2^{nd}, 3^{rd}, 4^{th} moments, u_n n=1,2,3,4	$\int_0^{t_{max}} t^n \log(f(t))dt$
Peak maximum, p	$\max[\log f(t)]$
Standard Deviation, σ	M_2^*
Skewness, s	$M_3 / M_2^{3/2}$
Kurtosis, k	$(M_4 / M_2^2) - 3$

* centered moment $M_n \equiv \int_0^{t_{max}} (t - \langle t \rangle)^n \log(f(t))dt$

2.5.2 *Calibration and sample quantification*

To understand the significance of the different statistical descriptors on the analysis, both SMLR and PLS regression approaches were used for estimating the absorption and scattering coefficients and apparent particle diameters. The set of samples comprising the calibration set was chosen randomly from one of the two replicate experimental measurements. The other portion of the samples comprised the prediction set. Both sets contained equal numbers of samples with different particle size and absorption levels. Fifteen descriptors listed in Table 2.1 were computed for each time distribution collected in the calibration set. The resulting values were autoscaled to avoid biasing the model due to the magnitude differences between descriptors.

To allow for practical on-line sample characterization, step multilinear regression was investigated. The SMLR technique identifies a linear combination of a subset of independent variables which optimally describe a dependent variable $\mathbf{Y}$, $(1\times p)$ in the form,

$$y = b_0 + b_1 x_1 + \ldots + b_m x_m \qquad (m < n) \tag{2.3}$$

where p is the number samples in the training set, x_1, x_2, ... , x_m are the independent variables or channels, n is the total number of channels and b_0, b_1, ... , b_m are the coefficients determined from the calibration. The SMLR method finds the optimal linear combination of data channels correlated with $\mathbf{Y}$. In constructing of the optimal set of m descriptors, the routine evaluates a number of intermediate regression models. Descriptors were selected based on the lowest standard error between $\mathbf{Y}$ and $\hat{\mathbf{Y}}$ in the training set. Descriptors were removed from the set if after the addition of others, the

new combination of descriptors produced a significantly better estimates. Partial F-tests at 95% significance were used for the evaluation of the models. The routine ended when there was no longer a statistical difference between two consecutive models. The SMLR analysis routine was written in Matlab[10] (The MathWorks, Natick, MA) and is based on algorithm by Draper and Smith.[21]

For a given sample property, four SMLR models were built using data collected at single source/detector separations (5, 10, and 15 mm) and a combination of all three. The relationship between the chosen descriptors (independent) and the absorption coefficient, scattering coefficient or mean particle size (dependent) follows from Equation 2.3.

Using the prediction set, absorption, scattering and apparent particle size estimates for a each sample were made by processing the time distributions with the m optimal descriptors and applying Equation 2.4 with the b_i parameters determined in the calibration. Each model was assessed by measuring the correlation about the line of identity between the estimated and reference values. Both r^2 and coefficients of variation (C.V.) between the reference and experimental values were computed. With each optimal model, a cross validation calibration was done to determine if any biasing was present by the inclusion of incorrectly characterized or prepared samples. A 'leave one sample-type out' approach was used. It was observed that in all cases a similar number of descriptors was needed for each estimation. No improvements in the estimations were obtained by removing samples from the original set at the 95% confidence level.

Analogously, models were constructed using Partial Least Squares regression. The PLS method is related to both Principal Components Regression (PCR) and Multi-Linear Regression (MLR). It attempts to simultaneously capture the greatest amount of

covariance between the descriptors (like in PCR) and to find a factor that best correlates the descriptors with the dependent variable **Y** (as with MLR). The one component PLS routine used in the analysis was based on the NIPALS algorithm.[22,23] For estimations of absorption and scattering coefficients and apparent particle diameters, the optimal number of factors was determined from the predicted residual error sum of squares (PRESS) values. PRESS values were calculated as the sum of the squares of residuals between the PLS estimates and reference values for each sample in the prediction set. An F-test at 95% significance on the ratios of adjacent PRESS values were used for determining the optimal number of statistically significant factors.

2.6 Results and Discussion

Diffuse reflectance measurements were made on absorbing silica samples of varying grain size. Typical diffuse reflectance time-of-flight profiles for a single sample coated with different dye concentrations, shown in Figure 2.2, demonstrate the sensitivity of the profiles to changing absorbance. The integrated intensity (area under the profile) decreases and the peak maximum shifts toward shorter times as sample absorption increases. This trend is due to an increased probability of longer pathlength photons being absorbed before they reach the detector. In addition, the slope of the trailing portion of the curve is no longer constant. Figure 2.3 demonstrates the change in the time-of-flight profile with changing sample grain size. As grain size is reduced, the scattering level increases which decreases the peak maximum and shifts it toward longer times. The increased number of scattering events the light experiences leads to

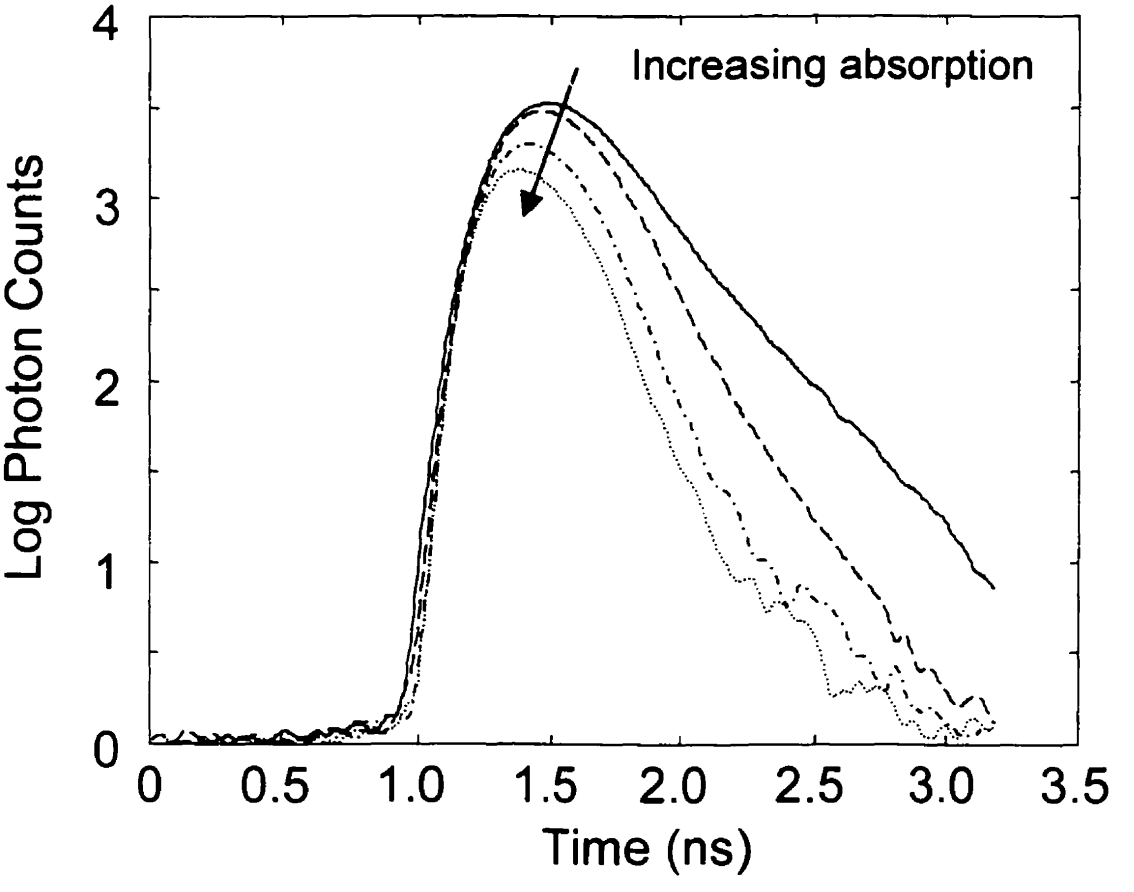

Figure 2.2. Photon time-of-flight profiles as a function of sample absorption at a 15mm source/detector separation. Legend: $\mu_a = 0.000$ mm^{-1}, solid; $\mu_a = 0.033$ mm^{-1}, dashed; $\mu_a = 0.236$ mm^{-1}, dash-dotted; $\mu_a = 0.472$ mm^{-1}, dotted.

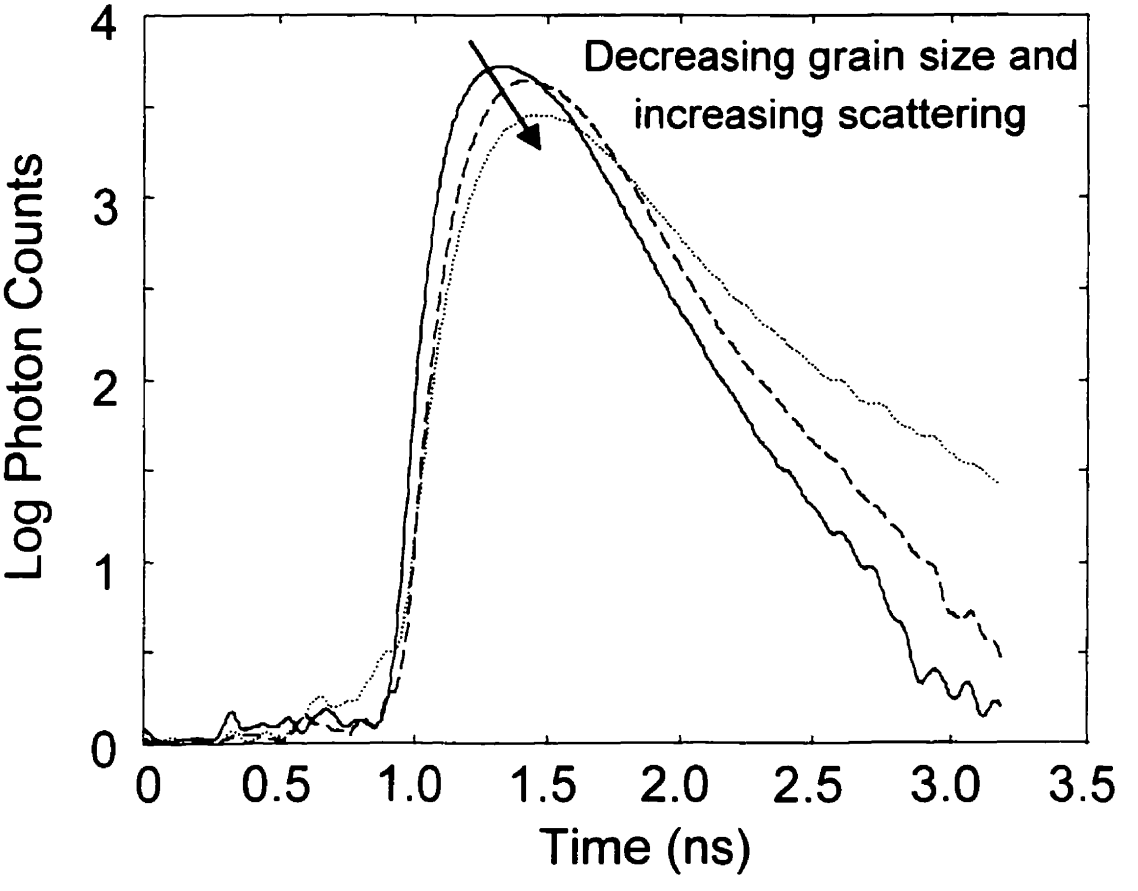

Figure 2.3. Photon time-of-flight profiles as a function of scattering coefficient at a 15mm source/detector separation. Legend: μ_s = 1.86 mm^{-1}, solid; μ_s = 3.25 mm^{-1}, dashed; μ_s = 20.01 mm^{-1}, dotted.

broadening of the profile and longer transit times from source to detector. Although photon transport theories have been developed for single scattering processes in coated spheres, multiple scattering models are not been fully developed for the range of grain size considered.[16] Therefore the diffusion model approach is used for comparison purposes only. The trends shown in Figures 2.2 and 2.3 are indeed in general agreement with what diffusion theory would suggest. However, when both scattering and absorption are simultaneously changed, marked differences are observed. This can be seen using the integrated intensity of each sample as a function of absorption coefficient relative to a similar sample with no added absorber as plotted in Figures 2.4 and 2.5. With both experimental (Figure 2.4) and theoretical[11] diffusion equation results (Figure 2.5), a general increase in attenuation is seen with the absorption coefficient. The difference between the two is that they have a different rate of change of sample attenuation with changing absorbance. Also, the ordering of the curves is reversed when the scattering coefficient is varied. One explanation of this effect is that in coated granular samples, light traversing from source to detector may spend relatively more time in non-absorbing regions than in a sample which absorbs light continuously between scattering events. This is because in a granular sample, light travels through the void spaces as well as the non-absorbing core. Another explanation is that the change in grain size affects not only the scattering coefficient but the scattering phase function. It is well known that diffusion theory does not characterize photon transport accurately through non-isotropic scattering media. A different approach should be taken when attempting to model the absorption, scattering or apparent particle size in crushed granular samples.

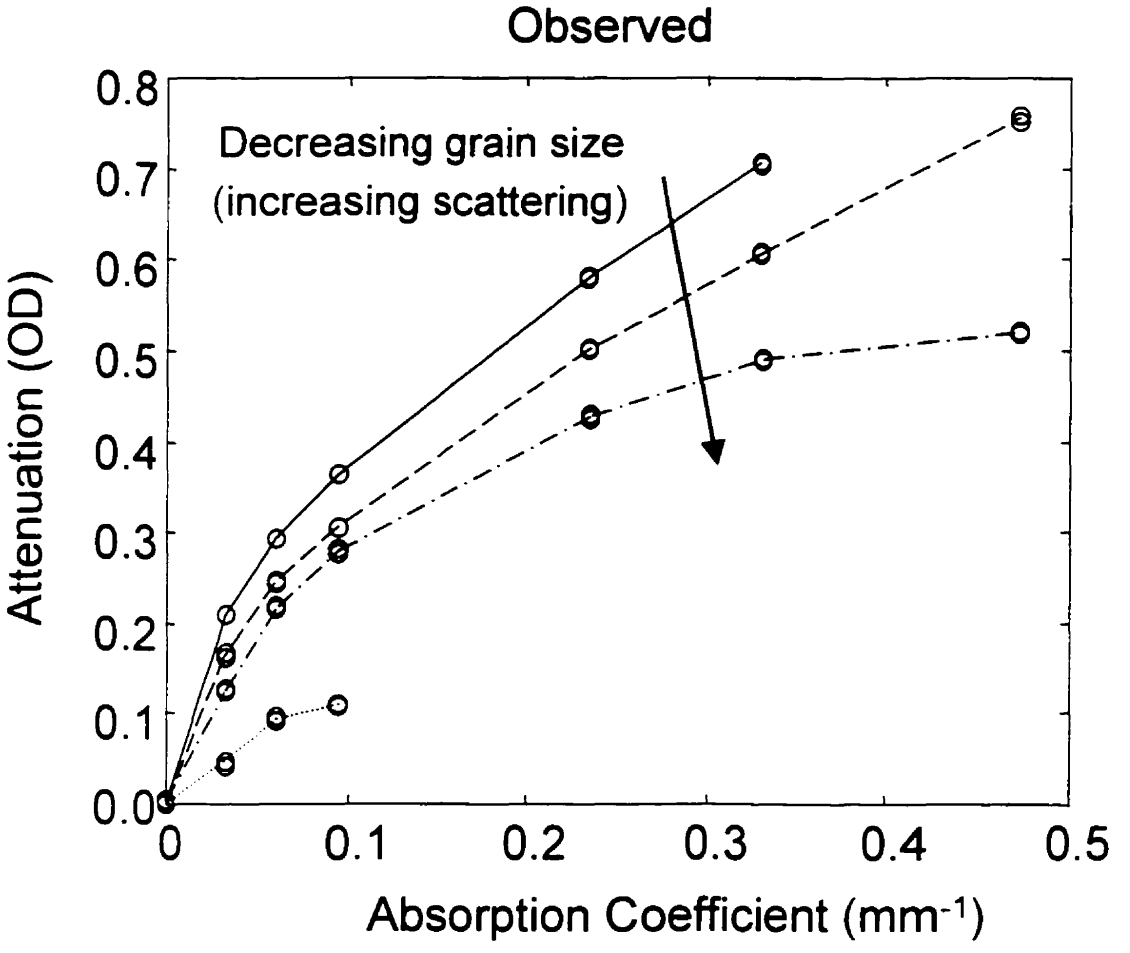

Figure 2.4. Experimental attenuation versus absorption coefficient at different scattering levels. Legend: μ_s = 1.86 mm^{-1}, solid; μ_s = 3.25 mm^{-1}, dashed; μ_s = 10.52 mm^{-1}, dash-dotted; μ_s = 20.01 mm^{-1}, dotted.

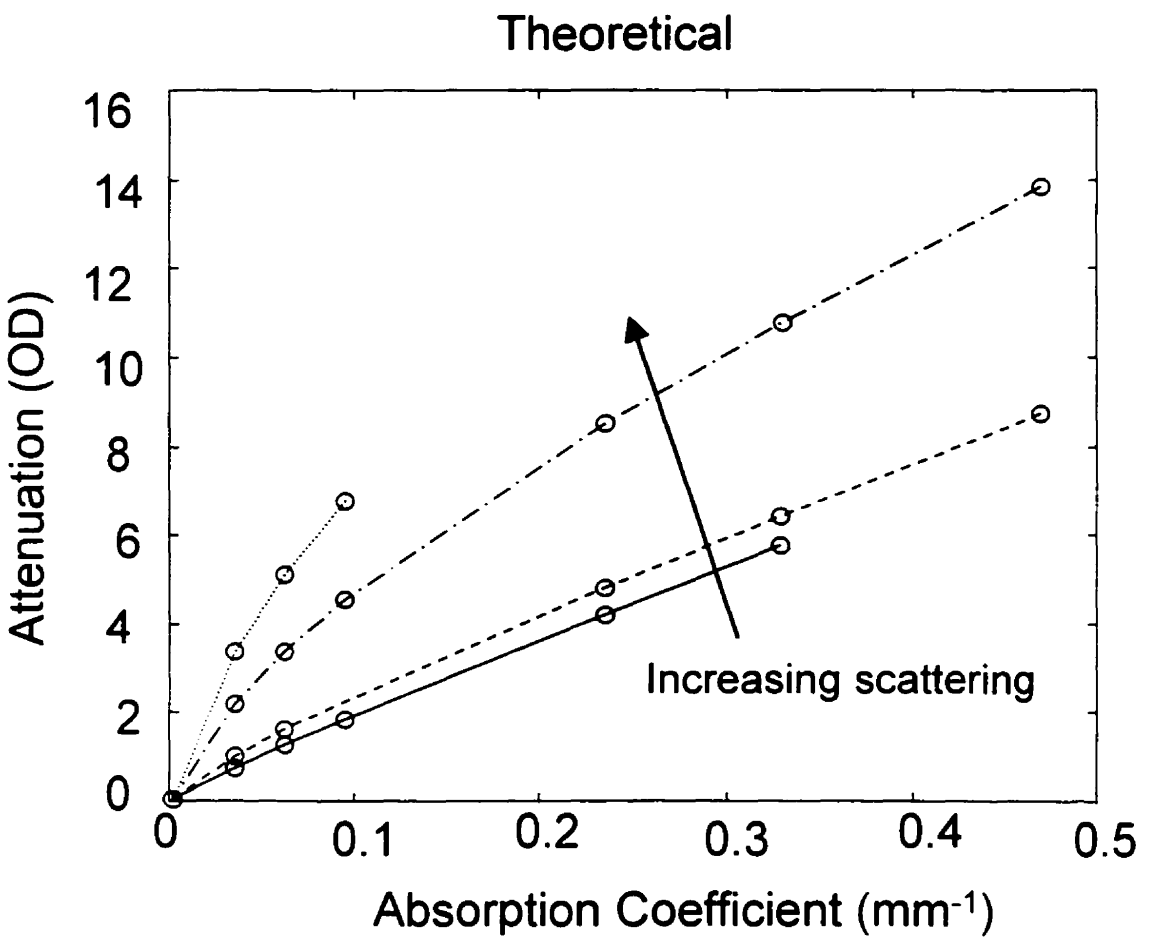

Figure 2.5. Theoretical attenuation versus absorption coefficient at different scattering levels based on the diffusion model (5mm source/detector separation, g=0.8). Legend: μ_s = 1.86 mm^{-1}, solid; μ_s = 3.25 mm^{-1}, dashed; μ_s =10.52 mm^{-1}, dash-dotted; μ_s = 20.01 mm^{-1}, dotted.

2.6.1 Estimates using time profiles taken at a single detector position

Three models were built for estimating absorption, scattering and mean particle size using both the PLS and SMLR approaches. The models were developed using 15 descriptors from the time-of-flight distributions taken at a single source/detector separation (either 5, 10 or 15 mm).

Results of the PLS estimates of the sample absorption are given in Table 2.2. In all cases, one or two factors were determined to be optimal using all 15 descriptors. In general, the absorption coefficient estimates were more accurate when the source/detector separation was small (5mm). The coefficient of variation between the estimated and reference values was 13.7 % ($r^2 = 0.962$). A regression about the line of identity resulted in a slope of 0.93 ± 0.09 and an intercept of $(1.9 \pm 0.9)\times10^{-2}$ mm^{-1}. At larger separation distances, i.e. 15 mm, increased error for the estimates was observed. Similar trends and levels of accuracy were obtained with the SMLR model. As shown in Table 2.3, the best absorption coefficient estimates were obtained with the smallest source/detector separation [C.V. = 13.4 %; $r^2 = 0.964$; regression slope = 0.95 ± 0.07; intercept = $(2.2 \pm 0.9)\times10^{-2}$ mm^{-1}]. The best linear combination of descriptors was the kurtosis, the area of the rising portion and the time of the trailing portion. The tailing portion of the time-of-flight profile is well known to be strongly affected by sample absorption.[12] Since the kurtosis is sensitive to changes in the extremities of a distribution, it is reasonable that it would correlate well with changes in sample absorption. The average times of the trailing and rising portions would also be affected in a similar manner.

Table 2.2. PLS estimates of the absorption coefficient, apparent particle size and scattering coefficient using descriptors from time distributions taken at a single detector position.

Quantity	Detector Position	C.V. (%)	r^2
μ_a (mm^{-1})	5 mm	13.7	0.962
	10 mm	20.6	0.917
	15 mm	24.7	0.899
d (mm)	5 mm	10.7	0.963
	10 mm	10.4	0.968
	15 mm	8.2	0.971
μ_s (mm^{-1})	5 mm	14.9	0.930
	10 mm	12.8	0.944
	15 mm	11.1	0.964

Table 2.3. SMLR estimates of the absorption coefficient, apparent particle size, scattering coefficient using data obtained at a single detector position.

Quantity	Detector Position	Chosen Statistical Descriptors	C.V. (%)	r^2
μ_a (mm^{-1})	5 mm	k a_r t_f	13.4	0.964
	10 mm	k a_r p	16.5	0.945
	15 mm	a a_r s k	24.8	0.895
d (mm)	5 mm	t_r p m_f	9.1	0.972
	10 mm	t_r p k m_r	9.1	0.973
	15 mm	t_r p m_r	7.7	0.979
μ_s (mm^{-1})	5 mm	t_r p m_r	16.8	0.921
	10 mm	t_r a_r m_r	13.0	0.948
	15 mm	t_r σ a_r t_f	11.3	0.960

For estimates of apparent particle size, better accuracies were obtained compared to estimates of absorption. The SMLR model produced more accurate estimates over PLS at each of the three source/detector positions. The best SMLR estimates were obtained with a source/detector separation of 15mm [C.V. = 7.7%; $r^2 = 0.979$; regression slope = 0.97 ± 0.06; intercept = $(2.8 \pm 2.1)\times10^{-1}$ mm]. Using a PLS approach the most

accurate model had a C.V. of 8.2% [$r^2 = 0.971$; regression slope = 0.98 ± 0.09; intercept = (3.6 ± 1.8)×10^{-1} mm]. With both models, larger errors were found in estimates of particle size at small source/detector separations. At small separations, the bulk of the detected photons have not penetrated deep into the sample and consequently, the pulse has not had time to significantly broaden. With SMLR, the best set of descriptors was identified to be the mean time and slope of the rising portion, and the peak maximum. The choice of descriptors is consistent with expected physical characteristics of the measurements. As grain size and the scattering coefficient are related quantities, it is reasonable that descriptors sensitive to the rising portion of the time-of-flight profile were chosen.

The scattering coefficient was also estimated. Both the PLS and SMLR estimates produced accurate estimates at large source/detector separations. However, there was no statistical difference between the two most accurate models. [PLS: C.V. = 11.1%; r^2 = 0.964; regression slope = 1.02 ± 0.06; intercept = -(3.4 ± 1.5)×10^{-1} mm^{-1}; SMLR: C.V. 11.3%, r^2 = 0.960; regression slope = 1.03 ± 0.07; intercept = -(3.8 ± 2.9)×10^{-1} mm^{-1}]. As expected, the chosen statistical descriptors were similar to those chosen for particle size estimates. The SMLR method included in the best fit linear combination, the mean time and area of the rising portion, the standard deviation, and mean of the trailing portion. In general, however, estimates of the scattering coefficient were worse than for the apparent particle size as expected by Equation 2.2.

2.6.2 *Estimates using time profiles taken at multiple detector positions*

Improved estimates were obtained when information from all three detected responses were incorporated into either the PLS or SMLR models. Tables 2.4 and 2.5 show the coefficients of variation and r^2 values for estimating the absorption coefficient, scattering coefficient and the apparent particle size with PLS and SMLR. Overall, little or no statistical differences were observed between the two approaches. However, SMLR allows one to identify which features of the time distribution are the most significant for quantification.

Table 2.4. PLS estimates of the absorption coefficient, apparent particle size, and scattering coefficient using descriptors from time distributions taken at multiple detector positions.

Quantity	C.V. (%)	r^2
μ_a (mm^{-1})	11.4	0.973
d (mm)	7.4	0.977
μ_s (mm^{-1})	8.9	0.979

Table 2.5. SMLR Estimates of the absorption coefficient, apparent particle size, and scattering coefficient using data obtained at multiple detector positions.

Quantity	Chosen Statistical Descriptors	C.V. (%)	r^2
μ_a (mm^{-1})	k(5)* a_r(5) k(10) t_f(5)	10.3	0.984
d (mm)	t_r(15) p(10) p(5)	6.7	0.983
μ_s (mm^{-1})	t_r(15) a_r(10) m_r(10) σ(15)	8.6	0.981

*bracketed values refer to detector position in mm

In Figures 2.6, 2.7 and 2.8, the estimates provided by SMLR are plotted against their assessed values. The solid line represents the line of identity for ideal estimation.

The slopes and intercepts of the regressions were calculated to be 0.97 ± 0.03 and (1.3 ± 0.6)×10^{-2} mm^{-1} respectively for the absorption estimate, 0.98 ± 0.03 and (1.7 ± 0.6)×10^{-3} mm for the apparent particle size estimate, and 1.04 ± 0.04 and -(2.6 ± 1.3)×10^{-1} mm^{-1} for the scattering estimate. Using a combination of descriptors from all three detected time-of-flight responses, a linear combination of the kurtosis and the area of the rising portion correlated the best with changes in sample absorption. For scattering coefficient estimations, the mean time and slope and area of the rising portion and the peak standard deviation were chosen.

Comparing the best absorption estimation obtained in this study with previous work using statistical descriptors with liquid scattering samples, similar errors were obtained. For absorption coefficient estimates, both types of samples required descriptors related to the trailing portion of the time-of-flight profile. The major difference between the two optimal descriptor sets was that the mean rise time was replaced with the kurtosis. Comparing scattering coefficient estimates for the two sample classes is more difficult. Although the mean time of the rising portion was chosen in both studies, the remaining descriptors were different. This may be expected as vastly different ranges in the scattering coefficient were covered in the two studies.

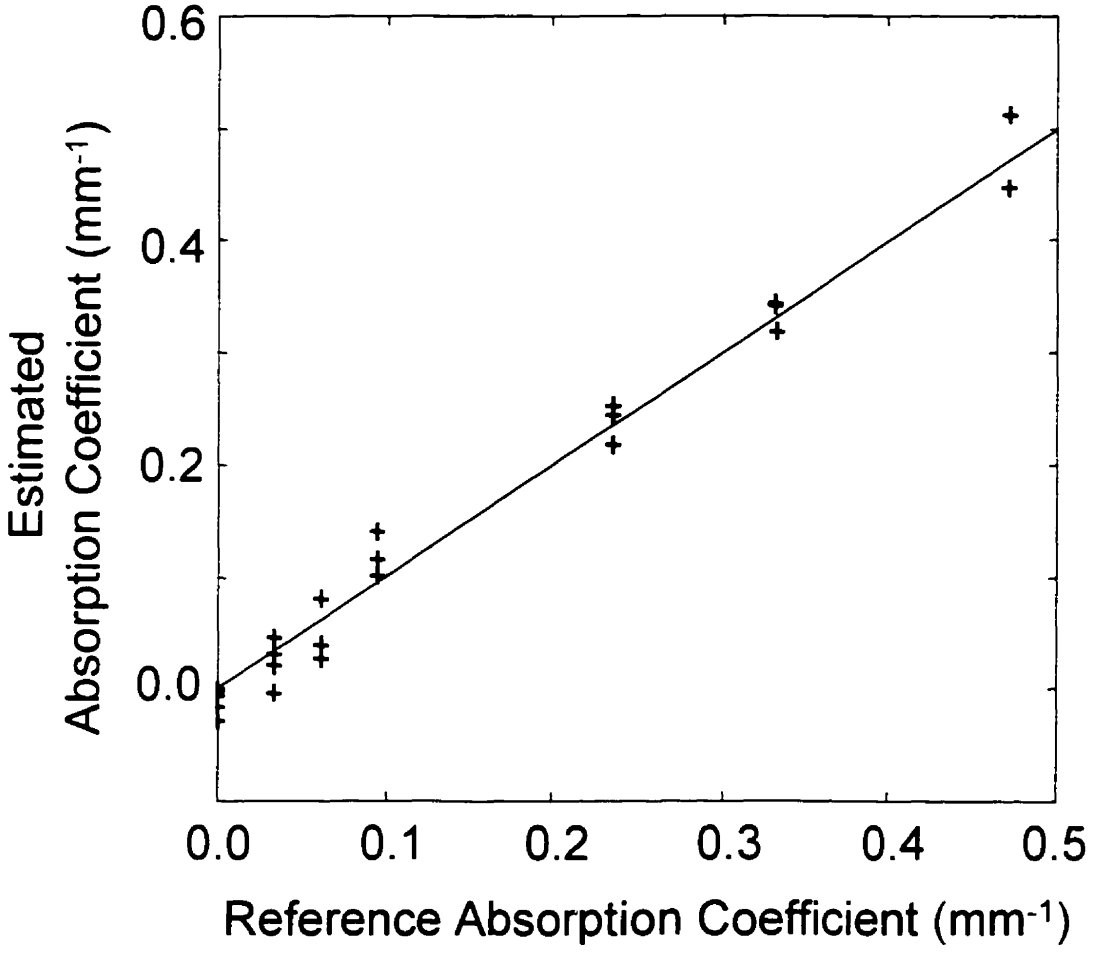

Figure 2.6. Descriptor estimates of the absorption coefficient using multiple time-of-flight distributions.

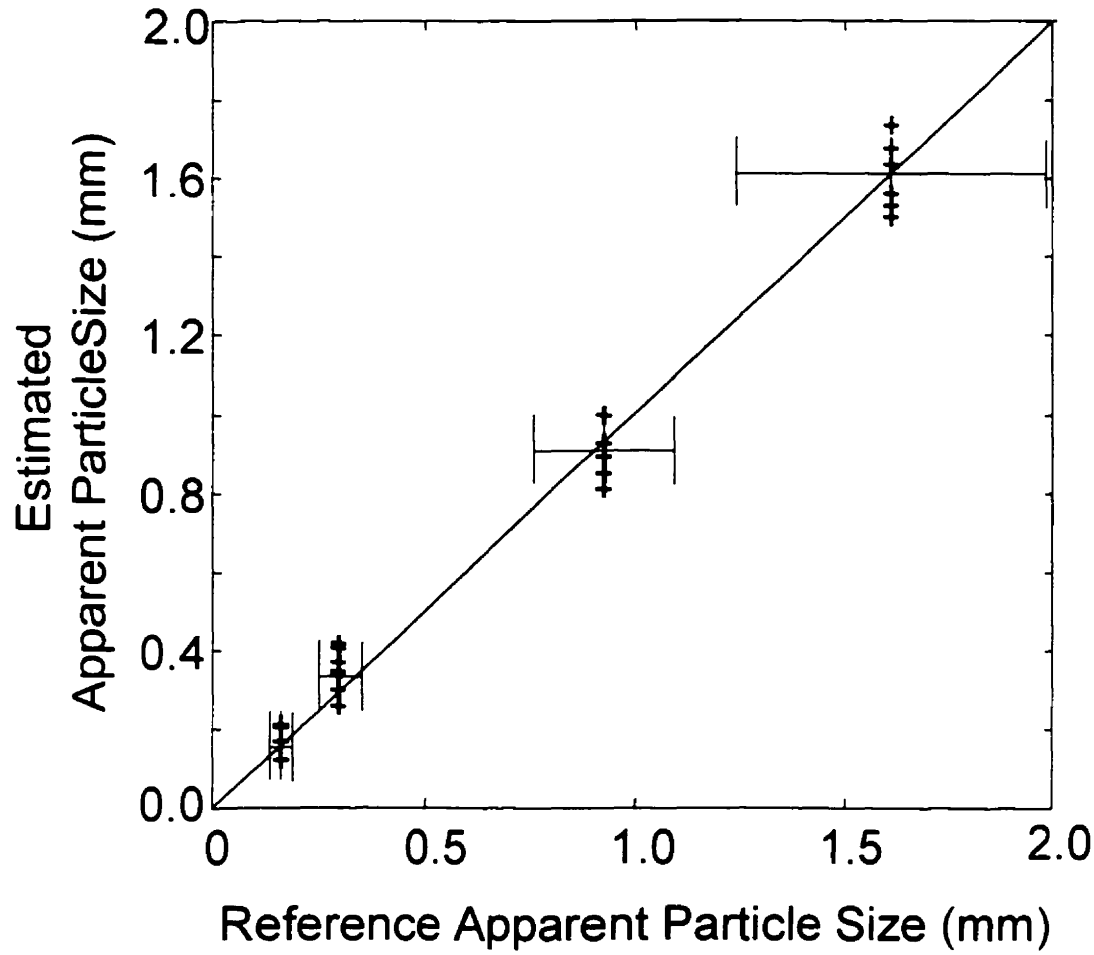

Figure 2.7. Descriptor estimates of the apparent particle diameter using multiple time-of-flight distributions. Horizontal error bars are drawn at ±1 standard deviation about the mean particle diameters.

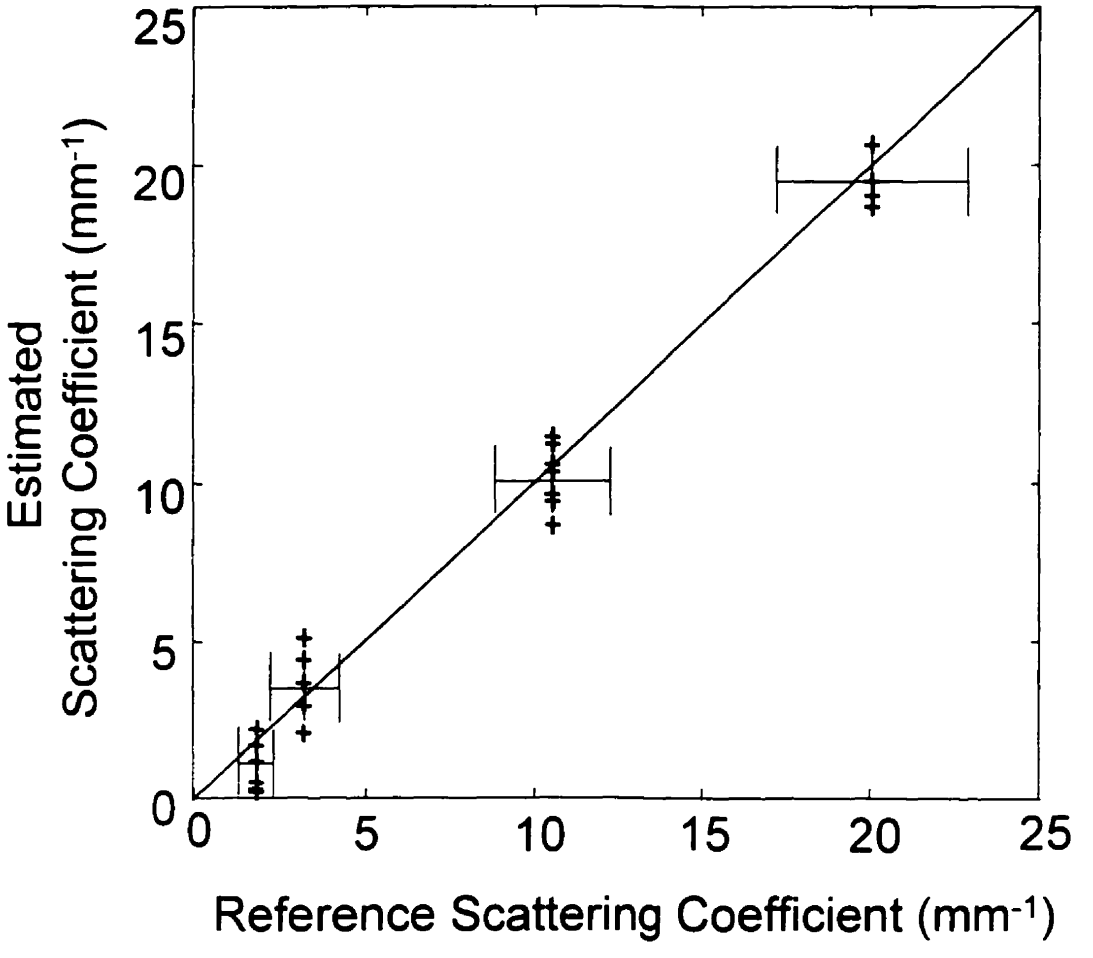

Figure 2.8. Descriptor estimates of the scattering coefficient using multiple time-of-flight distributions. Horizontal error bars are drawn at ±1 standard deviation about the mean scattering coefficients.

2.7 Conclusion

A method for the quantification of absorption, scattering and apparent particle size in a broad range of granular samples has been investigated. The approach employs the use of statistical descriptors to characterize photon time-of-flight distributions in relation to the optical parameters and particle size. Using SMLR, analytical descriptors describing the trailing portion and kurtotic nature of the time profiles were optimal for absorption estimates. When estimating either the scattering coefficient or apparent particle diameter, descriptors associated with the rising portion of the time profile were needed. Likewise, the choice of source/detector separation is important for optimal quantification. For absorption coefficient estimation, small source/detector separations were found to be optimal whereas larger separations were required for scattering and particle size estimations. In addition, it was generally found that the analytical descriptors used in each model were not highly dependent on choice of source/detector separation. However, when data from a combination of three detector positions was employed, the lowest errors in estimating the optical and physical characteristics in a sample were obtained. The relatively large spread about the line of identity may be due to variations in the sample packing density. Though attempts were made to ensure reproducibility between measurements, the sample cell used limited the possibilities for elaborate packing protocols. The results demonstrate that using statistical descriptors, a robust means for simplifying complex photon time distributions into measurable parameters is possible. In the future, descriptors may be used as a means in which to develop practical instrumentation for on-line, real-time characterization of absorbing granular media.

2.8 References

1. Grosenick, D.; Wabnitz, H.; Rinneberg, H. Time-Resolved Imaging of Solid Phantoms for Optical Mammography; *Appl. Opt.* **1997**, *36*, 221-231.
2. Bott S. E.; Hart, W. H. Extremely Wide Dynamic Range High-Resolution Particle Sizing by Light Scattering in Particle Size Distribution II Assessment and Characterization; In *ACS Symposium Series*; Provider, T., Ed.; ACS: Washington D.C., 1991. Vol. 471.
3. Jones, M. R.; Leong, K.H.; Brewster, M. Q.; Curry, B. P. Inversion of Light-Scattering Measurements for Particle Size and Optical Constants: Experimental Study; *Appl. Opt.* **1994**, *33*, 4035-4041.
4. Jiang, H.; Marquez, G.; Wang, L. V. Particle Sizing in Concentrated Suspensions by use of Steady-State, Continuous-Wave Photon-Migration Techniques; *Opt. Lett.* **1998**, *23*, 394-396.
5. Nefedov, A. P.; Petrov, O. F.; Vaulina, O. S. Analysis of Particle Sizes, Concentration and Refractive Index in Measurement of Light Transmittance in the Forward-Scattering-Angle Range; *Appl. Opt.* **1997**, *36*, 1357-1366.
6. Jones, M. R.; Curry, B. P.; Brewster, M. Q.; Leong, K. H. Inversion of Light-Scattering Measurements for Particle Size and Optical Constants: Theoretical Study; *Appl. Opt.* **1994**, *33*, 4025-4034.
7. Ilari, J. L.; Martens, H.; Isaksson, T. Determination of Particle Size in Powders by Scatter Correction in Diffuse Near-Infrared Reflectance; *Appl. Spectrosc.* **1988**, *42*, 722-728.

8. Ishimaru, A. *Wave Propagation and Scattering in Random Media*; Academic Press: New York, 1978.

9. Kubelka, P.; Munk, F. Ein Beitrag zur Optik der Farbanstriche; *Z. Tech. Phys.* **1931**, *12*, 593-599.

10. Leonardi, L.; Burns, D. H. Quantitative Constituent Measurements in Scattering Media from Statistical Analysis of Photon Time-of-Flight Distributions; *Anal. Chim. Acta* **1997**, *348*, 541-552.

11. Cope, M.; van der Zee, P.; Essenpreis, M.; Arridge, S. R.; Delpy, D. T. Data Analysis Methods for Near Infrared Spectroscopy of Tissue: Problems in Determining the Relative Cytochrome aa_3 Concentration; *Proc. SPIE* **1991**, *1431*, 251-262.

12. Patterson, M. S.; Chance, B.; Wilson, B. C. Time Resolved Reflectance and Transmittance for the Non-Invasive Measurement of Tissue Optical Properties; *Appl. Opt.* **1989**, *28*, 2331-2336.

13. Arakaki, L. S. L.; Kushermick, M. J.; Burns, D. H. Myoglobin Oxygen Saturation Measured Independently of Hemoglobin in Scattering Media by Optical Reflectance Spectroscopy; *Appl. Spectrosc.* **1996**, *50*, 697-707.

14. Ishimaru, A. Diffusion of a Pulse in Densely Distributed Scatterers; *J. Opt. Soc. Am.* **1978**, *68*, 1045-1050.

15. Richter, S. M.; Shinde, R. R.; Balgi, G. V.; Sevick-Muaraca, E. M. Particle Sizing using Frequency Domain Photon Migration; *Part. Part. Charact.* **1998**, *15*, 9-15.

16. Bohren, C. F.; Huffman, D. R. *Absorption and Scattering of Light by Small Particles*; John Wiley and Sons: New York, 1993, pp. 477-482.

17. Small, E. W. Laser Sources and Microchannel Plate Detectors for Pulse Fluorometry; In *Topics in Fluorescence Spectroscopy;* Lakowicz, J. R. Ed.; Plenum Press: New York, 1991, Vol. 1.

18. Allen, T. *Particle Size Measurement*; 4th ed.; Chapman and Hall: New York, 1990, pp. 124-170.

19. Dullien, F. A. L. *Structural Properties of Packings of Particles in Handbook of Powder Science and Technology*; 2nd ed. Fayed M. E.; Ottan L. Ed.; Chapman and Hall: New York, 1997, pp. 10-12.

20. Arridge, S. R.; Schweiger, M. Direct Calculation of the Moments of the Distribution of Photon Time-of-Flight in Tissue with a Finite-Element Method; *Appl. Opt.* **1995**, *34*, 2683-2687.

21. Draper, N.; Smith, H. *Applied Regression Analysis*; 2nd ed.; John Wiley and Sons: New York, 1981, p 307.

22. de Jong, S. SIMPLS: An Alternative Approach to Partial Least Squares Regression; *Chemom. Intell. Lab. Syst.* **1993**, *18*, 251-263.

23. Lorber, A.; Wangen, L. E.; Kowalski, B. R. A Theoretical Foundation for the PLS Algorithm; *J. Chemom.* **1987**, *1*, 19-27.

Chapter 3 Optical Tomographic Reconstruction from Diffuse Remittance in Scattering Media Using Partial Least Squares Estimation

In the previous chapter, quantification of scattering and absorption levels was done in uniform granular samples using statistical descriptors of the time-resolved diffuse reflectance signals. When a sample's absorption characteristics are varied, changes in the trailing edge of the time distribution are most apparent. Typically, for homogeneous scattering/absorbing samples, the trailing edge has a slope dependent on the absorption coefficient. Although statistical descriptors may be used for describing broad changes in the photon time distribution they are not easily applicable for quantifying more subtle changes. This is was found to be true when Monte-Carlo simulations were used to investigate both the time resolved and steady state diffuse reflectance photon intensity in layered samples. In order to capture these subtle changes, many more data channels are required. It was therefore decided to use chemometric methods for analyzing layered samples. As a initial approach to layer wise tomographic reconstruction, steady state diffuse reflectance (remittance) measurements were made.

Because tomographic sample reconstructions require multi-perspective information, remittance measurements were made as a function of source/detector separation. From a geometric standpoint, it is difficult to obtain a series of unique ray paths through a layered sample by employing transmission measurements. This is true even if the incident beam is allowed to penetrate the sample obliquely; the integrated intensity through the sample is simply a multiple of one obtained normal to the sample face.

In this chapter, tomographic reconstruction is done using partial least squares and inverse least squares methodologies. Estimates of the absorption coefficient are made independently of others in six regions in a given sample. Comparisons are made between this method and a classical backprojection approach to tomographic reconstruction. In addition, reconstruction accuracies using experimental data are compared to those obtained by Monte-Carlo simulation. The source code for the Monte-Carlo photon propagation model is listed in the Appendix. Layer 1 (Region 1) is defined as the surface region while Layer 6 (Region 6) is region at the bottom of the sample. Six regions were chosen to satisfy the Nyquist criterion for resolving a top/middle/bottom split in the specimen.

3.1 Abstract

The long term goal of this research is to develop a method for quantitative, three-dimensional optical imaging in scattering media. Towards this end, a reconstruction technique for depth-resolved absorption determinations based on diffuse reflectance measurements was developed. The approach employs an array of radial measurements of intensity to obtain multi-perspective information through a specimen. Both Monte Carlo simulations and experimentally obtained reflectance measurements of known phantoms were used to evaluate the sensitivity of the method to changing sample absorption. Diffuse reflectance experiments were made using a collimated incident light source and layered absorbing/scattering samples. A fiber optic detection system measured radial responses for a series of different phantom compositions. Results demonstrate that a well-defined ray path is obtained for light measured from each source and detector pair.

For image reconstruction, a comparison to volume element estimation were made for classical back projection, inverse least squares and partial least squares methodologies. Overall, PLS gave significantly better results with a 50% reduction in the coefficient of variation compared to the back projection method. This depth resolved tomographic approach is a new tool to study spatial relationships of chromogenic constituents in scattering media.

3.2 Introduction

In many scientific fields there is the need for quantitative observation of a specimen in three dimensions. Examples include the non-destructive inspection of materials to locate defects, measurement of atmospheric pollutants, or *in vivo* tissue measurements of bio-energetic activity. These types of analyses commonly employ optical measurements to determine concentration of analyte molecules.

Transmission and reflection measurements can be made conveniently using a single point detector for one dimensional sampling or with the use of a scanning arrangement for two dimensional concentration determinations. When the specimen is imaged onto a detector, the measured response probes a defined region and the information from the sample heterogeneity is integrated.

A common method employed in the resolution of the integrated information is tomographic reconstruction developed for x-ray Computer Aided Tomography (CAT) analysis. One way in which this can be achieved is by rotating the sample with respect to the imaging system and acquiring images at multiple perspectives. The multi-perspective

responses are mathematically reconstructed to obtain a quantitative three-dimensional estimate of the sample composition.

The concept of tomographic reconstruction was developed many years ago. Radon demonstrated that using an infinite number of noiseless projections, an object can be unambiguously reconstructed.[1] However if either of these conditions are not met, an exact reconstruction is not obtained. Many techniques have been developed in order to minimize errors associated with the limitations of real world reconstructions. Samples may be scanned using a variety of light projection geometries, however the chosen technique must be compatible with both the sample nature and the desired accuracy in the reconstruction.

A commonly used reconstruction algorithm is the Filtered Back Projection method.[2] The underlying concept of the method is to assign the measured intensity of the axial projection to each element in the sample along the line with which the integration was made. For the first estimate, this assumes that the sample is uniform along each projection. By summing all of the sample distributions from the projections, an approximate reconstruction of the original sample can be made. In the case where there is not a sufficient number of projections to describe the spatial character of an object (limited view), reconstruction errors increase dramatically. In order to obtain accurate results, iterative techniques with the use of *a priori* sample information are commonly employed.[3]

Recently, there has been significant interest in reconstructions from highly scattering samples. Non-invasive optical tomography of specimens which contain scatterers has many applications in fields such as diagnostic medicine, plastics

manufacturing or pharmaceutical analysis. For example, three-dimensional reconstruction techniques could provide additional information for measurements of heterogeneity of plastic composites, *in vivo* metabolic processes or batch fermentation. In these applications, measurement of the diffuse reflectance is preferred and can provide a practical means for non-invasive analysis of biological tissue samples, paints and other coatings. For diffuse reflectance measurements, a small fraction of the light is scattered such that it enters the detector located some lateral distance away from the source. In general, the further the detector is located from the source, the larger the depth of penetration and the lower the light intensity measured.[4,5] This depth information has been used to tomographically obtain three-dimensional reconstructions of the forearm.[6] However no quantitative comparisons of the reconstructed volume absorption were possible.

The goal of this paper is to investigate quantitative depth resolved estimations of scattering samples using tomographic reconstruction. Specifically, the application to depth resolved measurements in tissue is discussed. Both computer simulations and experimental measurements of light propagation through a layered medium are made using the diffuse reflectance measured at the surface of the sample. A comparison between a least squares back projection, an inverse least squares, and a partial least squares (PLS) reconstruction is presented. The results illustrate quantitative estimations are possible.

3.3 Background

The total attenuation of light through turbid materials can be described by two basic processes, i.e. absorption and scattering. When light propagates through a sample, a portion is absorbed by the constituents dispersed throughout the matrix. For many types of samples, attenuation from absorption occurs between scattering events, where the Beer-Lambert relation is assumed to hold. Tissue absorption between 700 – 1300 nm is small, with typical[7,8] absorption coefficients, μ_a, between 0.01 – 1 mm^{-1}. The major cause of absorption in the near infrared are due to low lying electronic transitions in chromophores such as hemoglobin, myoglobin and cytochrome and from molecular vibration overtone and combination bands due to OH, CH and NH stretching and bending modes.

In the near infrared region (NIR), light scattering in tissue is the major contributor to attenuation. Scattering can occur due to refractive index variations in the different components in tissue or by elastic scattering such as in the case of light interaction with collagen in the cell membranes. Typical scattering coefficients, μ_s for tissue in the NIR lie in the range of 10-100 mm^{-1}. Likewise, the scattering is wavelength dependent. For example, scattering coefficients such as those typical for dermal tissue are observed to have a $1.15 \times 10^9 \lambda^{-2.55}$ mm^{-1} dependence.[9]

A single photon will experience many scattering events as it travels through tissue. At a scattering event, scattering can be quantitated statistically in terms of a phase function $P(\theta)$, where θ is the angle of the scattered photon with respect to the original direction. The Henyey Greenstein phase function has found considerable use in tissue scattering studies.[10] Anisotropy in the phase function is described by the mean cosine of

the scattering angle, g, and typical[9] values for tissue in the near infrared vary from 0.8 to 0.95. These g values imply that even in relatively highly scattering tissue, the light is to a great degree, forward directed.

The high degree of forward scattering and low attenuation of light in tissue has allowed diagnostic measurements deep within tissue. For example, Cope and Delpy have measured light transmission through the neonatal skull to continuously monitor cerebral oxygenation in infants.[4] Likewise in clinical settings, transmittance measurements are common where the pathlength is short such as in a finger and earlobe, or reflectance measurements from the surface of the skin.

3.4 Reconstruction Methodology

3.4.1 Back projection

The back projection technique uses signal attenuation through a sample at various perspectives to determine the contribution of each component to the overall absorption. Signal attenuations are determined by ratioing observed responses to the incident intensity. Following a Beer-Lambert relationship, the expression for the total attenuation A_r, at a radial distance r, can be written as a linear combination of all components,

$$A_r = \sum_{i=1}^{p} l_{i,r}\mu_i \tag{3.1}$$

where the sum extends over p distinct component layers each of pathlength l through that layer, and for the layer absorption coefficient, μ. When multiple samples are considered, the equations can be conveniently rewritten in matrix form, where the m column vectors correspond to various samples. For measurements made along the surface, each lateral

position will travel through each layer a different amount. A set of attenuations made at discrete positions can be expressed as

$$\mathbf{A} = \mathbf{LM} \tag{3.2}$$

where **A** is the $n \times m$ response matrix of attenuations at n lateral positions for m different samples. **L** is an $n \times p$ distance weighting matrix for the n lateral positions and p component layers. The matrix **M** ($p \times m$) contains the absorption coefficients of the individual layers in each sample. The computation of the **L** distance weighting matrix is done prior to estimating unknown samples and is computed using a model of the light propagation. An estimate of **M** ($\hat{\mathbf{M}}$) is obtained by least squares where,

$$\hat{\mathbf{M}} = (\mathbf{L}'\mathbf{L})^{-1}\mathbf{L}'\mathbf{A} \tag{3.3}$$

where t denotes the matrix transpose and -1, the inverse. Several workers have applied constraints on $\hat{\mathbf{M}}$ or calculated the least squares in an iterative way.[3,11-13] Constraints can be placed on $\hat{\mathbf{M}}$ such that absorption coefficients can not become negative. For the most general case the least squares estimate is made without these approaches.

3.4.2 Inverse Least Squares

The ILS method, as the name implies, is based on an inverse model where the absorption coefficients of the individual components are expressed as a function of the responses. This approach has been used in a variety of spectroscopic calibrations. As applied in this study, a calibration set is used to first build the model and a prediction set is used to test it on unknowns. In matrix notation, a data set consisting of known

absorption coefficients for each of the component layers as related to the surface attenuation can be written as,

$$\mathbf{M}_c = \mathbf{A}_c\mathbf{B} \tag{3.4}$$

where $\mathbf{M_c}$ is a matrix containing of m sample absorption coefficients for p layers ($m \times p$), $\mathbf{A_c}$ contains the lateral attenuations for m samples at n lateral positions ($m \times n$) and the subscript c refers to the calibration set. **B** comprises $n \times p$ calibration coefficients. The **B** matrix is obtained using the calibration data set using least squares estimation in a similar manner as in Equation 3.3. The estimated coefficients $\hat{\mathbf{M}}$ for unknown samples are then computed by Equation 3.4.

3.4.3 Partial Least Squares

PLS analysis has demonstrated significant success for constituent estimation in complicated mixtures and in the analysis of data which spans large dynamic ranges. As in the inverse least squares approach, PLS is based on an inverse model. Both use training and prediction sets. Details of the PLS algorithm are given in several sources.[14-16] The technique for the determination of **B** involves decomposing **A** using an iterative approach into three matrices,

$$\mathbf{A} = \mathbf{UVW}^t \tag{3.5}$$

and then performing a pseudo-inverse to finally give,

$$\hat{\mathbf{B}} = \mathbf{WV}^{-1}\mathbf{U}^t \tag{3.6}$$

The algorithm generates an ordered series of factors such that each describes decreasing amounts of variance which correlates to **M**. The first factors describe the maximum non-

random variance in the intensity responses that also correlates with the absorption coefficients in **M**. The calibration coefficient vector $\hat{\mathbf{B}}$ associated with the optimal number of factors will thus yield the best possible estimate of the absorption coefficients. PLS predictions of absorption coefficients can be obtained by a multiplication of the intensity responses of test samples and the $\hat{\mathbf{B}}'$ vector which was determined using the optimal number of factors.

For each prediction set, the optimal number of factors was determined from the Predicted Residual Error Sum of Squares (PRESS) values computed. PRESS values were calculated as the sum of the squares of residuals between the PLS estimates and known absorption coefficients for each of the samples in the prediction set. An F-test at 95% significance on the ratios of adjacent PRESS values were used as a criterion to determine the optimal number of statistically significant factors. Reconstructions were done by applying one component PLS to obtain a calibration for each layer separately.

3.5 Computer Simulations

Computer simulations were done to determine the light paths through the sample (**L** matrix). Likewise, the use of a light propagation model provided additional information not possible by simple experiment which greatly aided in interpreting experimental results.

3.5.1 Monte-Carlo simulations

Statistically based simulation methods have been used to describe neutron propagation since the 1950's. To estimate the distribution of photons in a scattering

media such as tissue, a Monte Carlo simulation of a photon migration in a slab of varying absorption coefficient, μ_a and a constant scattering coefficient, μ_s, was developed. This method determines on the basis of random deviates, the distance a photon travels between scattering events and the new direction of photon travel after scattering. Intensity attenuation is computed by absorptive processes between scattering events. The model is applied to many such photon packet trajectories until a statistical distribution of the steady state photon distribution is obtained. At each scattering event, the probability function, which approximates the Henyey-Greenstein phase distribution was used to determine photon direction.[6] With the use of the pseudo-random parameters R_1, R_2, and R_3 distributed in [0,1], the equations used to determine a photon's path through a scattering sample are given below. The scattering longitudinal and azimuthal angles are receptively:

$$\Phi = 2\pi R_1 \tag{3.7}$$

$$\Theta = \cos^{-1}\left\{\frac{1}{2g}\left[1+g^2-\left(\frac{1-g^2}{1-g+2gR_2}\right)^2\right]\right\} \tag{3.8}$$

as according to the Henyey-Greenstein phase function. A photon's free path, l, between each scattering event was chosen randomly based on the expression,

$$l = \frac{-\ln(R_3)}{\mu_s} \tag{3.9}$$

These three ordinates (Θ,Φ,l) form the vector to the next scattering event. However this coordinate is relative to the previous scattering event and must be expressed in terms of the global Cartesian coordinates of the simulation. The global rotation of the coordinates

can be accomplished with knowledge of the angles, θ and ϕ of the previous scattering event. The new photon positions are given by,

$$\zeta = l\sin\Theta\cos\Phi \qquad \xi = l\sin\Theta\sin\Phi \qquad \eta = l\cos\Theta \tag{3.10a,b,c}$$

$$\Delta x = \zeta\cos\phi\cos\theta - \xi\sin\phi + \eta\cos\phi\sin\theta \tag{3.11}$$

$$\Delta y = \zeta\sin\phi\cos\theta - \xi\cos\phi + \eta\sin\phi\sin\theta \tag{3.12}$$

$$\Delta z = \zeta\sin\theta + \eta\cos\theta \tag{3.13}$$

$$x' = x + \Delta x \qquad y' = y + \Delta y \qquad z' = z + \Delta z \tag{3.14a,b,c}$$

where primed values represent the new global coordinates. New global angles θ and ϕ after scattering are,

$$\theta = \cos^{-1}\left(\frac{\Delta z}{l}\right) \qquad \phi = \tan^{-1}\left(\frac{\Delta y}{\Delta x}\right) \tag{3.15a,b}$$

Attenuation due to absorption was treated as if each photon was a packet of photons of some initial intensity I_0 and underwent exponential attenuation as it traversed. For an absorbing medium that varies in a layered fashion in the z direction, a general expression for the final intensity of a remitted packet is

$$I = I_0 \exp\left(-\sum_{j=1}^{m} \int_{l_{j-1\to j}} \mu_a(\tau)d\tau\right) \tag{3.16}$$

where the sum extends over m scattering events and τ is a generalized xyz coordinate. Each contribution to attenuation was computed by integrating in a straight line path between scattering events where $l_{j-1\to j}$ is the length between the j-1 and jth scattering events. This integral is easily computed for cases where the path between scattering events does not extend through regions of different μ_a. For longer paths which extended

through two or more layers, the integral was determined as a weighted contribution of the μ_a's over the entire length.

Information obtained from each simulation included the steady state photon distribution throughout the volume, radial functions of the back-scattered light intensity, and photon path distributions. A lateral profile of the weighted average distance (**L** matrix) that photons traverse through each layer was obtained by multiplying the average total length traveled from source to a surface location at r, with the average fraction of distance that photons extends through each layer. This relation is,

$$\mathbf{L}(r,j) = \left(\sum_{i=1}^{n(r)} \frac{l(i,r)}{n(r)}\right)\left(\sum_{i=1}^{n(r)} \frac{l(i,r,j)}{l(i,r)\cdot n(r)}\right) \tag{3.17}$$

where r is the radial distance from the source, j is the layer, n(r) is the number of photon packets reaching a lateral distance r, and the functions $l(i,r)$ and $l(i,r,j)$ are the total length and length through jth layer of the ith bolus reaching r.

3.5.2 Model characteristics

The chosen medium for the model was comprised of 6 parallel layers with respect to the surface with absorption coefficients typical[7] to that found in tissue (0.00 – 0.50 mm^{-1}). Likewise, the values of the scattering coefficient, μ_s, and the anisotropy factor, g, were chosen to be similar to human tissue and were set at 9.4 mm^{-1} and 0.85 respectively.[17] The three dimensional domain of the problem was fixed to a maximum 1.5 cm lateral distance from the source and to a maximum depth of 1 cm. Simulations were started with all photons collimated and perpendicular to the surface with the light injection equidistant from the boundaries approximating a laser illumination. The

"source" diameter was 1.0 mm. Photon packets were followed until they either escaped the domain or were detected. A total of 10^6 photon packets were released. The model, written in C, was run on a 166 MHz PC using the Linux operating system. Remitted intensity data recorded at 0.1 mm intervals for 15 mm was averaged to simulate the responses that would be typical of the resolution capable of the fiber optic positioning system used in the experimental case.

3.5.3 Data set pretreatment and sectioning

The modeled data was evaluated with added noise. To simulate the limitations of a photomultiplier tube detection system, 0.001% RMS Gaussian noise was added. The 89 different simulations were sectioned into two data sets for reconstruction purposes. For reconstructions based on ILS or PLS, two data sets each containing sets for calibration and prediction were chosen. The first prediction set encompassed 25% of the 89 simulations and was chosen randomly (Data Set I). The second prediction set was chosen to demonstrate the efficacy of the reconstruction method in distinguishing a single layer with a different absorption coefficient from otherwise homogeneous surrounding layers of low absorbance (Data Set II). Because of the limited number of samples available, a third independent data set was not used for the evaluation of the method.

3.6 Experimental Work

Experimental diffuse reflectance measurements in layered media were made to determine multi-position lateral responses to evaluate the efficacy of the reconstruction

methods with real data. Also, comparisons could be made between the complexities of the real sample and simulation.

3.6.1 Equipment

The experimental apparatus used to obtain the lateral steady-state diffusely reflected light distribution is shown in Figure 3.1. A 5.8 mW HeNe laser attenuated by a 1.0 O.D. neutral density filter served as the source. The detection system used was a 1.0 mm diameter fiber optic attached to a Hamamatsu HC-050 photomultiplier detector. Output signals were recorded by computer using a 12 bit A/D converter. To increase the dynamic range, scaling and offset electronics were used to pre-treat the signal prior to A/D conversion. A 3:1 solution of distilled water to 10% milk fat cream was chosen as the scattering medium (μ_s = 9.4 mm^{-1}).[17] Dr. Ph. Martin's transparent water color (12A juniper-green) was used for the absorber because it was found to be highly water soluble and not fat soluble as measured through the microscope.[9] This ensures that absorption occurs in the medium and not in the scatterers, to mimic tissue constituents which absorb between scattering events. The six reservoirs were made of 40 x 50 x 0.15 mm glass plates separated by 1.0 mm thick U shaped rubber gaskets and were clamped in position. The incident laser source intensity was determined by focusing the beam directly into the detector after attenuating with a suitable neutral density filter.

3.6.2 Data collection

Detector responses were recorded as a function of the lateral position of the fiber optic from the detector (1 – 15 mm in 0.5 mm increments) and as a function of absorber

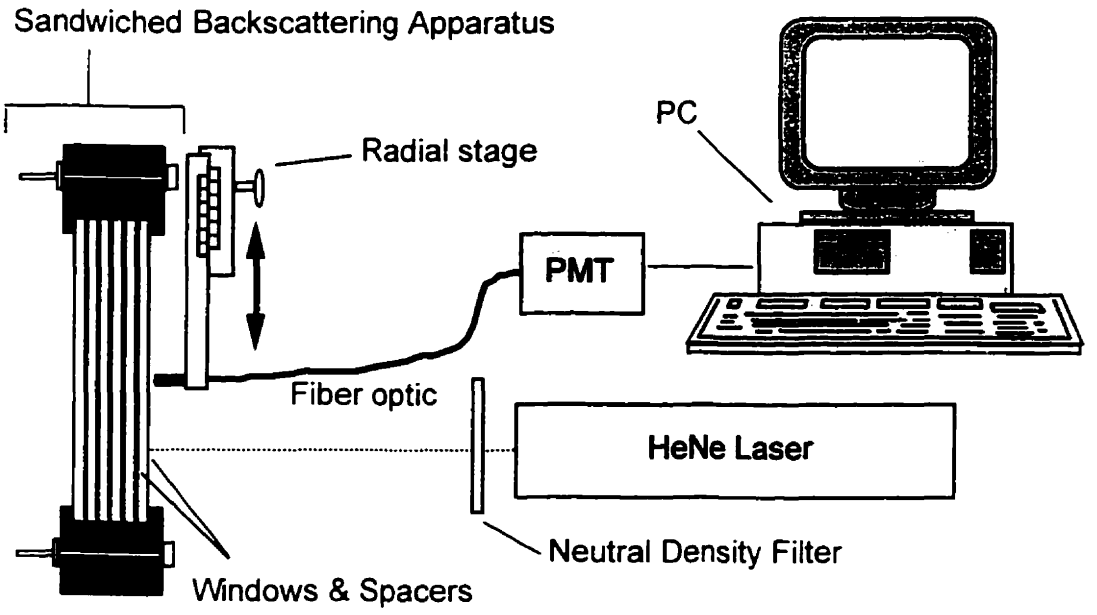

Figure 3.1. Backscattering experimental setup.

composition. The range of 63 measurements made was designed to be similar to the simulations and used the same absorption coefficient. The various data sets and partitioning of the data into calibration and prediction components was identical to that done for the modeled data.

3.7 Results and Discussion

3.7.1 Diffuse reflectance measurements

For remittance measurements, the sample was illuminated at one point on the surface and the diffusely reflected light is collected some distance away. An estimate of these measurements may be obtained using the modeled results in a scattering sample for samples of different crossectional composition. As mentioned previously, samples with six distinct absorption layers were studied. The modeled remittance as a function of source/detector lateral distance for a series of multi-layer slab compositions is shown in the lower series of graphs in Figure 3.2. The layer compositions were chosen to be starkly contrasting so as to show a stepwise progression from all six layers containing no absorber to all six containing a strong absorber. To allow comparisons between the separate experiments and simulations, the measured remittance at each lateral position is referenced to the source intensity to obtain the attenuation. The general trend shown in Figure 3.2 is that absorption deep within a sample has a greater effect on the attenuation made at large lateral spacing of the source and detector as compared to measurements made at small lateral spacings.

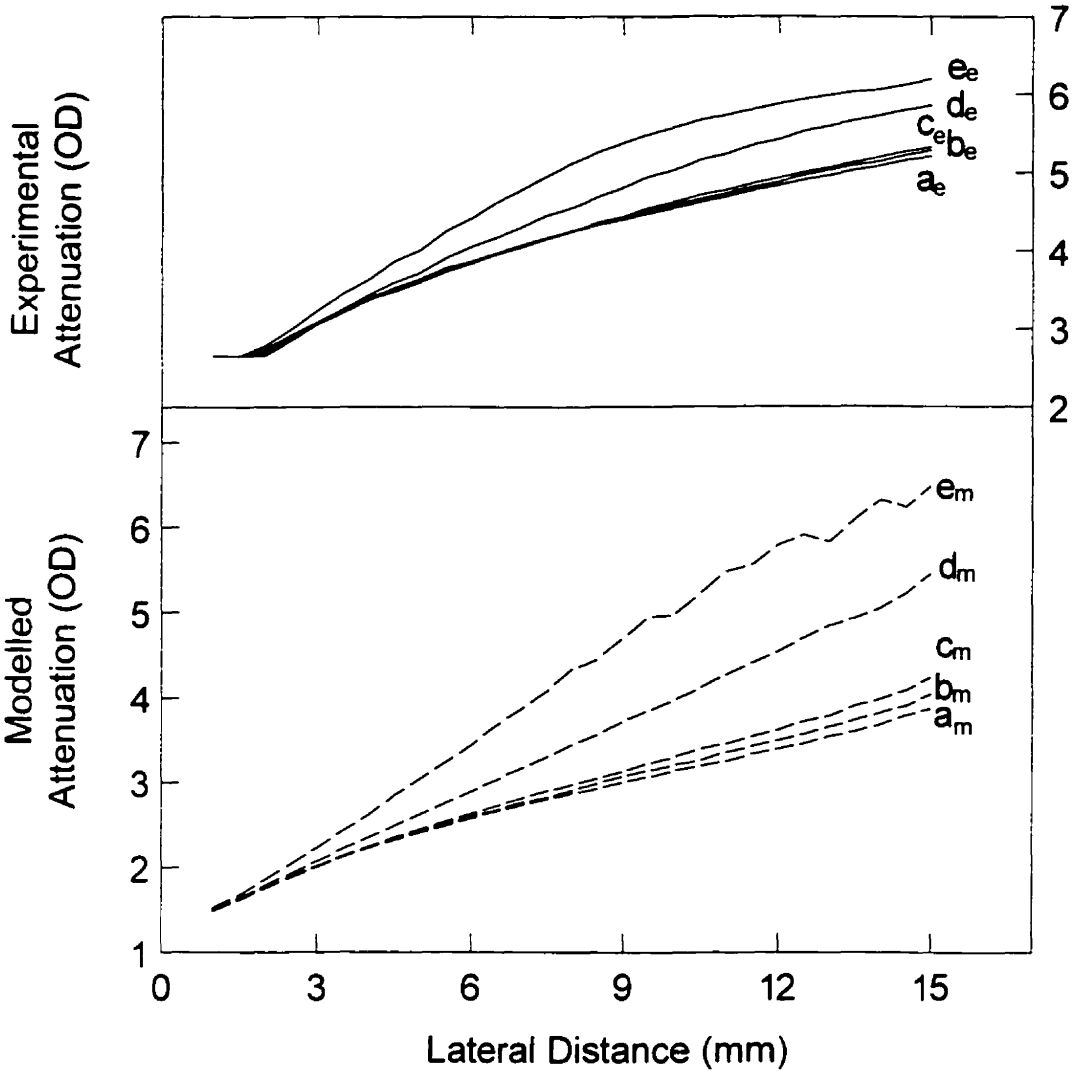

Figure 3.2. Experimental and modeled lateral surface light attenuations for various absorbers in a slab (μ_a = 9.4 mm^{-1}, g = 0.85). All absorption coefficients for layers 1 though 6 are either 0.00 or 0.50 mm^{-1}. a) no absorber; b) absorber layer 6; c) absorber layers 5,6; d) absorber layers 3-6; e) absorber layers 2-6. Subscripts m and e refer to modeled and experimental data respectively.

To determine if a similar relationship to the results obtained in a real scatterer compared to the model, experiments were made using the phantoms as described in the experimental section. The results are plotted in the upper series in Figure 3.2. Like the modeled remittances, the presence of an absorber has a marked effect on the surface light attenuation. Whereas the general trend is the same, the experimental data has some differences with regard to linearity. Also the simulated responses span over five orders of magnitude where the real responses span over 3.5 orders. This lower dynamic range is partly due to detector saturation when the reflections from the window of the sandwiched backscattering apparatus are significant near the source.

For the lateral source/detector spacings of 5 and 10 mm, considerable differences in the effect of absorber placement is observed. A detector positioned at 5 mm exhibits large changes in attenuation when the absorber is close to the surface (compared with no absorber), whereas at 10 mm detector spacing, changes in attenuation occur throughout the absorber placement.

The depth through which the photon travel can be seen when the light paths through the sample from a source to the detector are considered. The computation of the photon path distribution for back-scattered light reaching the surface at a certain radial distance from the source required several steps. The photon packet path was rotated about some angle θ about the z axis where θ is the angle between positive x axis and the point on the plane where the packet exited. Each rotated path was weighted with unit value and projected onto the x axis. A distribution was built up over many trials. After the simulation, the distribution was normalized so that a slice through any region containing the total photon flux integrated to unit value. This two dimensional "flux

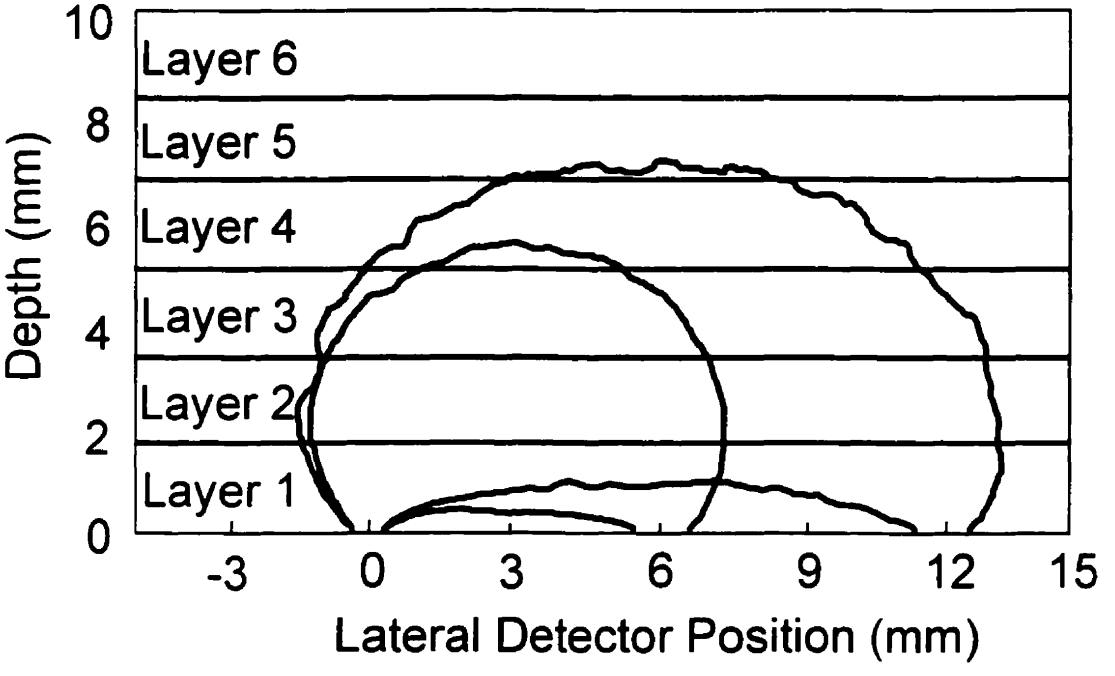

Figure 3.3. Light path distribution at the 90% contour through a multi-layer absorbing/ scattering medium where a source is located at position 0 and detectors are placed at 6 and 12 mm away.

normalized" distribution gives a measure of the path probabilities that a photon may take from source to a detector. For the layered sample in Figure 3.3, light reflected into detector positions at 6 mm and 12 mm show different average penetration depths. Contours enclose the 90% probability that a photon reaching the detector has traversed some path. The overall distribution of collected light is localized between the source and detector with a "banana shaped" appearance. For a 12 mm separation, such paths cover a much broader range of depths as compared to a detector placed at 6 mm. If the probability distribution is sliced in the z direction centered equidistant between the source and detector, as shown in Figure 3.4, the depth of penetration for a range of source/detector pairs can be seen. It is clear that there is a correlation between lateral detector placement and the average depth sampled by the photons. If a 95% probability envelope is considered, than it is observed that the maximum depth penetration through the sample is 5.2 mm and 7.5 mm for detectors placed at 3 mm and 12 mm distances. The increased diffuse nature of the distribution for photons reaching 12 mm is also evident due the greater number of scattering events that occurs when photons penetrate the sample deeper. These general findings agree well with other work[5] which has suggested that the average depth, z, for different separations between source and detector, Δx, vary according to $z = 0.22\ \Delta x + 0.92$. Although a similar trend is observed here it should be pointed out that this relationship is strongly dependent on the scattering anisotropy.

Because photons traversing from source to detector penetrate through many layers, one can determine a weighted average pathlength for each layer. These weightings determined by simulation using Equation 3.17 are used in the back projection

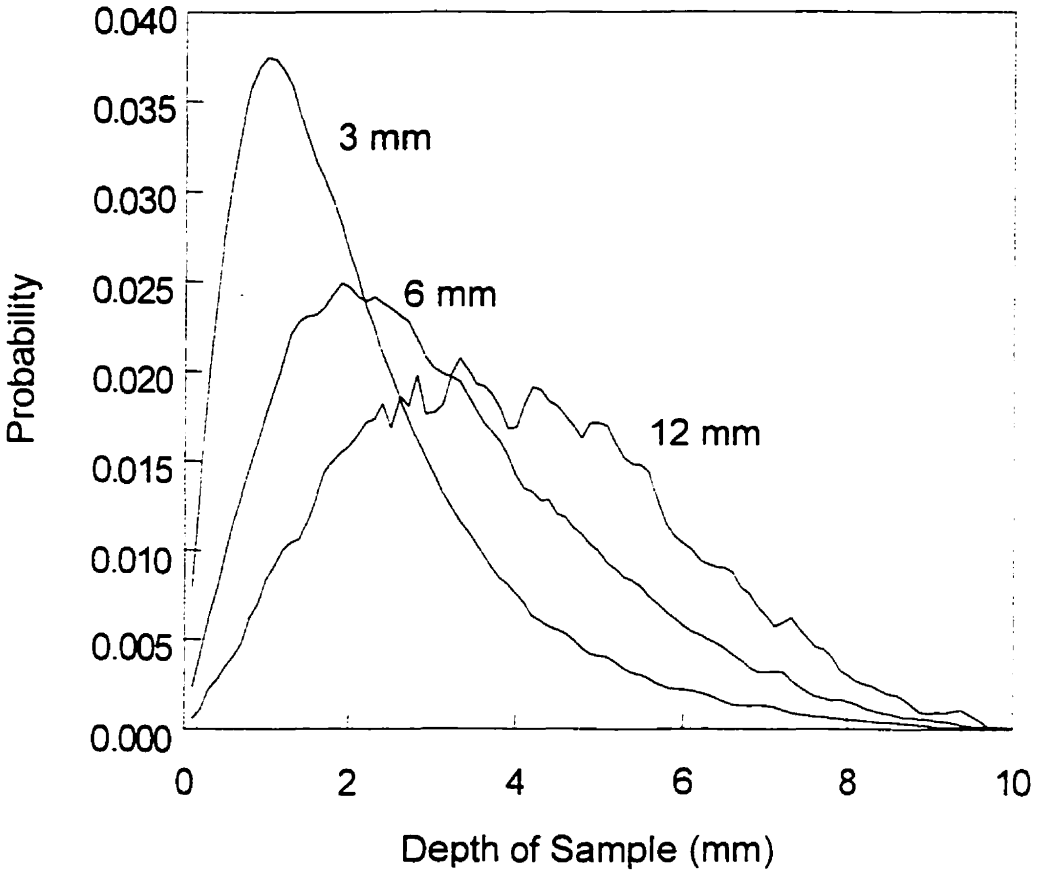

Figure 3.4. Depth profile of photon path distribution at various lateral detector positions as seen equidistant between source and detector.

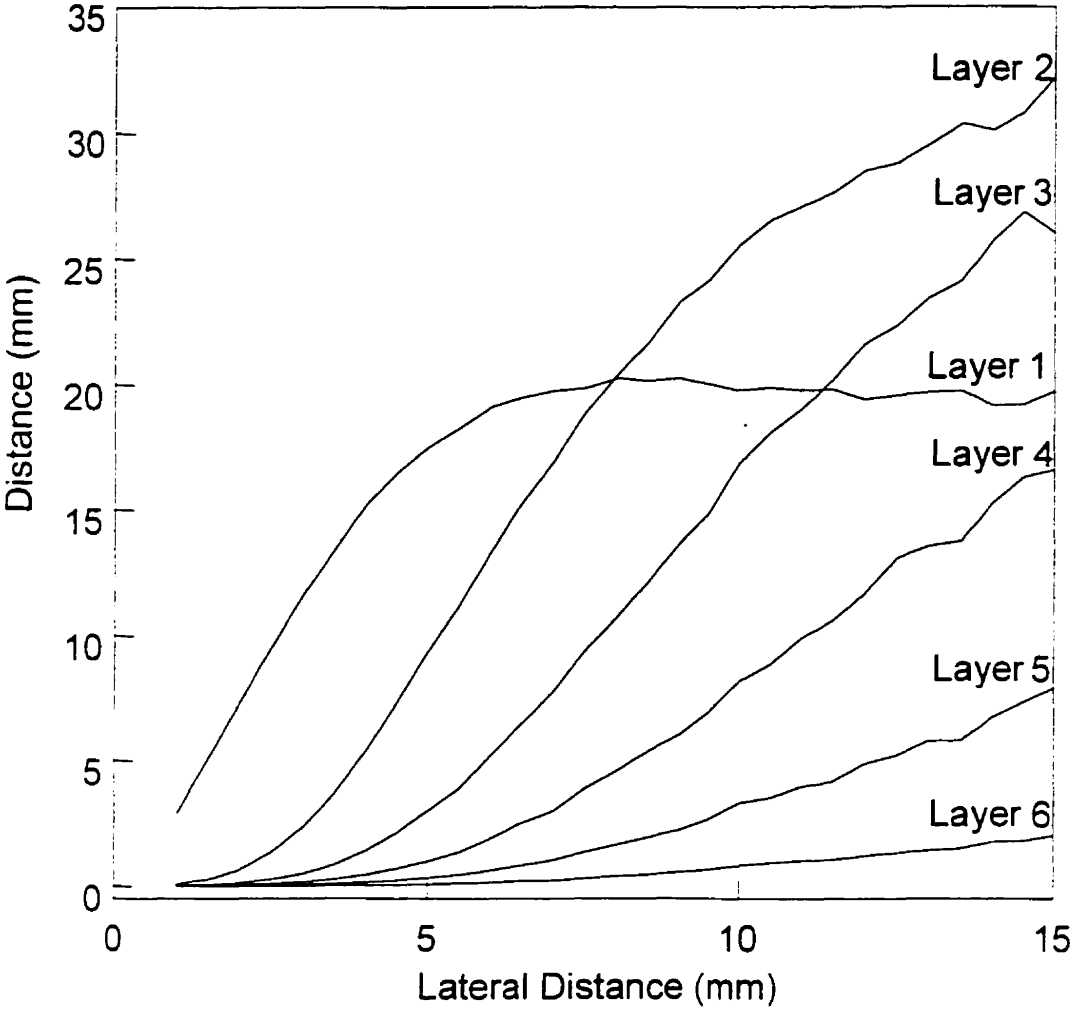

Figure 3.5. Modeled weighted average distance that photons spend in each of the six layers (labeled 1 through 6) as a function of lateral position (**L** matrix in Equation 3.2).

reconstruction (**L** matrix). A plot of the row values of the **L** matrix against lateral detector displacement for each layer (columns) are shown in Figure 3.5. This plot demonstrates that as the source/detector separation increases, more of the detected photons have penetrated the sample deeper. The plateau observed for photons traversing layer 1 suggests that most photons reaching the surface at these larger radii do not travel in straight paths from the source to the surface. For a source/detector separation of 10 mm, a mean path length of 77 mm was measured. This value is in excellent agreement with the result of 80.6 mm reported by Patterson *et al.* [18] for a similar sample.

3.7.2 Back projection reconstruction results

Using the **L** matrix of pathlength weightings for each of the six layers, estimated absorption coefficients were obtained. Coefficients of variation between the real and experimental attenuations are tabulated for each of the six layers in Table 3.1. Similar results are obtained in both cases except in the deeper layers where the reconstruction using modeled data with the inclusion of noise produced significant errors. The estimates of absorption were slightly better in Data Set II where five of the six layers contained only small absorption coefficients. The general trend is that an increasing error in the estimation is obtained with increased sample depth. This is due to the ill conditioned nature of technique, even though the **L** matrix was not determined to be rank deficient. Light paths that penetrate deeply into the sample must go through upper layers twice and this leads to an increased error in the absorption coefficient estimations at lower depths. Estimations of absorbance in layers five and six are particularly bad for the simulated data as attenuations obtained at the most extreme radial distances are too noisy.

3.7.3 ILS reconstruction results

Results in Table 3.2 show the coefficients of variation between actual and predicted absorption coefficients for modeled data for each of the six layers using the ILS method. As seen in Table 3.2, reconstructions are very good for the first layer and then degrade with depth. It is reasonable that the reconstruction can estimate absorption in the first layer well since all of the measured signal travels through it.

Table 3.1. Back projection reconstruction results.

	Layer 1	Layer 2	Layer 3	Layer 4	Layer 5	Layer 6
Modeled data						
Data Set I*	54.46**	76.71	129.38	254.32	637.92	1300.27
Data Set II	45.79	84.91	96.15	120.91	477.58	1975.58
Experimental data						
Data Set I	53.32	99.56	69.48	103.34	80.67	193.16
Data Set II	47.26	93.83	72.78	92.71	73.28	117.28

*Data Sets I and II contain 15 and 11 samples respectively.
**Errors are given as coefficients of variation, %

Table 3.2. ILS reconstruction results.

	Layer 1	Layer 2	Layer 3	Layer 4	Layer 5	Layer 6
Modeled Data						
Data Set I*	18.87**	119.49	134.60	103.24	101.05	117.31
Data Set II	15.32	64.88	86.19	71.11	75.61	66.69
Experimental Data						
Data Set I	7.68	51.95	91.22	86.77	78.71	102.33
Data Set II	5.48	38.48	58.37	62.92	48.68	58.05

*Data Sets I and II contain 15 and 11 samples respectively.
**Errors are given as coefficients of variation, %

If differences in the reconstruction error between modeled Data Sets I and II are considered, we can see that there is approximately a two fold reduction in the error when comparing absorbance estimation in the deeper layers. This is expected as the Data Set II contains samples with only one differing absorbing layer in an otherwise small but homogeneous absorption in the other layers. This data set is not unlike many of the types of phantoms used in other tomographic reconstructions in scattering media studies.

Absorption estimations using real data were worse than for the modeled data especially for Data Set I. For Data Set II, estimates in the deep layers are 15 – 20 % worse using real data. To a certain extent, the increased error in the reconstruction was due to non-reproducibilities that exist in the fiber positioning system.

3.7.4 PLS reconstruction results

The coefficients of variation between actual and predicted absorption coefficients for modeled data for each of the six layers using PLS in given in Table 3.3. For all layers except layer 1, two or three factors were chosen as optimal (based on a 95% confidence level). However layer 1 required six factors. The reconstructions in general show a two fold decrease in the error over the ILS approach for both Data Sets I and II. Variation in the results obtained between modeled and experimental data used in the reconstructions are minimal. For the first two layers, the error is worse than with the ILS reconstruction. However in the lower layers there was a 27% error overall when using PLS as compared to a 60% error when using ILS on experimental Data Set II.

Table 3.3. PLS reconstruction results.

	Layer 1	Layer 2	Layer 3	Layer 4	Layer 5	Layer 6
Modeled Data						
Data Set I*	15.33**	44.23	53.04	44.40	62.11	69.43
Data Set II	7.83	21.51	36.91	37.54	31.00	27.60
Experimental Data						
Data Set I	17.83	66.09	54.81	51.68	59.92	66.24
Data Set II	11.71	19.64	36.52	41.63	28.25	24.98

*Data Sets I and II contain 15 and 11 samples respectively.
**Errors are given as coefficients of variation, %

This significant improvement in deep layer reconstruction is inherent in the nature of the PLS method. Figure 3.6 shows a plot of the weighting coefficients as a function of lateral distance obtained using real data. Knowing that the majority of photons only penetrate the few layers for a detector placed within close proximity to the source, it is expected that the weightings of the detector responses would be higher at small lateral distances from those further out. Indeed, the calibration coefficients weight the responses from the smaller source/detection separations to a much greater extent than responses further out. From Figure 3.6, it can be seen that for detector responses at large radial distances the weightings are small. This is expected as photons reaching those extreme points do not play a great role in the determination of absorbances for layer 1. The effect of oppositely weighting coefficients between adjacent detector groupings suggests that signal differencing leads to a cancellation of information that is seen by both detectors leaving only the variations. Referring to Figure 3.4, if two closely spaced detector responses are subtracted, it can be seen that the result would be a sampling of a deeper region (i.e. the contribution from layer 1 would cancel). This is further evidenced by

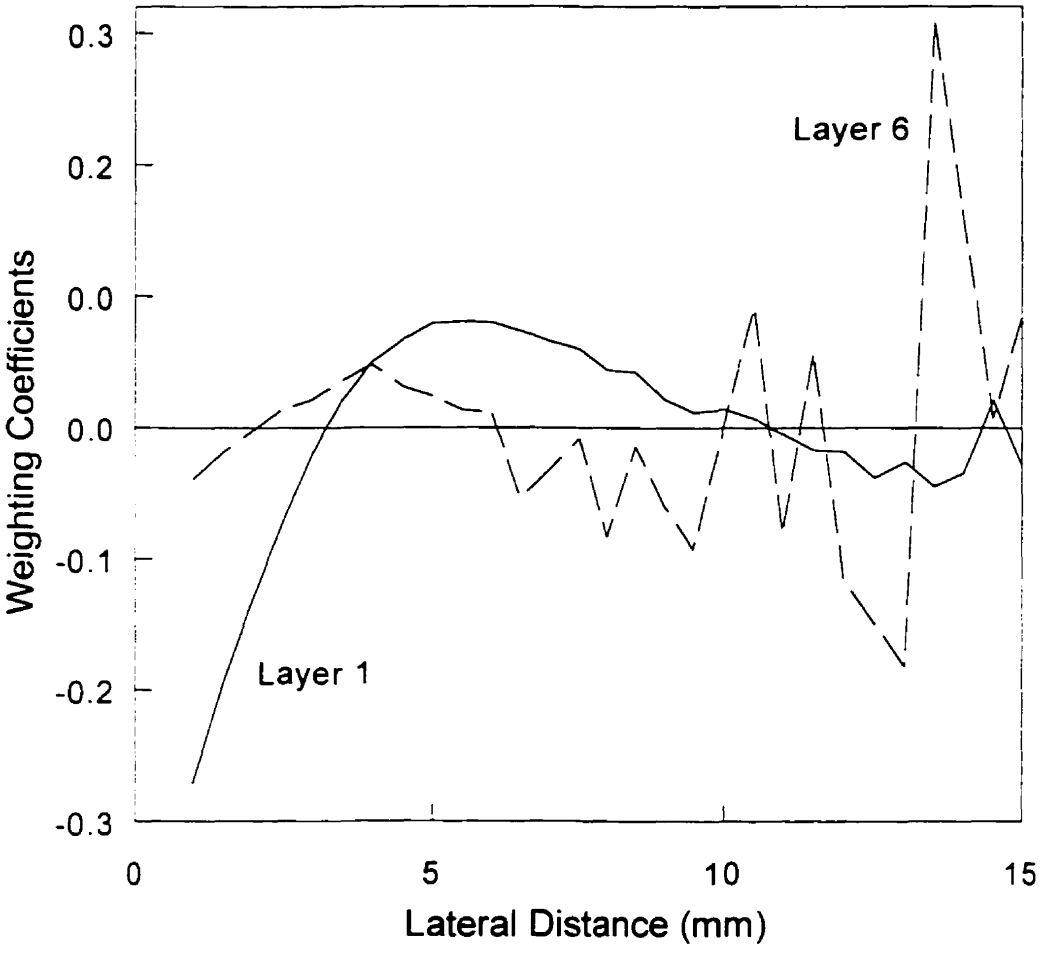

Figure 3.6. Calibration coefficients of lateral detector responses as obtained by PLS for both a surface layer (layer 1) and a deep layer (layer 6).

considering the weightings for layer 6 where an opposite effect is seen. The detector responses at small lateral distances contribute very little in the determination of the overall absorbance, whereas they contribute to a greater extent further out. Again the weightings indicate a differencing in the signals for responses sensitive to changes in absorbance in the deep layers. Therefore the PLS method suggests a powerful way in which depth resolved absorption coefficient determinations can be made in a layered medium.

3.8 Conclusion

A depth resolved tomographic reconstruction of a layered media was shown. Using a Monte Carlo model, the simulation of the weighted photon path distribution through the composite layers demonstrated that a significant fraction of the photon paths extended deep within the sample. For both real and simulated data, depth resolved estimations of the layer absorption were made using least squares back projection, inverse and partial least squares methodologies. For all the methods, absorbance was better estimated in surface layers as compared to deeper layers. Both the ILS and PLS methods provided significantly better estimation of sample absorption as compared to the back projection method. Overall, PLS gave distinctly better results with a 50% reduction in the coefficient of variation compared to the back projection method. However, it should be noted that no constraints were made on the back projection method. Added constraints may improve the estimation. Whereas better estimation is required for many applications, the encouraging results indicate that with further improvement of quantitative depth resolved measurements may be possible. This depth resolved

tomographic approach is a new tool to study spatial relationships of chromogenic constituents in scattering media.

3.9 References

1. Radon, J. On the Determination of Functions from their Integrals Along Certain Manifolds; *Berichte uber die Verhandlungen der koniglich Saechsischen Gesellschaft der Wissenshaften zu Leipzig Mathematisch-Physische Klasse* **1917**, *69*, 262-278.
2. Kak, A. C.; Slaney, M. *Principles of Computerized Tomographic Imaging*; IEEE Press: New York, 1988.
3. Rangayyan, R.; Dhawan, A. P.; Gordon, R. Algorithms for Limited-View Computed Tomography: An Annotated Bibliography and a Challenge; *Appl. Opt.* **1995**, *24*, 4000-4009.
4. Cope, M.; Delpy, D. T. System for Long Term Measurement of Cerebral Blood and Tissue Oxygenation on Newborn Infants by Near Infrared Transillumination; *Med & Biol. Eng. & Comput.* **1988**, *26*, 289-295.
5. Cui, W.; Kumar, C.; Chance, B. Experimental Study of Migration Depth for the Photons Measured at Sample Surface; *Proc. SPIE.* **1991**, *1413*, 180-191.
6. Zhang, K.; Rolfe P.; Wickramasinghe, Y. A. B. D. Study of NIR Imaging Reconstruction Algorithm; *Proc. SPIE.* **1993**, *2082*, 21-29.
7. Cheong, W.; Prahl, S. A.; Welch, A. J. A Review of the Optical Properties of Biological Tissues; *IEEE Journal of Quantum Electronics* **1991**, *26*, 2166-2180.
8. Wilson, B. C.; Jacques, S. L. Optical reflectance and transmittance of tissues: principles and applications; *IEEE Journal of Quantum Electronics* **1990**, *26*, 2186-2199.

9. Marble, D. R.; Burns, D. H.; Cheung, P. W. Diffusion-Based Model of Pulse Oximetry: In Vitro and In Vivo Comparisons; *Appl. Opt.* **1994**, *33*, 1279-1290.

10. van de Hulst, H. C. *Light Scattering by Small Particles*; Dover: New York, 1981.

11. Jacobi, C. G. *Crelle J.* **1846**, *30*, 51-59.

12. Bracewell, R. N. Strip Integration in Radio Astronomy; *Aust. J. Phys.* **1956**, *9*, 198-217.

13. Lawson, C. L.; Hanson, R. L. *Solving Least-Squares Problems*; Prentice-Hall: Englewood Cliffs, 1974.

14. Lorber, A.; Wangen, L. E.; Kowalski, B. R. A Theoretical Foundation for the PLS Algorithm; *J. Chemom.* **1987**, *1*, 19-27.

15. Haaland, D. M.; Thomas, E. V. Partial Least-Squares Methods for Spectral Analyses. Relation to Other Quantitative Calibration Methods and the Extraction of Quantitative Information; *Anal. Chem.* **1988**, *60*, 1193-1202.

16. Beebe, K. R.; Kowalski, B. R. An Introduction to Multivariate Calibration and Analysis; *Anal. Chem.* **1987**, *59*, 1007-1018.

17. Arakaki, L. S. L.; Kushmerick, M. J.; Burns, D. H. Myoglobin Oxygen Saturation Measured Independently of Hemoglobin in Scattering Media by Optical Reflectance Spectroscopy; *Appl. Spectrosc.* **1996**, *50*, 697-705.

18. Patterson, M. S.; Chance, B.; Wilson, B. C. Time Resolved Reflectance and Transmittance for the Non-Invasive Measurement of Tissue Optical Properties; *Appl. Opt.* **1989**, *28*, 2331-2339.

Chapter 4 Optical Tomography in Scattering Media from Photon Time of Flight Diffuse Reflectance Measurements: A Chemometric Approach

In Chapter 3, optical tomographic reconstructions of layered scattering/absorbing samples were made with steady state diffuse reflectance data. Although quantification is possible when all absorbing regions are varied simultaneously, significant errors in estimating sub-surface absorption occurred. To better understand the effects of changing layer absorption on the reflectance measurements, in this study the number of distinct absorbing layers in a specimen is limited to two.

Analysis of the weighting coefficients obtained by partial least squares regression of the steady state intensity signals demonstrated how absorption estimates deep within a specimen were possible. By oppositely weighting responses from adjacently spaced detectors, subtle differences is sample absorption in a given layer were resolved. To further improve sample reconstruction, photon pathlength information may be included in the analysis. This may be obtained by recording the time-of-flight distribution that photons take through a scattering sample. A similar analysis using the partial least squares weighting coefficients on each data channel may be made using time resolved intensity data. In this approach, chemometrical methods may be used not only as a means for tomographic reconstruction but as a tool for understanding the mode of action.

Stepwise multilinear regression may also employed for sample reconstruction. As only a few data channels are retained in the optimal linear model estimating absorption

levels in given layer, noisy data channels are typically not included. Using a stepwise multi-linear regression approach, robust quantification may be possible.

One of the problems encountered in obtaining reproducible time-profiles is precise positioning of the sample. In this chapter, a novel approach for helping to eliminate this problem is investigated. This degree of freedom in the time distribution may be eliminated by computing the autocorrelation function of time-of-flight distribution. Sample reconstruction is then made using autocorrelated data. In addition, by utilizing an optical correlator for detection or an electronic signal mixer, autocorrelated time measurements may significantly reduce the complexity of instrumentation.

4.1 Abstract

The goal of this project is to develop practical methods for quantitative, depth-resolved optical imaging in scattering media. Toward this end, reconstruction techniques based on photon time-of-flight and autocorrelation measurements of diffuse reflectance are being studied. The approach employs an array of radial intensity measurements to obtain information sensitive to sub-surface changes in absorption. Both Monte-Carlo simulations and experimentally obtained measurements of known phantoms were used in the evaluation of reconstruction techniques. Time-gated single photon reflectance measurements were made using a pulsed laser illuminating a layered absorbing/ scattering sample.

For image reconstruction, stepwise multi-linear regression, inverse and partial least squares methodologies were investigated. With all methods, absorbance was better estimated in the top regions as compared to deeper regions. Both PLS and SMLR

methods gave significantly better estimation of sample absorption as compared to the ILS technique. Reconstruction results using autocorrelated data were found to provide a similar estimation of absorption in comparison with time domain data. The use of autocorrelation measurements could significantly reduce the complexity of instrumentation for obtaining time-resolved information to study spatial relationships of absorbing constituents in scattering media.

4.2 Introduction

In recent years considerable efforts have been made to observe and characterize a sample in three dimensions. The analysis of turbid media commonly employs optical measurements to determine the concentration of the desired analyte. Examples range from non-destructive inspection of materials to diagnostic *in vivo* measurements of bio-energetic activity. There is currently considerable interest in the analysis of multi-layered samples. Multi-layer media are common in medicine such as study of the skin/adipose/muscle system, or the bladder or the head. Likewise, industrial examples of two-layered media include products such as capsules, polyethylene container/product systems, or coated surfaces. Indeed, the ability to make a quantitative non-invasive assessment of drug content in capsules would be invaluable to the pharmaceutical industry both in terms of quality assurance and public safety. In complex layered media, the analysis method is often based on a model, which assumes specimen homogeneity. However this assumption is often not valid, and as a result, serious artifacts in the measured optical properties are introduced.[1,2] Therefore, it is necessary to consider the measurement technique, sample structure and theoretical models in the interpretation of

results since changes in the optical properties in a single layer will affect measurements made on the bulk.

Many optical measurement techniques have been investigated to obtain depth resolved information from a sample. Common approaches have used either several source and detector separations or time gating of the detected signal.[3,4] In a steady state experiment, the specimen is imaged onto a detector, and the measured responses probe a defined region in which absorption from the layer sample is integrated. For thick samples with little scattering, the acquisition of multi-perspective responses is made in the reflectance geometry where detectors are placed at a series of lateral distances away from the source. With this source/detector geometry, samples may be probed non-invasively and depth-resolved information may be obtained using analysis techniques similar to Computer Aided Tomography (CAT).[5] However, in highly scattering samples, the optical path from source to detector is ill-defined and the reconstruction becomes ambiguous.

For generalized reconstruction procedures in highly scattering media, many researchers have approached the reconstruction as a linear problem.[2,6,7] However, for reasonable estimation of subsurface information, the linear reconstruction techniques require *a priori* information usually obtained though knowledge of the sample structure together with computer simulation. Therefore, in layered media, efforts have been mainly directed toward a qualitative interpretation of samples. Several investigators have derived approximate formulas for the steady state[8,9] and time resolved[2,10,11] reflectance from two layered samples based on the diffusion approximation of the radiative transport equation. Likewise, random walk[12], finite element[13] and Monte Carlo methods[14] have

been employed to investigate changes in surface reflectance as a function of scattering, absorption and layer thickness. Least squares estimation of the optical properties of the sample has provided a qualitative interpretation of the simulated reflectance signals. It is well established that the overall success of a reconstruction is strongly dependent on the signal-to-noise of acquired signals. This is especially pertinent with time resolved data, where rich information about sample composition is contained in the subtleties of the time profile and can be affected by instrumental noise.[16]

Previously, we have investigated depth resolved quantification in layered scattering media from steady state measurements using chemometric reconstruction techniques.[15] Results indicate that although quantification is possible, the use of integrated information from a sample limits the accuracy of the estimation. The goal of this paper is to examine the use of time resolved measurements for quantitative depth resolved estimations of layered turbid samples. In addition, to increase the signal-to-noise and reduce the error in the reconstruction, the use of the autocorrelation of the time-gated signal is investigated. For sample estimation, a comparison between reconstructions based on inverse least squares (ILS), partial least squares (PLS) and stepwise multi-linear regression (SMLR) is shown. The SMLR technique, which utilizes only a small subset of total time-gated signal, was investigated as it has been shown to provide both a means for robust estimation and for simplified instrumentation. The accuracy of sample reconstruction using time gated data is compared to the autocorrelated signal for both experimental and computer-simulated measurements. The results show significant improvement in sample layer estimation using the autocorrelation and either PLS or SMLR estimation as compared to classical reconstruction methods.

4.3 Theory

For homogeneous scattering/absorbing media irradiated with a short pulse of light, the time response of the system may be approximated using the diffusion approximation of the radiative transport equation.[17-19] The result for source and detector positioned in a reflectance geometry is given as,

$$g(\mathbf{r},t) = \frac{z_0}{(4\pi cD)^{3/2} t^{5/2}} \exp(-\mu_a ct) \exp\left(\frac{-\mathbf{r}^2}{4ct/D}\right) \tag{4.1}$$

where **r** is the source-detector separation distance, $z_0 = [(1-g)\mu_s]^{-1}$, c is the speed of light and D is the diffusion coefficient given as, $D = 3\,[\mu_a + (1-g)\mu_s]$. The diffusion coefficient depends on the absorption coefficient μ_a, the scattering coefficient μ_s, and g the scattering anisotropy (mean cosine of the scattering angle). Note, that the first exponential term relates light attenuation to a Beer's Law relation where light is absorbed by the medium, and the second exponential is essentially a Fick's law diffusion term where light is attenuated by scattering. When the logarithm of Equation 4.1 is considered then for $\mu_a << \mu_s$, the time resolved response becomes linear in μ_a, for any given time and radial separation.

Autocorrelation of a signal has long been used to increase the signal-to-noise in the response from time varying measurements. Likewise, the autocorrelation offers a solution to the problem of imprecise measurements of the absolute time delay between a pulse entering and exiting a sample. The autocorrelation of a function h(t) is defined as,

$$A(\tau) = h(t) * h(-t) = \int_{-\infty}^{\infty} h(t)h(t+\tau)dt \tag{4.2}$$

where τ is defined as the phase delay. The multiplication in the autocorrelation function combines all parts of the time signal and provides an average which enhances repetitive features and reduces the magnitude of random noise. Using the autocorrelated response, information about the width and shape of a pulse can still be determined. In fact, for laser alignment applications, optical autocorrelation is a standard method to measure pulse shapes.

To examine the effect of the sample absorption on the autocorrelation, the diffusion approximation in Equation 4.1 can be substituted into Equation 4.2. The resulting function is given as,

$$A(\mathbf{r},\tau) = e^{-\mu_a c\tau} \int_{-\infty}^{\infty} \left[\alpha^2 t^{-5/2}(t+\tau)^{-5/2} e^{-\beta/t-\beta/(t+\tau)}\right] e^{-2\mu_a ct}\, dt \qquad (4.3)$$

where, $\alpha = z_0/(4\pi c/D)^{3/2}$ and $\beta = \mathbf{r}^2 D/4c$. For $\mu_a << \mu_s$, the bracketed term of the integrand is the autocorrelation kernel of the lossless diffusion equation when $\mu_a = 0$ and can be denoted by $\sigma(\mathbf{r},t,\tau)$. Expanding the last exponential term in Equation 4.3 in a MacLaurin series, the following expression is obtained,

$$A(\mathbf{r},\tau) = e^{-\mu_a c\tau}\left[\int_{-\infty}^{\infty}\sigma(\mathbf{r},t,\tau)dt - \frac{2\mu_a c}{1!}\int_{-\infty}^{\infty} t\sigma(\mathbf{r},t,\tau)dt + \frac{4\mu_a^2 c^2}{2!}\int_{-\infty}^{\infty} t^2\sigma(\mathbf{r},t,\tau)dt - \ldots\right] \qquad (4.4)$$

Further, by examining the expansion, it can be shown that each integral term is proportional the nth moment of $\sigma(\mathbf{r},t,\tau)$, represented by $\langle t^n \sigma(\mathbf{r},t,\tau)\rangle$. Therefore, Equation 4.4 can alternately be written as an expansion of moments where,

$$A(\mathbf{r},\tau) = e^{-\mu_a c\tau}\langle\sigma(\mathbf{r},t,\tau)\rangle\left[1 - 2\mu_a c\langle t\sigma(\mathbf{r},t,\tau)\rangle + 2\mu_a^2 c^2\langle t^2\sigma(\mathbf{r},t,\tau)\rangle - \ldots\right. \qquad (4.5)$$

In general, the series will converge rapidly (for $\beta<1$), as the second and subsequent terms are much less than one. The expansion of moments is very useful since it has been shown that moments provide robust estimation of absorption from the time of flight profiles.[20]

To interpret the physical significance of autocorrelated time-of-flight data, the relationship between $g(\mathbf{r},t)$ and $A(\mathbf{r},\tau)$ for a series of absorptions can be considered. The time distributions from the diffusion approximation are shown in Figure 4.1. The corresponding autocorrelation of the time distributions for positive phase delay times are shown in Figure 4.2. For both figures the logarithm of the intensity was taken. Overall, it can be seen that $A(\mathbf{r},\tau)$ has a similar shape to $g(\mathbf{r},t)$ at longer delay times. In Figure 4.1, it can be seen that the light arriving at late times in the distribution are significantly more affected by changes in absorption than light at early times in the distribution. The difference in the sensitivity to absorption is caused by a Beer's law weighting of the difference in pathlength through the sample. The relationship of $A(\mathbf{r},\tau)$ with changing absorption is markedly different than the time distributions. As absorption increases, the signal at all values of τ decrease and there is a change in slope of the signal. The decrease in signal magnitude and shape is consistent with Equation 4.5 where $A(\mathbf{r},\tau)$ decreases as $e^{-\mu_a c\tau}$. Therefore, absorption estimates based on the autocorrelation signal should be possible.

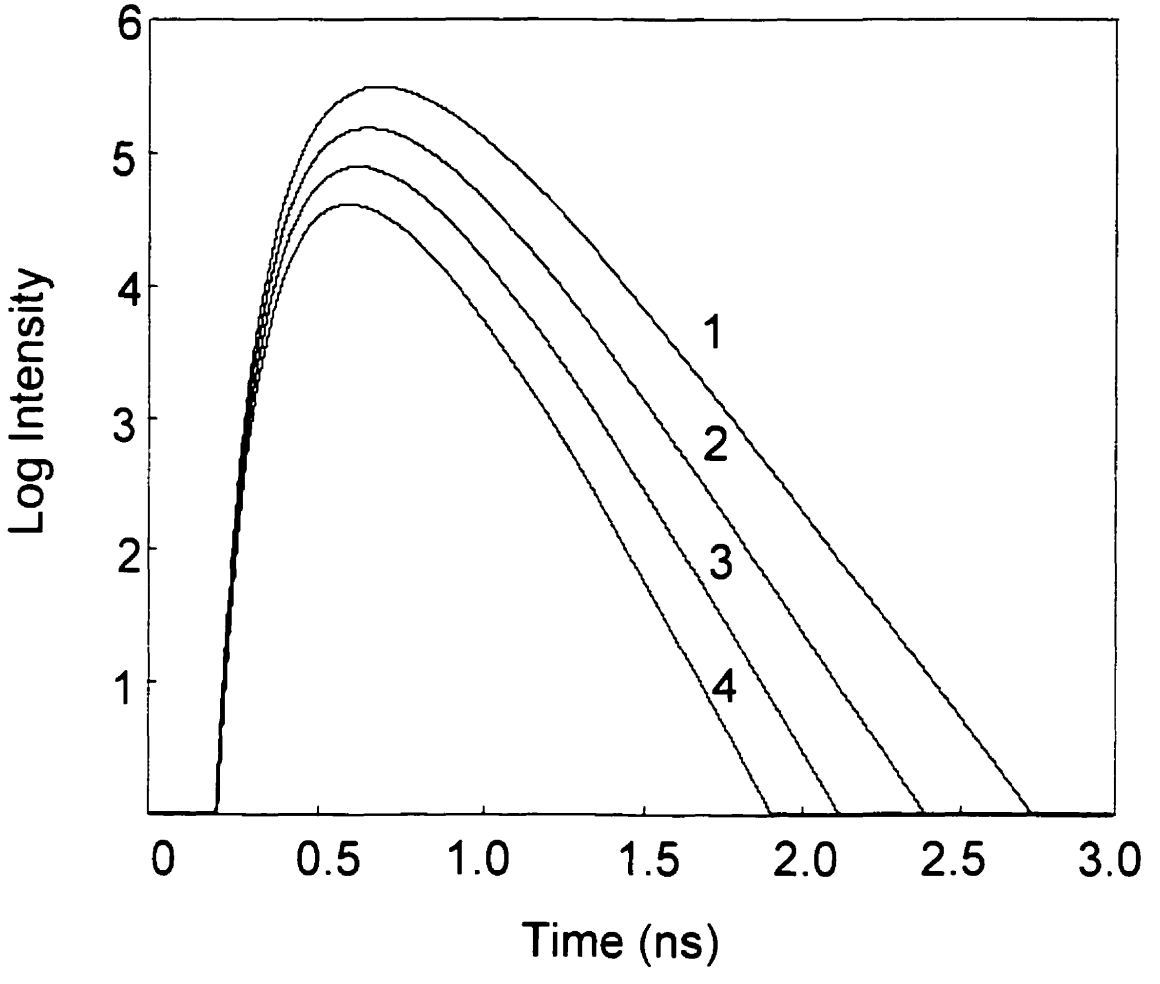

Figure 4.1. Modeled time resolved photon flux at various absorption levels with all other constants held constant. (μ_s = 40 mm^{-1}, g = 0.80, r = 15 mm). 1) μ_a = 0.025 mm^{-1}; 2) μ_a = 0.030 mm^{-1}; 3) μ_a = 0.035 mm^{-1}; 4) μ_a = 0.040 mm^{-1}.

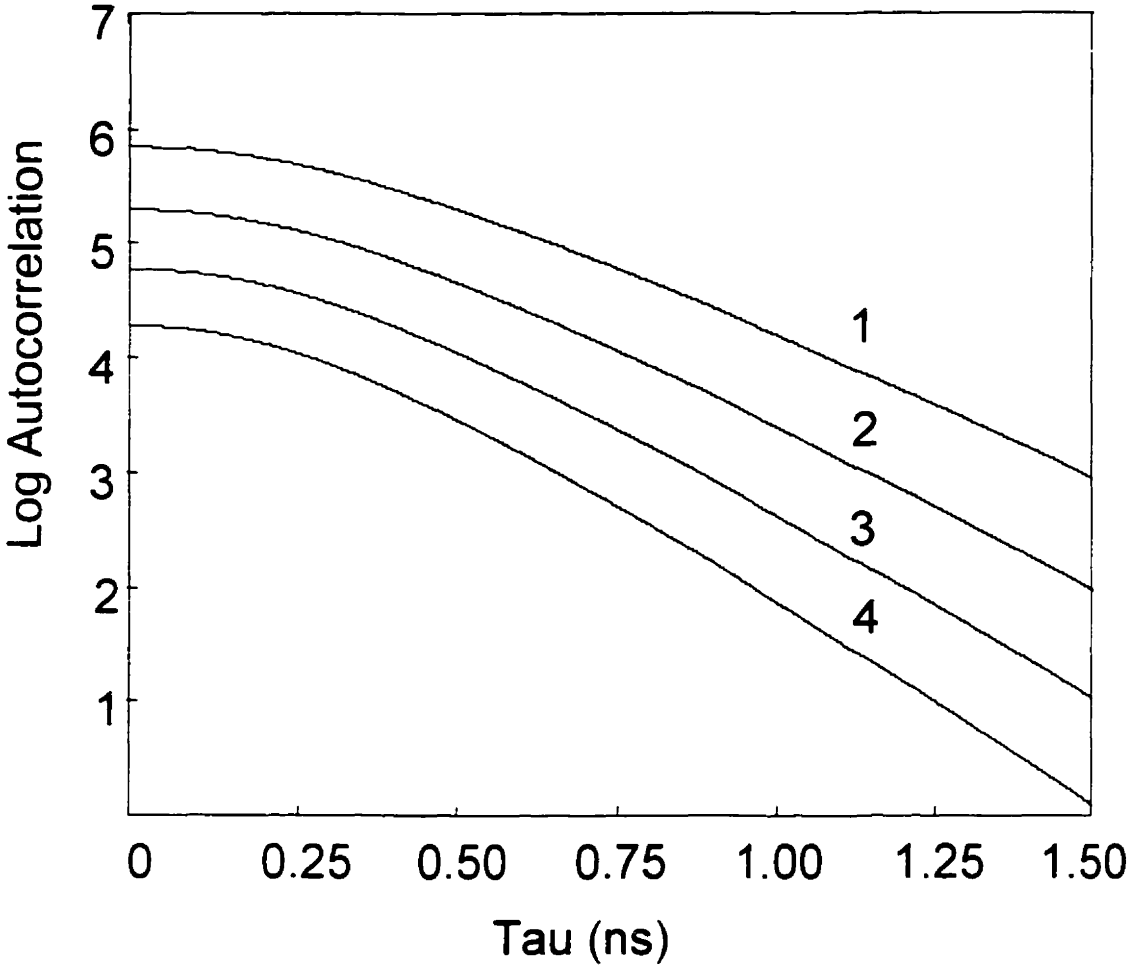

Figure 4.2. Modeled autocorrelated photon flux at various absorption levels with all other constants held constant. (μ_s = 40 mm^{-1}, g = 0.80, r = 15 mm). 1) μ_a = 0.025 mm^{-1}; 2) μ_a = 0.030 mm^{-1}; 3) μ_a = 0.035 mm^{-1}; 4) μ_a = 0.040 mm^{-1}.

4.4 Reconstruction Methodology

Three methods were used for sample reconstruction, inverse least squares (ILS), partial least squares (PLS) and stepwise multi-linear regression (SMLR). All of these techniques are based on an inverse model where the absorption coefficients of the discrete regions are expressed as function of the responses. The ILS method is a base of many reconstruction methods such as the Algebraic Reconstruction Technique (ART).[21,22] In the ART method as with those presented here, image resolution is made possible with the assumption that sample constituents are linearly additive in the acquired signals. Both the ART and ILS methods estimate all of the constituent absorption coefficients in a sample at once. The PLS method uses a more directed approach to the reconstruction, providing less ambiguous estimates for each of the regions independent of the others.[15] Similarly, the SMLR technique uses only a subset of the data to eliminate uncorrelated responses from the estimation.

In this study, a two layer system is considered with variable layer thickness and a fixed total thickness. Sample layers varied within six discrete depth regions. From each sample, time resolved distributions similar to that shown in Figure 4.1 were collected at several lateral positions from the source. In the case of autocorrelated data, the autocorrelation function was determined at each of the lateral positions. The time-resolved or autocorrelated responses from each lateral detector position was collapsed into a single response vector using lexiographic stacking of the data. The 1 by *ns* vector was formed for each sample as:

$$\mathbf{X}_m = \left[x_{m1}(t_1)\ldots x_{m1}(t_s)\, x_{mi}(t_1)\ldots x_{mi}(t_s)\, x_{mn}(t_1)\ldots x_{mn}(t_s)\right] \tag{4.6}$$

where s is the number of time intervals, n is number of lateral positions and $x_{mi}(t_j)$ denotes the response at the ith position and jth time for the mth sample. The lateral position vector was assumed to be linearly additive with the absorption from each region. The overall relationship for the reconstruction is written in matrix notation as,

$$\mathbf{M}_c = \mathbf{X}_c\mathbf{B} \tag{4.7}$$

where $\mathbf{M}_c$ is a matrix containing m sample absorption coefficients for p regions ($m \times p$), $\mathbf{X}_c$ contains ns responses (time resolved or autocorrelated lateral responses) for m samples ($m \times ns$) and the subscript c refers to the calibration set. $\mathbf{B}$ comprises $ns \times p$ calibration coefficients relating the responses to the region absorption. The difference between the reconstruction methods is in the computation of the $\mathbf{B}$ matrix.

The ILS approach is commonly used in a variety of spectroscopic calibrations and is closest in relation to the ART method. For ILS, the computation of the B matrix is obtained using the calibration data set and least squares estimation where,

$$\mathbf{B} = \left(\mathbf{M}_c'\mathbf{M}_c\right)^{-1}\mathbf{M}_c'\mathbf{X}_c. \tag{4.8}$$

The estimated absorption coefficients for unknown sample are then computed using Equation 4.7.

PLS analysis has demonstrated significant success for constituent estimation in complicated mixtures. Details of the PLS algorithm are given in several sources.[23-25] One component PLS was used to obtain a calibration vector for each of the six regions separately. The algorithm generates a series of factors where each describes a decreasing amount of the co-variance correlated to $\mathbf{M}$ and $\mathbf{X}_c$. The calibration vector $\mathbf{B}_k$ associated with the optimal number of factors yield the best estimate of the absorption coefficients.

PLS estimation of absorption coefficients in an unknown sample are obtained by multiplying the responses by the optimal vector, $\mathbf{B}_k$.

The SMLR method is used to identify a linear combination of a subset of responses in $\mathbf{X}_c$ which are most correlated with the sample absorption coefficients. Similar to the PLS method, each iteration of the algorithm finds the response x_i that describes the residual amounts of variance which improves estimation of $\mathbf{M}$. A new calibration vector $\mathbf{B}_i$ is generated at each iteration. Again, the calibration vector $\mathbf{B}_k$ associated with the best estimation determines the optimal number of responses. The estimated sample absorption coefficients $\hat{\mathbf{M}}$ are computed by

$$\hat{\mathrm{M}} = \mathrm{b}_0 + b_1 x_1 + b_2 x_2 + \ldots + b_k x_k \tag{4.9}$$

where b_0, b_1, ...,b_k are the coefficients in $\mathbf{B}_k$. The same region by region approach taken with the PLS calibration was also used in this method.

From the prediction set, the optimal number of factors for PLS or responses for SMLR was determined from the Predicted Residual Error Sum of Squares (PRESS). PRESS values were calculated as the sum of the squares of residuals between the PLS or SMLR estimates and known absorption coefficients for each of the samples in the prediction set. An F-test at the 95% confidence level on the ratios of adjacent PRESS values were used as a criterion to determine the optimal number of statistically significant factors or responses.

4.5 Computer Simulations

Computer simulations were done to determine the theoretical time resolved reflectance responses from layered scattering media. The simulation provided

information which greatly aided in interpreting both experimentally determined time profiles and the effect of varying sample composition on the reconstruction.

A Monte Carlo method was used to model the migration of photons in scattering media. The specifics of the Monte-Carlo technique have been described previously.[15] However, the algorithm was modified to incorporate a time resolved distribution at each radial position. Photon time-of-flight was determined by ratioing the length of the photon trajectory from the source to detector by speed of light in the medium. The time resolution was 1 ps.

The chosen medium for the model was comprised of 2 *distinct* parallel layers with respect to the surface, with series of absorption coefficients typical to values found in tissue and plastics (0.0 – 0.5 mm^{-1}).[26] Likewise, the scattering coefficient, μ_s, and the anisotropy factor, g, were set at 9.4 mm^{-1} and 0.85 respectively. The three dimensional size of the model and source/detector geometry closely approximated the experimental sample. For acceptable photon counting statistics, a total of $2x10^6$ photon packet histories were run. Remitted time resolved intensity data was recorded in 0.1 mm lateral increments over a total of 15 mm. For each detector position, spatially adjacent time distributions were averaged to simulate the responses that would be typical of the resolution capable of the fiber optic detection system used in experiments. A data set consisting of ten equally spaced lateral positions from 1.5 mm to 15.0 mm was determined.

4.6 Data Sets And Pretreatment

A two layered system was modeled where the thickness of the absorbing layers was partitioned in six evenly graduated regions. For each of the six thickness combinations, six absorbing levels were permutated. The resulting full factorial designed set consisted of 156 distinct samples. The samples were sectioned into two sets for reconstruction purposes. Half of the 156 samples comprised the calibration set. The remaining half of the data was further split into prediction and validation sets. Care was taken to avoid biasing. The prediction and validation sets were chosen to demonstrate the efficacy of the reconstruction method in distinguishing different absorbances throughout the medium. Besides lexiographic data stacking, the log of the time responses were taken. The autocorrelation was calculated using the square magnitude of the Fourier transform for each of the individual time distributions. The logarithm of the autocorrelation was taken to linearize the result for absorption estimation. Due to the symmetry of the autocorrelation function, only positive τ's were considered.

Because of limited processing speed for the Monte Carlo simulations, the absorption levels were reduced by 70%. In order to make comparisons between experiment and simulation, absorption estimates from the Monte Carlo simulation were rescaled using a single coefficient.

4.7 Experimental Work

Experimental time resolved reflectance measurements in layered media were made to evaluate the efficacy of the reconstruction methods with real data. The experimental apparatus developed for the reflectance measurements is shown in

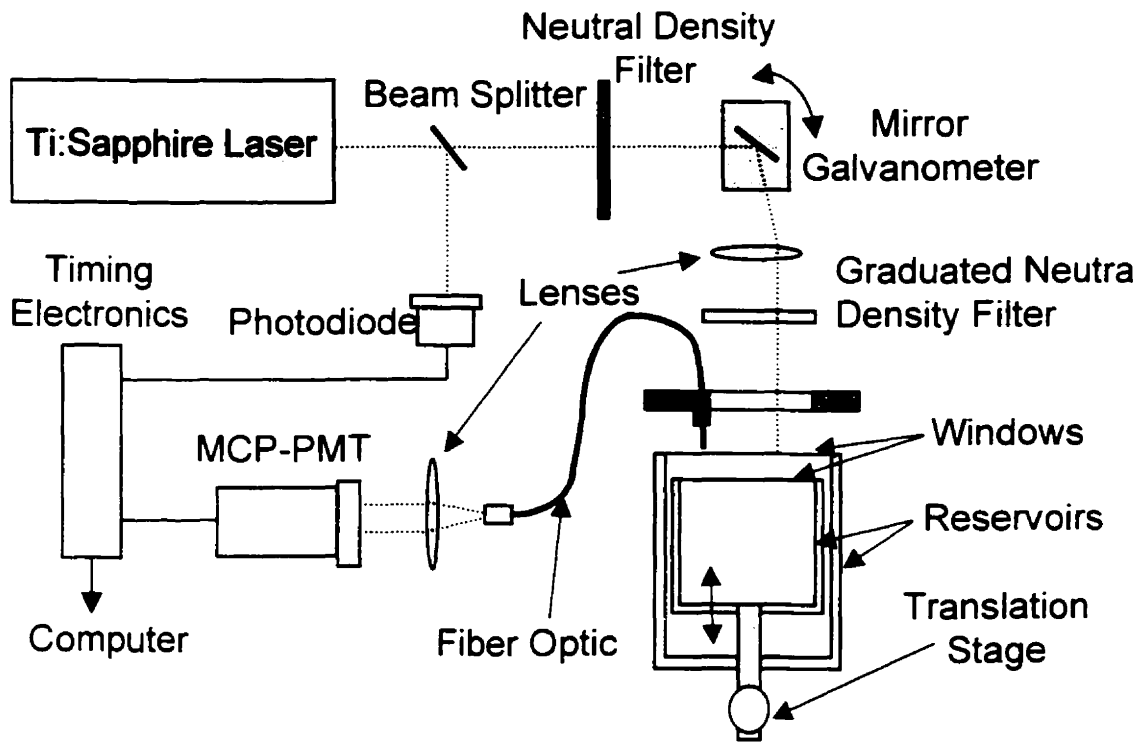

Figure 4.3. Optical layout for the diffuse reflectance, time-resolved photon-counting system.

Figure 4.3. The heart of the system is a time-correlated single photon counting instrument which is similar to devices found in fluorescence life-time studies.[27] A mode-locked Ti:Sapphire laser (Mira 900B, Coherent, Santa Clara, CA) pumped by an Argon laser (Innova 310, Coherent) was used to produce laser pulses with a repetition rate of 76 MHz. The laser pulse shape was measured using a high-resolution autocorrelator and was found to have a width of 170 fs. The laser was tuned to 780nm for the experiment and the power was measured as 0.613 W corresponding to peak pulse powers of 61 kW. The output beam was split by a beamsplitter after which 4% of the light was focused onto a fast photodiode (ET2000, Electro-Optics Technology Inc., Traverse City, MI). The remaining portion of the pulse was attenuated by a neutral density filter and was directed onto the sample using a computer controlled mirror galvanometer (CX660, General Scanning Inc., Watertown, MA). With the aid of a lens, the beam was swept across a sample perpendicular to the face. To keep light levels entering the detector relatively uniform, the pulsed beam was further attenuated by a linear graduated neutral density filter before entering the sample.

To detect the diffuse light from the sample a 0.6 mm diameter fiber optic was used which guided light to a cooled microchannel plate photomultiplier tube (MCP) (R3808U, Hamamatsu Corp., Bridgewater, NJ). Output from the photodiode and MCP were each connected to separate constant fraction discriminators (CFD) (Model 2126, Canberra Industries Inc., Meriden, CT). Logic pulses from the CFDs were sent into a time-to-amplitude converter (TAC) (Model 2145, Canberra). The MCP response was used to start the TAC timing and the photodiode response stopped the timing. This 'reversed timing' technique is commonly used when the start rate is higher than the stop rate and

reduces dead time of the TAC.[28] The output of the TAC was a DC voltage signal proportional to the elapsed time between the start and stop pulses. The TAC output was digitized using a high speed 400Khz 12-bit A/D converter (AT2000, National Instruments, Austin, TX). Time increments were sampled at 4.9 ps. The instrument response with no sample present was measured to be 300 ps FWHM. The significant time blurring was unavoidable and mainly due to the fiber optic. Software running on a 486/66 MHz PC written in C was used for data acquisition, beam positioning and time binning.

The sample container consisted of two black reservoirs each fitted with 40 x 50 mm glass windows, 0.15 mm in thickness. The window of the outer reservoir was designed with a groove separating the source from the detector so that internal reflections in the glass did not couple into the collection fiber. Positioning of the inner reservoir was adjusted with a micrometer. An opaque plastic black sheet was positioned in the inner reservoir so that the total thickness of the sample was maintained at 12 mm. A 1:1 solution of dilute dye to 10% milk fat cream was used as the scattering/absorbing medium for both reservoirs (μ_s = 18.8 mm^{-1}).[26] A suitable water soluble dye (Dr. Ph. Martin's transparent water color #33 Black, Hollywood, FL) was used for the absorber because it was found to be highly water soluble and not fat soluble as measured through the microscope.[29] Absorption between scattering events from the scattering media approximates the assumptions of the Monte Carlo model. [15,29]

Time distributions were recorded as a function of the source/detector separation (1.5 – 15 mm in 1.5 mm increments) and with varying sample composition. Typically, each acquisition required 5 minutes with total counts ranging between $1.5x10^5$ to $4x10^5$ in

each distribution. A series of 130 samples were designed which provide a similar range covered by the simulations. Five different dye concentrations were used in the two layers. The top layer had μ_a values of 0.0000, 0.0038, 0.0075, 0.0150 and 0.0300 mm^{-1}. The lower layer had a series of absorption values of 0.030, 0.060, 0.090, 0.120 and 0.150 mm^{-1}.

To minimize temporal jitter in the time distributions and to make the distributions comparable at all lateral positions, each profile was shifted to a common rising edge time. High frequency periodic artifacts caused by the TAC were reduced by smoothing the measured time profiles. A Gaussian smoothing window (σ = 25 ps) was found to reduce the artifact by 94%. An example of experimentally obtained time distributions after preprocessing is shown in Figure 4.4. The apparent non-linear progression of the time distributions is due to the graduated linear density filter. Further data preprocessing and sectioning into calibration, prediction and validation sets were done in a similar manner as with the simulated data.

4.8 Results and Discussion

4.8.1 Reconstruction results based on time resolved data

The ILS, PLS and SMLR approaches provide an inverse model where absorption coefficients in each region of the sample could be estimated from time resolved reflectance data. Both experiment and modeled data were considered for the comparison. Table 4.1 summarizes reconstruction results for each of the six regions. Both the absolute standard errors and the coefficients of variation for each region are given.

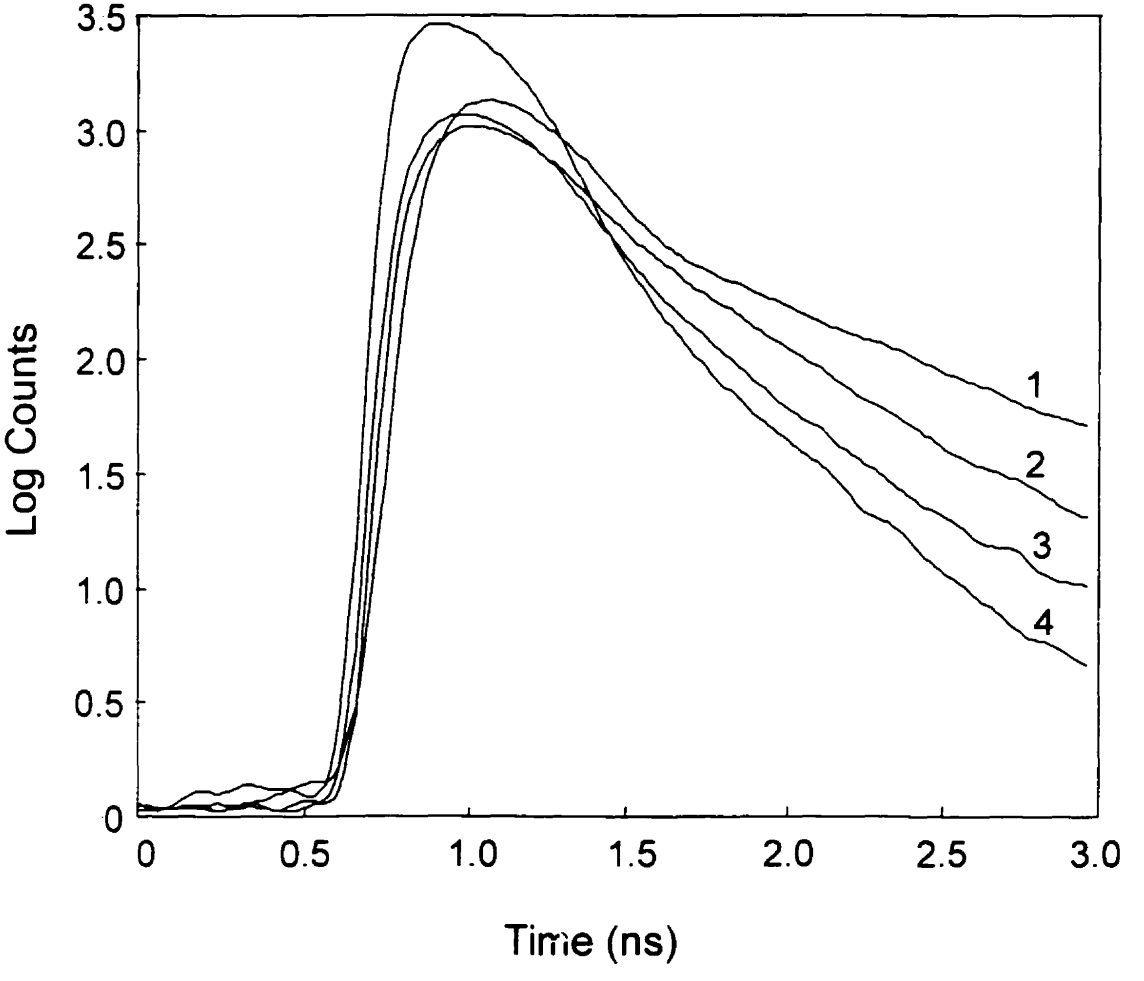

Figure 4.4. Experimentally obtained time-resolved diffuse reflectance responses as a function of source/detector separation. 1) r = 1.5 mm; 2) r = 6 mm; 3) r = 10.5 mm; 4) r = 15.0 mm.

Region 1 represents the upper most portion of the sample (0 - 2mm) whereas region 6 represents the deepest (10 - 12 mm).

The results indicate that reconstructions using the ILS method with both the experimental and modeled data provided inaccurate estimations of sample absorption. With the modeled data however, absorption coefficients in both the first and second layers were estimated to a reasonable degree before rapidly degrading with increased depth. The large amount of error is not surprising due to the ill-conditioned nature of the reconstruction. Due to the ambiguity of the reconstruction, the ILS method estimates absorption coefficients considerably outside the range of physically possible values. To obtain better quantification, constraints and *a priori* information must be included as is used in ART reconstruction methods.

Table 4.1. Reconstruction results with time resolved data.

Method	Region 1	Region 2	Region 3	Region 4	Region 5	Region 6
Experiment						
ILS	1.1×10^{-2}	1.1×10^{-1}	2.1×10^{-1}	6.3×10^{-1}	7.3×10^{-1}	6.9×10^{-1}
	(94 %)*	(471 %)	(479 %)	(1115 %)	(970 %)	(784 %)
PLS	2.2×10^{-3}	2.5×10^{-2}	3.9×10^{-2}	4.3×10^{-2}	4.9×10^{-2}	4.3×10^{-2}
	(19.1 %)	(102.5 %)	(89.5 %)	(75.7 %)	(64.5 %)	(48.2 %)
SMLR	1.5×10^{-3}	2.5×10^{-2}	3.9×10^{-2}	4.6×10^{-2}	5.0×10^{-2}	4.7×10^{-2}
	(13.3 %)	(103.6 %)	(88.6 %)	(80.5 %)	(65.7 %)	(52.5 %)
Modeled						
ILS	1.7×10^{-2}	3.1×10^{-2}	2.2×10^{-1}	6.2×10^{-1}	6.6×10^{-1}	7.1×10^{-1}
	(22.9 %)	(40.1 %)	(302 %)	(831 %)	(881 %)	(958 %)
PLS	1.3×10^{-2}	1.6×10^{-2}	2.3×10^{-2}	2.9×10^{-2}	4.3×10^{-2}	4.3×10^{-2}
	(17.5 %)	(22.0 %)	(31.3 %)	(39.6 %)	(57.8 %)	(57.3 %)
SMLR	2.8×10^{-4}	1.5×10^{-2}	2.6×10^{-2}	4.1×10^{-2}	4.5×10^{-2}	4.5×10^{-2}
	(0.3 %)	(20.6 %)	(34.7 %)	(54.5 %)	(60.5 %)	(60.1 %)

*Standard errors given mm^{-1}, coefficients of variation in (%)

For less ambiguous quantification in each of the regions, the PLS method was used to provide a more directed approach to the reconstruction. Estimates for all of the regions required either four or five factors as optimal for both experimental and simulated data sets. This higher number of factors is believed to be related to both the presence of noise and to non-linearities in the time-of-flight response with absorber concentration. Overall, absorption results indicate an order of magnitude decrease in the error over the ILS technique. Similar trends are seen in comparing errors obtained in the simulated and experimental data. However, a significant difference is seen between the two data sets in regions 2 and 3, where the experimental results have large errors. The large error is probably due to the nature of the sample cell. When the inner compartment occupies these regions, positioning variation of the glass window plays a significant role in the observed results. The experimentally determined time profiles were slightly different when the glass divider was positioned close to the surface with a sample containing identical solutions in each compartment.

For the experimental data, significant improvement in the reconstruction in deeper regions is inherent in the PLS method. Figures 4.5 and 4.6 show a plot of the calibration vector **B**, for regions 1 and 6. Weighting coefficients are arranged to clearly see the relative weighting as a function of time and detector position. For region 1, the weighting coefficients of the calibration vector for all source/detector separations show the same general trend. A strong weighting of peak maximum follows with source/detector position (see Figure 4.4). Each profile is weighted positively at early times (around the peak maxima), and negatively at longer times. The effect of oppositely weighting coefficients suggests that signal differencing leads to a cancellation of

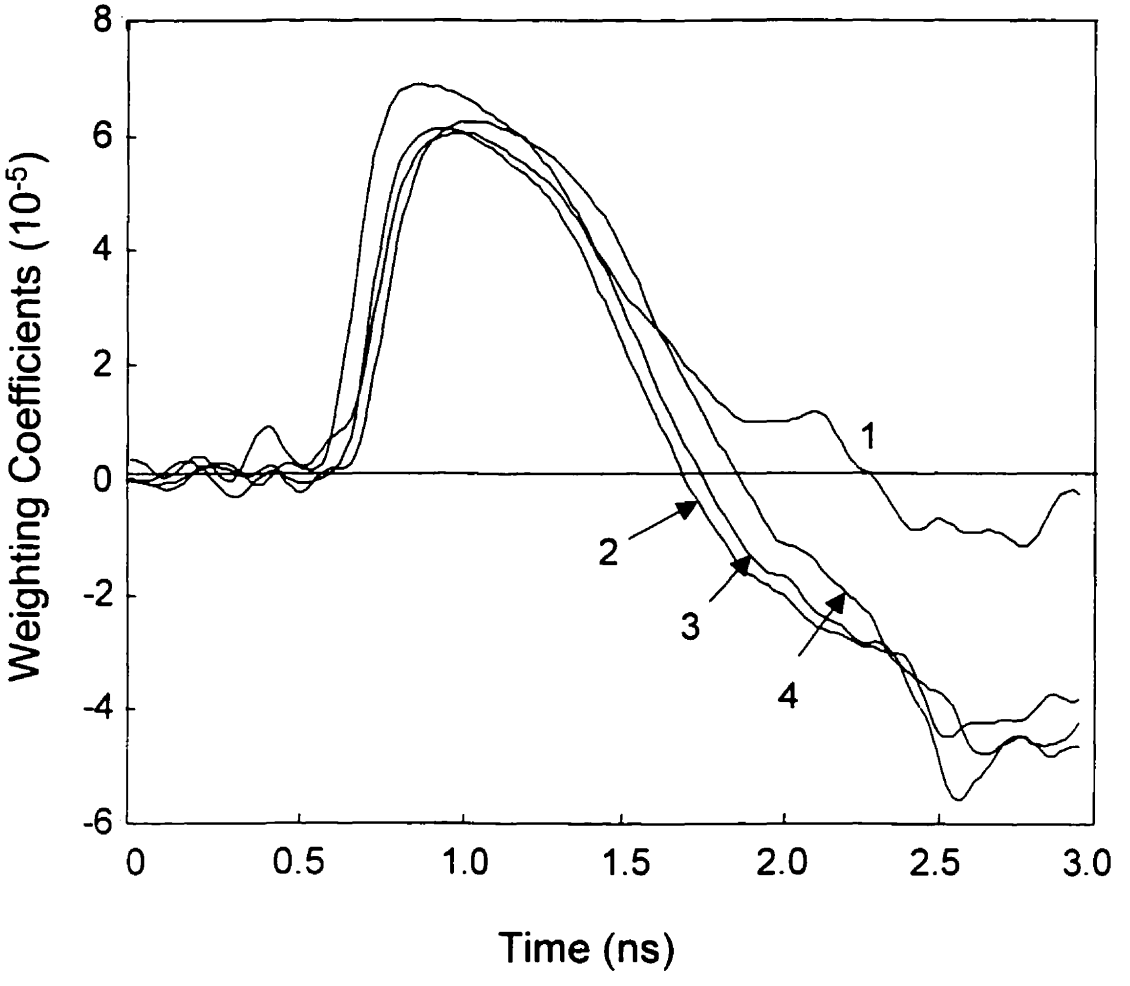

Figure 4.5. Calibration coefficients stacked as a function of time and detector position as determined by PLS regression for region 1 with time-resolved data. 1) r = 1.5 mm; 2) r = 6 mm; 3) r = 10.5 mm; 4) r = 15 mm.

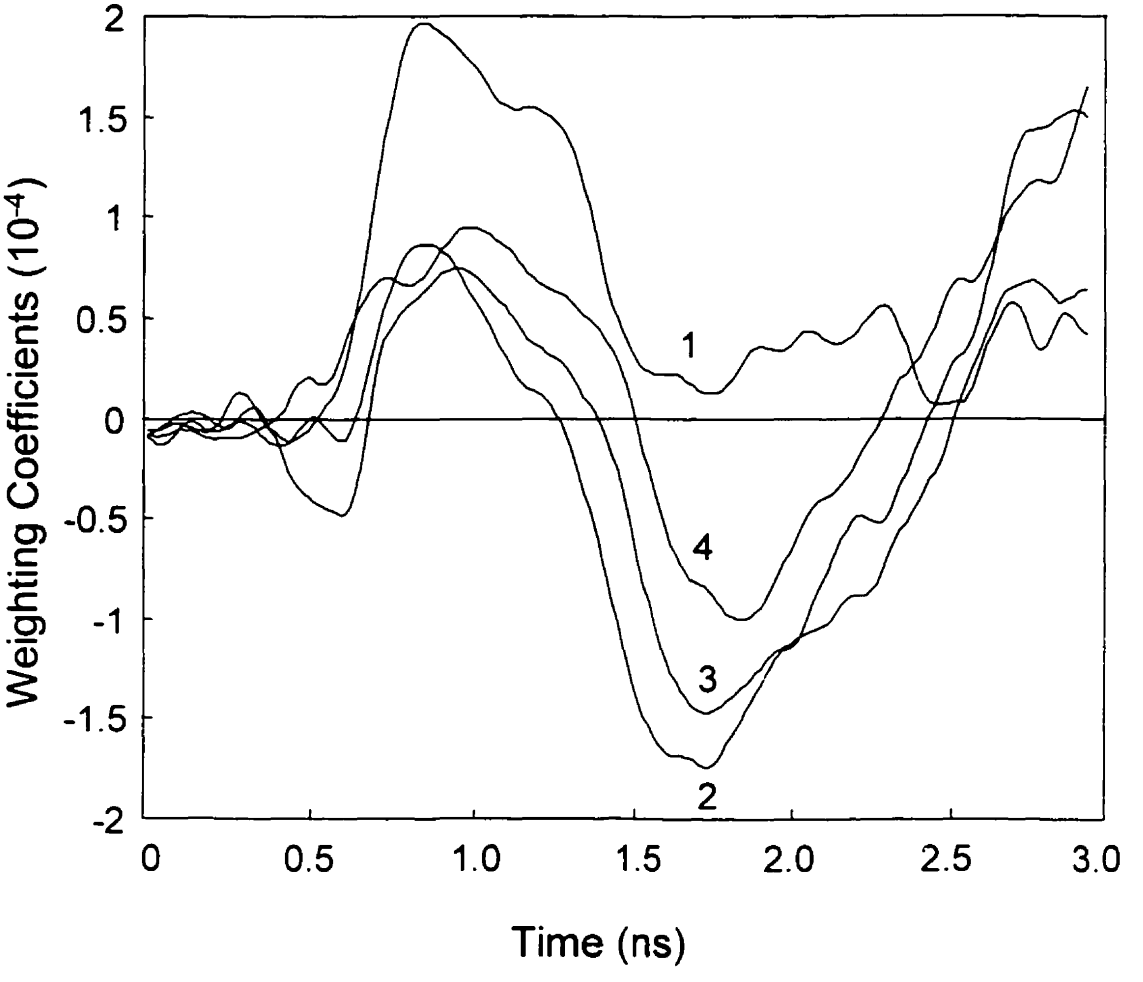

Figure 4.6. Calibration coefficients stacked as a function of time and detector position as determined by PLS regression for region 6 with time-resolved data. 1) r = 1.5 mm; 2) r = 6 mm; 3) r = 10.5 mm; 4) r = 15 mm.

information from deeper regions. By subtracting the contribution of the peak maximum (mean photon paths) from that of the trailing edge (longer path photons which penetrate deeper) a region in the sample may be selected. A slightly different profile is seen for the calibration vector of region 6. Whereas the same form of differencing is seen at short times, the peak maximum is less significant at larger source/detector separations than before. Likewise, there is a shift to positive weighting at longer times which contain information from light having longer pathlengths through the sample. Analyzing the calibration vector as a function of source/detector position, however, has proved more difficult. Although source/detector positioning has been previously demonstrated as a means to discriminate between absorption changes within a sample using a continuous source,[15] the present role is complicated with time-resolved data. Nevertheless, the PLS calibration vector provides both a means for tomographic reconstruction and a useful tool in which information about the nature of the photon propagation in scattering media.

Reconstructions results using SMLR were similar to the PLS results. For modeled data, ten individual time responses for region 1 were determined. This number decreased to two in region 6. Similar regions of the time distributions were chosen as the most correlated with both experimental and simulated data. Referring to Table 4.2, in the case of region 1, the selected times and positions suggest that changes in the peak maximum at small source/detector separations are important. For a deep region, the data responses corresponding to long times at large source/detector separations were selected. A similar differencing of the signal is seen as compared to the PLS results considering the coefficients for each of the responses selected.

Table 4.2. Optimal data points chosen by SMLR with experimental time resolved data.

Region	Time (ps)	Detector Position (mm)	Weighting Coefficient
1	1320	1.5	-0.1598
	1510	4.5	-0.0330
	870	1.5	-0.0159
	1480	12.0	-0.00547
	2900	1.5	+0.00092
6	2740	12.0	-0.3373
	2755	13.5	+0.3246

Both SMLR and PLS provided similar results for regions 2 to 6 however a marked improvement was found for the uppermost region using the SMLR technique. In this case, almost a 50 fold improvement is found in the simulated data. Likewise, for experimental data, a two fold improvement over estimates by PLS was observed. This improvement in absorption coefficient estimation in region 1 is understandable considering that the most correlated time/position information regarding region 1 is contained in a tight bolus of photons that have traveled the shortest path. The use of only a few data responses allows for better estimations because unnecessary information which tends to weight in noise is not included. This effect is well recognized with other spectroscopic measurements.

Three images of reconstructed samples as determined by the SMLR technique are shown in Figure 4.7. Images were chosen to illustrate the major cause of the error in the estimation of the absorption coefficients in the vicinity of the discontinuous boundary between the two layers. Instead of an abrupt change, only broad sloping changes are produced. Regions with constant absorption coefficient are also poorly estimated and

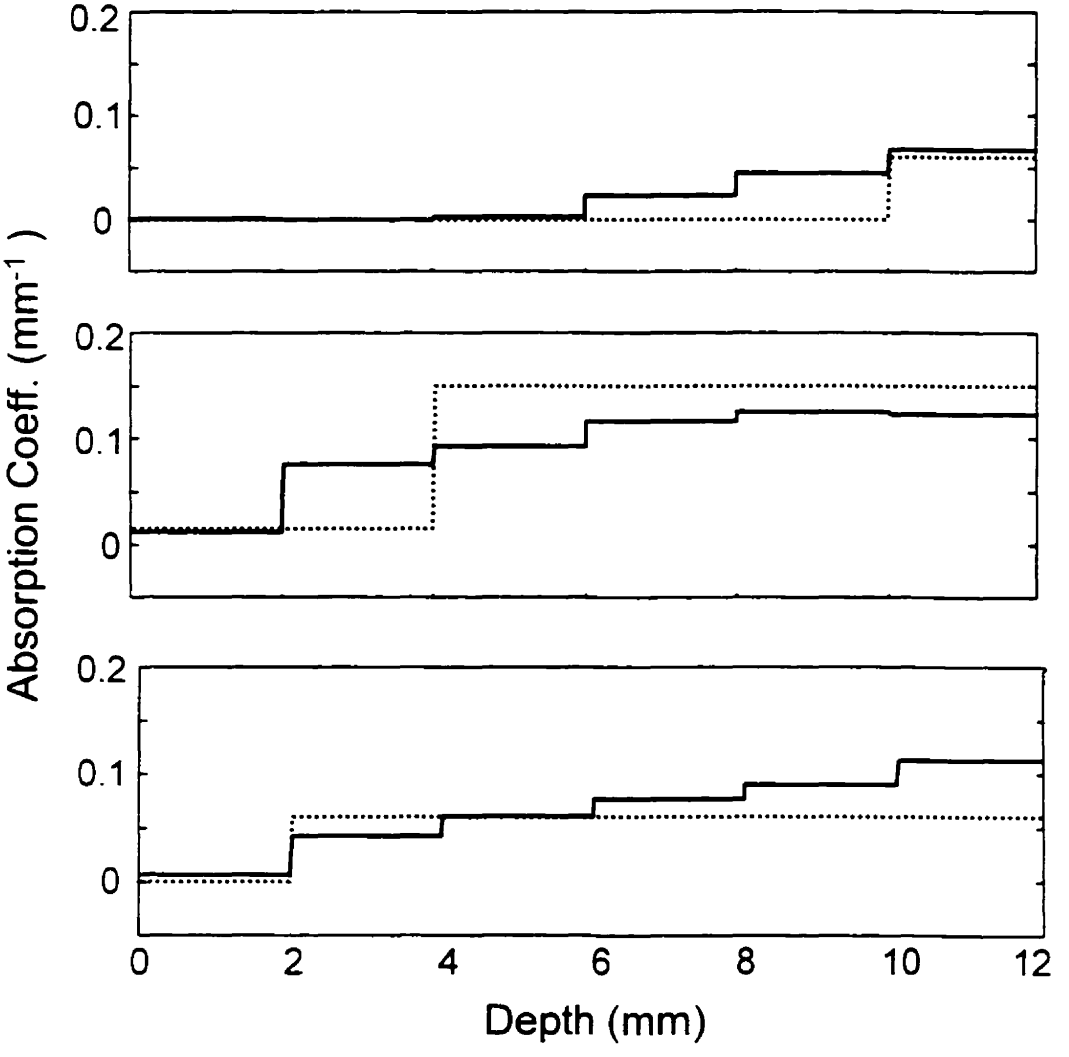

Figure 4.7. Images of reconstructed samples (dashed lines) as determined by the SMLR technique. Solid lines represent actual composition.

give an average over the range. This is not unlike other reconstruction techniques where ambiguity and noise in the data produces bandwidth-limited images. Estimation may be improved for bandwidth limited images using *a priori* constraints.

4.8.2 Reconstruction results with autocorrelated data

Autocorrelated data was evaluated with the reconstruction methods in order to make comparisons to normal time resolved data. As shown in Table 4.3, similar results are seen when comparing reconstructions with a slight improvement in the top two regions.

Table 4.3. Reconstruction results with autocorrelated data.

Method	Region 1	Region 2	Region 3	Region 4	Region 5	Region 6
Experiment						
PLS	1.7×10^{-3}	2.3×10^{-2}	3.6×10^{-2}	3.9×10^{-2}	4.6×10^{-2}	4.2×10^{-2}
	(15.0 %)	(94.1 %)	(82.4 %)	(68.4 %)	(60.6 %)	(47.6 %)
SMLR	1.0×10^{-3}	1.8×10^{-2}	3.5×10^{-2}	4.1×10^{-2}	4.8×10^{-2}	3.7×10^{-2}
	(9.0 %)	(73.8 %)	(80.7 %)	(72.6 %)	(63.4 %)	(41.3 %)
Modeled						
PLS	5.1×10^{-3}	9.6×10^{-3}	2.2×10^{-2}	2.8×10^{-2}	4.1×10^{-2}	4.2×10^{-2}
	(6.8 %)	(12.8 %)	(30.1 %)	(37.1 %)	(55.0 %)	(55.7 %)
SMLR	6.6×10^{-4}	5.7×10^{-3}	2.7×10^{-2}	3.2×10^{-2}	4.4×10^{-2}	4.2×10^{-2}
	(0.9 %)	(7.6 %)	(36.3 %)	(42.7 %)	(58.3 %)	(56.4 %)

*Standard errors given mm^{-1}, coefficients of variation in (%)

The factor of two improvement in the estimation using PLS with simulated data was due to the smoothing inherent to the autocorrelation technique. For the autocorrelation signal, the optimal number of factors increased to five or six factors. This was observed for both the modeled and experimental data. Though there errors decreased as compared to the

time distribution estimates, the increased number of factors needed with autocorrelated data suggests that there is an increase in the non-linearity of the absorption estimates. From the calibration vectors shown in Figures 4.8 and 4.9, it is observed that the most of the weightings are placed on both short and long phase delays. This corresponds to maximal weightings placed on the mean and long photon paths respectively. For intermediate values of phase delay, the two partially overlapped time distributions produce the highest degree of non-linearity and as a consequence are the least significant. From Figures 4.8 and 4.9 it can be seen that the weightings of the responses vary as a function of source/detector separation. A change in sign is observed for low phase delay values as source/detector is increased. The effect of oppositely weighting coefficients between detector positions again suggests that differencing of the responses provide the method to discriminate between regions. The trend of oppositely weighting coefficients as a function of source/detector separation at low phase delay is analogous the results observed with time distributions. The autocorrelation function for small phase delay is approximately proportional to the steady state response (integrated square of the time distribution). This is consistent with previous work where source/detector positioning was demonstrated as the sole means to discriminate between absorption changes within a sample.[15] Although a more complicated relation exists between $A(\mathbf{r},\tau)$ and the absorption coefficient for a two layer medium, the PLS method provides a similar error of the estimate.

Reconstruction with SMLR of the autocorrelated response showed similar results to the PLS estimates. An increased number of responses were required in the SMLR model to yield a similar level of estimation as provided by the estimation made with the

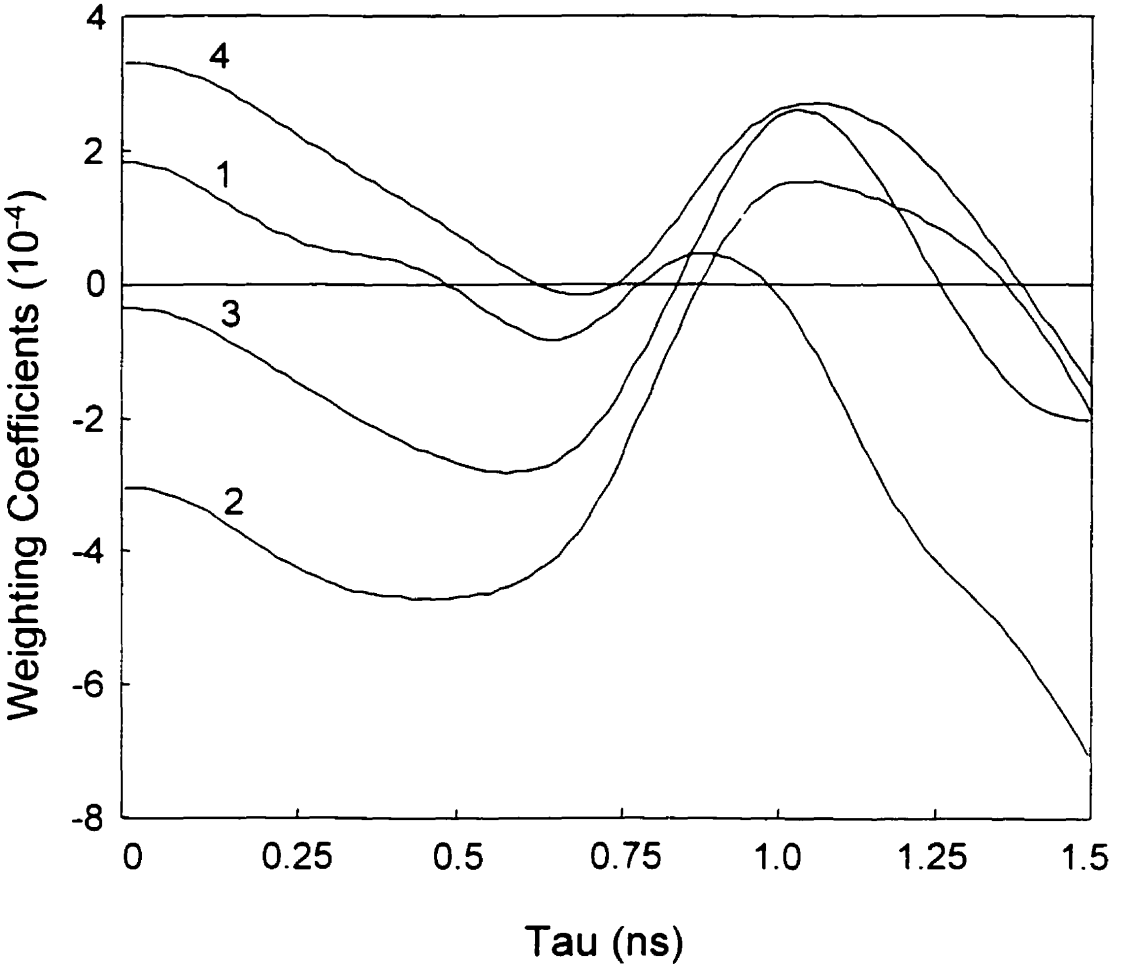

Figure 4.8. Calibration coefficients stacked as a function of phase delay and detector position as determined by PLS regression for region 1 with autocorrelated data. 1) r = 1.5 mm; 2) r = 6 mm; 3) r = 10.5 mm; 4) r = 15 mm.

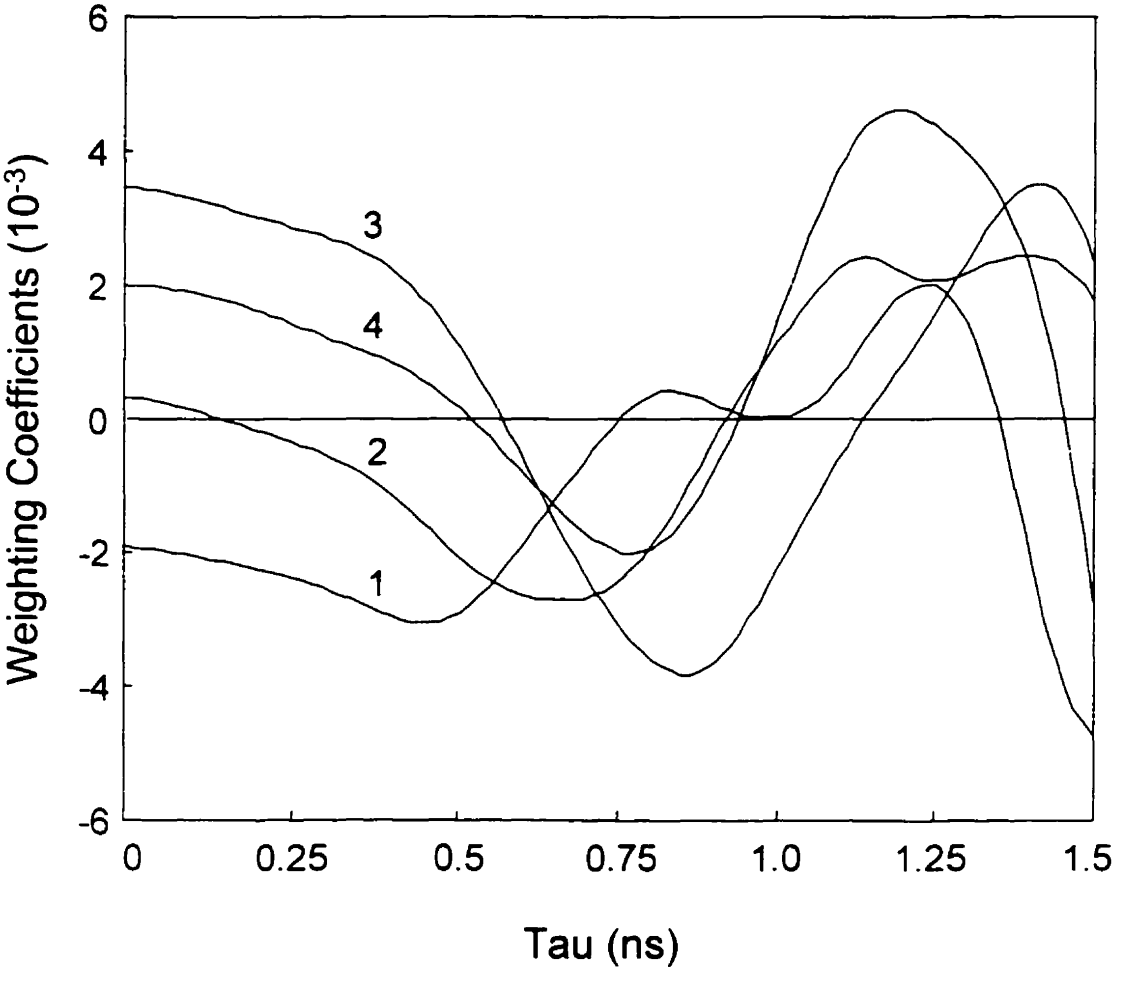

Figure 4.9. Calibration coefficients stacked as a function of phase delay and detector position as determined by PLS regression for region 6 with autocorrelated data. 1) r = 1.5 mm; 2) r = 6 mm; 3) r = 10.5 mm; 4) r = 15 mm.

time distributions. The responses chosen by the method, shown in Table 4.4, heavily weighted small phase delays at small source/detector separations for estimations of absorption in region 1. For region 6, the opposite effect is observed where large source/detector separations and large phase delays are the most correlated with changes deep within the sample. These results are consistent with the interpretation of the autocorrelation function where large phase delays are most sensitive to changes in the trailing edge of the time distribution.

Table 4.4. Optimal data points chosen with SMLR with autocorrelated data.

Region	τ (ps)	Detector Position (mm)	Weighting Coefficient
1	90	1.5	-2.6317
	15	1.5	+2.3619
	390	1.5	+0.1711
	380	15.0	-0.0770
	245	7.5	+0.0752
	305	12.0	-0.0677
	230	6.0	-0.0283
6	1450	15.0	-0.3373
	1100	1.5	+0.3323
	1420	1.5	+0.0782
	15	1.5	-0.0034

4.9 Conclusion

A depth resolved tomographic reconstruction of layered scattering/absorbing media was shown. Using both Monte-Carlo simulations and experimental data, a comparison between reconstructions of samples was done using photon time-of-flight diffuse reflectance and autocorrelated data. With both real and simulated data, depth

resolved quantification of the absorption in each region of a sample was made using stepwise multi-linear regression, inverse and partial least squares methodologies. For all methods, absorbance was better estimated in the top regions as compared to deeper regions within the sample. Likewise, reconstruction results using the autocorrelation of the time responses were found to provide similar estimation in comparison with time distribution data. Both PLS and SMLR methods gave significantly better estimation of sample absorption as compared to the ILS technique. In comparing results from simulated data, SMLR gave the best results with a 0.9% error in the top layer. However in lower regions, no improvement was seen between SMLR and PLS. The results are encouraging as new directed methods may be developed which include estimates obtained in upper regions to better approximate absorbance deep within a sample. Likewise, adding constraints and *a priori* information about the sample may improve the estimation. In the future, incorporating time resolved information together with advanced reconstruction methods may provide new tools for solid sample analysis in clinical and industrial environments.

4.10 References

1. Farrell, T. J.; Patterson, M. S.; Essenpreis, M. Influence of Layered Tissue Architecture on Estimates of Tissue Optical Properties Obtained from Spatially Resolved Diffuse Reflectometry; *Appl. Opt.* **1998**, *37*, 1958-1972.
2. Kienle, A.; Patterson, M. S.; Dognitz, N.; Bays, R.; Wagnieres, G.; van den Burgh, H. Noninvasive Determination of the Optical Properties of Two-Layered Turbid Media; *Appl. Opt.* **1998**, *37*, 779-791.
3. Nichols, M. G.; Gutsche, A. S.; Schwartz, J.; Wang, L.; Tittel, F. K. *Appl. Opt.* **1996**, *35*, 2304-2314.
4. Patterson, M. S.; Chance, B.; Wilson, B. C. Time Resolved Reflectance and Transmittance for the Non-Invasive Measurement of Tissue Optical Properties; *Appl. Opt.* **1989**, *28*, 2331-2336.
5. Cui, W.; Kumar, C.; Chance, B. Experimental Study of Migration Depth for the Photons Measured at Sample Surface; *Proc. SPIE* **1991**, *1431*, 180-191.
6. Chang, J.; Graber, H. L.; Barbour, R. L. *OSA Proc. On Advances in Optical Imaging and Photon Migration*; Alfano, R. R. Ed.; OSA: New York, 1994; Vol 21, pp 193-220.
7. Yao, Y.; Wang, Y.; Pei, Y.; Zhu, W.; Barbour, R. L. Frequency-Domain Optical Imaging of Absorption and Scattering Distributions by a Born Iterative Method; *J. Opt. Soc. Am. A* **1997**, *14*, 325-342.
8. Takatani, S.; Graham, M. D. Theoretical Analysis of Diffuse Reflectance from a Two-Layer Tissue Model; *IEEE Trans. Biomed. Eng.* **1979**, *BME-26*, 656-664.

9. Schmitt, J. M.; Zhou, G. X.; Walker, E. D.; Wall, R. T. Multilayer Model of Photon Diffusion in Skin; *J. Opt. Soc. Am. A* **1990**, *7*, 2141-2153.

10. Dayan, I.; Havlin, S.; Weiss, G. H. Photon Migration in a Two-Layer Turbid Medium; *J. Mod. Opt.* **1992**, *39*, 1567-1582.

11. Hielsher, A. H.; Lui, H.; Chance, B.; Tittel, F. K.; Jacques, S. L. Time-Resolved Photon Emission from Layered Turbid Media; *Appl. Opt.* **1996**, *35*, 719-728.

12. Nossal, R.; Kiefer, J.; Weiss, G. H.; Bonner, R.; Taitelbaum, H.; Havlin, S. Photon Migration in Layered Media; *Appl. Opt.* **1988**, *27*, 3382-3391.

13. Keijzer, M.; Star, W. M.; Storchi, P. R. M. Optical Diffusion in Layered Media; *Appl. Opt.* **1988**, *27*, 1820-1824.

14. Groenhuis, R. A. J.; Ferwerda, H. A.; Ten Bosch, J. J. Scattering and Absorption of Turbid Materials Determined from Reflection Measurements. 1 Theory; *Appl. Opt.* **1983**, *22*, 2456-2462.

15. Long, W. F.; Burns, D. H. Optical Tomographic Reconstruction from Diffuse Remittance in Scattering Media using Partial Least Squares Estimation; *Anal. Chim. Acta* **1997**, *348*, 553-563.

16. Hebden, J. C.; Arridge, S. R.; Delpy, D. T. Optical Imaging in Medicine: I. Experimental Techniques; *Phys. Med. Biol.* **1997**, *42*, 825-840.

17. Ishimaru, A. Diffusion of a Pulse in Densely Distributed Scatterers; *J. Opt. Soc. Am.* **1978**, *68*, 1045-1052.

18. Patterson, M. S.; Chance B.; Wilson, B. C. Time Resolved Reflectance and Transmittance for the Non-invasive Measurement of Tissue Optical Properties; *Appl. Opt.* **1989**, *28*, 2331-2336.

19. Arridge, S. R; Cope, M.; Delpy, D. T. The Theoretical Basis for the Determination of Optical Pathlengths in Tissue: Temporal and Frequency Analysis; *Phys. Med. Biol.* **1992**, *37*, 1531-1560.

20. Arridge, S. R.; Schweiger, M. The use of Multiple Data Types in Time-resolved Optical Absorption and Scattering Tomography (TOAST) in Mathematical Methods in Medical Imaging II; Wilson, B. C.; Wilson N. J., Eds.; *Proc. Soc. Photo-Opt. Instrum. Eng.* Wiley: New York, 1993; Vol. 2035, pp 218-229.

21. Gordon, R. A Tutorial on ART; *IEEE Trans. Nucl. Sci.* **1974**, *NS-21*, 78-93.

22. Gordon, R.; Bender R.; Herman, G. T. Algebraic Reconstruction Technique (ART) for Three Dimensional Electron Microscopy and X-ray Photography; *J. Theor. Biol.* **1970**, *29*, 471-481.

23. Lorber, A.; Wangen L. E.; Kowalski, B. R. A Theoretical Foundation for the PLS Algorithm; *J. Chemom.* **1997**, *1*, 19-34.

24. Haaland, D. M.; Thomas, E. V. Partial Least-Squares Methods for Spectral Analyses. 1 Relation to Other Quantitative Calibration Methods and the Extraction of Quantitative Information; *Anal. Chem.* **1988**, 60, 1193-2001.

25. Beebe, R.; Kowalski, B. R. An Introduction to Multivariate Calibration and Analysis; *Anal. Chem.* **1987**, *59*, 1007-1016.

26. Arakaki, L. S. L.; Kushmerik, M. J.; Burns, D. H. Myoglobin Oxygen Saturation Measured Independently of Hemoglobin in Scattering Media by Optical Reflectance Spectroscopy; *Appl. Spectrosc.* **1996**, 50, 697-705.

27. Small, E. W. Laser Sources and Microchannel Plate Detectors for Pulse Fluorometry; In *Topics in Fluorescence Spectroscopy;* Lakowicz, J. R., Ed.; Plenum Press: New York, 1991, Vol. 1.

28. *Canberra Model 2145 TAC User Manual*; Canberra Inc.: Meriden, Connecticut, 1990, pp. 7-8.

29. Marble, D. R.; Burns, D. H.; Cheung, P. W. Diffusion-Based Model of Pulse Oximetry: In Vitro and in Vivo Comparisons; *Appl. Opt.* **1994**, *33*, 1279-1285.

Chapter 5 A Hierarchical Local Weighted Calibration and Classification Approach to Depth Resolved Quantification in Scattering Media using Photon Time-of-Flight Measurements

In Chapter 4 optical tomographic reconstruction in layered liquid samples was made using stepwise multi-linear regression and partial least squares regression. Estimates of the absorption coefficient in each sample region were made independent of other regions. Although sample quantification in the top region improved markedly over those using steady state measurements, large errors in the estimates remain in the bottom regions.

To further reduce the error in sample reconstruction, *a priori* information and constraints are needed. It was observed that accurate absorption estimates in the lower regions may be made if the samples used for calibration contained a fixed level in the upper regions. Layer absorption estimates may therefore be improved by narrowing the range of samples used for calibration. By embedding this approach into an overall tomographic reconstruction methodology, better sample quantification at each sample depth may be possible. *A priori* information regarding sample composition in the upper regions may therefore direct subsequent calibration for lower regions. This approach is similar to locally weighted regression (LWR) methods which have been applied in NIR diffuse reflectance studies for estimating non-linear regression surfaces. Further, by discretizing the possible outcomes with classification methods, enhancements in quantification may be obtained. A classification based reconstruction will naturally

constrain absorption estimates to positive values or to a given range. In this chapter, these concepts are explored for depth resolved quantification.

5.1 Abstract

Chemometric methods for quantitative analysis in layered scattering/absorbing paper samples are described. A radial array of time-resolved diffuse reflectance measurements have been made to obtain multi-perspective information sensitive to changing sample composition. For analysis, the stepwise multilinear regression (SMLR) method was used a basis of a hierarchical locally weighted sample calibration. Estimates of the absorption coefficient in each sample region were made either by linear regression following by binning of the result (HLRB) or by K-nearest neighbour classification analysis (HCKNN). With these approaches, the tomographic reconstruction problem may be linearized by utilizing *a priori* information about sample composition in upper regions to direct subsequent calibrations for lower regions. A comparison of different reconstruction methodologies is made along with their efficacy in the presence of added noise. Results demonstrate that estimations of the absorption coefficient deep within a highly scattering/absorbing sample are obtainable at greater than 50% accuracy using the HCKNN approach. This represents a 20% improvement at all sample depths over the SMLR approach. The use of locally weighted calibrations and sample classification to constrain the solution of a tomographic reconstruction is shown as a powerful new tool for quantification in layered scattering/absorbing media.

5.2 Introduction

In many fields there is a need to observe and characterize a specimen in three dimensions. In the analysis of turbid media, optical methods are commonly used to determine the concentration of the desired analyte. Recently, there is considerable interest in the analysis of layered samples. Layered systems such as skin/bone/brain tissue in the head or the skin/adipose/muscle system are common in biology. Other common examples of layered media include the gel capsule/drug system and paper/mylar composites. Indeed, the ability to make a quantitative non-invasive assessment of product freshness inside composite translucent packaging would be a valuable quality assurance tool to the food industry. In complex media, the analysis method is often based on an invalid model which assumes sample uniformity. This assumption, introduces artifacts into the measured properties. When analyzing turbid layered samples, it is necessary to consider both the sample structure and measurement technique when interpreting the results since changes in the optical properties in a single region affect the measurements made on the bulk.

Several techniques have been developed to obtain depth resolved information from a turbid sample. For thick samples where transmission measurements may be impractical, reflectance based geometries can be employed.[1] Steady state optical signals gathered from detectors situated at several lateral positions from an incident light source may be used to obtain multi-perspective information from a sample. Using multiple optical paths through the sample, depth resolved information may be elucidated with analysis techniques similar to Computer Aided Tomography (CAT).[2,3] In highly scattering samples, the optical path from source to detector is poorly defined and

reconstruction becomes ambiguous. To improve the accuracy of a reconstruction, the detected signal may be time-gated.[4,5] With time-resolved photon detection, the path between source and detector may be more clearly defined by eliminating randomly scattered photons which have an unknown geometry.

Using multi-perspective sample attenuation data, sample reconstruction is often approached as a linear problem.[6,7] However for reasonable estimates of sample composition, linear reconstruction techniques typically require *a priori* structural information together with finite element analysis methods. Several approximate methods have been developed to model the time-resolved reflectance from two-layered samples using the diffusion approximation of the radiative transport equation.[6,8,9] Although more general models have been developed, the success of any sample reconstruction is highly dependent on the quality of the acquired signals. This is especially true for time-resolved data where the subtle shapes in the time-profile contain rich information about sample composition.

Previously, we have investigated depth resolved quantification in layered scattering media with time-resolved measurements using chemometric reconstruction methods.[10] Estimates of sample composition were made independently at each sample depth using partial least squares (PLS) and stepwise multiple regression (SMLR) calibrations. Results demonstrated that reasonable reconstructions were obtained with the SMLR method. As the SMLR technique only uses a few data channels from the total signal, better estimations were possible because unnecessary information and noise was not included. With the SMLR approach, the absorption coefficient in the top layer could be

estimated to within 0.3%. In lower regions however, errors in the absorption estimates increased to 80%.

It is known that the ambiguity in a reconstruction may be reduced by selecting a narrow sample composition range.[11] Two chemometric techniques, locally weighted regression (LWR) and hierarchical methods of analysis, may therefore aid in improving quantification. For near-infrared diffuse reflectance analysis of samples, LWR has been applied successfully as a means for estimating non-linear regression surfaces.[12] In LWR, a new weighted calibration is made for each prediction sample based on the *n* calibration points closest to it. Further, by discretizing the possible outcomes with classification methods such as hierarchical or binary partition trees, enhancements in quantification may be obtained.[13] Likewise, classification may naturally constrain absorption estimates to positive values or to a given range.

In this study, our goal is to enhance quantification over that provided by SMLR by employing hierarchical locally weighted calibration and classification methodologies for samples with discretely variable composition. This method uses *a priori* information about sample composition in upper regions to direct subsequent locally weighted calibrations for lower regions. Two classification methodologies are investigated: K-nearest neighbour classification and simple discrete binning of the estimated absorption coefficients obtained from SMLR. A comparison of different reconstruction methodologies is made along with their efficacy in the presence of added noise. Results demonstrate a marked improvement in reconstruction accuracy compared to that obtained by SMLR.

5.3 Experimental

The experimental apparatus developed for time-resolved diffuse reflectance measurements, shown in Figure 5.1, consists of a time-correlated single photon counting instrument similar to devices found in fluorescence life-time studies.[14] Details of the instrumental setup and basic signal post-processing has been described previously.[10] However, the photon time-of-flight profiles were digitized in 4.9 ps increments over a 3 ns window and the instrument response with no sample present was measured to be 250 ps FWHM. Furthermore, the layered samples were held in position with a black metal clamp which allowed light to penetrate and exit the sample freely from the front face.

Absorbing paper samples were made by soaking individual sheets of Whatman #1 filter paper (Whatman Ltd., Maidstone, England) in an aqueous dye solution (Dr. Ph. Martin's Transparent Water Color #33 Black, Hollywood, FL) for 20 seconds followed by air drying. A 1.0 mm stack of homogeneously dyed filter paper cut to 50 mm × 80 mm were glued around the edges. Care was taken to ensure that the illuminated portion of the sample was free from adhesives. Paper stacks prepared in this manner were calculated to have corresponding relative absorption coefficients, μ_a, of 0.000, 0.006, 0.012, 0.018, 0.024, and 0.030 mm^{-1}. From the Beer-Lambert relation, A = abc, the absorption coefficient, $\mu_a = 2.303$ ac (absorptivity × concentration), is the constant of proportionality between the absorbance, A and the pathlength, b. Each sample of a specific dye concentration profile was comprised of six paper stacks pressed together to form a 6 mm thick specimen.

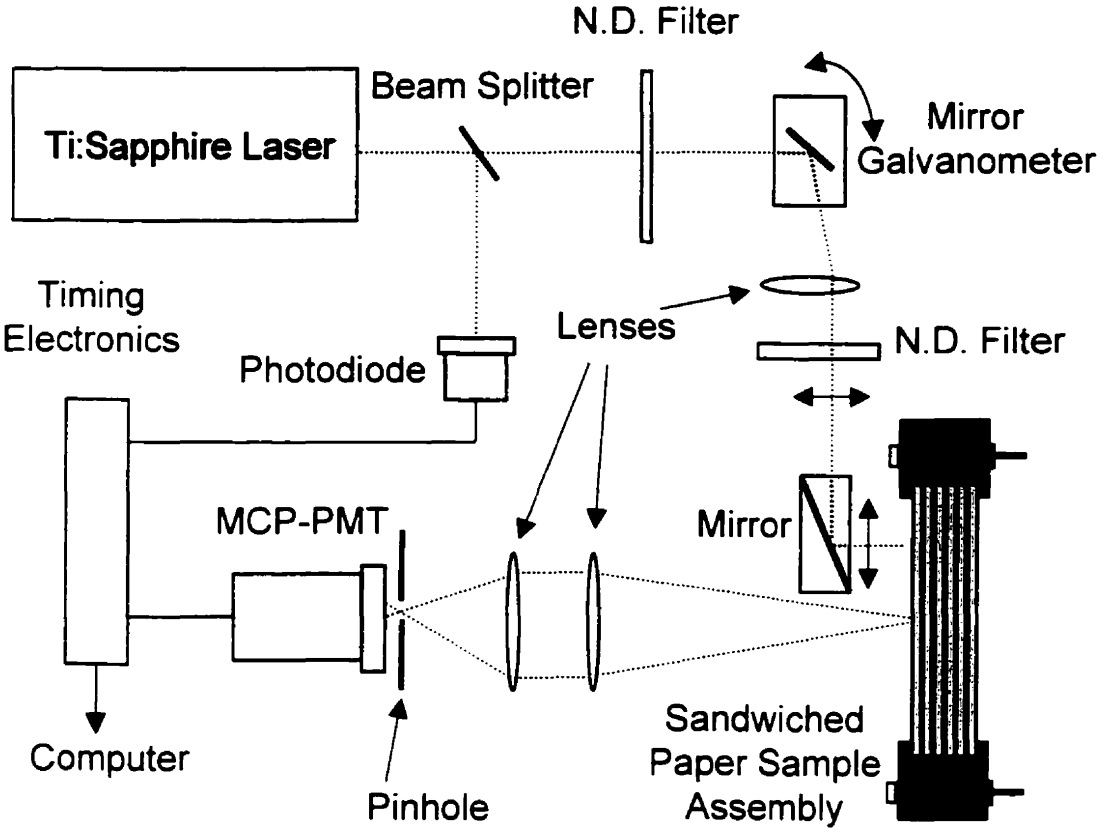

Figure 5.1. Diffuse reflectance photon time-of-flight instrumentation.

A set of 196 distinct samples of varying dye concentration in each layer were made to generate a calibration set which spanned the measured absorption range. Six samples were of a homogeneous absorption coefficient, 150 samples contained two different contiguous absorption regions and 40 samples contained three contiguous absorption regions. Half of the 196 samples comprised the complete calibration sample set. The remaining half of the samples were used for the prediction and validation sets.

Replicate time distributions were recorded at five lateral source/detector separations (2, 5, 8, 11 and 14 mm) for each sample. Each acquisition required 5 minutes with total counts ranging from 4.5×10^5 to 1.2×10^6 in each distribution. To minimize temporal jitter in the time distributions and to make the distributions comparable at all lateral positions, time profiles were shifted to a common incident time of the laser pulse at the detector. Examples of the photon time distributions after smoothing and logarithmic preprocessing are shown in Figure 5.2. It may seen that the intensity and breadth of the distribution vary with source/detector separation.

5.4 Reconstruction Methodologies

The methods used for sample reconstruction were divided into three different categories. First, using the full time distribution, a standard multilinear regression (SMLR) model was developed. Next, to localize the regression according to the sample, a hierarchical locally weighted calibration followed by linear regression with discrete binning (HLRB) was used. This approach allows for a linearization of the reconstruction. Finally, the locally weighted calibration was extended using a non-parametric approach

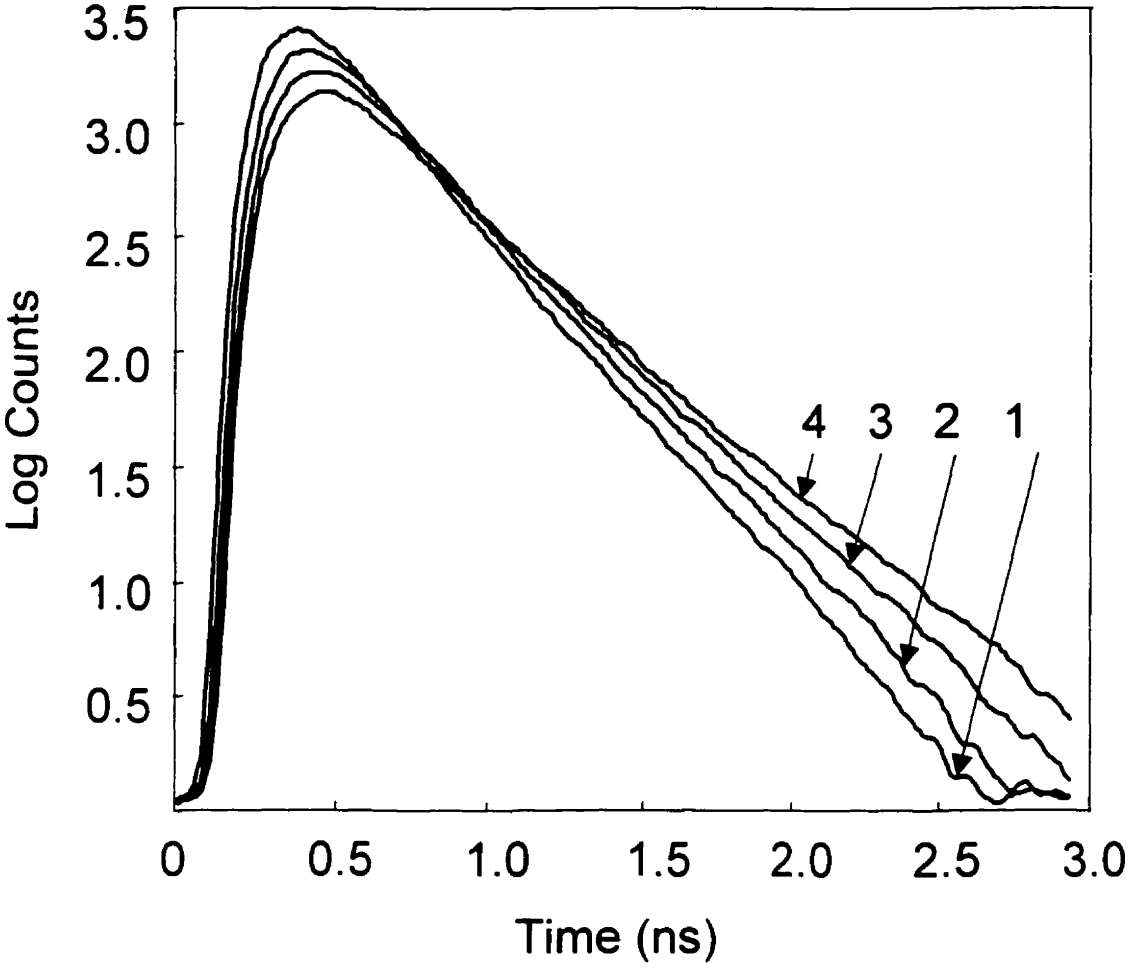

Figure 5.2. Experimental obtained time-resolved diffuse reflectance responses as a function of source/detector separation. 1) r = 2 mm; 2) r = 5 mm; 3) r = 8 mm; 4) r = 11 mm.

by using K-nearest neighbour classification analysis (HCKNN). Common to all of these is the general background of the formation of the reconstruction problem.

For all reconstruction methods, mathematical analysis of the time/position data was facilitated by first lexicographically stacking the total response into a $1 \times ns$ vector,

$$\mathbf{X}_m = \left[x_{m1}(t_1)\ldots x_{m1}(t_s)\, x_{mi}(t_1)\ldots x_{mi}(t_s)\, x_{mn}(t_1)\ldots x_{mn}(t_s)\right] \tag{5.1}$$

where s is the number of time intervals, n is number of lateral positions and $x_{mi}(t_j)$ denotes the response at the ith position and jth time for the mth sample. This vector is assumed to be linearly additive with the absorption from each region. For a linear reconstruction such as SMLR, the overall relationship can be written in matrix notation as,

$$\mathbf{M}_c = \mathbf{X}_c\mathbf{B} \tag{5.2}$$

where $\mathbf{M}_c$ is a matrix containing m sample absorption coefficients for p regions ($m \times p$), $\mathbf{X}_c$ contains n data channels for m samples ($m \times n$) and the subscript c refers to the calibration set. **B** comprises $n \times p$ calibration coefficients relating the responses to the region absorption level.

5.4.1 SMLR reconstruction method

The linear SMLR method was used to identify an optimal linear combination of data channels, $x_1, x_2, \ldots, x_k$ ($k < n$) correlated with the sample absorption coefficients **M.** Details of the particular SMLR algorithm used in this study has been described previously.[10,11] However it should be mentioned that estimates of the m absorption coefficients for a given sample region in the validation set are computed by

$$\hat{\mathrm{M}} = b_0 + b_1x_1 + b_2x_2 + \ldots + b_kx_k \tag{5.3}$$

where b_0, b_1, ... , b_k are the coefficients determined by linear regression.

5.4.2 HLRB reconstruction method

The hierarchical locally weighted regression and classification (HLRB) reconstruction technique pictured in Figure 5.3 is based on the LWR approach[12] followed by discrete classification. For absorption estimates in the top surface region (region 1), SMLR was applied to the complete calibration set. The optimal subset of time/position data channels, x_1, x_2, ... , x_k most correlated to changes in the absorption coefficient in region 1 was found. After applying Equation 5.2 with the b_k parameters on the validation set, the absorption level in region 1 was classified as belonging to one of six possible discrete levels. Classification was done by binning the estimated absorption coefficients into one of six discrete levels as shown with the dashed-line in Figure 5.4. The solid line demonstrates an idealized reconstruction with data points distributed evenly about the line of identity between the actual absorption coefficients and the estimated values. With this information, unique calibration sets for estimation of the absorption coefficient in region 2 were selected for each sample in the validation set such that it contained samples which best matched the absorption levels determined for region 1. Next, SMLR was applied to each new calibration subset for absorption coefficient estimations in region 2. By this method, the optimal data channels for region 2 given *a priori* knowledge of region 1 were determined. The process was applied repeatedly in each successive region of the sample for all validation set members.

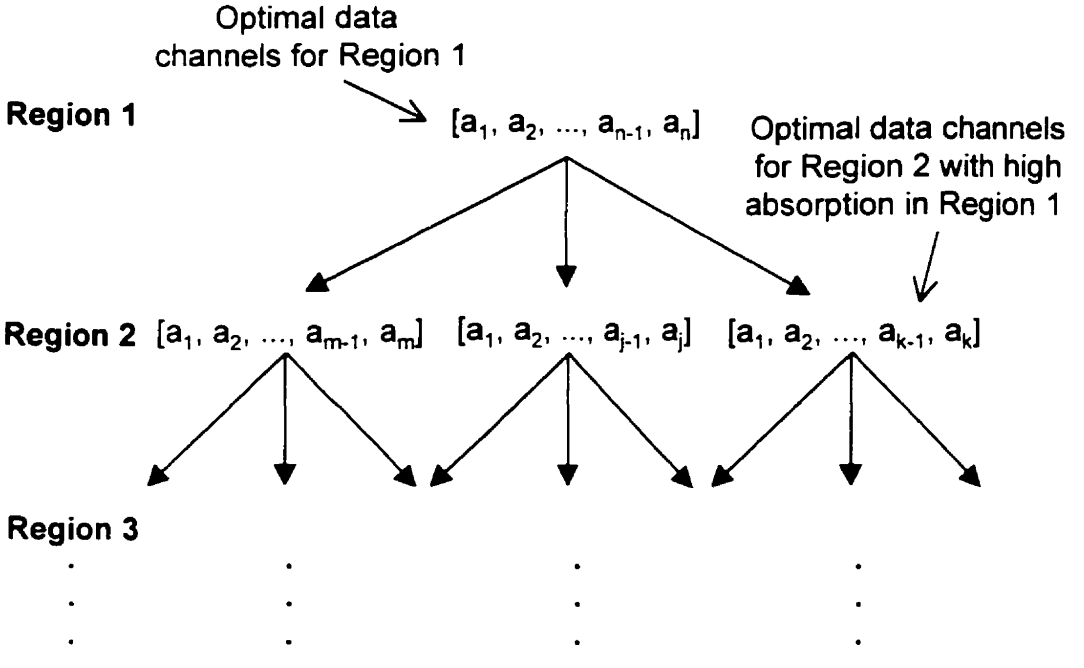

Figure 5.3. Pictorial diagram of the HLRB reconstruction methodology.

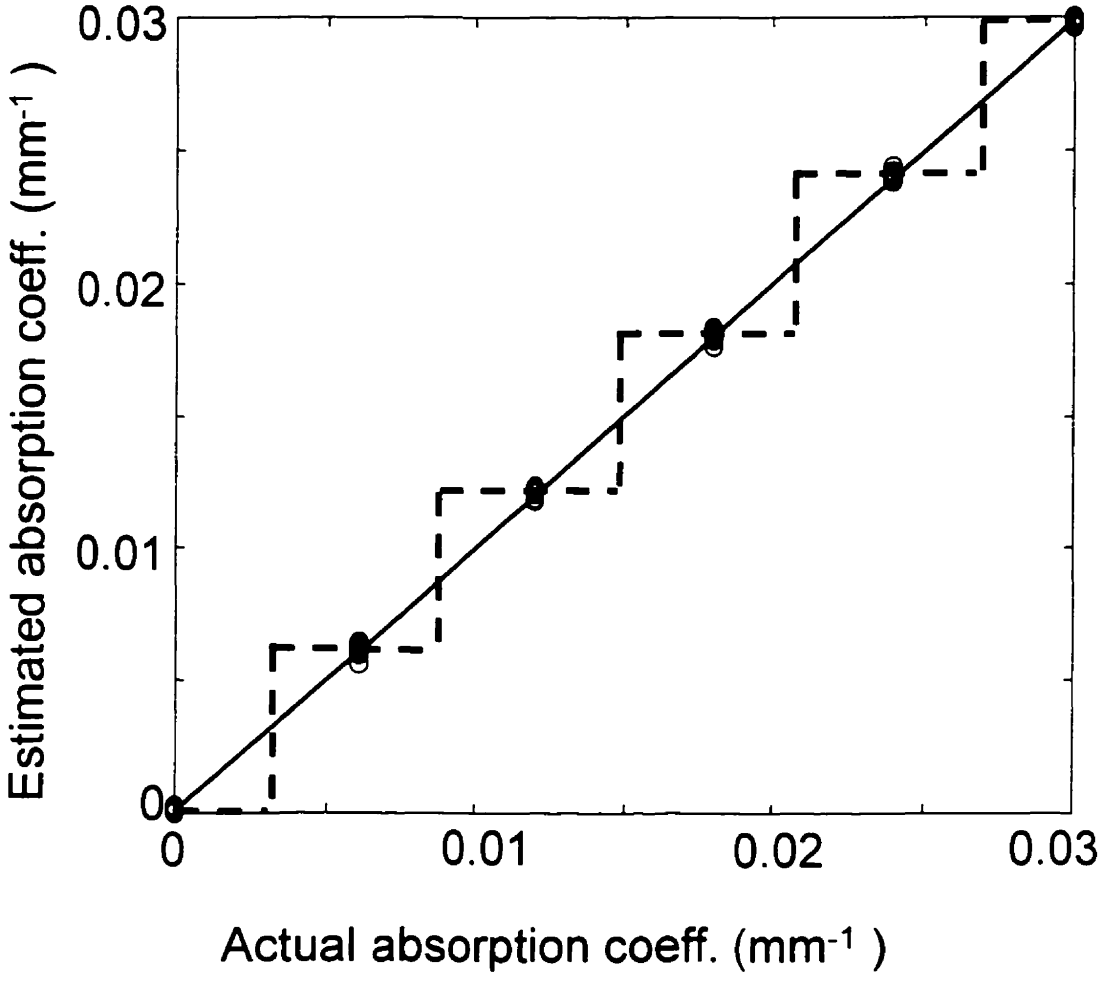

Figure 5.4. Pictorial diagram of linear versus classification based calibration.

5.4.3 HCKNN reconstruction method

The HCKNN method operates in a similar manner to the HLRB technique except that no linear regression models are constructed from the optimal time/position channels. Instead, the optimal data channels of the local weighted calibration set are decomposed into their principal components. Similarly, corresponding time/position channels of each member in the validation set are projected into the same principal component space for comparison to the calibration set. Absorption levels are determined by *k*-nearest neighbour (KNN) classification analysis. The KNN technique finds the *k* spatially closest neighbours in calibration set and determines which group a test point belongs. Once the algorithm decides on the closest absorption level, the method is applied again in each region for all validation set members. In both the HLRB and HCKNN approaches to sample reconstruction, the methods seek to identify those samples in the calibration set which closely match the absorption properties above the one of interest for each member of the validation set in order to optimize the calibration.

5.5 Results and Discussion

5.5.1 SMLR reconstruction results

As an initial approach to tomographic reconstruction, the SMLR approach was used. For all depth regions in the sample five time/position data channels were determined to be optimal. Considering only the sample surface layer, region 1 (0 – 1 mm), the selected times and positions are centered around the peak maxima of the

detected time distributions recorded at small lateral source/detector separations. For a deep region, i.e. region 5 (4 – 5 mm), longer times in distributions recorded at large lateral source/detector separations were chosen. These trends are consistent with observations in previous work with layered scattering/absorbing systems.[10]

Reconstruction results using SMLR for the uppermost five regions in the sample are summarized in Table 5.1. Errors in the reconstruction are listed both as coefficients of variation (%) and in absolute units of mm^{-1}. These values quantify the error between the actual and estimated absorption coefficients. A third quantity, the classification rate, is the percentage of samples with correctly classified absorption levels in each region. Results indicate that absorption coefficient may be estimated to within 1% of the actual value in region 1. A 100% accuracy is obtained if the estimated absorption coefficients are categorized into six discrete levels. When the SMLR technique is applied to deeper layers the error in the estimate increases to 32% in region 5. This translates into only 30.5% of samples being classified with the correct absorption level. The large amount of error is not surprising due to the way light traverses from source to detector. The reconstruction problem becomes ill-conditioned since light detected from the deeper regions of the sample must always travel through the upper regions at least twice. To reduce ambiguities in the reconstruction, a more directed approach may be useful.

Table 5.1. SMLR reconstruction results with time resolved data.

	Region 1	Region 2	Region 3	Region 4	Region 5
Coeff. of Variation (%)	0.8	13.4	20.9	22.1	32.0
Standard Error (mm^{-1})	0.0002	0.0018	0.0031	0.0033	0.0048
Classification Rate (%)	100.0	66.7	58.3	47.2	30.5

5.5.2 HLRB reconstruction results

The HLRB method was used to provide an enhanced means of linear calibration for each sample region. Using absorption coefficient estimates in upper regions, a better linear calibration may be obtained by eliminating samples from the calibration set which strongly ill-condition the model. The locally weighted calibration selects only those samples with absorption coefficients in the upper layers which best resemble those estimated in a given validation sample. For each sample region, similar sections of the data vector were chosen when compared to those determined using the SMLR approach. A 12% improvement in the classification rate in region 2 (1 – 2 mm depth) was found with the HLRB method as shown in Table 5.2.

Table 5.2. Comparison of SMLR, HLRB, and HLKNN reconstruction results listed as the percentage of samples correctly classified.

	Region 1	Region 2	Region 3	Region 4	Region 5
SMLR	100.0	66.7	58.3	47.2	30.5
HLRB	100.0	74.2	63.1	51.8	34.3
HCKNN	100.0	85.6	77.3	64.8	53.2

However, no significant improvements are seen in regions 3 to 5. Integral to absorption coefficient estimations of a sample region is the development of the calibration set. The importance of this was determined by excluding 10% of the calibration data for region 4. When this was done, is was found that the classification rate dropped on average from 51.8 % to 44.1%. It is clear that the results are not independent of the number of calibration points. This is supported by previous work where the number of calibration samples necessary to improve classification dramatically increases.[13]

5.5.3 HCKNN reconstruction results

Building on the calibration concept used in HLRB, KNN classification analysis was used for discrete estimates of the absorption coefficients. As the HCKNN method does not use linear models, better classification rates should be achieved. As a first step, the optimal time/position data channels selected from locally weighted calibration set were decomposed into their principal components. In all cases, three principal components, capturing ~98% of the data variance, were retained. Corresponding validation set data was projected onto each of the principal components. Figure 5.5 shows a plot of the first two principal components of the optimal calibration data for absorption estimates in region 1. A linear relationship between the absorption coefficient and principal component 1 is clearly seen. However when a similar analysis is made using optimal calibration data for absorption estimates in region 2, a non-linear trend is observed as shown in Figure 5.6. Calibration set members having the same absorption coefficient in region 2 are nevertheless clustered together. A k-nearest neighbour classification algorithm with $k = 1$, applied to members of the validation set for each region yielded much improved classification rates. As shown in Table 5.2, a 20% improvement in the classification rate is observed for all regions using the HCKNN method compared with SMLR. Likewise, estimations of the absorption coefficient deep within a highly scattering/absorbing sample are obtainable at greater than 50% accuracy.

Three representative images of reconstructed samples determined by the HCKNN technique are shown by the dashed lines in Figure 5.7. In general, improved absorption estimates in the vicinity of discontinuous boundaries between different absorbing regions were found in comparing corresponding SMLR reconstructions (dotted lines). The broad

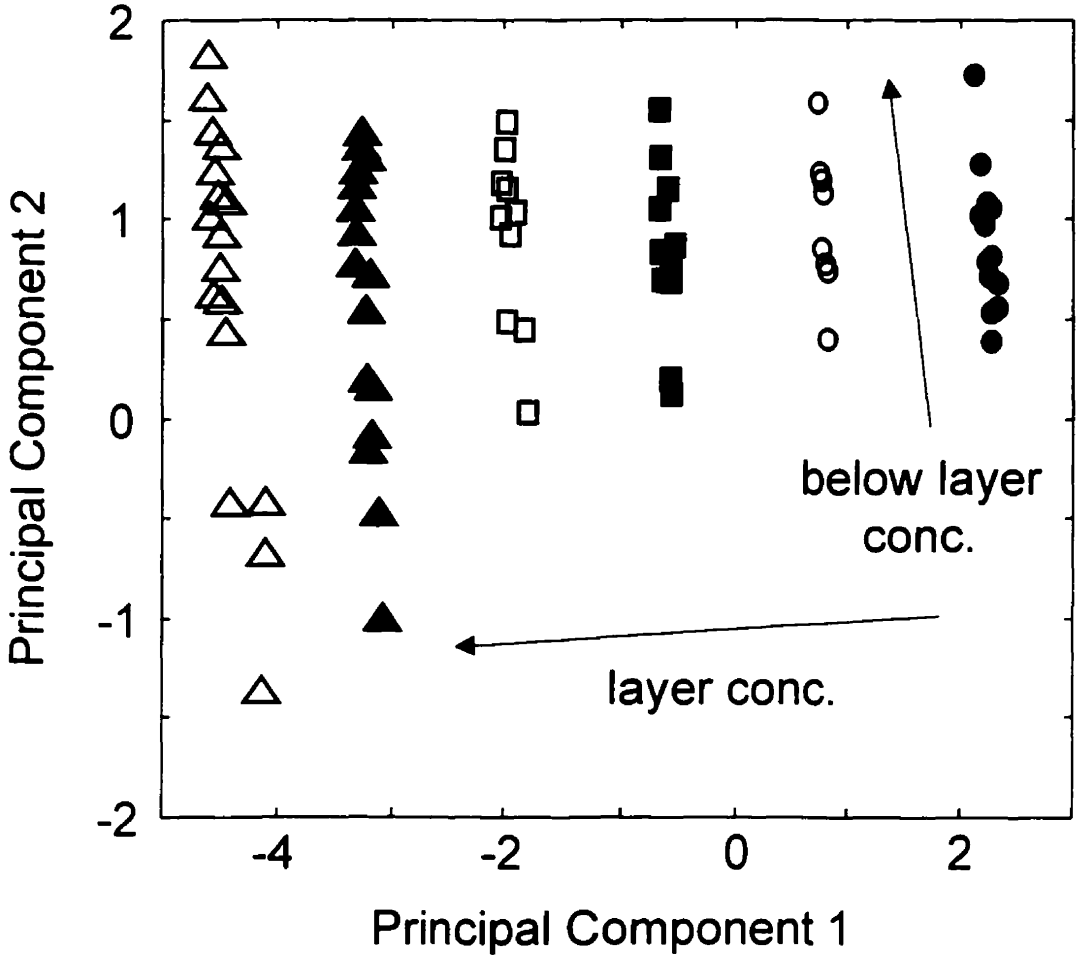

Figure 5.5. Principal component analysis of region 1. Absorption coefficient legend: 0.000 mm^{-1}, open circles; 0.006 mm^{-1}, solid circles; 0.012 mm^{-1}, open squares; 0.018 mm^{-1}, solid squares; 0.024 mm^{-1}, open triangles; 0.030 mm^{-1}, solid triangles.

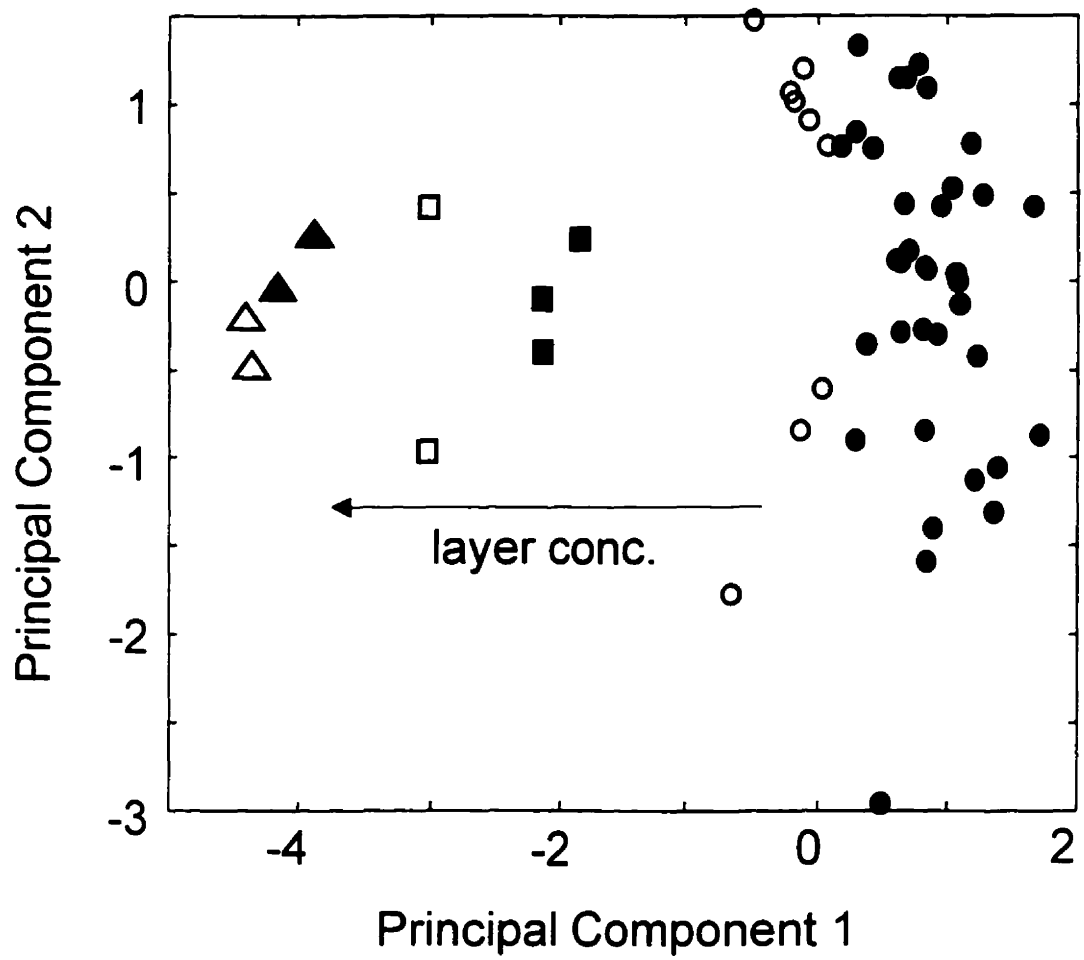

Figure 5.6. Principal component analysis of region 2. Absorption coefficient legend: 0.000 mm^{-1}, open circles; 0.006 mm^{-1}, solid circles; 0.012 mm^{-1}, open squares; 0.018 mm^{-1}, solid squares; 0.024 mm^{-1}, open triangles; 0.030 mm^{-1}, solid triangles.

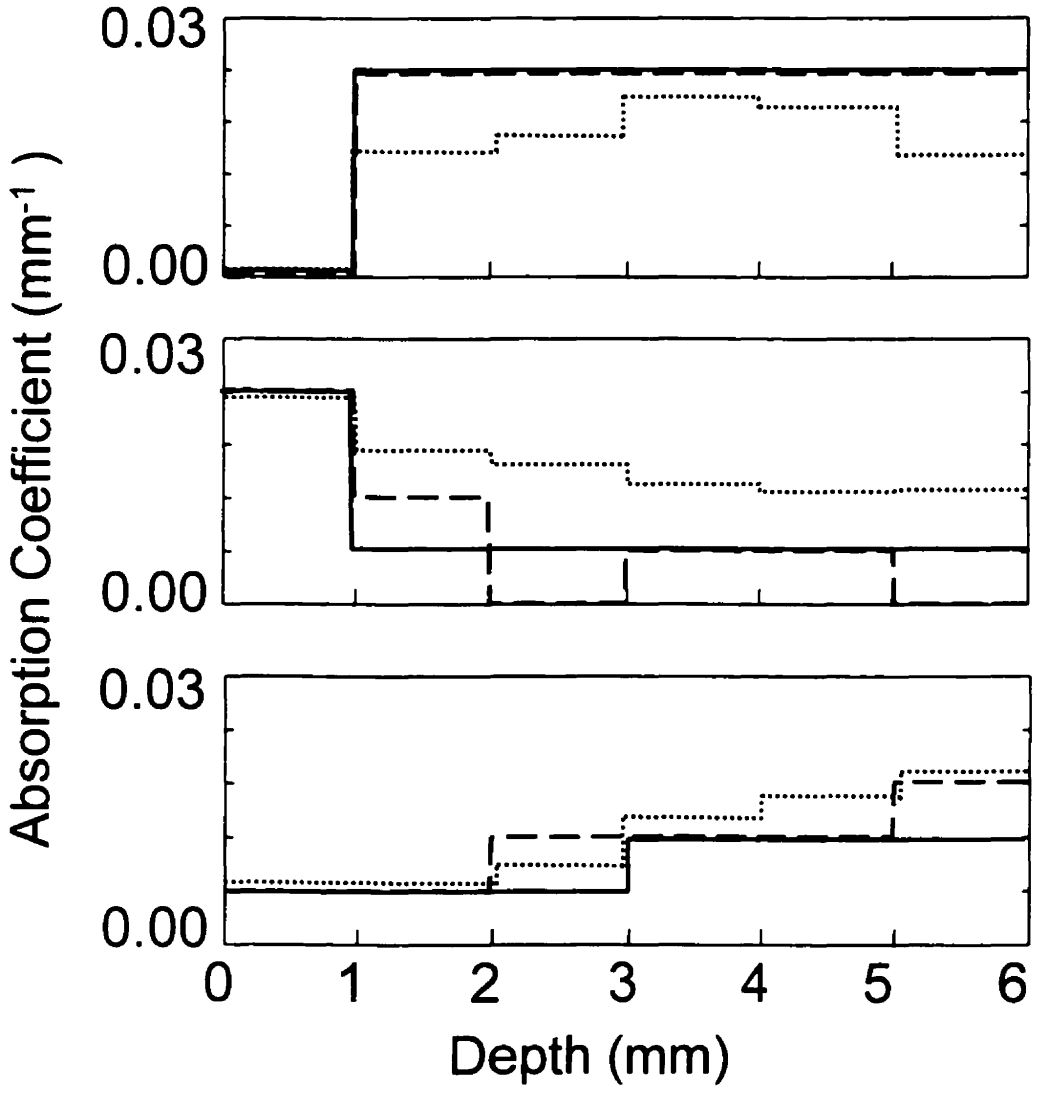

Figure 5.7. Images of reconstructed samples as determined by the HCKNN technique (dashed lines) and SMLR (dotted lines). Solid lines represent actual composition.

sloping changes produced with the SMLR are 'sharpened' when the HCKNN approach was applied. Reconstructions of samples containing regions with a constant absorption coefficient produced images which were within one absorption level of the actual value. This classification based technique markedly improves reconstruction accuracies over linear methods which tend to produce blurred images in highly scattering media.

5.5.4 Effect of noise on the reconstructions

To investigate the effect of noise on tomographic reconstruction, 0.0%, 0.5% and 1.0% RMS Gaussian noise was added to the validation set data. Table 5.3 shows reconstruction results as a percentage of samples correctly classified for each reconstruction method in regions 1, 2 and 5. In general, absorption coefficient estimates were good in region 1 for all methods even with the addition of 1% noise. However, classification rates in region 5 with 1% noise were decreased by half. The rate (~20%) corresponds approximately to what would be obtained by choosing one of the six absorption levels at random. The results are not surprising as the subtle shapes in the time-profile which contain information about sample sub-surface regions are obscured by noise. Considering absorption classification rates in region 2, the SMLR method performed very poorly in the presence of noise. In contrast, classification rates were better with the HCKNN technique. This is to be expected due to the nature of the KNN classification method which provides robust classification in the presence of noise.

Table 5.3. Comparison of the reconstruction methods in the presence of added noise listed as the percentage of samples correctly classified.

	% Noise Added	Region 1	Region 2	Region 5
SMLR	0.0	100 ± 0	67 ± 0	31 ± 0
	0.5	99 ± 1	42 ± 4	22 ± 3
	1.0	96 ± 1	28 ± 4	18 ± 5
HLRB	0.0	100 ± 0	74 ± 0	34 ± 0
	0.5	99 ± 1	48 ± 3	21 ± 3
	1.0	96 ± 1	46 ± 4	17 ± 5
HCKNN	0.0	100 ± 0	86 ± 0	53 ± 0
	0.5	95 ± 1	77 ± 3	37 ± 3
	1.0	93 ± 1	69 ± 4	23 ± 4

5.6 Conclusion

In this study, three chemometric approaches for depth-resolved quantification in scattering/absorbing media have been investigated. Stepwise multilinear regression (SMLR), a hierarchical locally weighted SMLR calibration followed by a linear regressive estimation and binning (HLRB), and a hierarchical locally weighted calibration followed by K-nearest neighbour classification analysis (HCKNN) were used in the analysis of photon time-of-flight measurements of layered samples with discretely variable composition. With these methods, the tomographic reconstruction problem is linearized by utilizing *a priori* information about sample composition in upper regions to direct subsequent locally weighted calibrations for lower regions. Results indicate that the HLRB method demonstrates an 8% improvement in the classification rate of the absorption coefficient for a region 1-2 mm below the surface of a sample compared to stepwise multilinear regression (SMLR). However no improvement was seen for deep regions where only 34% of the samples' absorption coefficients were correctly classified.

Using the HCKNN reconstruction method, a 20% improvement in the classification rate was observed for all regions compared to SMLR. Estimations of the absorption coefficient deep within a highly scattering/absorbing sample were obtainable at greater than 50% accuracy. In addition, the HCKNN technique performed better than the other methods in the presence of 1.0% RMS noise added to the validation set time-profiles. These encouraging results may be attributed in part to the *k*-nearest neighbour classification method integral to the HCKNN technique. The non-parametric KNN method provides robust classification both in the presence of noise and with few calibration points. This is especially important for absorption coefficient estimation deep within a sample where only subtle changes in the time-of-flight distribution are present. The combination of locally weighted calibrations and classification techniques to constrain the solution of a tomographic reconstruction provide a powerful new tool for quantification in layered scattering/absorbing media.

5.7 References

1. Dahm, D. J.; Dahm, K. D. Representative Layer Theory for Diffuse Reflectance; *Appl. Spectros.* **1999**, *53*, 647-654.
2. Cui, W.; Kumar C.; Chance, B. Experimental Study of Migration Depth for the Photons Measured at Sample Surface; *Proc. SPIE* **1991**, *1431*,180-191.
3. Brown, C. S.; Burns, D. H.; Spelman, F. A.; Nelson, A. C. Computed Tomography from Optical Projections for Three-Dimensional Reconstruction of Thick Objects; *Appl. Opt.* **1992**, *31*, 6247 6254.
4. Patterson, M. S.; Chance, B.; Wilson, B. C. Time Resolved Reflectance and Transmittance for the Non-invasive Measurement of Tissue Optical Properties; *Appl. Opt.* **1989**, *28*, 2331-2336.
5. Polishchuk, A. Y.; Dolne, J.; Liu, F.; Alfano, R. R. Average and Most-Probable Photon Paths in Random Media; *Opt. Lett.* **1997**, *22*, 430-432.
6. Kienle, A.; Patterson, M. S.; Dognitz, N.; Bays, R.; Wagnieres G.; van den Burgh, N. Noninvasive Determination of the Optical Properties of Two-Layered Turbid Media; *Appl. Opt.* **1998**, *37*, 779-791.
7. Chang, J.; Graber, H. L.; Barbour, R. L. *OSA Proceedings On Advances in Optical Imaging and Photon Migration*; Alfano, R. R., Ed.; OSA: New York, 1994; Vol 21, pp 193-220.
8. Dayan, I.; Havlin, S.; Weiss, G. H. Photon Migration in a Two-Layer Turbid Medium; *J. Mod. Opt.* **1992**, *39*, 1567-1582.
9. Hielsher, A. H.; Lui, H.; Chance, B.; Tittel, F. K.; Jacques, S. L. Time-Resolved Photon Emission from Layered Turbid Media; *Appl. Opt.* **1996**, *35*, 719-728.

10. Long, W. F.; Burns, D. H. Optical Tomography in Scattering Media from Photon Time-of-Flight Diffuse Reflectance Measurements: A Chemometric Approach; *J. Chemom.* **1999**, *13*, 251-264.

11. Leonardi, L.; Burns, D. H. Quantitative Constituent Measurements in Scattering Media from Statistical Analysis of Photon Time-of-Flight Distributions; *Anal. Chim. Acta* **1997**, *348*, 543-551.

12. Naes, T.; Isaksson, T.; Kowalski, B. Locally Weighted Regression and Scatter Correction for Near-Infrared Reflectance Data; *Anal. Chem.* **1990**, *62*, 64-673.

13. Breiman, L.; Friedman, J.; Olshen, R. A.; Stone, C. J. *Classification and Regression Trees*; Wadsworth: New York, 1984.

14. Small, E. W. Laser Sources and Microchannel Plate Detectors for Pulse Fluorometry; In *Topics in Fluorescence Spectroscopy;* Lakowicz, J. R., Ed.; Plenum Press: New York, 1991, Vol. 1.

Chapter 6 Quantification in Highly Scattering/ Absorbing Layered Samples using Photon Time-of-Flight Measurements and Confocal Optical Geometry

In Chapter 5, *a priori* information about sample composition was employed to improve quantification in layered specimens. In each of the previous chapters, quantification was done using the properties of the diffusely reflected detected light. Depth-resolved measurements in layered samples were possible, in part, by varying the detector position relative to the source. However, as discussed in Chapter 1, many approaches to optical imaging in scattering media employ ballistic light. In this chapter, spatial filtering of the backscattered light is investigated in order to enhance the detection of light which follows a geometric path through the sample.

Beginning in the 1970s, confocal optical systems have revolutionized the microscopy of living systems. In a confocal optical approach to imaging, a precise volumetric region in a specimen may be probed. Typically, confocal optics are employed for making luminescence measurements in minimally scattering samples. In specimens which can not be made to luminesce, transmission or reflection measurements are made. The application of confocal illumination and light collection optics for quantitative analysis in highly scattering media to date, has not been thoroughly investigated. Since the path that light takes though a scattering system is not clearly defined, it is unclear as to the potential of confocal imaging in the presence of scatterers.

One of the goals in this chapter is to gain a better understanding of the advantages and limitations of confocal optical geometry for quantification, in dense scattering media.

The information gained in this study will aid in the design of optimal illumination and detection geometries which maximize the information from absorbing constituents deep within a specimen. In addition, information concerning the use of confocal optics for quantification in highly scattering media is important in the fields of optical microscopy and spectroscopy.

6.1 Abstract

A method for depth-resolved quantification in layered scattering/absorbing samples is described. Confocal optical geometry was used in conjunction with time gated detection for non-invasive quantification of subsurface absorbing constituents. For analysis, the time-resolved remittance intensities from a series of layered absorbing samples were ratioed to that of a similar, non-absorbing specimen. Using this approach, absorbance information sensitive to changing sample composition was obtained. The effect of confocal optical geometry focussing on depth resolved quantification was characterized using different portions of the time profile. In addition, imaging performance is assessed with varying focal depth, numerical aperture and effective pinhole size. Results indicate that the effect of multiple scattering on the detected signal may be reduced by using a larger numerical aperture objective and small effective pinhole size. Also, the sample absorbance was found to be more linear over a wider concentration range when compared with a large pinhole. When time information was included, the initial rising portion of the time profile was found to enhance sample absorbance linearity when a large pinhole is used. However little enhancement was observed when the imaging pinhole size was small. Similar effects were seen at each

focal depth in the sample. This finding suggests that although including time information may be beneficial, it is not needed when confocal light collection is employed in the analysis of macroscopic scattering samples.

6.2 Introduction

Depth resolved quantification in highly scattering media is an active area of research because of its relevance to the analysis of many biological and industrial samples. Examples include, sub-surface vibrational spectroscopy of coatings and thin films, diagnostic medical imaging of tumors, and remote hyperspectral imaging of geographical features. For remote sensing applications such as synthetic aperture infrared imaging, new tools are necessary to reduce the effects of atmospheric scattering.[1] In the laboratory, however, two approaches for optical assessment of complex, scattering samples are typically used: diffuse reflectance/transmission measurements and microscopic imaging.

In a classical diffuse reflectance measurement, the incident source and detector are separated by some distance. This distance may need to be large so that the sensitivity of a measurement to an analyte deep within a specimen may be maximized.[2] This large source/detector separation however, tends to favour the detection of light which has undergone many scattering events. Unfortunately, the presence of a highly scattered light component in the signal creates problems for sample quantification. A significant amount of research has been done to reduce the highly scattered component of light.[3,4] Typically, time resolved measurements are used as a means to discriminate between those photons which have taken the shortest path toward the detector (ballistic photons),

and those which have taken longer, more random paths. By retaining only the initial rising portion of the photon time-of-flight distribution, the light path between the source and detector may be more clearly defined. Using this approach, the effects of scattering on the measurement may reduced.

The effect of optical illumination and light collection geometry is not well understood for the analysis of highly scattering media. One approach for analyzing such materials is with the use of reflectance confocal optics. Confocal optical illumination and detection offers the advantage over other imaging methods in scattering media in that multiply scattered light arising out of the focal plane may be rejected. However in highly scattering samples where the mean free path (MFP) between scattering events is <100 μm, a significant portion of the detected signal may be due to highly scattered light. As a consequence, many imaging applications using confocal optics are made on microscopic samples where the thickness is on the same order as the optical mean free path.[6-8] If measurements are extended into thicker samples, it has shown that image contrast is poor.[9-11]

Recently, it has been shown that by combining time-gating methods with confocal light collection, enhancements in spatial resolution in the axial direction may be made.[12] It has been demonstrated that confocal optics in combination with time gating provide two mechanisms for selecting light from the in-focus layer: the time-gate and the pinhole spatial filter.[12,13] Although this dual approach to photon discrimination has been employed for microscopic analysis, it has not been widely applied in highly scattering macroscopic systems. It has been suggested that when imaging in turbid media, 3 to 9 MFPs through the sample represent the limit to which diffraction limited confocal

imaging may be done.[9] However, this limit is strongly dependent on the object size as seen at the detector. This may be adjusted by varying the pinhole diameter. Typically, a fairly large pinhole is used when imaging deep into a scattering sample so that enough backscattered light from the sample volume of interest may be collected.[10] When such a large spot in the object plane is imaged, the resolution and maximum image contrast range are diminished.[9,10] Although the pinhole size is critical for diffraction limited imaging of microscopic samples, it is not known how it may affect quantification of regions within macroscopic objects. A relaxation of strict image quality criteria may therefore extend confocal illumination and light detection in the analysis of macroscopic specimens.

In this study the goal is to examine the relationship of photon path with optical detection geometry for quantification of absorbing constituents in layered paper samples. The effect of numerical aperture on the time profile is investigated to provide optimal imaging conditions. Measurements made over a range of effective pinhole sizes, υ_p, are used to demonstrate the effect of multiple scattering on depth discrimination. In addition, the efficacy of using time resolved measurements with confocal detection on sample quantification is investigated.

6.3 Experimental

6.3.1 Confocal photon time-of-flight instrumentation

The scanning mirror/slit confocal microscope for this experiment utilizes a divided aperture and slit illumination as shown in Figure 6.1. The geometry of the system

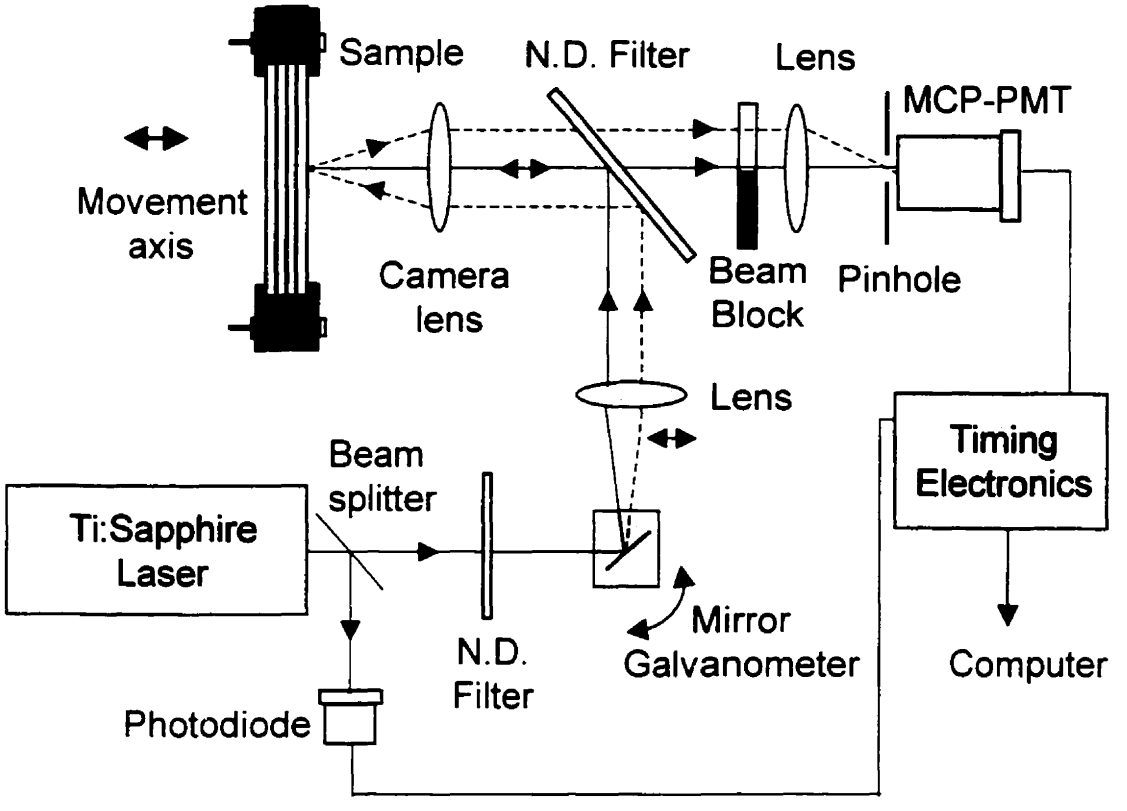

Figure 6.1. Schematic diagram of the scanning slit confocal reflectance photon time-of-flight instrument.

is a variant of a similar microscope developed by Koester.[14] At the core of the system is a time-correlated, single photon instrument similar to devices found in fluorescence life-time studies.[15] Specific details of the hardware used has been discussed previously.[16] In general, a mode-locked Ti:Sapphire laser pumped by an argon ion laser was used to produce 780 nm laser pulses with a full width of 170 fs. The output beam was split by a beamsplitter after which 4% of the light was focussed onto a fast photodiode. The remaining portion of the light was attenuated by a neutral density filter before being directed toward the sample. With the use of a controlled mirror galvanometer, the beam was rapidly swept back in forth in the saggital plane of a camera lens (Fujinon TV 1:0.85 /25, Fuji Corp., Japan) and focussed into the sample. This lens was used because of the particularly long working distance (7 mm). By changing the oscillation amplitude of the mirror galvanometer, the effective numerical aperture of the light of the illumination optics was controlled. The range of possible numerical apertures spanned from 0.07 (zero beam deflection) to 0.25 (beam deflection equal to the half of the camera lens diameter). The focal depth of light incident on the sample was controlled by moving the sample on a micrometer stage. The focal depth could be adjusted from 0 to 4 mm. For the detection optics, the numerical aperture was fixed at 0.25.

The light pulse reflected back from the sample was focussed with a half-covered lens onto a pinhole of a specific diameter before entering a cooled microchannel plate photomultiplier tube (MCP). Output from the photodiode and MCP were each connected to a separate constant fraction discriminators (CFD). Logic pulses from the CFDs were sent into time-to-amplitude converter (TAC). The output of the TAC was a DC voltage

proportional to the time difference between the two logic pulses. The signals were digitized into 4.9 ps time windows and binned in a computer.

Absorbing paper samples were made by soaking individual sheets of Whatman #1 filter paper in an aqueous dye solution (Dr. Ph. Marten's Transparent Water Color #33 Black, Hollywood, FL) for 20 seconds followed by air drying. One millimeter stacks of dyed filter paper were glued so that the illuminated portion of the sample was free from adhesives. The paper stacks were calculated to have corresponding absorption coefficients, μ_a, of 0.000, 0.006, 0.018 and 0.030 mm^{-1} referenced to the stock paper. The absorption coefficient, μ_a arises from the Beer-Lambert relation ($A = \varepsilon cl$) as a combination of the concentration (c) and molar absorptivity (ε) terms. Each sample had a specific dye concentration profile was comprised of four paper stacks pressed together forming a 4 mm thick specimen.

6.3.2 Measurements

Time distributions were recorded with the light focussed into the sample at seven different focal depths ranging from 0.5 mm to 3.5 mm in 0.5 mm intervals. Each acquisition required three minutes. Replicate time profile measurements were made on all samples. In addition, time profiles were recorded with a mirror positioned in the focal plane in the absence of a sample (blank). All time profiles were then shifted such that they had a common rising edge with the blank. This minimized the effect of temporal jitter in the time distributions and allowed for comparison between samples. The time profiles were smoothed using a Gaussian window (σ = 25 ps) to reduce the high frequency periodic noise due to the timing electronics.

Four series of measurements were made using the above procedure. The purpose of the first series of measurements was to study the effect of the numerical aperture on the width of the time-distribution. For this series, sample 4 (see Table 6.1) was analyzed using five different numerical apertures: 0.03, 0.12, 0.15, 0.18 and 0.24. The pinhole diameter was fixed at 1000 μm.

Table 6.1. Absorption coefficient profiles of samples analyzed in confocal study.

Sample*	0 – 1 mm	1 – 2 mm	2 – 3 mm	3 – 4 mm
1	0**	0	0	0
2	3	3	3	3
3	0	3	3	3
4	0	0	3	3
5	0	0	0	3
6	3	0	0	0
7	0	3	0	0
8	0	1	2	3
9	3	2	1	0

*Replicate samples 10 – 18 have the same composition as 1 – 9.
**Absorption coefficients (0) 0.000 mm^{-1}; (1) 0.006 mm^{-1}; (2) 0.018 mm^{-1}; (3) 0.030 mm^{-1}.

To study the effect of the pinhole size on the time-of-flight distribution, three other series of measurements were made by varying the pinhole diameter. For comparative purposes, the effective pinhole diameter in optical units is used. It is defined as $\upsilon_p = \pi d_p a/\lambda f$ where d_p is the physical diameter of the pinhole, a and f are the radius and focal length of the lens focussing onto the pinhole and λ is the wavelength of the light. The numerical aperture was fixed at an optimal value of 0.15. Three different pinhole sizes were used: 100 μm, 1000μm and 2500 μm. These sizes correspond to υ_p's of 12, 125 and 300 which are much greater than 1, the value typically required for true

diffraction limited confocal optical light collection.[9] A total of nine samples of specific dye concentration profiles, shown in Table 6.1, were analyzed. The profiles ranged from completely uniform to one with four different contiguous absorbing regions.

6.4 Data Analysis and Quantitative Image Reconstruction

For each time-of-flight profile recorded at a given focal depth, the time of the peak maximum (t_{max}) and the peak standard deviation were calculated along with measures of the sample's relative absorbance. Both partial and full temporally integrated absorbances were calculated. The fully integrated absorbance given in Equation 6.1 follows from the classical Beer-Lambert law,

$$A_{\exp}(z,t) = -\log\left(\int_0^t R_z(\tau)d\tau \Big/ \int_0^t R_{0,z}(\tau)d\tau\right) \tag{6.1}$$

where $t = \infty$, and $R_z(t)$ and $R_{0,z}(t)$ are the time distributions of the test and reference samples respectively. The steady state absorbance at a given focal depth, z was measured relative to a sample with no absorber present (sample 1). This technique is widely used when the relative absorbance difference between two similar samples is required.[17] In a similar manner, the partial temporally integrated absorbance $A_{exp}(z,t)$, was calculated by integrating to a cutoff time, t. If the cutoff time is close to the shortest time-of-flight through the sample, the absorbance quantity $A_{exp}(z,t)$ excludes the scattered light which does not travel along a geometric path from source to detector.[17]

In addition to experimental absorbance values, theoretical steady state sample absorbances, $A_{theo}(z,\infty)$, were computed at each focal depth. For this calculation, it was assumed that the detected light followed an oblique geometric path through the sample to

the focal point and was reflected back. Although not all of the detected light from a scattering sample would follow such a path, this quantity is useful for making comparisons. The theoretical absorbance can be given as,

$$A_{theo}(z,\infty) \approx \frac{2}{\cos\bar{\theta}} \int_0^z \mu_a(z)dz \tag{6.2}$$

where $\mu_a(z)$ is the absorption coefficient profile as a function of depth, z. The cosine factor is needed because the light obliquely enters and exits the sample at an average angle θ. The factor of 2 is necessary because the light reflected back to the detector must traverse twice the focal depth.

Equation 6.2 may also be used for depth resolved sample quantification. By differentiating Equation 6.2 with respect to depth and rearranging, the absorption coefficient profile as a function of depth may be written as,

$$\mu_a(z) = \frac{\cos\bar{\theta}}{2} \frac{\partial}{\partial z} A_{\exp}(z,t) \approx \frac{\cos\bar{\theta}}{2\Delta z} \left[A_{\exp}(z_{i+1},t) - A_{\exp}(z_i,t) \right] \tag{6.3}$$

where t is either t_{max} or the cutoff time and i is the ith measurement made along the z axis. Equation 6.3, however, only provides a relative measure of $\mu_a(z)$, because one degree of freedom is gained with the differentiation of Equation 6.2. Since the constant offset value is not known *a priori*, all measures of $\mu_a(z)$ may be simply shifted such that $\mu_a(0.5) = 0$ where the first measurement was taken.

6.5 Results and Discussion

6.5.1 Determination of the optimal numerical aperture

Initially, measurements were made to determine the best numerical aperture for focussing light on a sample. Photon time-of-flight distributions were recorded at seven focal depths over a range of numerical apertures. This range spanned from ~0.07 with a collimated incident 1 mm beam to 0.24. The numerical aperture was controlled by changing the oscillation amplitude of the mirror galvanometer. Although higher numerical apertures were possible, the quality of focal point was degraded due to aberrations from the camera lens. In addition, unavoidable reflections from other optical components interfered with the image formed at the detector. The effect of numerical aperture on the time distribution is shown in Figure 6.2. To facilitate comparison, the time profiles have been normalized to the same height. With the lowest NA, the time distribution is quite broad in comparison to profiles collected at higher numerical apertures. The large width suggests that the detected light has been highly scattered. This result is not surprising because at such a low NA, the light is essentially unfocussed on the sample. For a NA of 0.15 however, the time distribution is skewed toward shorter times containing a significant portion of geometric photons. These photons have undergone few scattering events and more likely have penetrated to the apparent focal point. If higher numerical apertures are used, the time distribution broadens again, due to aberrations in the camera lens. The effect of numerical aperture on the time distribution may be further demonstrated by plotting the standard deviation of the time distribution as a function of numerical aperture as shown in Figure 6.3. The solid line for the scattering sample demonstrates that the optimal numerical aperture is centered around 0.15 when

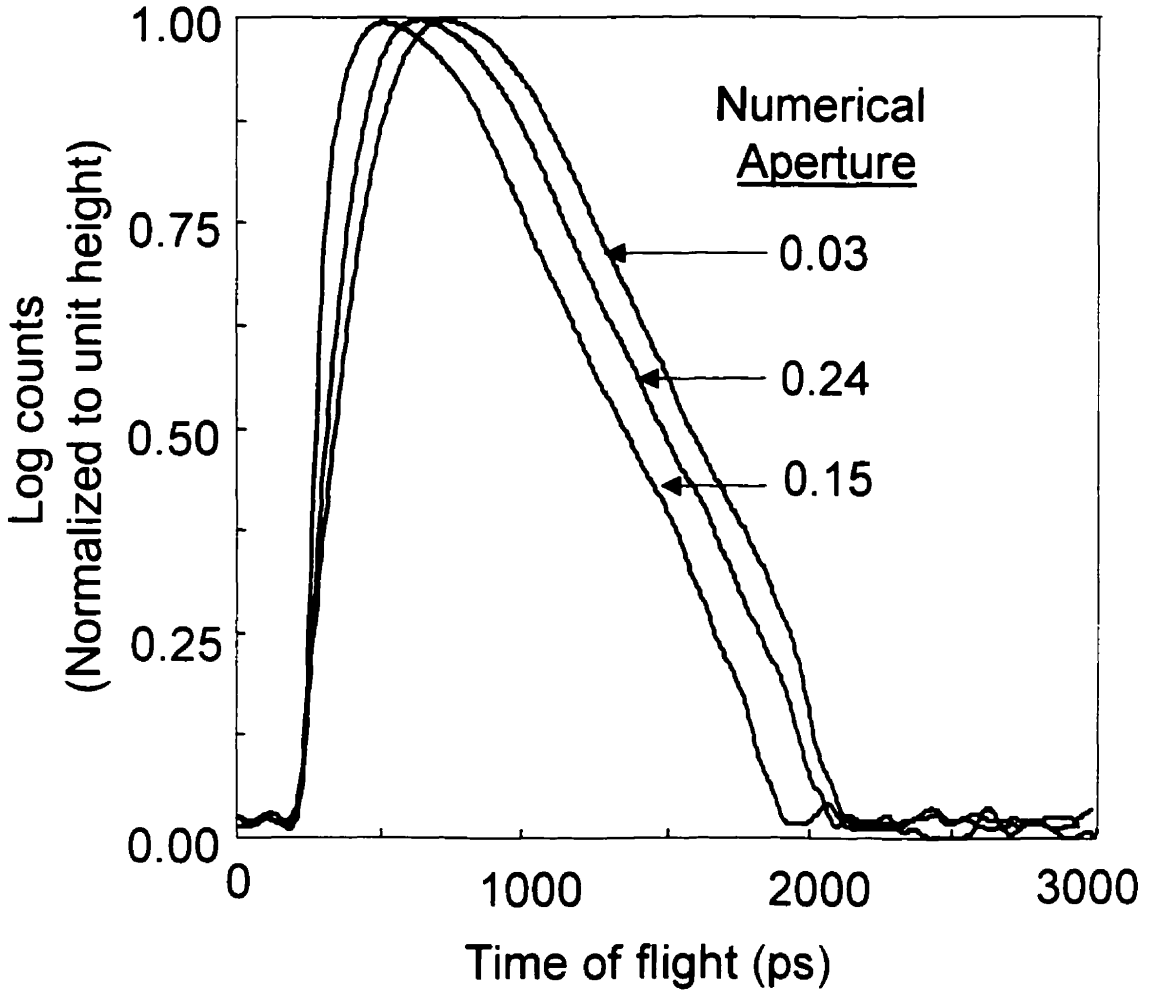

Figure 6.2. Normalized time profiles of a scattering sample recorded at a focal depth of 2.5 mm as a function of numerical aperture.

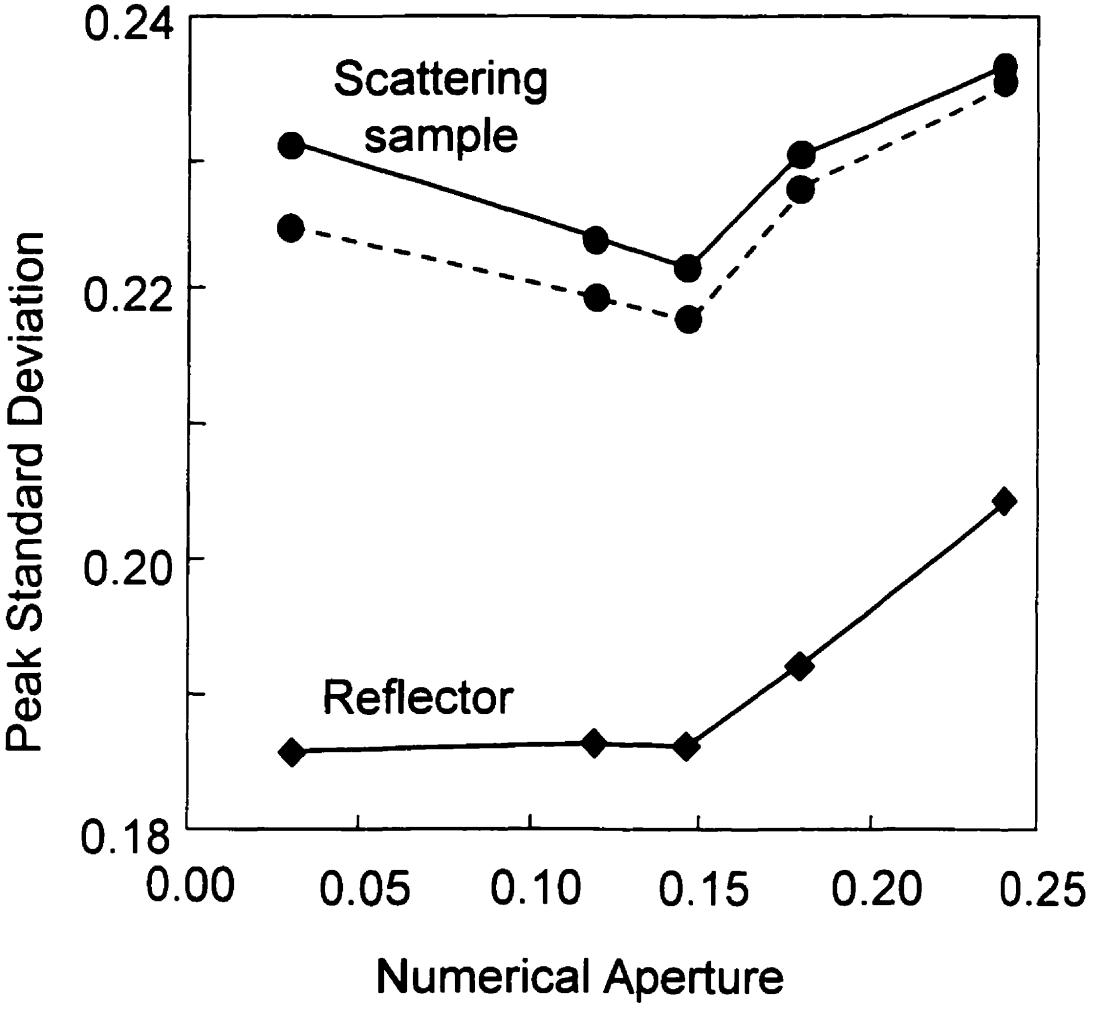

Figure 6.3. Effect of numerical aperture on the time profile peak standard deviation for a scattering sample and a blank (reflector). Solid line: 3.0 mm focal depth into sample. Dashed line: 2.0 mm focal depth into sample.

the focal depth is 3 mm. A similar trend is shown by the dashed line when the focal depth into the scattering sample was decreased. In addition, it is seen that as the focal depth is decreased, the peak widths also decrease. This is due to a greater proportion of shorter pathlength geometric photons being detected. When a similar plot is made using data taken from measurements of a reflector (blank), it becomes clear that optical aberrations or reflections are responsible for peak broadening at higher numerical apertures. A numerical aperture of 0.15 was therefore chosen as optimal even though higher NAs may further enhance optical sectioning in the sample.

6.5.2 Effect of effective pinhole size on absorbance linearity

A series of sample measurements were made to assess the effect of the pinhole size, υ_p at the detector on both the photon time-of-flight profiles and sample absorbance linearity. The value of υ_p was controlled by varying the pinhole diameter. Three pinholes were used: 2500 μm (υ_p ~300), 1000 μm (υ_p ~125) and 100 μm (υ_p ~12).

Results shown in Figure 6.4 demonstrate the effect of varying υ_p on the width of the time distribution. This figure, produced by differencing a time-of-flight distribution of a scattering sample and the blank, gives a relative measure of the scattering in the sample. Figure 6.4 demonstrates that as the effective pinhole size is increased, more scattered light is detected. This trend is expected as fewer longer pathlength photons which have undergone multiple scattering are blocked.

To illustrate how changes in sample composition affect the time-of-flight distribution, two samples are compared in Figure 6.5. Samples 1 (solid lines) and 3 (dashed lines) have similar time profiles at a focal depth of 0.5 mm. This is expected

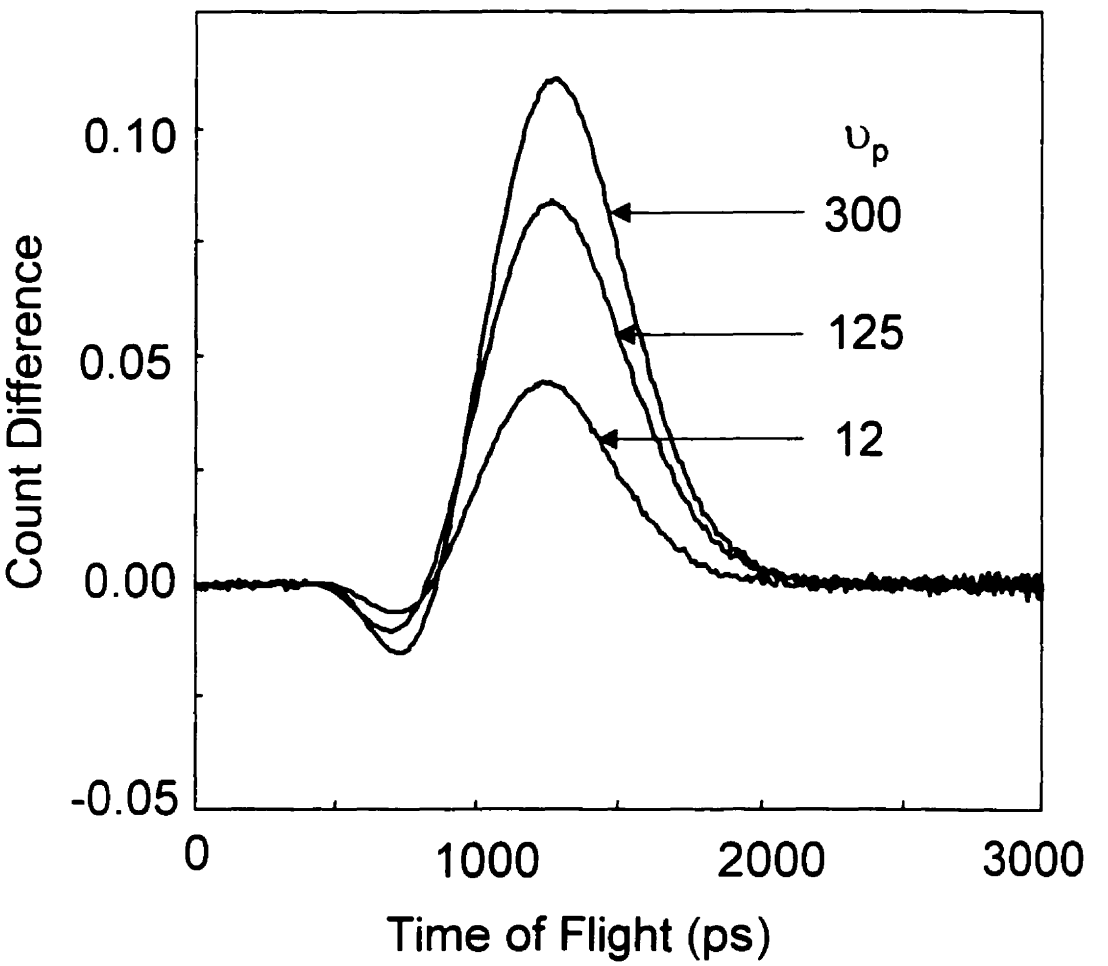

Figure 6.4. Difference between a time profile of a blank and a time profile of a scattering sample recorded at a focal depth of 3.0 mm. Each profile was normalized to unit height before subtraction.

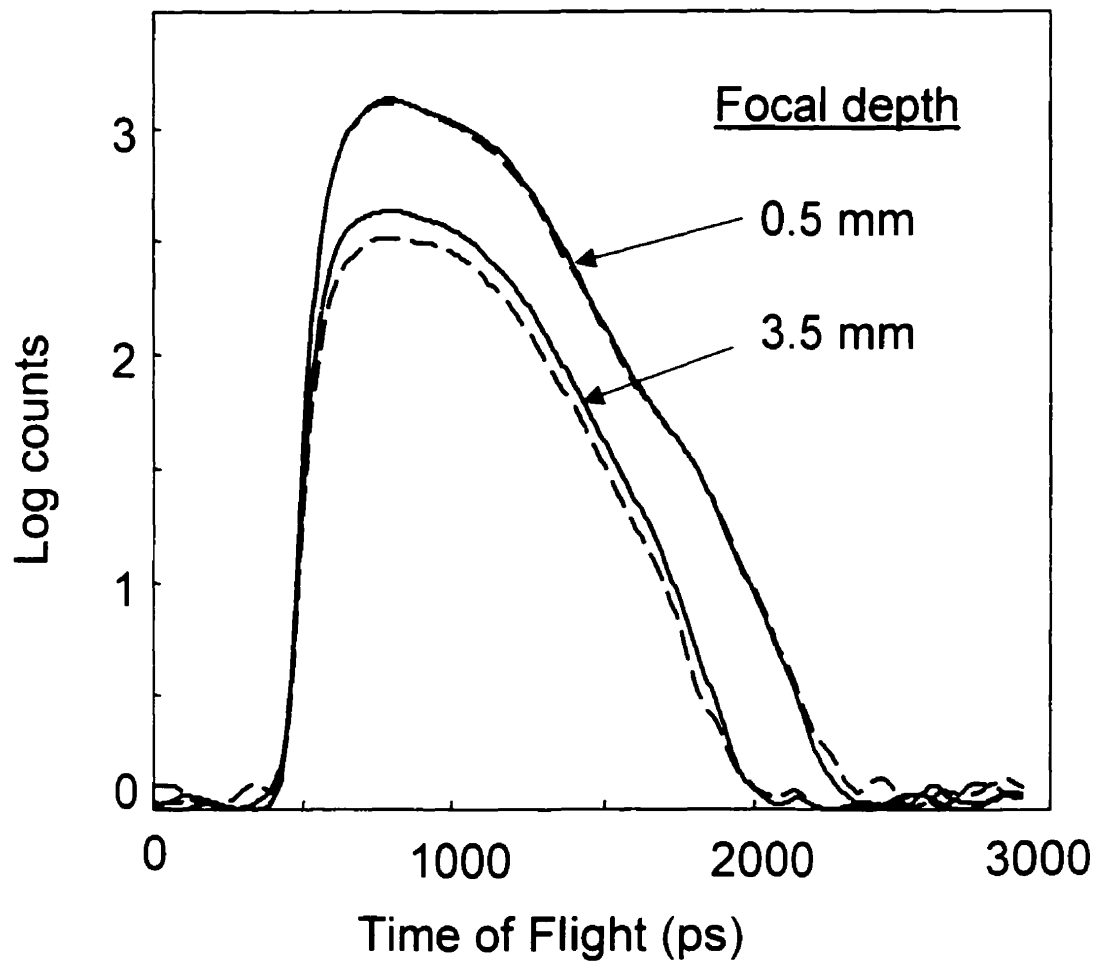

Figure 6.5. Effect of focal depth on the time profiles for two different samples. Solid line: sample 1. Dashed line: sample 3.

because the absorption coefficients in the top 0.5 mm of the two samples are the same. However, at a focal depth of 3.5 mm, the focused incident light is attenuated quite differently due to the difference in sample composition. In addition, it may be seen that sample 3 will have a steady state absorbance, $A(0.5,\infty)$, close to zero when compared to the reference. Likewise, $A(2.5,\infty)$ will be large.

A quantitative measure of this effect is shown in Figure 6.6 for a range of effective pinhole sizes. At a focal depth of 2.5 mm, the most linear changes in the steady state response were found when υ_p was small. The spread in the data about the calibration line is less severe with a small υ_p than with a large υ_p where the coincidence focussing is weak. This spread is caused from unknown ray paths through the sample. In addition, strong deviations from linearity are observed when $\upsilon_p > 125$. This is observed even when light was focussed into the sample at shallower depths. Comparing responses obtained when $\upsilon_p > 125$ to a line of unit slope, it is seen that relatively less light is being detected in a highly absorbing medium than is expected. This presents difficulties for accurate sample quantification over a large range of absorption.

6.5.3 Effect of time window size on absorbance linearity

Using the same series of measurements made to assess the effect of pinhole size, a set of partially integrated absorbances $A_{exp}(z,t)$, were calculated. The time-of-flight distributions were integrated to at most, the peak maximum (0 – 490 ps). By integrating only the rising edge of the distribution, significant amounts of the highly scattered light may be eliminated.[17,18] Experimentally determined sample absorbances as function of time window and light collection geometry are shown in Figure 6.7. The depth at which

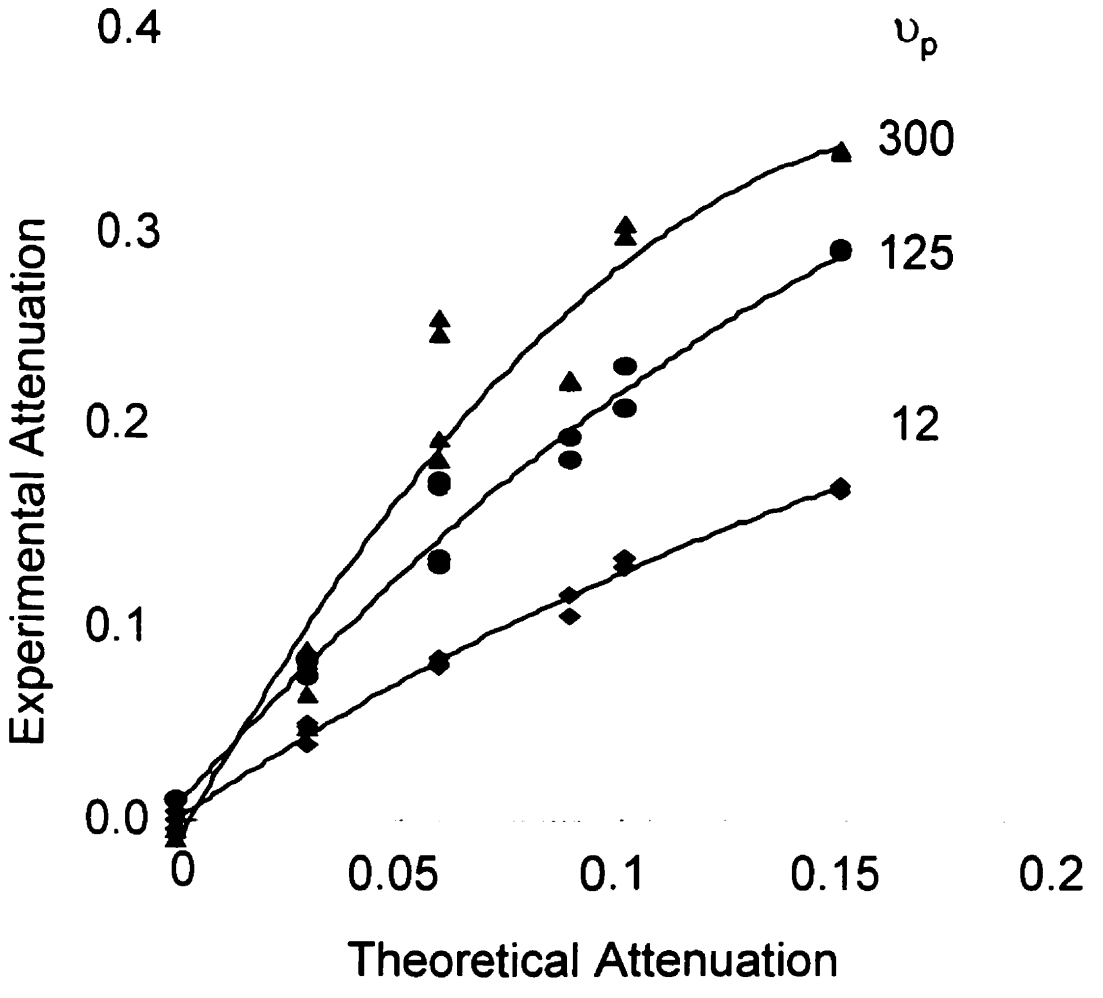

Figure 6.6. Effect of effective confocal pinhole size on sample absorbance linearity at a focal depth of 2.5 mm. Diamonds: 100 μm. Circles: 1000 μm. Triangles: 2500 μm.

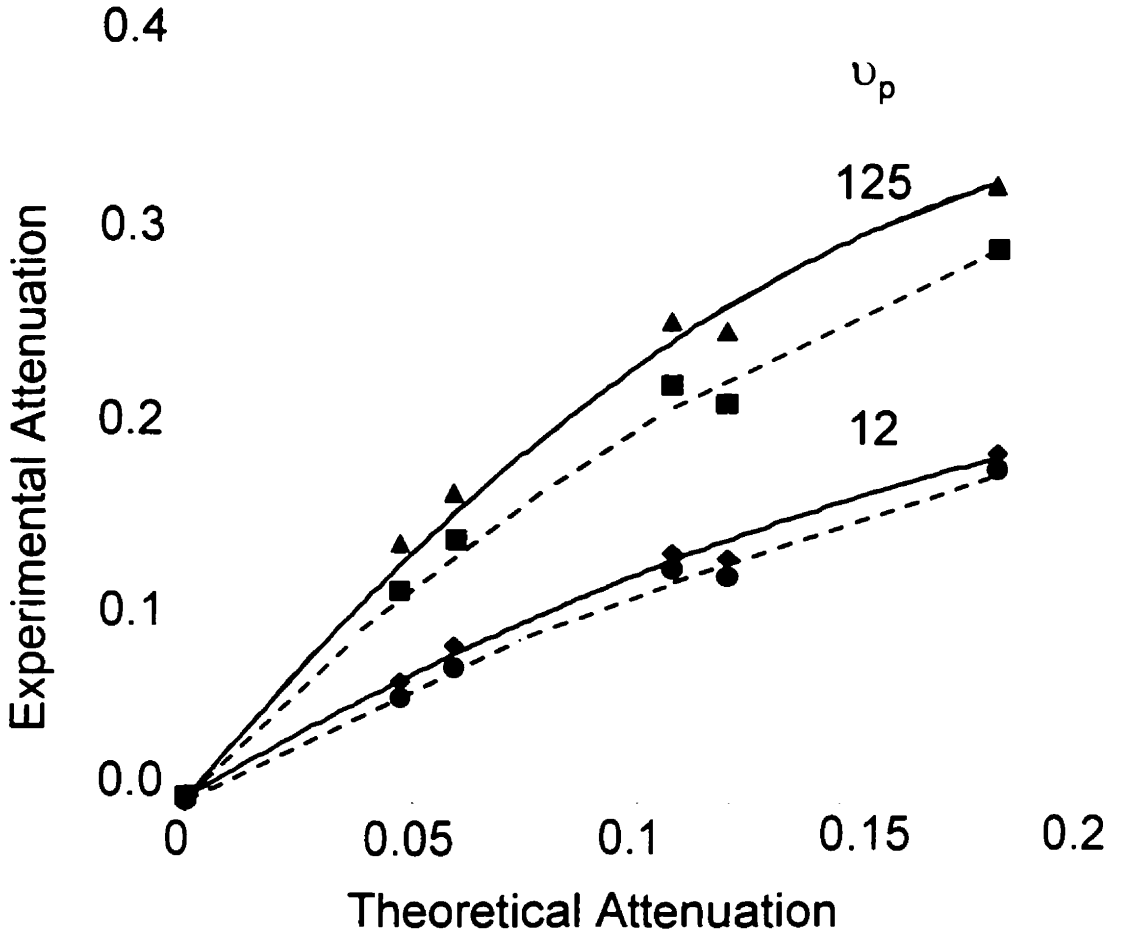

Figure 6.7. Effect of choice of time window on sample absorbance linearity at a focal depth of 3.0 mm. Solid lines: 0 – 2940 ps. Dashed lines: 0 – 490 ps.

the light was focussed was 3.0 mm. In general, a better linear response to changing sample absorption was found using partially integrated time profiles as compared to the steady state absorbance. However, results suggest little improvement in the linearity by time windowing when υ_p is small. This result may be expected as many of the highly scattered photons have been removed prior to detection by the pinhole. In contrast, time windowing is seen to markedly improve absorption linearity when $\upsilon_p > 125$.

If a similar plot is made using measurements made at a focal depth of 3.5 mm, the response curves start to plateau and with the smallest υ_p, fall below the line of identity. This suggests a limit to how deep into this type of sample, light may penetrate. Results by Kempe *et al.*[9] demonstrate that even at a relatively low scattering level of 1.9 mm^{-1}, very poor contrast results when imaging a mirror grating structure positioned 3.8 mm below the surface of a scattering sample. However, the results in this study have shown that quantification at this depth is still possible in the presence of much higher scattering levels. One explanation for this is the difference in the geometric configuration of the confocal illumination and collection optics used. In the Kempe study, a microscope objective was employed in a classic confocal reflectance arrangement and in the present study, a camera lens in an scanning mirror/slit confocal arrangement. This arrangement allows for significant variations in the mean positions where the source light enters, and the detected light exits the sample. Over a 3.5 mm focal depth range, the change in mean source/detector separation distance is ~5.5 mm. As shown in previous work, this source/detector separation distance is adequate for observing sub-changes in absorption.[19]

6.5.4 *Sample reconstruction*

To demonstrate the application of Equation 6.3 for depth-resolved reconstruction of the absorption profile in the layered specimens, three representative images are shown in Figure 6.8. In each case Equation 6.3 was applied to A_{exp} determined at each depth integrated over a 490 ps time window. The solid lines represent the sample's actual absorption profile while the dashed lines represent the estimates. Since each sample attenuation was made relative to measurements taken at $z = 0.5$ mm, the absorption coefficient, $\mu_a(0.5)$ was set at 0 mm^{-1}. It can be seen that at the discontinuous boundaries, the computed $\mu_a(z)$ is closer to the absorption coefficient above the boundary, than below it. This effect is expected due to the nature of the reconstruction method. With each calculation, the errors in the estimation propagate.

As shown in Table 6.2, the errors in the reconstruction generally increase with sample depth. The error is listed as the standard error between the estimated and reference absorption coefficients at a given sample depth. Although the average error was calculated with only 17 samples, a clear trend is observed. Roughly a two fold decrease in the reconstruction error was observed when effective pinhole size, υ_p is small. Furthermore, only small improvements in sample reconstruction are seen when time-windowing is used in conjunction with the confocal optical arrangement. This demonstrates that confocal collection optics aid in blocking significant numbers of longer pathlength photons from reaching the detector.

Overall, the results are encouraging when a small effective pinhole size is used. The absorption coefficient deep within a sample may be estimated to within $\pm$ 0.006 mm^{-1}. This represents 20% of the absorption coefficient range used in this

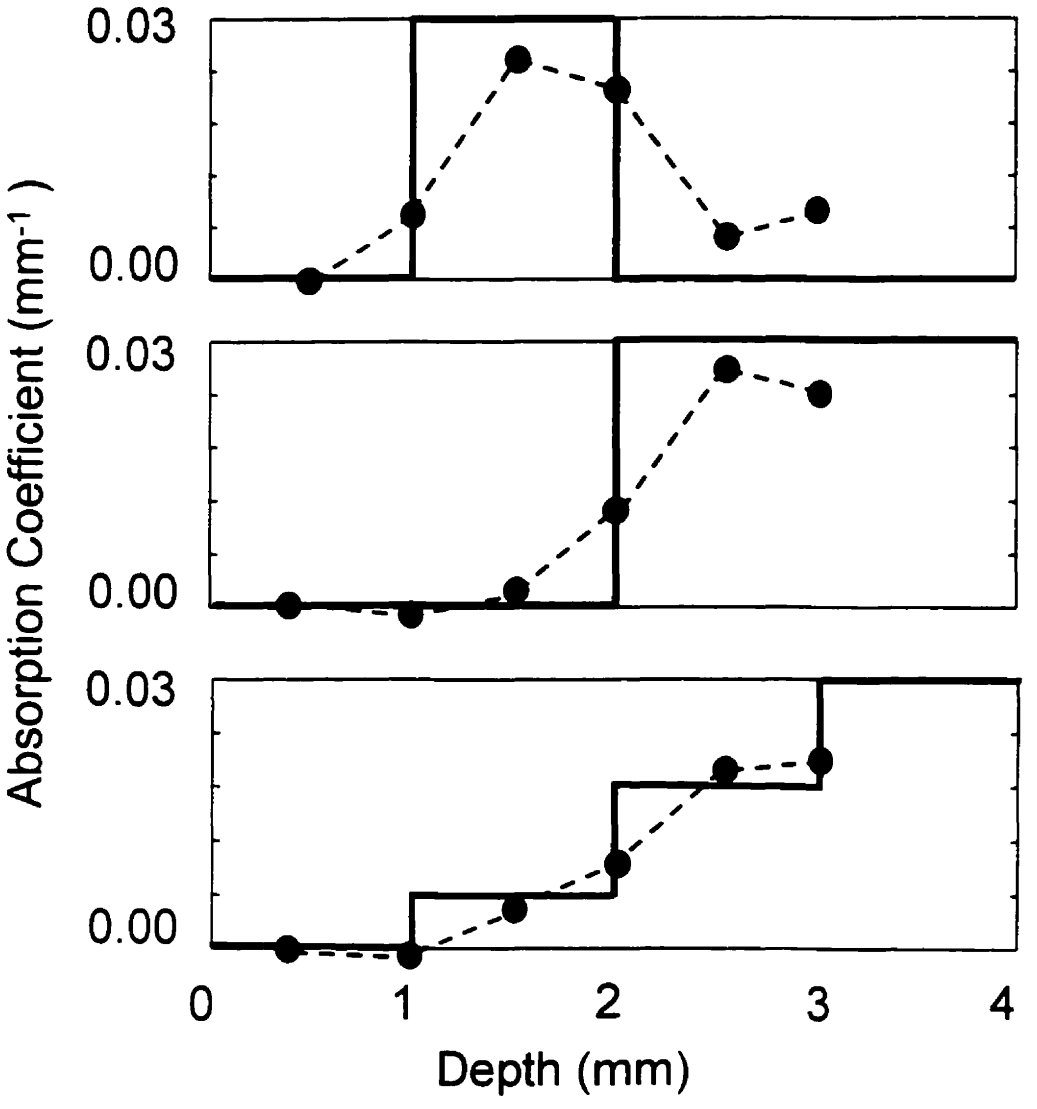

Figure 6.8. Depth-resolved reconstruction of three samples. Solid line: Actual sample absorbance profile. Dashed line: calculated absorption coefficient relative to a measurement made at a focal depth of 0.5 mm.

study. The result demonstrates that the optical geometry plays a important role in the collection of photons and should be considered when making photon time-of-flight measurements.

Table 6.2. Standard Error in the estimates of the absorption coefficient as a function of sample depth (units are in $mm^{-1} \times 10^{4}$).

		Sample Depth (mm)				
υ_p	Time Window (ps)	1.0	1.5	2.0	2.5	3.0
125	0 – 2940	109*	136	151	152	164
125	0 – 490	97	122	134	140	151
12	0 – 2940	53	55	69	63	74
12	0 – 490	49	47	58	59	66

*Absorbances were calculated relative to measurements taken at z = 0.5 mm.

6.6 Conclusion

In this study, a method for depth-resolved quantification in layered scattering/absorbing samples using confocal optical geometry in conjunction with time gated detection was investigated. A series of time-resolved confocal reflectance measurements were made using the instrument as various focal depths in a sample. The numerical aperture of the light focussed into the sample was optimized to decrease pathlength variation and enhance optical sectioning in the scattering sample. Measurements were made to assess the effective pinhole size, υ_p on the time-of-flight distribution and absorbance linearity. Results indicate that when υ_p is small, the best sample absorbance linearity and the lowest errors in sample quantification were obtained. By incorporating a small pinhole, enhancements were obtainable because non geometric

photons may rejected. When confocal light collection was used together with time information from the initial rising edge of time-of-flight distribution, little image enhancement was observed in comparison to an integrated signal. This important finding demonstrates that confocal illumination and collection optics can play an information role and should be considered when imaging in scattering media.

6.7 References

1. Fitch, J. P. *Synthetic Aperture Radar*; Springer-Verlag: New York, 1998.
2. Cui, W.; Kumar C.; Chance, B. Experimental Study of Migration Depth for the Photons Measured at Sample Surface; *Proc. SPIE* **1994**, *1431*,180-187.
3. Chang, J.; Graber, H. L.; Barbour, R. L. *OSA Proceedings On Advances in Optical Imaging and Photon Migration*; Alfano, R. R., Ed.; OSA: New York, 1994; Vol 21, pp 193-220.
4. Jiang, H.; Paulsen, K. D.; Osterberg, U. L.; Pogue B. W.; Patterson, M. S. Optical Image Reconstruction using Frequency-Domain Data: Simulations and Experiments; *Opt. Image Sci.* **1996**, *13*, 253-266.
5. Visser, T. D.; Groen, F. C. A.; Brakenhoff, G. J. Absorption and Scattering Correction in Fluorescence Confocal Microscopy; *J. Microsc.* **1991**, *163*, 189-200.
6. Painchaud, Y.; Mailloux, A.; Morin, M.; Verreault, S.; Beaudry, P. Time-Domain Optical Imaging: Discrimination Between Scattering and Absorption; *Appl. Opt.* **1999**, *38*, 3686-3693.

7. Kempe, M.; Genack, A. Z.; Rudolph, W.; Dorn, P. Ballistic and Diffuse Light Detection in Confocal and Heterodyne Imaging Systems; *J. Opt. Soc. Am. A* **1997**, *14*, 216-223.

8. Izatt, J. A.; Hee, M. R.; Owen, G. M.; Swanson, E. A.; Fujimoto, J. G. Optical Coherence Microscopy in Scattering Media; *Opt. Lett.* **1994**, *19*, 590-592.

9. Kempe, M.; Rudolph W.; Welsch, E. Comparative Study of Confocal and Heterodyne Microscopy for Imaging Through Scattering Media; *J. Opt. Soc. Am. A* **1996**, *13*, 46-52.

10. Schmitt, J. M.; Knuettel A.; Yadlowsky, M. Confocal Microscopy in Turbid Media; *J. Opt. Soc. Am. A* **1994**, *11*, 2226-2235.

11. Gu, M.; Tannous, T.; Sheppard, J. R. Effect of an Annular Pupil on Confocal Imaging Through Highly Scattering Media; *Opt. Lett.* **1996**, *21*, 312-314.

12. Gu, M. Time-Resolved Three-dimensional Imaging Based on Confocal Interferometry under Ultrashort Pulsed Illumination; *Optik* **1996**, *101*, 32-34.

13. Gu, M. Confocal Imaging of Thin and Line Objects under Ultrashort Laser-Pulse Illumination; *Optik* **1996**, *101*, 118-122.

14. Koester, C. J. A Scanning Mirror Microscope with Optical Sectioning Characteristics: Applications in Ophthalmology; *Appl. Opt.* **1980**, *19*, 1749-1757.

15. Small, E. W. Laser Sources and Microchannel Plate Detectors for Pulse Fluorometry; In *Topics in Fluorescence Spectroscopy;* Lakowicz, J. R., Ed.; Plenum Press: New York, 1991, Vol. 1.

16. Long, W. F.; Burns, D. H. Optical Tomography in Scattering Media from Photon Time-of-Flight Diffuse Reflectance Measurements: A Chemometric Approach; *J. Chemom.* **1999**, *13*, 251-264.

17. Yamada, Y.; Hasegawa, Y. Simulation of Time-Resolved Optical-CT Imaging; *Proc. SPIE* **1991**, *1431*, 73-82.

18. Leonardi, L.; Burns, D. H. Quantitative Constituent Measurements in Scattering Media from Statistical Analysis of Photon Time-of-Flight Distributions; *Anal. Chim. Acta* **1997**, *348*, 543-551.

19. Long, W. F.; Burns, D. H. Optical Tomographic Reconstruction from Diffuse Remittance in Scattering Media Using Partial Least Squares Estimation; *Anal. Chim. Acta* **1997**, *348*, 553-563.

Chapter 7 Conclusions

This dissertation has demonstrated the application of NIR spectroscopy in the determination of absorbing constituents in scattering media. The project began with the investigation of the scattering and absorption properties of granular samples using time-resolved diffuse reflectance measurements. Statistical descriptors of the photon time-of-flight distributions were used to simplify analysis. The set of descriptors was developed to be sensitive to broad changes in the time-of-flight profile as particle size and sample absorption were varied. Using stepwise multi-linear regression, combinations of descriptors were chosen which best correlate with changes in sample composition. It was found that the absorption and scattering coefficients and apparent particle size could be estimated to within 10, 9 and 7% of their respective reference values. Statistical descriptors which describe the trailing portion of the time profile were found to be optimal for absorption estimation. Likewise, descriptors of the rising edge of the time distribution were needed for scattering and apparent particle size estimates. Using separate calibrations for each physical property, quantification was possible when sample particle size and absorption characteristics were varied simultaneously. Recent developments in high speed switching, diode laser and detector technologies are now beginning to provide inexpensive components useful for compact instrumentation. In the future, simple electrical circuits may be constructed for real-time, on-line analysis of scattering media.

By understanding the effect of absorption on the time-resolved reflectance measurement in uniform samples, depth-resolved quantification in layered media was then investigated. Although statistical descriptors were shown to be useful in quantifying

broad changes in the time-of-flight distribution, there are not entirely suitable for describing subtle changes. This is especially true of the time-of-flight distributions from layered absorbing samples. Instead, a series of steady-state reflectance measurements at different source/detector separation distances were made in layered liquid samples to obtain multi-perspective information sensitive to sample composition. The reflectance geometry was used because of its suitability for non-invasive analysis of thick samples and for obtaining unique ray paths through a sample not obtainable with transmission based measurements. Sample reconstruction was done using least squares backprojection, inverse least squares (ILS) and partial least squares (PLS) regression. Overall, the PLS method provided a 50% decrease in the error of the estimated absorption compared that obtained using the back projection approach. In general, however, the absorbance coefficients were best estimated in the surface layers as compared to deeper layers in all reconstruction approaches.

To gain a better understanding of the effect of sample heterogeneity, time-resolved measurements were made in a series of two-layered absorbing samples. Autocorrelated time data was also investigated because it may provide for simplified instrumentation. For tomographic reconstruction, stepwise multi-linear regression and partial least squares regression were employed. Results demonstrated that better estimates of layer absorption were made using time-resolved data as compared to that obtained using steady state measurements. Again, errors in the estimated absorption coefficients were significantly lower in surface layers (<1 %) than in deeper regions (~50 %). One of the reasons for this is due of the ill-conditioned nature of the reconstruction. This is caused because incident light travelling through a specimen towards a detector placed on the surface must

penetrate through the upper regions twice. To reduce ambiguities in the tomographic reconstruction, constraints and *a priori* information must be included.

For improved quantification in the lower regions of a sample, hierarchical locally weighted calibration and classification approaches were developed. The tomographic reconstruction problem was linearized by utilizing *a priori* information about sample composition in the upper regions to direct subsequent calibrations in the lower regions. With the classification approach, a further 20% improvement in the estimated absorption coefficient for all sample regions sample was realized. Correct classification of the estimated absorption coefficient deep within a highly scattering/absorbing sample were obtainable at greater than 50% accuracy. The approach also was found to be robust in the presence of added noise.

In addition to using chemometric methods for obtaining depth-resolved information from layered samples, confocal reflectance measurements were also made. Photon time-of-flight profiles collected from each sample were integrated and ratioed to those obtained from a similar, non-absorbing specimen. The confocal illumination and light collection arrangement enhances detection of photons which follow geometric paths into and out of a sample. In this way, the detection of highly scattered light is suppressed. Results indicated that confocal light detection provided superior sample absorbance linearity and the lowest errors in tomographic reconstruction over non-confocal detection. When sample reconstruction was performed using only the rising edge of the time distribution, little improvement was seen over using integrated intensity information. Confocal light collection used in conjunction with time information from the initial rising edge of time-of-flight distribution showed little enhancement in

quantification compared to that obtained using a fully integrated signal. This important finding demonstrates that confocal illumination and collection optics can play an information role and should be considered when imaging in scattering media.

The approaches to tomographic reconstruction in layered scattering media presented in this work were significant advances for two reasons. First, the use of chemometric techniques for depth-resolved quantification in turbid media has enabled the construction of calibration models. Such approaches are advantageous in that they are not restricted to quantification in uniform, isotropic scattering media. Second, the chemometric methods developed allow for quantification over a wide range of absorption even in thick, highly scattering samples. To date, competing methods such as optical coherence, photoacoustic and acousto-optic tomographies have been successful in producing qualitative images in scattering media. Although these methods may, in the future, provide more quantitative information about a sample, they either rely on physical models or are only applicable in certain media. This severely limits the possibilities for developing and implementing new approaches to quantification in complex samples.

There are several future directions for this research. The interactions between the three variables (time, source/detector separation, and sample composition) explored in this work may be further investigated by multi-way decomposition methods. Techniques such as PARAFAC generalize principal component analysis to higher order arrays. In such an analysis the 'pure components' of the photon time-of-flight profile at each source/detector separation may be estimated. Using this technique, the 'inverse' approach to sample reconstruction may be considered in greater detail.

The hierarchical locally weighted calibration method developed in Chapter 5 demonstrated that information about sample composition in the upper regions may be used to improve quantification in lower regions. When both scattering and absorption vary in a sample, the method could be used with statistical descriptors of the time distribution. The relative insensitivity of the descriptors to subtle variations in the time-distribution arising from absorbers deep in specimen may be exploited for robust of estimations of scattering. Using this general hierarchical approach, both the scattering and absorption properties in each sample region may be characterized. Although many different samples may be required for calibration, a greater range of samples would be amenable to analysis. This approach would especially be of use in two layered systems where the scattering levels vary between layers. Examples of such systems include of skin and muscle, and fruit peel and pulp.

The trend in modern analytical instrumentation is for miniaturization, portability and ease of use. Although many of the measurements made in this project required great care and elaborate calibrations, these findings will provide a framework for future work. As advanced optic-electronic devices become available, practical instruments for routine measurements in scattering media will be developed. The results of this research suggest promising new approaches for depth-resolved quantification of chromogenic constituents in scattering/absorption systems.

Appendix

A Monte-Carlo program for simulating photon propagation in layered scattering/ absorbing media is listed below. The source code, written in C, is spread over 2 files: main.c and var.c. Main.c contains the program and var.c contains the global variable definitions. The program relies on an ASCII parameter file which provides all information required for running a simulation. An example of one is listed below.

The number of photons to release, sample size and resolution, layer composition, and source and detector geometries are set in the parameter file. In addition, the filenames of the output files are specified. Program output is saved to four ASCII files:

run.xxx - steady state light intensity exiting the top or bottom sample surface

vol.xxx - steady state light intensity in the sample projected onto the x plane

tof.xxx - time resolved light intensity exiting the top or bottom sample surface

mov.xxx - a series of 20 instantaneous light intensities in the sample projected onto the x plane taken every 25 ps

If the extension .000 is used then no file will be written and the particular quantity will not be calculated.

A model of the layered scattering/absorbing sample simulated in the program is shown in Figure A.1. Top and bottom surfaces of the sample are square and are separated by a distance, z, the sample thickness. Each layer may be chosen to have arbitrary scattering, absorption and refractive index properties. A each scattering event,

the Henyey-Greenstein phase function is used for computing the direction of the scattered light. Further computational details of the photon trajectory and light attenuation are discussed in Chapter 3.

Light reflection and refraction which occurs at a boundary between two regions of differing refractive index are also handled. When light crosses a boundary, the intensity and trajectory of the refracted ray are adjusted according to Fresnel's law. After the refracted ray exits the sample or has undergone more than the maximum number of scattering events, the trajectory of the reflected ray is determined.

The simulated incident light source is focussed into the sample through the top face. The aperture size and focal length of the lens may be set arbitrarily. In this manner, sample illumination may be done with either focussed or collimated light. Light exiting the sample may be detected either from the top or bottom surfaces allowing for simulation of diffuse reflectance or transmission. In addition, reflectance mode confocal light collection may be simulated. To enhance photon counting statistics, photons exiting the sample at a given radial distance away from the z axis may be binned. This technique is possible due to the assumed radial symmetry of the sample. After simulation, a mathematical correction is applied so that the radial light intensity appears to be emanating from a point on the surface.

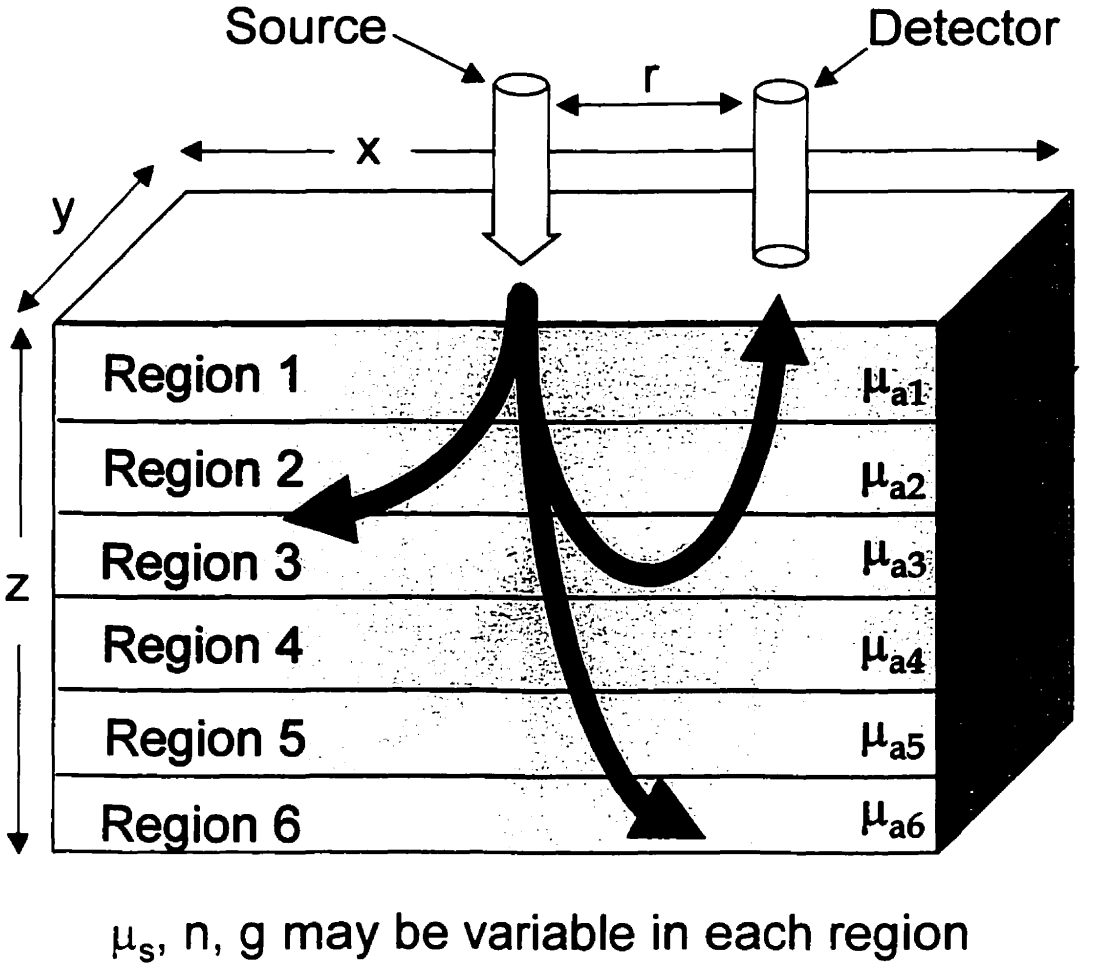

Figure A.1. Schematic diagram of layered specimen used in Monte-Carlo model.

A typical parameter file:

```
Output Files (xxx.000 to xxx.999  use 000 for no output)
------------
run.000          Output filename for scattered intensity
vol.001          Output filename for XZ projection
tof.000          Output filename for time of flight profile
mov.000          Output filename for time lapsed photon distribution sequence
api.000          Output filename for confocal intensity
Sample Illumination Parameters
------------------------------
1                Collimated (0), confocal (1), or isotropic (2) illumination
2000000          Number of photons to release
16               Source or lens diameter (mm)
100.0            Lens focal length (mm)
1.0              Lens distance from sample (mm)
Detection Parameters
--------------------
1                Integrate over an annulus?
1                Trace photons anywhere (0) upper surface (1) lower surface (2)
1.1              Detector position for movies or XZ projection (mm from source)
1.5              Detector size (for movies or XZ projection) or conf. aper.size
Sample Characteristics
----------------------
15               XY range from source (mm)
10               Sample depth (mm)
6                Number of layers (max 20)
2000             Maximum number of scattering events per photon (max 8000)
1                Heterogeneous intra-layer scattering?
1                Compute Fresnel reflections at surfaces?
10               Number of pixels per millimeter
ua  1/mm)     us  1/mm)       g     RI
---------     ---------     -----  -----
0.0           10.0          0.85   1.00
0.0           10.0          0.85   1.00
0.0           10.0          0.85   1.00
0.0           10.0          0.85   1.00
0.0           10.0          0.85   1.00
0.0           10.0          0.85   1.00
```

```
/* main.c                                                                  */
/* 02-jul-98  wl                                                           */
/*                                                                         */
/* Monte Carlo photon scattering model through absorbing media based       */
/* on Henyey-Greenstein phase functions                                    */

#include <stdio.h>
#include <math.h>
#include <string.h>
#include <time.h>
#include "var.c"
FILE* DataFilePtr;


/* ----------------------------------------------------------------------- */
/*  Random number generator, ran2.  Taken from Numerical Recipes in C      */
/* ----------------------------------------------------------------------- */
float Random(long *idum)
{
    int j;
    long k;
    static long idum2=123456789;
    static long iy=0;
    static long iv[NTAB];
    float temp;

    if (*idum <= 0) {
        if (-(*idum) < 1) *idum=1;
        else *idum = -(*idum);
        idum2=(*idum);
        for (j=NTAB-7;j>=0;j--) {
            k=(*idum)/IQ1;
            *idum=IA1*(*idum-k*IQ1)-IR1*k;
            if (*idum < 0) *idum += IM1;
            if (j < NTAB) iv[j] = *idum;
        }
        iy=iv[0];
    }
    k=(*idum)/IQ1;
    *idum=IA1*(*idum-k*IQ1)-k*IR1;
    if (*idum < 0) *idum += IM1;
    k=idum2/IQ2;
    idum2=IA2*(idum2-k*IQ2)-k*IR2;
    if (idum2 < 0) idum2 += IM2;
    j=iy/NDIV;
    iy=iv[j]-idum2;
    iv[j] = *idum;
    if (iy < 1) iy += IMM1;
    if ((temp=AM*iy) ==0) return 0.0001;
    else return temp;
}


/* ----------------------------------------------------------------------- */
/*  this procedure gets variables from disk from the file specified at the */
/*  command prompt                                                         */
/* ----------------------------------------------------------------------- */
Initialize(int *argument_count, char **argument_array)
{
    float Sgn;
    FILE* InitFile;

    if (*argument_count < 2) {
```

```
    printf "\n This program requires an initialization file argument.
         n\n"
     ;
    exit 0;
;
InitFile = fopen(argument_array[*argument_count -1],"r");
if (InitFile == NULL) {
  printf("\n The initialization file, %s, was not found.\n\n",
      argument_array[*argument_count -1]
   );
  exit 0 ;
}

fscanf (InitFile, "%*s %*s %*s %*s %*s %*s %*s %*s %*s", Dummy);
fscanf (InitFile, "%*s", Dummy);

    /* Inputs file names to be used */

fscanf (InitFile, "%s", &File1);
fscanf (InitFile, "%*s %*s %*s %*s %*s", Dummy);
fscanf (InitFile, "%s", &File2);
fscanf (InitFile, "%*s %*s %*s %*s %*s", Dummy);
fscanf (InitFile, "%s", &File3);
fscanf (InitFile, "%*s %*s %*s %*s %*s %*s %*s", Dummy);
fscanf (InitFile, "%s", &File4);
fscanf (InitFile, "%*s %*s %*s %*s %*s %*s %*s %*s", Dummy);
fscanf (InitFile, "%s", &File5);
fscanf (InitFile, "%*s %*s %*s %*s %*s", Dummy);
fscanf (InitFile, "%*s %*s %*s", Dummy);
fscanf (InitFile, "%*s", Dummy);

    * Confocal or collimated geom. */

fscanf (InitFile, "%i", &IGeom);
fscanf (InitFile, "%*s %*s %*s %*s %*s %*s %*s %*s", Dummy);

    * Number of photons */

fscanf (InitFile, "%ld", &s);

    * Source Size (mm) */

fscanf (InitFile, "%*s %*s %*s %*s %*s ", Dummy);
fscanf (InitFile, "%f", &SourceSize);

    /* Focal Length (mm) */

fscanf (InitFile, "%*s %*s %*s %*s %*s", Dummy);
fscanf (InitFile, "%f", &f);

    * Lens dist. from surface */

fscanf (InitFile, "%*s %*s %*s %*s", Dummy);
fscanf (InitFile, "%f", &d);

    /* Integrate over annulus */

fscanf (InitFile, "%*s %*s %*s %*s %*s", Dummy);
fscanf (InitFile, "%*s %*s", Dummy);
fscanf (InitFile, "%*s", Dummy);
fscanf (InitFile, "%i", &IntOverAnnulus);

    /* Det. placement */
```

```
fscanf (InitFile, "%*s %*s %*s %*s", Dummy);
fscanf  InitFile, "%i", &DetectPlace);

    /* Detector Position (mm) */

fscanf  InitFile, "%*s %*s %*s %*s %*s %*s %*s %*s %*s %*s %*s", Dummy);
fscanf (InitFile, "%f", &DetectPos);

    /* Detector Size (pixels) */

fscanf  InitFile, "%*s %*s %*s %*s %*s %*s %*s %*s %*s %*s", Dummy);
fscanf  InitFile, "%f", &DetectSize);

fscanf(InitFile,"%*s %*s %*s %*s %*s %*s %*s %*s %*s %*s %*s %*s",Dummy);
fscanf  InitFile, "%*s %*s", Dummy);
fscanf  InitFile, "%*s", Dummy);

     * Maximal Radial Boundary      */

fscanf  InitFile, "%i", &RSize);
fscanf  InitFile, "%*s %*s %*s %*s %*s", Dummy);

    /* Maximal Depth          */

fscanf (InitFile, "%i", &ZSize);
fscanf (InitFile, "%*s %*s %*s", Dummy);

     * Number of Layers in Sample   */

fscanf  InitFile, "%i", &NumLayer);
fscanf (InitFile, "%*s %*s %*s %*s %*s", Dummy);

    /* Maximum # of scat. events    */

fscanf  InitFile, "%d", &MaxScat);
fscanf  InitFile, "%*s %*s %*s %*s %*s %*s %*s %*s %*s", Dummy);

     * Heterog. scattering or RI    */

fscanf  InitFile, "%i", &HeteroScat);
fscanf  InitFile, "%*s %*s %*s", Dummy);

    /* Compute Reflections?  */

fscanf  InitFile, "%i", &ComputeReflec);
fscanf (InitFile, "%*s %*s %*s %*s %*s", Dummy);

    /* Points per Pixel             */

fscanf (InitFile, "%i", &ppu);
fscanf (InitFile, "%*s %*s %*s %*s %*s", Dummy);

fscanf (InitFile, "%*s %*s %*s %*s %*s %*s", Dummy);
fscanf (InitFile, "%*s %*s %*s %*s", Dummy);

    /* Load in ua, us, g, RI     */


for (i=1; i<=NumLayer; i++) {
    fscanf (InitFile, "%f", &A[i]);
    fscanf (InitFile, "%f", &us[i]);
    fscanf (InitFile, "%f", &g[i]);
```

```
    fscanf  InitFile, "%f", &nu[i]);
}
fclose(InitFile);

     * Define some defaults */

SaveScatInten = 1;
Proj = 1;
DoTOF = 1;
DoMovie = 1;
DoConf = 1;

     * Save intensities at surface? */

if   File1[4] == '0'  && (File1[5] =='0') && (File1[6] =='0')
   SaveScatInten = 0;

     * Save depth resolved projection? */

if   File2[4] == '0'  && (File2[5] =='0') && (File2[6] =='0')) Proj = 0;

     * Calculate TOF profiles */

if   (File3[4] == '0') && (File3[5] =='0') && (File3[6] =='0')) DoTOF = 0;

     * Compute TOF photon dist seq */

if   File4[4] == '0') && (File4[5] =='0') && (File4[6] =='0')) DoMovie=0;

     * Confocal system */

if   File5[4] == '0') && (File5[5] =='0') && (File5[6] =='0')) DoConf=0;

     * random seed  for random number generator */
     * elapsed_seconds = # of s since 1970 */

time &elapsed_seconds);
idum = -elapsed_seconds;
if  DataFilePtr=fopen("seed","w+t")==NULL) {
    printf "\n Error opening Output data File \n");
    exit 1 ;
}
fprintf DataFilePtr, "%ld", idum);
fclose DataFilePtr);

     * convert everything to pixel units

c = 0.299792458*ppu;
SourceSize = (SourceSize/2.0)*ppu;
RSize *=ppu;
ZSize *=ppu;
f *=ppu;
d *=ppu;
DetectPos *=ppu;
DetectSize *=ppu;

     * convert us to (pixels^-1) */

for  i=1; i<=NumLayer; i++) {
    us[i] = us[i]/ppu;
}
```

```
        * Seed random number gen */
        * Limit range of Source Size */
        * h = thickness of each layer */
        * abs outside medium = 0 */
        * used for hv paths that cross boundaries */

    Random(&idum);
    if  SourceSize > RSize) SourceSize = RSize;
    h =  float) ZSize/NumLayer;
    A[0] = 0.0;
    Ap[0] = 0.0;

        * transform abs. into Ap in pixels^-1 */

    for  i=0; i<=(NumLayer-1); i++) {
        A[i+1] = A[i+1] / ppu;
        if  A[i+1] >= A[i]) Sgn = 1.0;   /* find correct sign */
        if  A[i+1] < A[i])  Sgn = -1.0;
        Ap[i+1]=Sgn* abs(A[i] - A[i+1]); /* from Ap in Terms of Ap U(x-nh) */
    }
    return;
}


 * ------------------------------------------------------------------------ */
 *  Set initial photon every point and direction based on SourceSize and    */
 *  NLevel.  Returns a value for x(0), y(0) and z(0) and a theta and phi     */
 * ------------------------------------------------------------------------ */
SetInit
{

        * source function */


    float r,phiprime,sinb,CX,CY,CZ,t,ET;
    layer = 1;
    r = SourceSize*Random(&idum);
    phiprime = 2*PI*Random(&idum);

        * Collimated source */

    if  IGeom == 0  {
        theta = 0;
        phi =  PI-phiprime);
        Coord[0].X = RSize + r*cos(phiprime);
        Coord[0].Y = RSize + r*sin(phiprime);
        Coord[0].Z = 0.0;
        Coord[0].T = 0.0;
    }

        * Confocal source */

    if  IGeom == 1) {
        phi = -(PI-phiprime);  /* initial phi pointed toward focus  */
        theta = atan(r/f);
        r = r*(1.0 - d/f);     /* focused beam positions at surface */

        Coord[0].X = RSize + r*cos(phiprime);
        Coord[0].Y = RSize + r*sin(phiprime);
        Coord[0].Z = 0.0;

            * compute time when photon stikes */
```

```
        t = f.pow(
            pow(Coord[0].X - RSize ,2) +
            pow(Coord[0].Y - RSize ,2) +
            pow(Coord[0].Z - (f-d) ,2),0.5
        ;


             * surface + 33.35 ps */

        CX = (r*cos(phiprime))*t + RSize;
        CY = (r*sin(phiprime))*t + RSize;
        CZ = (0.0-(f-d))*t + (f-d);
        ET = pow(
            pow(Coord[0].X - CX ,2) +
            pow(Coord[0].Y - CY ,2) +
            pow(Coord[0].Z - CZ ,2),0.5)/c
        ;
        Coord[0].T =  CZ > 0.0) ? 33.35 - ET : 33.35 + ET;
        sinb = sin(theta)/nu[1];

             * theta after refraction */

        theta =  sinb < 1. ? acos(pow(1.0 - sinb*sinb, 0.5)) : PI/2.0;
    .


        * Hemispheric isotropic source */


    if  (Geom == 2) {
        theta = Random(&idum)*PI/2;
        phi = (PI-(Random(&idum)*PI*2));
        Coord[0].X = RSize + r*cos(phiprime);
        Coord[0].Y = RSize + r*sin(phiprime);
        Coord[0].Z = 0.0;
        Coord[0].T = 0.0;
    .

    bounce=1;
    Reflected[bounce] = 1.0;
    Refracted[bounce] = 1.0;
    Z[bounce] = 0;
    scatter = 0;
    done = 0;
    return;
.


 * ------------------------------------------------------------------- */
 *  Calculates the direction of the scattering event based on the g value  */
 *  Returns a theta and phi for the new global direction, returns values   */
 *  for the new global (x,y,z) position, time of flight and path length    */
 *  Angle convention: theta:  0 along +ve z axis, Pi along -ve z axis      */
 *  phi: 0 along +ve x axis, Pi/2 along +ve y axis, -Pi/2 along -ve y axis */
 * ------------------------------------------------------------------- */
FindDirection()
{

        * find value of phase function */

    float r,q,rr;
    r = Random(&idum);
    if (g[layer] != 0) {
```

```
        q = (1.0 - g[layer]*g[layer] - pow( (1.0 - g[layer]*g[layer])
              1.0 - g[layer] + 2.0*g[layer]*r) ,2.0)) /(2.0*g[layer])
        ;
        newtheta = (q != 0) ? acos(q) : PI/2;
    else
        newtheta = r * PI;

    newphi = 2.0*PI*Random(&idum);

        * compute cos and sin of old angles */

    cosphi = cos(phi);
    costheta = cos(theta);
    sinphi = sin(phi);
    sintheta = sin(theta);

        * new vector length to next scattering event */

    r = Random(&idum);
    length = -1.0*log r)/us[layer];

        * compute loc Cartes. coord based on newtheta, newphi & newtheta */

    xp = sin newtheta)*cos(newphi)*length;
    yp = sin(newtheta)*sin(newphi)*length;
    zp = cos(newtheta)*length;

        * convert local (xp,yp,zp) coord to global (xx,yy,zz) */

    xx = cosphi*costheta*xp - sinphi*yp + cosphi*sintheta*zp;
    yy = sinphi*costheta*xp + cosphi*yp + sinphi*sintheta*zp;
    zz = -sintheta*xp + costheta*zp;
    rr = pow(xx*xx+yy*yy+zz*zz,0.5);

        * compute global theta and phi values */

    theta =  rr != 0.0) ? acos(zz/rr) : 0.0 ;
    phi = atan2(yy,xx);
    Coord[scatter].X = Coord[scatter-1].X + xx;
    Coord[scatter].Y = Coord[scatter-1].Y + yy;
    Coord[scatter].Z = Coord[scatter-1].Z + zz;
    Coord[scatter].T = Coord[scatter-1].T + length*nu[layer]/c;

    return;
}



 * ------------------------------------------------------------------------ */
 *  Tests the new coordinates of the photon to see if it is still within   */
 *  the boundaries or layer change has occured or if number of scattering  */
 *  events has reached its maximum value                                   */
 * ------------------------------------------------------------------------ */
TestCoord()
{
    int k,a,b;
    k = scatter;
    surface = 0;
    if   Coord[k].X > (2*RSize)) || (Coord[k].X < 0)) done = 1;
    if   Coord[k].Y > (2*RSize)) || (Coord[k].Y < 0)) done = 1;
    if   Coord[k].Z > ZSize) || (Coord[k].Z <= 0)) surface = 1;
    if  k >= MaxScat) done = 1;
    if  (surface == 1) && (ComputeReflec == 0)) done = 1;
```

```
    a = floor(Coord[k-1].Z/h + 1);
    b = floor(Coord[k].Z/h + 1);
    if ((a != b) && ((b >= 1) && (b <= NumLayer))) crosslayer = 1;
    return;
}


/* ---------------------------------------------------------------------- */
/*  Force scattering event to occur at a boundary and change direction and */
/*  speed of propagation with an index of refraction change                */
/* ---------------------------------------------------------------------- */
ForceScatter()
{
    int k,a,b;
    float t,zlayer,sina,sinb;
    crosslayer = 0;
    k = scatter;
    a = floor(Coord[k-1].Z/h + 1);
    b = floor(Coord[k].Z/h + 1);

        /* new layer that photon is entering */

    layer = (a > b) ? a-1 : a+1;
    b = layer;

        /* angle of incidence, a;       angle of refraction, b  */
        /* change direction of photon propagation if necessary  */

    if (nu[a] != nu[b]) {
        sina = (a < b) ? sin(PI-theta) : sin(theta);
        sinb = sina*(nu[a]/nu[b]);
        theta = (sinb < 1) ? acos(pow(1.0 - sinb*sinb, 0.5)) : PI/2.0;
        theta = (a > b) ? PI-theta : theta;
    }

        /* compute fraction of distance spent in layer a                */
        /* and compute (x,y,z) based on point where photon exits layer a */
        /* and if necessary, force scattering event at boundary          */

    zlayer = (a < b) ? a*h : (a-1)*h;
    t = 0.001 + (zlayer-Coord[k-1].Z)/(Coord[k].Z - Coord[k-1].Z);
    Coord[k].X = (Coord[k].X - Coord[k-1].X)*t + Coord[k-1].X;
    Coord[k].Y = (Coord[k].Y - Coord[k-1].Y)*t + Coord[k-1].Y;
    Coord[k].Z = (Coord[k].Z - Coord[k-1].Z)*t + Coord[k-1].Z;
    Coord[k].T = Coord[k-1].T + length*t*nu[a]/c;
    return;
}


/* ---------------------------------------------------------------------- */
/*  Recalculates where exactly the photon emerges from the surface and    */
/*  adjusts the Coord[i] array and distance appropriately.                */
/* ---------------------------------------------------------------------- */
AdjustPath()
{
    float t;
    int k;
    k = scatter;

        /* compute fraction of path inside sample */

    if (Coord[k].X > (2*RSize))
        t = ((2*RSize)-Coord[k-1].X)/(Coord[k].X - Coord[k-1].X);
```

```
    if (Coord[k].Y > (2*RSize))
        t = ((2*RSize)-Coord[k-1].Y)/(Coord[k].Y - Coord[k-1].Y);
    if (Coord[k].X < 0)
        t = -Coord[k-1].X /(Coord[k].X - Coord[k-1].X);
    if (Coord[k].Y < 0)
        t = -Coord[k-1].Y /(Coord[k].Y - Coord[k-1].Y);
    if (Coord[k].Z < 0)
        t = -Coord[k-1].Z /(Coord[k].Z - Coord[k-1].Z);
    if (Coord[k].Z > ZSize)
        t = (ZSize-Coord[k-1].Z)/(Coord[k].Z - Coord[k-1].Z);

        /* compute (x,y,z) based on point where photon exits surface  */
        /* and correct TOF */

    Coord[k].X = (Coord[k].X - Coord[k-1].X)*t + Coord[k-1].X;
    Coord[k].Y = (Coord[k].Y - Coord[k-1].Y)*t + Coord[k-1].Y;
    Coord[k].Z = (Coord[k].Z - Coord[k-1].Z)*t + Coord[k-1].Z;
    Coord[k].T -= length*nu[layer]*(1.0-t)/c;

        /* in case that 2 or more coord at out of range artificially. set */
        /* set flags done = 1 and surface = 0                             */

    if (Coord[k].X > (2*RSize)) {
        Coord[k].X = 2*RSize;
        done = 1;
        surface = 0;
    }
    if (Coord[k].Y > (2*RSize)) {
        Coord[k].Y = 2*RSize;
        done = 1;
        surface = 0;
    }
    if (Coord[k].X < 0) {
        Coord[k].X = 0;
        done = 1;
        surface = 0;
    }
    if (Coord[k].Y < 0) {
        Coord[k].Y = 0;
        done = 1;
        surface = 0;
    }
    return;
}


/* ------------------------------------------------------------------- */
/*  Computes the reflected and refraction ray intensities at the boundary  */
/*  where the photon enters into another region of varying refractive index*/
/*  Adjusts theta and phi for the exiting ray and stores the coordinates   */
/*  the ray that remains in the volume.                                    */
/* ------------------------------------------------------------------- */
DoFresnel()
{
    float t,sina,sinb,beta,cosa;
    int k;
    k= scatter;

        /* angle of incedence, refrac. & beta factor in Fresnel formula*/

    if ((nu[layer] != 1.0 ) && (ComputeReflec == 1)) {
        sina = (Coord[k].Z == 0) ? sin(PI-theta) : sin(theta);
        beta = 1.0 - pow(nu[layer]*sina, 2);
```

```
        sinb = nu[layer]*sina;
        if  beta > 0 ) {
            cosa = pow(1.0 - sina*sina, 0.5);
            beta = pow(beta,0.5);

                /* transmission inten (both reflec. / refrac. occuring) */

            t = 2*nu[layer]*beta*cosa*(1.0/(pow(cosa+nu[layer]*beta,2)) +
                 1.0/(pow(nu[layer]*cosa-beta,2)))
            ;
        } else t = 0;    /* transmission intensity (refraction only) */
    }

    if  (nu[layer] == 1.0 ) || (ComputeReflec == 0)) t = 1;
    bounce++;
    RefractedI[bounce] = ReflectedI[bounce-1]*t;
    ReflectedI[bounce] = ReflectedI[bounce-1]*(1.0-t);
    if  ReflectedI[bounce] < 0.01) done = 1;
    S[bounce] = scatter;

         * change theta of reflected ray if necessary */

    if  ComputeReflec ==1)
        theta =  Coord[k].Z >= ZSize) ? theta + PI/2.0 : theta - PI/2.0;
    return;
}



 * ------------------------------------------------------------------------ */
 * Tests exiting ray to see whether or not its trajectory through a lens   */
 * radius SourceSize would focus into an aperature of size DetectSize      */
 * Returns  -999.0   if it fails otherwise returns the extra Time of       */
 * Flight through the air (lens) assuming a spherical wavefront plus 33.35 */
 * ps corresponding to 1 cm past lens                                      */
 * ------------------------------------------------------------------------ */
float Confocal(int i)
{
    float sina,sinb,RTheta,fdist,CX,CY,CZ,t,LensR,CenterDist,ET;
    sina =  Coord[i].Z == 0) ? sin(PI-theta) : sin(theta);
    sinb = nu[layer]*sina;
    RTheta =  sinb < 1  ? acos(pow(1.0 - sinb*sinb, 0.5)) : PI/2.0;
    ET = -999.0;
    if  RTheta != PI/2.0) {
        fdist = fabs(f-d);
        CX = Coord[i].X - fdist*tan(RTheta)*cos(phi);
        CY = Coord[i].Y - fdist*tan(RTheta)*sin(phi);
        CZ = fdist;
        CenterDist = pow(pow((RSize-CX),2) + pow((RSize-CY),2),0.5);
        if  CenterDist <= DetectSize) {
            t = f/pow(pow(Coord[i].X - CX ,2) + pow(Coord[i].Y - CX ,2) +
                pow(Coord[i].Z - CZ ,2),0.5)
            ;
            CX = (Coord[i].X - CX)*t + CX;
            CY = (Coord[i].Y - CY)*t + CY;
            CZ = (Coord[i].Z - CZ)*t + CZ;
            LensR = pow(pow(RSize - CX,2) + pow(RSize - CY,2),0.5);
            if (LensR <= SourceSize) {
                ET = pow(pow(Coord[i].X - CX ,2) + pow(Coord[i].Y - CY ,2) +
                    pow(Coord[i].Z - CZ ,2),0.5)/c
                ;
                ET =  ((DetectPlace==1) && (CZ < 0.0)) || ((DetectPlace==2)
                     && (CZ > ZSize))) ? 33.35 + ET : 33.35 - ET
                 ;
```

```
    }
    return ET;
}


/* ------------------------------------------------------------------- */
/*  Calculates the attenuation of the photon from Beer's Law and considers */
/*  the different absorptions based on the abs. properties of the layers   */
/*  Save absorptions in array also.  If desired the TOF dist is computed.  */
/*  Computes and stores Time of Flight information based on the placement  */
/*  of a detector and its physical size  (Integrates over a ring of some   */
/*  thickness)  Builds up a distribution with 1 ps resolution              */
/* ------------------------------------------------------------------- */
PhotonAbsAndTOF()
{
    int a,b,Raa,ind1,ind2,index;
    float limit1,limit2,w,Len,d;
    int j,i,m;

        /* set initial absorbance level */

    absorb = 0.0;
    if ((done == 1) && (bounce == 0)) {
        bounce = 1;
        Q[1] = scatter;
    }

        /* integrate abs over photon path                                 */
        /* by computing layer # for start & end z values of the 2 vertices */
        /* and the length between scattering events                       */

    for (m=0; m<=(bounce-1); m++) {
        for (i=Q[m]; i<=(Q[m+1]-1); i++) {
            a = floor(Coord[i].Z /h + 1);
            b = floor(Coord[i+1].Z /h +1);
            Len = pow(pow(Coord[i+1].X - Coord[i].X,2) + pow(Coord[i+1].Y -
                 Coord[i].Y,2)+pow(Coord[i+1].Z-Coord[i].Z,2),0.5)
             ;

                /* if points in same layer abs is easy */

            if (a == b) absorb += A[a]*Len;

                /* if points are in different layers */

            if (a != b) {
                limit1 = 0.0;
                limit2 = 0.0;

                    /* integrate over all layers which hv traverses */

                for (j=1; j<=NumLayer; j++) {
                    w = (j-1)*h;
                    if (Coord[i+1].Z > w) limit1 += Ap[j]*(Coord[i+1].Z - w);
                    if (Coord[i].Z > w) limit2 += Ap[j]*(Coord[i].Z - w);
                }
                if ((Coord[i+1].Z-Coord[i].Z) != 0) {
                    absorb += Len*fabs((limit2-limit1)/(Coord[i+1].Z -
                        Coord[i].Z))
                     ;
                } else {
```

```
                absorb += Len*A[a];
            }
        }

            /* calculate absorbance at the ith event */

        Coord[i+1].A = exp(-absorb)*ReflectedI[m];
    }

    if (((DetectPlace == 1) && (Coord[i].Z <= 0.0)) || ((DetectPlace == 2)
        && (Coord[i].Z >= ZSize))) {

            /* if integrating over an annulus  */

        if (IntOverAnnulus == 1 ) {
            Rad = floor(pow(pow((RSize-Coord[i].X),2) + pow((RSize -
                Coord[i].Y),2),0.5))
            ;
            BackInten[RSize+Rad][RSize] += exp(-absorb)*RefractedI[m+1];
        }

            /* if not integrating over an annulus */

        if (IntOverAnnulus == 0 ) {
            ind1 = floor(Coord[i].X);
            ind2 = floor(Coord[i].Y);
            BackInten[ind1][ind2] += exp(-absorb)*RefractedI[m+1];
        }

            /* Do Time of Flight computation */

        if (DoTOF == 1) {

                /* compute r from center to exit point */

            Rad = ceil(pow(pow((RSize-Coord[i].X),2)+pow((RSize-
                 Coord[i].Y),2),0.5))
            ;
            TOF = ceil(Coord[i].T);       /* Time of Flight in ps    */
            index = ceil(TOF);            /* convert TOF to integer */
            if (TOF > 500 ) index = 500;
            if (TOF < 1) index = 1;
            TOFArray[index][Rad] += exp(-absorb)*RefractedI[m+1];
        }

        if (DoConf == 1) {
            ExtTime = Confocal(i);
            if (ExtTime != -999.0) {
                CInten += exp(-absorb)*RefractedI[m+1];
                TOF = ceil(Coord[i].T + ExtTime); /*TOF thru med & air */
                printf("%f %f %f %f \n",Coord[0].T,Coord[i].T-Coord[0].T,
                    ExtTime,Coord[i].T + ExtTime)
                ;
                index = ceil(TOF);
                if (TOF > 500 ) index = 500;
                if (TOF < 1) index = 1;
                CTOF[index] +=exp(-absorb)*RefractedI[m+1];
            }
        }
    }
}
return;
}
```

```
/* ------------------------------------------------------------------ */
/*  Calculates a the projection of the paths onto the positive x plane */
/*  Photons reaching the Detector position when integrated over an annulus */
/*  there paths are rotated in the positive x plane and then the      */
/*  path projection is taken                                          */
/* ------------------------------------------------------------------ */
DoProj()
{
    float Rad,Dx,Dy,Tt;
    int i,k,X1,Z1;

    k = scatter;
    if ((IntOverAnnulus == 1) && (ComputeReflec == 0)) {

            /* if integating over an annulus then compute path */

        if (((DetectPlace == 1) && (Coord[k].Z <= 0)) ||
            ((DetectPlace == 2) && (Coord[k].Z >= ZSize))) {

            Rad=pow(pow((RSize-Coord[k].X),2)+pow((RSize Coord[k].Y),2),0.5);

                /* compute r from source to exit point    */
                /* on surface. If r is at a detector pos */

            if ((Rad >= DetectPos) && (Rad <= (DetectPos+DetectSize))) {
                Dy = Coord[k].Y - RSize;
                Dx = Coord[k].X - RSize;
                Tt = atan2(Dy,Dx);

                    /* compute angles Tt from +ve x axis to point */
                    /* compute delta x and y for each vertex      */
                    /* rotate point about angle Tt and project    */
                    /* Z stays the same but convert to int        */

                for (i=1; i<=k; i++) {
                    Dx = Coord[i].X - RSize;
                    Dy = Coord[i].Y - RSize;
                    X1 = floor(Dx*cos(Tt) + Dy*sin(Tt) + RSize);
                    Z1 = floor(Coord[i].Z);
                    DepthInten[X1][Z1] += Coord[i].A;
                }
            }
        }
    }

        /* if not int. over an annulus compute proj */

    if (IntOverAnnulus == 0)  {
        for (i=1; i<=k; i++) {
            X1 = floor(Coord[i].X);
            Z1 = floor(Coord[i].Z);
            DepthInten[X1][Z1] += Coord[i].A;
        }
    }
    return;
}

/* ------------------------------------------------------------------ */
/*  Calculates several projections of the photon distributions taken at */
/*  various times onto the  x plane                                   */
/*  Photons reaching the Detector position when integrated over an annulus */
```

```
/*  will have their paths rotated in the positive x plane before the      */
/*  path projection is taken.                                             */
/* ---------------------------------------------------------------------- */
ComputeFrames()
{
    float Rad,Dx,Dy,Tt,t;
    int i,k,m,X1,Z1,frame;

    if ((IntOverAnnulus == 1) && (ComputeReflec == 0)) {

            /* if int. over an annulus and compute path */

        k = scatter;
        if ((DetectPlace == 1) && (Coord[k].Z <= 0)) ||
           (DetectPlace == 2) && (Coord[k].Z >= ZSize))) {

            Rad=pow(pow((RSize-Coord[k].X),2)+pow((RSize-Coord[k].Y),2),0.5);

                /* compute r from source to exit point     */
                /* on surface. If r is at a detector pos   */

            if ((Rad >= DetectPos) && (Rad <= (DetectPos+DetectSize))) {
                Dy = Coord[k].Y - RSize;
                Dx = Coord[k].X - RSize;
                Tt = atan2(Dy,Dx);
                for (frame=1; frame<=19; frame++) {

                        /* do for all frames (times) */

                    for (i=1; ((Coord[i].T<(frame*5))&&(i<=(k-1))); i++) { }
                      if (i<k) {

                        /* interpolate path to time = frame*25     */
                        /* compute delta x and y                   */
                        /* rotate point about angle Tt and project */
                        /* Z stays the same but convert to int     */

                       t=(frame*5-Coord[i-1].T)/(Coord[i].T-Coord[i-1].T);
                       Dx = (Coord[i].X-Coord[i-1].X)*t+Coord[i-1].X-RSize;
                       Dy = (Coord[i].Y-Coord[i-1].Y)*t+Coord[i-1].Y-RSize;
                       X1 = floor(Dx*cos(Tt) + Dy*sin(Tt) + RSize);
                       Z1 = floor((Coord[i].Z-Coord[i-1].Z)*t+Coord[i-1].Z);
                       MovieFrame[frame][X1][Z1] += Coord[i].A;

                    }
                }
            }
        }
    }

        /* if not int. over an annulus compute proj */

    if (IntOverAnnulus == 0)  {
        for (frame=1; frame<=19; frame++) {
            for (i=1; ((Coord[i].T<(frame*5))&&(i<=(scatter-1))); i++) { }
            if (i<scatter) {

                    /* interpolate path to time = frame*25 */

                t = (frame*5 - Coord[i-1].T)/(Coord[i].T - Coord[i-1].T);
                X1 = floor((Coord[i].X - Coord[i-1].X)*t + Coord[i-1].X);
                Z1 = floor((Coord[i].Z - Coord[i-1].Z)*t + Coord[i-1].Z);
                MovieFrame[frame][X1][Z1] += Coord[i].A;
```

```
        }
    }
    return;
}

/* ------------------------------------------------------------------------ */
/*  Saves information to disk                                               */
/* ------------------------------------------------------------------------ */
DiskWriteData()
{
    int i,j,v,frame;
    float times;

        /* Output Scattered Intensity */

    if  SaveScatInten == 1) {
        if (DataFilePtr=fopen(File1,"w+t"))==NULL) {
            printf("\n Error opening Output data File \n");
            exit(0);
        }
        if  IntOverAnnulus == 1 ) {
            for (i=0; i<=RSize; i++) {
                fprintf(DataFilePtr, "%f\n", BackInten[i+RSize][RSize]);
            }
        } else {
            for  i=1; i<=(2*RSize); i++) {
                for (j=1; j<=(2*RSize); j++) {
                    fprintf(DataFilePtr, "%f  ", BackInten[i][j]);
                }
                fprintf DataFilePtr, "\n");
            }
        }
        fclose(DataFilePtr);
    }

        /* Output projection information */

    if  Proj == 1) {
        if (DataFilePtr=fopen(File2,"w+t"))==NULL) {
            printf("\n Error opening Output data File \n");
            exit(0);
        }
        for  i=1; i<=(2*RSize); i++) {
            for (j=1; j<=ZSize; j++) {
                fprintf(DataFilePtr, "%f  ", DepthInten[i][j]);
            }
            fprintf(DataFilePtr, "\n");
        }
        fclose(DataFilePtr);
    }

        /* Output Movie frames */

    if (DoMovie == 1) {
        if((DataFilePtr=fopen(File4,"w+t"))==NULL) {
            printf("\n Error opening Output data File \n");
            exit(0);
        }
        for (frame=1; frame<=19; frame++) {
            for (i=1; i<=(2*RSize); i++) {
```

```
                for (j=1; j<=ZSize; j++) {
                    fprintf(DataFilePtr, "%f  ", MovieFrame[frame][i][j]);
                }
                fprintf(DataFilePtr, "\n");
            }
        }
        fclose(DataFilePtr);
    }

        /* Output TOF profile */

    if (DoTOF == 1) {
        if ((DataFilePtr=fopen(File3,"w+t"))==NULL) {
            printf("\n Error opening Output data File \n");
            exit(0);
        }
        for (i=1; i<=500; i++) {
            for (j=1; j<=RSize; j++) {
                fprintf(DataFilePtr, "%f  ", TOFArray[i][j]);
            }
            fprintf(DataFilePtr, "\n");
        }
        fclose(DataFilePtr);
    }

        /* Output Confocal Intensity and TOF profile */

    if (DoConf == 1) {
        if((DataFilePtr=fopen(File5,"w+t"))==NULL) {
            printf("\n Error opening Output data File \n");
            exit(0);
        }
        fprintf(DataFilePtr, "%f\n\n", CInten);
        for (i=1; i<=500; i++) {
            fprintf(DataFilePtr, "%f\n", CTOF[i]);
        }
        fclose(DataFilePtr);
    }
    return;
}


 * ------------------------------------------------------------------------ */
main(int argument_count, char **argument_array)
{

        /* Process command line init. file */

    Initialize(&argument_count, argument_array);
    for (i=1; i<=s; i++) {

            /* Scatter the photons */

        if ((i%10000) == 0) {

                /* print status out to file */

            if((DataFilePtr=fopen("status","w+t"))==NULL) {
                printf("\n Error opening Output data File \n");
                exit(0);
            }
            fprintf(DataFilePtr,"\n  Percent done:  %f \n",(float) i*100/s );
            fprintf(DataFilePtr,"  Program will write to:  %s, %s, %s, %s, %s
```

```
            \n\n", File1, File2, File3, File4, File5)
        ;
        fclose(DataFilePtr);
    }
    SetInit();

        /* Loop until out of domain or maxscatter < #scattering events */

    do {

            /* Find Scattering Distance                                    */
            /* Increment # of scat. events & find new coord of photon */
            /* Test to see if photon is still in domain                    */

        scatter++;
        FindDirection();
        TestCoord();

            /* Force scattering event at boundary */

        if ((crosslayer == 1) && (HeteroScat==1)) ForceScatter();

            /* Adjust path length after photon exits medium */

        if (surface == 1) || (done == 1)) AdjustPath();

            /* Calculate reflected photon/refracted trajectory */

        if (surface == 1) DoFresnel();

    } while (done == 0);

        /* Calculate Absorption of Photon and Time of Flight  */
        /* Calculate time lasped photon distribution sequence */
        /* Compute Depth Resolved Projection                  */

    PhotonAbsAndTOF();
    if (DoMovie == 1) ComputeFrames();
    if (Proj == 1)  DoProj();
}

   /* Write data to disk */

DiskWriteData();
```

```
/* var.c                                                              */
/* 02-jul-98 wli                                                      */
/*                                                                    */
/* Monte Carlo photon scattering model through absorbing media based  */
/* on Henyey-Greenstein phase functions                               */

#define MaxPhotonScatter 8000        /*  Maximum array size          */
#define IA1 40014                    /*  Needed for random number gen */
#define IM1 2147483563
#define IM2 2147483399
#define IA2 40692
#define AM  1.0/IM1
#define IMM1  IM1-1
#define IQ1 53668
#define IQ2 52774
#define IR1 12211
#define IR2 3791
#define NTAB 32
#define NDIV  1+IMM1/NTAB)
#define EPS 1.2e-7
#define RNMX  1.0-EPS)

time_t elapsed_seconds;
long int s;                          /*  s photons to be released    */
long int i;                          /*  indexing variable           */
long int n;                          /*  number of photons in dist   */
long int idum;                       /*  Random Number initial int   */
float us;                            /*  scattering coefficient      */
int MaxScat;                         /*  max. # of scattering events */
int ReachedSurface;                  /*  hv reached surface once?    */
float g;                             /*  Henyey-Greenstein g factor  */
char File1[12];                      /*  Output filename #1          */
char File2[12];                      /*  Output filename #2          */
char File3[12];                      /*  Output filename #3          */
char File4[12];                      /*  Output filename #4          */
char File5[12];                      /*  Output filename #5          */
int RSize,ZSize;                     /*  Radial Boundary Constants   */
float NLevel;                        /*  Noise Level                 */
float SourceSize;                    /*  Size of Beam                */
char Dummy[40];                      /*  Dummy string variable       */
float length;                        /*  Length of Photon Path       */
int scatter;                         /*  Number of scattering Events */
int SaveScatInten;                   /*  Save steady state distrib.  */
float RTheta,RPhi;                   /*  things                      */
int surface, done;                   /*  hv reached surface? / done? */
float ReflectedI[100];               /*  Reflected intensity of hv   */
float RefractedI[100];               /*  Intensity of exiting wave   */
float distance;                      /*  Distance of hv travel (pm)  */
float phi;                           /*  Polar coord angle Phi       */
float theta;                         /*  Polar coord angle Theta     */
float newphi;                        /*  Temp Polar coord angle Phi  */
float newtheta;                      /*  Temp. Polar coord angle Theta*/
float TOF;                           /*  Time of Flight of Photon    */
float nu;                            /*  Refractive index            */
int ppu;                             /*  pixels per unit (pixel/mm)  */
float c;                             /*  speed of light              */
float r;                             /*  dummy variable              */
float f;                             /*  focal length of lens        */
float d;                             /*  lens/surface distance       */
float absorb;                        /*  Photon intensity            */
int NumLayer;                        /*  Number of Layers            */
int Finished;                        /*  Finished simulation flag    */
int Proj;                            /*  Compute depth projection    */
```

```
int ComputeReflec;                          *  Compute Reflections          *
int DoTOF;                                  *  Compute Time of Flight       *
int DoExtra;                                *  Compute extras with TOF also *
int DoMovie;                                *  Compute TOF photon dist seq  *
int DetectPlace;                            *  Detector on top or bottom    *
int bounce;                                 *  number of reflections for nv *
float DetectSize;                           *  Detector size in pixels      *
float DetectPos;                            *  Detector Position in mm      *
int IntOverAnnulus;                         *  Integrate of annulus         *
int [illegible] = 0;                        *  Index of each bounce         *
float BackInten[510][510] = 0;              *  Backscattered intensities    *
float DepthInten[510][150] = 0;             *  Depth Intensities            *
float TOFArray[510][510]=0;                 *  Array for TOF profile        *
float MovieFrame[21][510][150] =0.0;        *  Movie Frames                 *
float A[ ];                                 *  Absorbances of layers        *
float Ap[ ];                                *  Used for Absorbance Function *
float n;                                    *  Thickness of each layer      *
float Etof1[510][21] =0 ;                   *  Extra TOF values             *
float Etof2[510] =0;                        *  Extra TOF values             *
long int Etof3[510] = 0;                    *  Extra TOF values             *
float xx,yy,zz,xp,yp,zp,rr;                 *  Temporary variables          *
float sinphi,sinttheta,cosphi,costheta;     *  Temporary variables          *
struct XYZ {float X; float Y; float Z; float T; float A;};
struct XYZ Coord[MaxPhotonScatter];         *  Photon path array            *
```